Fatigue Behaviour of the Novel Titanium Alloys TIMETAL® 407 & TIMETAL® 412

William Davey

Submitted to Swansea University in fulfilment of the requirements for the Degree of Doctor of Engineering

Swansea University

December 2020

Please Note: A five year bar on access has been approved for this thesis.

DECLARATION

This work has not previously been accepted in substance for any degree and is not being concurrently submitted in candidature for any degree.

Signed ..[redacted]..... (candidate)

Date ..23/12/2020.....

STATEMENT 1

This thesis is the result of my own investigations, except where otherwise stated. Where correction services have been used, the extent and nature of the correction is clearly marked in a footnote(s).

Other sources are acknowledged by footnotes giving explicit references. A bibliography is appended.

Signed [redacted]..... (candidate)

Date ..23/12/2020.....

STATEMENT 2

I hereby give consent for my thesis, if accepted, to be available for photocopying and for inter-library loans **after expiry of a bar on access approved by the Swansea University.**

Signed ..[redacted]..... (candidate)

Date ..23/12/2020.....

ABSTRACT

TIMETAL®407 (Ti-407) is a medium strength (~650MPa 0.2%YS) titanium alloy, recently developed by TIMET, in conjunction with Rolls-Royce plc for use in applications requiring high energy absorption at impact. Preliminary Charpy Impact (V notch) testing showed Ti-407 to absorb nearly twice the impact energy of Ti-6-4 and exhibit more than 2.5 times the lateral expansion. Further initial testing suggested the high cycle fatigue (HCF) run out stress of Ti-407 matches that of Ti-6-4 and other high strength alpha-beta titanium alloys. Ti-407 displayed more than double the tool life than that of Ti-6-4. The reduction in tool wear supports lower forces required for faster, more efficient machining. Compared to Ti-6-4, the relatively low elevated temperature flow stress, greater malleability and wide process window should allow Ti-407 to be processed with fewer reheats, while exhibiting reduced surface cracking and giving a consistently good surface finish. Optimised Ti-407 manufacturing processes should allow parts to be formed closer to net shape giving higher yields and requiring less machining to the components finished size.

This project has evaluated HCF, as well as low cycle fatigue (LCF) and dwell fatigue crack initiation mechanisms in Ti-407, to clarify the effects of alloy chemistry, microstructural morphology and scale, and crystallographic texture. A derivative of Ti-407, Ti-412 (~750MPa 0.2%YS) was also tested towards the end of the project and helped to further elucidate understanding of the fatigue characteristics of the two alloys. Of interest was the strong HCF response displayed relative to the monotonic tensile strength. As well as the investigation into the crack initiation mechanisms, an assessment of crack propagation across a range of microstructural conditions was carried out on Ti-407 material.

Acknowledgements

First and foremost I would like to thank my academic supervisors, Professor Martin Bache and Dr Helen Davies and my industrial supervisors, Dr Matthew Thomas and Iain Berment-Parr who have helped me throughout the project. Thank you for all your time and patience over the course of the last four years. I would like to also express my gratitude to Dr Kayla Calvert and Dr Michael Gram for the final check and organsing of clearance.

Thank you to Dr Paul Jones and Dr Chris Newton for your help and support with the mechanical testing. Your time and assistance is very much appreciated.

At TIMET I would like to thank, in particular, Louise Ramsden-Hare and Alun Goulding for the technical insights which helped to tie the thesis together. And to Alun Watts, Simon Howley, Nick Harlin, Nick Watts, Matthew Harris, Eileen Lloyd, Helen Young, Simon Medicke, Phillip Aitchison thank you for putting up with me; it was a pleasure sharing the office with you. I very much enjoyed the banter against the English, I hope I have helped you to understand that the likes of Mike Brown and Owen Farrell are great human beings as well as quality rugby players.

Contents

1 Literature Review

1.1 History of Titanium

In the rural depths of Cornwall, a picturesque church stands in the middle of a small village. Inside the church, underneath one of the large, stained glassed windows, a plaque reads: 'In Recognition of an Outstanding Contribution to the Titanium Industry; 200th Anniversary of the Discovery of Titanium – 1791; Manaccan, Cornwall, England, Presented to William Gregor (1761-1817) "The Scientific Parson"'.

A few hundred yards from the church at the bottom of a hill steep enough to get your legs working on the way back up, a small, unassuming stream works its way peacefully past the village. It was underneath the bridge over the stream, where Gregor discovered the 'black sand' that we now know as ilmenite. From ilmenite, he isolated the calx of an unknown metal which he named mechanite after the place where it was found.

A short time later, Martin Heinrich Klaproth discovered the same element in the mineral rutile. Believing this to be a new discovery, Klaproth named it 'titanium' after the titans of Greek mythology. It was later clarified that Gregor made the discovery first, but the element kept the name chosen by Klaproth.

As a result of the high affinity with oxygen and nitrogen, titanium could not be produced in a commercially viable sense until 1925, more than 130 years after its discovery by Gregor and Klaproth. The key stages in the discovery and development of the production of titanium are listed below [1].

- 1791 – Rev William Gregor discovered 'black magnetic sand' [2] (ilmenite) in riverbeds of the Menchan Valley, Cornwall. After removing the iron with a magnet and treating the remains with hydrochloric acid he noted the remains must be the oxide of the unknown metal, which he named Mechanite.
- 1795 – The German Chemist, Martin Heinrich Klaproth, isolated titanium dioxide (TiO_2) from rutile, a Hungarian mineral. He was the first to name it titanium, somewhat aptly after the mythological Titans. The Titans were 'utterly hated by their father and so detained in captivity by him in the earth's crust [3].'
- 1825 – The extraction of pure titanium proved a difficult task and chemists struggled with it for many years. Jons Berzelius managed to produce very

impure titanium and in 1826 Jean-Baptiste Dumas obtained $TiCl_4$ by chlorinating TiO_2.

- 1887 – Through sodium reaction with the chloride, 95% purity of titanium was achieved by Lars Nilson and Otto Petterson.
- 1910 – Matthew Albert Hunter obtained 99.5% pure titanium sponge by heat treating $TiCl_4$ with sodium in a steel bomb. This became known as the Hunter process.
- 1932 – The Hunter process was optimised by Wilhelm Justin Kroll by changing the reducing agent from sodium to liquid magnesium. In doing this, the production of titanium sponge was finally economically viable. Kroll is therefore seen as the father of the titanium industry and his process is almost completely unchanged since its invention.

Titanium is the ninth most abundant element on earth and its oxide is widely distributed, making up 0.57% of the earth's crust. It is the fourth most abundant metal found in the earth's crust after aluminium, iron and magnesium. The two most common minerals from which titanium is extracted are rutile (TiO_2) and ilmenite ($FeTiO_3$) [4][5], though Gregor later found titanium in corundum from Tibet and in a tourmaline from a local tin mine. Rutile contains 95% titanium dioxide and is the starting point for the majority of titanium metal production. Whilst the ilmenite mineral only contains 50–60% titanium dioxide it still serves an industrial purpose and is used largely for the production of pigments, fillers and other associated products.

1.2 Melting

1.2.1 Sponge production

The production of titanium from its ore and the subsequent melting to produce ingots is constrained by the high affinity of the metal for oxygen and its natural tendency to absorb small interstitial elements such as nitrogen and hydrogen. In order to produce titanium alloys with the high performance capabilities required by the aerospace industry, it is essential that the level of these elements is carefully controlled.

Metallic titanium as produced from the ore is called sponge due to its porous and sponge-like appearance. Titanium sponge, is titanium in its purist form and is the base

for the various alloys and product forms that it will then be processed into. The extraction of metallic titanium from rutile has 5 distinct stages:

1. Chlorination of the ore to produce $TiCl_4$. The basic chlorination reaction happens as follows:

$$TiO_2 + 2\,Cl_2 + C \rightarrow TiCl_4 + CO_2 \text{ and,}$$

$$TiO_2 + 2\,Cl_2 + 2C \rightarrow TiCl_4 + 2CO_2$$

2. Distillation of the $TiCl_4$ to purify it.

The second step is the distillation process. The starting grade of $TiCl_4$ from the chlorination process requires further purification. This is done through fractional distillation of $TiCl_4$.

3. Reduction of the $TiCl_4$ to produce metallic titanium (the kroll process).

The purified $TiCl_4$ is put into a reactor filled with molten magnesium and an inert gas to prevent the violent reaction of magnesium with oxygen. The reactor is heated to 850℃ to drive the following reduction reaction:

$$TiCl_4 + 2Mg \rightarrow Ti + 2MgCl_2$$

This actually occurs in two steps as follows:

$$TiCl_4 + Mg \rightarrow TiCl_2 + MgCl_2$$

$$TiCl_2 + Mg \rightarrow Ti + MgCl_2$$

4. Purification of the metallic titanium to remove by-products of the reduction process. This leaves titanium sponge which can contain up to 30% of impurities, mainly $MgCl_2$. This is removed by heating at a high temperature. The graph below displays the amount of titanium sponge produced each year from 2005-2016.

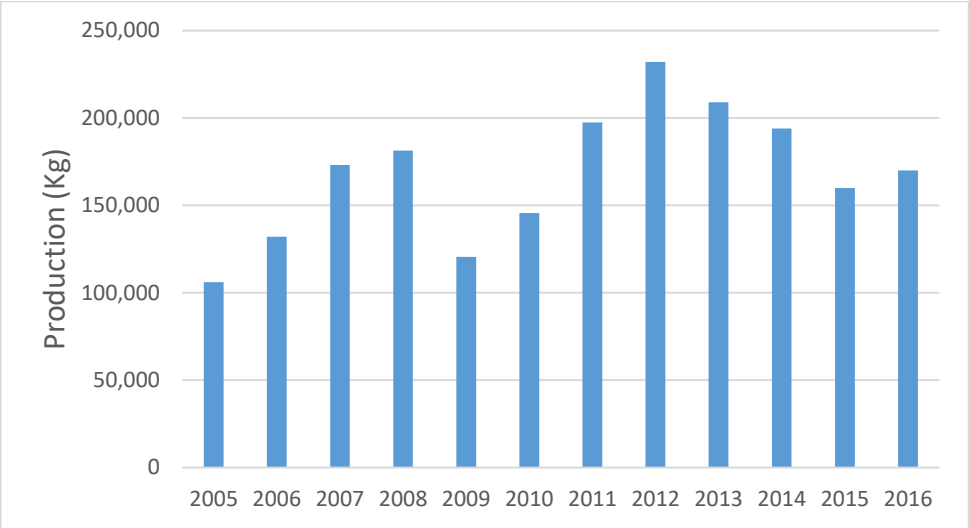

Figure 1.1: World production of titanium sponge from 2005-2016.

5. The final step, after the removal of the excess Mg and $MgCl_2$, is the crushing and sizing of the sponge into granules, in order to create a suitable product for the subsequent melting of commercially pure (CP) titanium and titanium alloys.

1.2.2 Ingot Production

The titanium granules from sponge production are blended with the master alloying elements and are dry pressed to form compacts. The compacts are welded together in a plasma welding chamber to produce a consumable electrode for the subsequent melting operation. The electrode is melted in a copper crucible which is cooled either by water or a sodium-potassium eutectic. Because water reacts with titanium, water-cooled processes must be placed inside bomb proof chambers. When this process was first implemented, explosions occurred within water-cooled cells when the arc pierced the reactor wall. For this reason sodium-potassium eutectic is preferred as these furnaces can be placed on open shop floors.

During the melting operation, only a small volume of metal is molten at any one time. As a result, mixing is limited and overall homogeneity is largely dependent on the homogeneity of the original compaction. This means that after a single melt variations in compositions may persist. These can be removed by further melting operations. Usually when the ingots are to be machined for aerospace applications the electrode is melted three times. Figure 1.2 shows a schematic diagram of the vacuum arc remelting (VAR) process [6]. The VAR process is both expensive and difficult, with complex

interactions between the electromagnetic flow and heat transfer processes and therefore is employed only in high value applications. However, it does allow for good control over the solidification rate of the molten material which means that the microstructure can be controlled, and the degree of alloying element segregation can be limited. When these stages have been completed the resultant ingot is machined to facilitate the further processing operations.

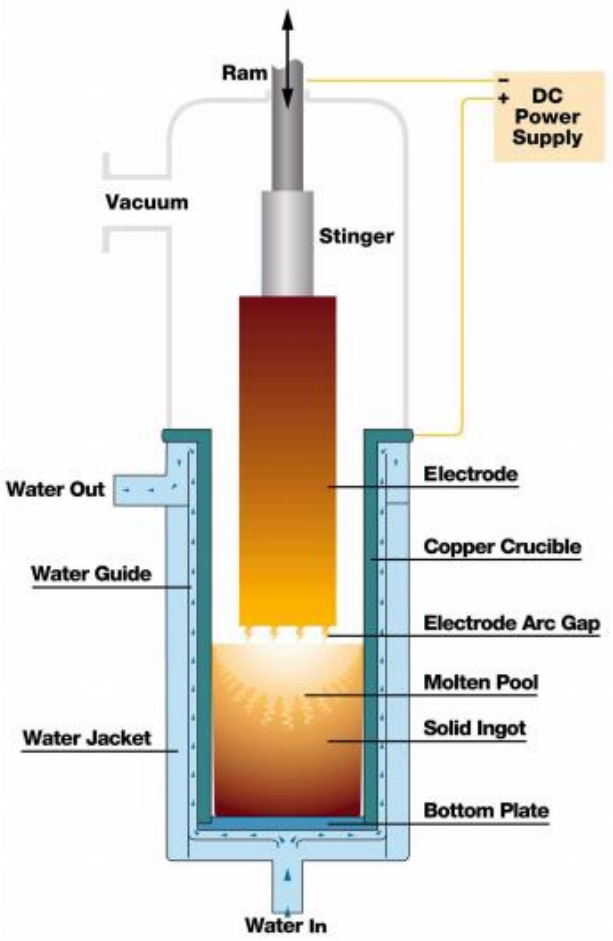

Figure 1.2: Schematic of vacuum arc re-melting process.

1.2.3 Melting Defects

There are three main defects associated with the VAR process. These are: the occurrence of high density inclusions (HDI's); hard alpha inclusions referred to as low density inclusions (LDI's) and beta fleck. These inclusions can be difficult to detect and in the past have resulted in catastrophic jet engine failures, Sioux city being the most notable.

The high density inclusions (HDI's) are based on heavy elements such as molybdenum, tungsten and tungsten carbide. Their introduction occurs through contamination of the raw materials used in the ingot production, for example tungsten carbide cutting tool debris. For this reason, ballpoint tungsten pens are prohibited from titanium production areas. These elements have high melting temperatures and therefore they do not dissolve. Because they are high density they drop straight through the melt to the cold zone and solidify. Since these heavy elements have a different thermal expansion coefficient they contract differently to the melt, meaning they de-bond from the surrounding titanium on cooling. This means that HDI defects may audibly rattle. If they are badly bonded they are relatively easy to detect by ultrasonic scans. However when de-bonding does not occur detection is more difficult.

The hard alpha defect is a low density inclusion (LDI). These are particles or regions which arise during melt processing and are associated with high concentrations of the interstitial alpha stabilisers; nitrogen, oxygen and carbon. The short residence time of the material in the molten pool is not sufficient to remove these defects. To eliminate this defect the cold hearth process has been introduced. This method helps to eliminate the defect population.

Finally beta fleck is a problem associated with β eutectoid elements, these being Fe, Cr, Mn, Ni and Cu. As the electrode melts, macro-segregation may occur, resulting in regions of very high beta content. These regions tend to be softer and consequently are a source of crack initiation. The only way of detection is by macro etching and looking at the surface microstructure. Large beta grains would be seen in the areas to which the eutectoids have segregated.

One other problem associated with the VAR process is a melt defect called a 'dark etching area' (DEA). This is where the lighter elements evaporate during the melting process resulting in an area at the top of the ingot with very limited alpha content. This results in a decrease of strength in this area. While easy to detect, DEA's result

in a loss of yield, with the affected material at the top of the ingot removed and scrapped.

Avoidance and detection of defects associated with melting is extremely important to ensure the integrity of components on which hundreds of lives could depend. The number of accidents per flight has been continually reducing so that now flying is extremely safe thanks to the robust processes in place. In 2019 you were more likely to die falling out of bed than you were in a plane crash!

1.2.4 Advanced Melting Techniques

A newer melting technique is cold hearth melting [7]. In cold hearth melting the raw materials enter a water-cooled cooper hearth at one end where they are melted by means of plasma torches or electron beam guns. Heating is maintained as the molten metal progresses along the hearth and is deposited in an ingot mold at the other end. A solid skull develops between the pool of molten metal and the copper hearth. HDI's entering the feed material sink to the bottom of the pool and become trapped in the skull. The hard alpha particles will behave in a similar way if they are denser than the liquid metal. If not they are carried out along the stream and are dissolved as they move along the molten pool. Figure 1.3 shows a schematic of the process [8].

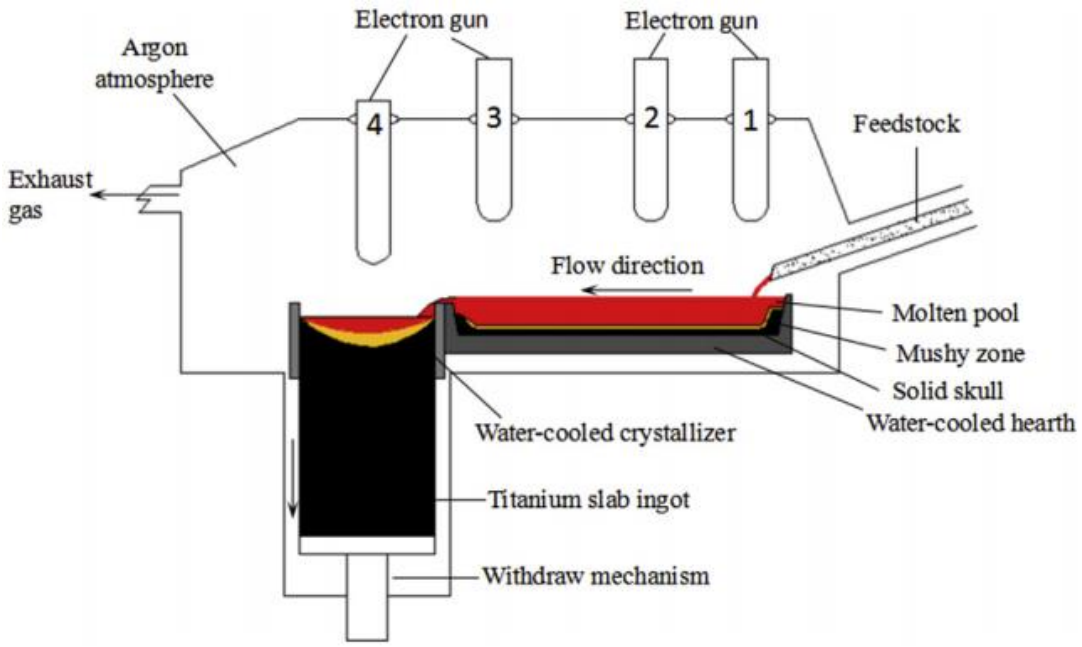

Figure 1.3: Schematic of cold hearth melting process.

1.3 Industrial Production and Applications

From a commercial perspective the high strength, low density and very good corrosion resistance of titanium make it attractive for use in a wide variety of areas including aerospace, biomedical, automotive and for components in chemical processing equipment. The high cost of titanium has limited its use to some extent, for example within automotive applications. Designers must take into consideration the performance benefits that come from titanium against the reduced cost of other materials [9]. With stricter environmental legislations being introduced, requiring the use of higher performance materials that enable more efficient engines, there is scope for future demand in this area to increase.

Following the invention of the Kroll process in 1932, the USA lead the titanium production industry from 1947, which grew rapidly due to military demand. As a result of these requirements the US government funded companies such as TIMET, founded in 1950, and RMI, founded in 1958, to erect large titanium sponge production plants.

In the United Kingdom, commercial production commenced in the early 1950s with Imperical Chemical Industries (ICI) – more recently IMI – and Jessop Saville producing a range of alloys. On the continent, France and Germany began production in the mid 1950's with Japan and the USSR starting production at about the same time. Titanium production has steadily grown at an average rate of 8% per annum from the 1960s to the present day.

From a historical perspective, the titanium industry is split into two main phases. The first phase, starting from the mid-1950s and lasting up until the 1980s is characterised by the technical progress made, with the development of new alloys [4]. The second phase saw a transition to a more commercially driven industry where economics became the most important consideration [10].

The titanium market has seen significant fluctuations over time in terms of metric tonnes produced per year, and cost of titanium sponge per kilogram, driven mostly by demand from the aerospace market. For example, North American titanium sponge production dropped by roughly 60% between 1989 and 1994. In this period the world-wide capacity for the production of titanium sponge dropped by 25%. This was due to lower demands from both the US and Soviet Union following military budget cuts. Following 1994 which was the lowest point in terms of titanium sponge production, a general upward trend has been seen, (demonstrated in Figure 1.1) resulting from

increased commercial aircraft sales. Cycles of overcapacity, followed by supply shortages have been a key business issue for the titanium industry.

The most common applications for titanium alloys are the airframe, of which titanium takes up roughly 10% of the total weight, and the jet engine, with titanium alloys comprising up to 25% of the weight. However a sign of decreasing demand is that the fan blades of the GE90 which were previously manufactured from Ti-6-4 material, are now made from polymer composites.

In order to reduce the dependence of the titanium market on the aerospace sector, considerable effort has been made to develop other non-aerospace applications. An area which titanium supply grew into in the 1990s was sporting goods. In 1997, 4,500 metric tonnes of Ti-6-4 was used in golf club driver heads. Relative to steel used previously, titanium offers higher strength and lower density, meaning larger club heads could be used creating a larger 'sweet spot' on the club head whilst retaining club head speed. Titanium is also used in bicycle frames, tennis rackets and ski edges, amongst many other pieces of sporting equipment [11].

The biomedical field uses titanium for implant materials. In the past CP titanium and Ti-6-4 were most commonly used, but more recently aluminium and vanadium free alloys were developed due to the suspicion of the toxicity of aluminium and vanadium in the human body [12].

Another more recent application for titanium is armour. Its use is driven by the need for lighter and more mobile units which can be transported by air. Titanium offers the good impact strength required by armour and offers significant weight savings for armoured vehicles.

Motivated by the production of titanium at a lower cost, research has been conducted to find a method that does not involve the Kroll process which is a labour and energy intensive, environmentally unfriendly and multi-step semi-batch process lasting five days. For every kilogram of titanium produced, 50kW of energy is required and 2 Kg of carbon dioxide is produced. If an alternative, cheaper method were to become successful it would help to bring stability to the titanium industry as it would open up the market to more price sensitive applications. This would help to dampen the dramatic market swings generated by the capricious aerospace industry. Over the course of the last couple of decades, much research has been focused on the Fray-Farthing-Chen (FFC) Cambridge Process, invented in the 1990s [13]. This reduces TiO_2 directly using calcium chloride molten salts and offers potential to make both

cheaper and better quality titanium. Current estimates of the optimised process suggest an energy consumption of 12.5kW/Kg, and energy saving of 75%. There are still obstacles associated with this process that require further understanding and so it may be some time before this method is implemented commercially.

1.4 Crystal Structure

A crystal structure can be explained as a physically homogeneous solid in which atoms are arranged in a repeating pattern. The crystal structure plays an important role in determining the physical properties of the metal. The most common crystal structures among metals are body-centred cubic (BCC), face-centred cubic (FCC) and hexagonal close packed (HCP).

Titanium is an allotropic material meaning it changes crystal structure depending on the temperature. The word allotrope comes from Greek; allos meaning other and tropos meaning form [14]. Pure titanium undergoes a change in crystallographic arrangement at 882.5℃ but for titanium alloys this temperature is governed by the alloying elements. Below the transformation temperature the crystal structure is HCP and this arrangement is known as the alpha phase. When the temperature is raised above 882℃ the crystal structure changes from HCP to BCC, known as the beta phase. The two crystal structures are displayed below in Figure 1.4(a) and 1.4(b) [4]. The β transus temperature is defined as the lowest equilibrium temperature at which the material is 100% beta. The beta transus temperature is a critical parameter in the thermomechanical processing of titanium alloys and for Ti-407, this temperature is 877℃.

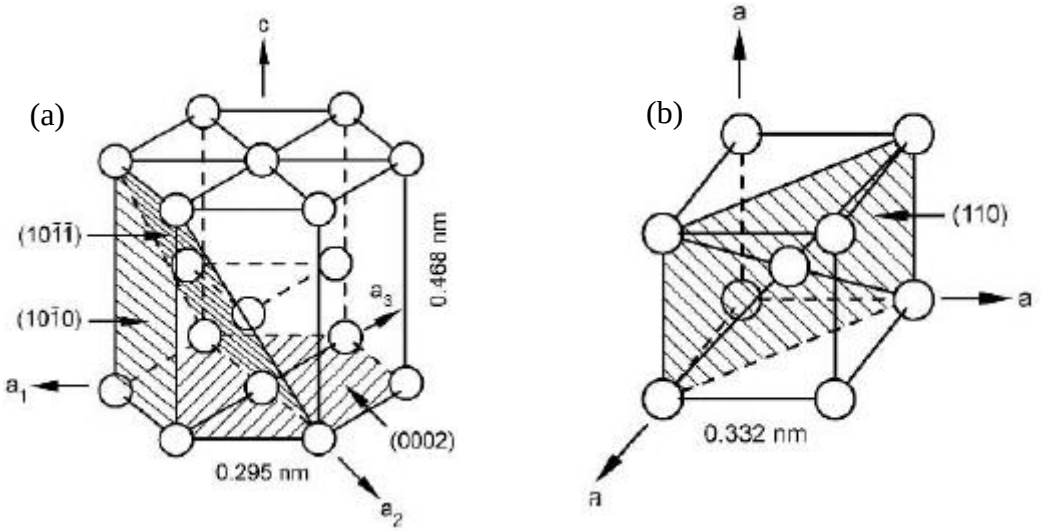

Figure 1.4: (a) Unit cell of HCP crystal structure (b) Unit cell of BCC crystal structure.

As shown in Figure 1.4(a), the room temperature lattice parameters of the titanium HCP unit cell are a (0.295nm) and c (0.468nm) giving a c/a ratio of 1.587. This is smaller than the ideal ratio for hexagonal close packed structures, this being 1.633.

The smaller than ideal ratio means that a titanium HCP cell will tend to yield more easily under tension than compression in the <c> direction. The ideal ratio is calculated based on the ideal geometry of the hexagonal close packed unit cell [15].

The atomic packing fraction (APF), or the fraction of the total lattice volume occupied by atomic spheres for an ideal c/a ratio can be calculated based on equation 1.1 below.

$$\text{APF} = \frac{V_{particles}}{V_{unit\ cell}} \tag{1.1}$$

In this case there are twelve corner atoms having one-sixth contribution each, two face centred atoms having half contribution each and three body atoms having one contribution each. This results in an APF of 0.74. This is an important value because it describes material properties, so can be used as a comparison between metals and alloys. Metals with a higher atomic packing factor have a higher workability because it is easier for planes of atoms to slide past each other. This is analogous to rolling a piece of chalk across 4 or 5 pieces of chalk glued to a surface. The closer the pieces of chalk are to one another, the easier it is to roll the piece of chalk over the top.

The lattice parameters have significant implications on the alloy's deformation mechanisms, and change based on alloying elements. Increasing the c/a ratio means that the cell is elongated in the c-axis. Indicated on Figure 1.1(a) are the three most densely packed lattice planes, the (0002) basal plane, the $(10\bar{1}0)$ prismatic plane and the $(10\bar{1}\bar{1})$ pyramidal plane. The (0002) basal plane spacing is c/2, and the $(10\bar{1}0)$ prism plane spacing (derived based on equilateral triangle of sides a) is $\sqrt{3}a/2$ [15].

The unit cell of the BCC phase shows a lattice parameter value for pure titanium at 900℃ of a=0.332nm. It also indicates one variant of the six most densely packed (110) lattice planes. The BCC structure has a higher symmetry level than that of HCP, which means it has more slip systems on which dislocations can glide. For this reason the beta phase is more formable and ductile.

1.5 Physical and Mechanical Properties

An atom consists of a nucleus, made up of neutrons and positrons, orbited by electrons which travel around the shells surrounding the nucleus. As electrons are electrically attracted to the nucleus of the atoms, electrons will generally occupy the outer shell (valence shell), only if the inner shells are completely filled by electrons. This,

however, is not the case with titanium. Titanium has two electrons in both the third and fourth shell.

When the outer shells are filled before the inner shells are completely occupied it is known as a transition metal and it is this arrangement of electrons that is responsible for the unique physical properties of titanium, including its high hardness and melting temperature. A few other example of transition metals include nickel, iron and cobalt.

Some basic characteristics of titanium are given Table 1.1 and are compared to iron, nickel and aluminum [16] [17].

Table 1.1: Physical and Mechanical properties of Titanium, Nickel, Iron and Aluminium.

Property	**Titanium**	**Nickel**	**Iron**	**Aluminium**
Density (g/cm^3)	4.505	8.89	7.86	2.7
Melting Temperature (℃)	1665	1455	1535	660
Young's Modulus (GPa)	120	190	210	70
0.2% Proof Stress (MPa)	340	150	185	35
Tensile Strength (MPa)	440	450	340	80
Elongation (%)	29	47	39	47

Titanium is lightweight, strong and corrosion resistant. Its density is 56% that of steel and it has a good strength to weight ratio. However, due the high cost of extraction, titanium is used only where performance is the priority. The high cost of extraction comes from the reactivity of titanium with oxygen. This reactivity does, however, also provide benefits to the properties of titanium. The reaction with oxygen results in the formation of a stable and adherent oxide layer which, when exposed to air offers superior corrosion resistance in various types of aggressive environments. However, this reactivity limits the maximum temperature of titanium alloys to roughly 600℃. Above this temperature, the diffusion of oxygen through the oxide surface layer becomes too fast, resulting in excessive growth of the oxide layer and embrittlement of the adjacent enriched oxygen layer on the surface of the titanium alloy [18].

Figure 1.5 shows a comparison of the strength to weight ratio (specific strength) of titanium, nickel, steel and aluminum as a function of temperature. As can be seen, the performance of titanium is significantly better than that of nickel up to a certain temperature (600℃–700℃) where the strength then rapidly drops off. The high

specific strength and specific stiffness accounts for the fact that the major influence behind the development of titanium has been the aerospace industry. This interest has led to the development of a wide range of high-performance alloys.

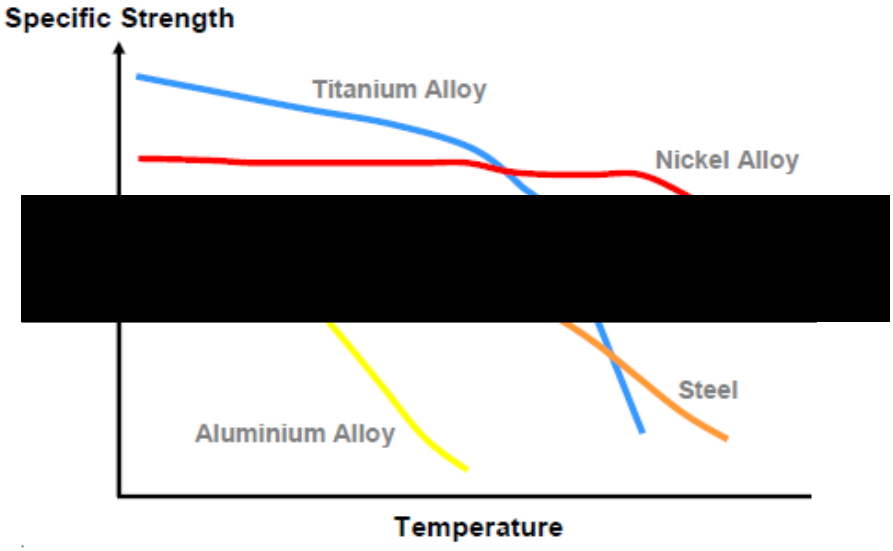

Figure 1.5: Specific strength versus temperature comparison [19].

The yield strength is of particular importance when considering the mechanical properties of alloys, as this is the point at which the material starts to deform plastically. In polycrystalline materials the Young's modulus and yield strength change with crystallographic orientation, depending on the maximum Schmid factor, which links the tensile direction to the slip direction. The macroscopically observed yield is related to the critically resolved shear stress (CRSS) by an average Schmid factor. The critically resolved shear stress is the component of shear stress, resolved in the direction of slip, required to initiate slip in a grain [20]. The resolved shear stress is related to the applied shear stress as shown by equation 1.2.

$$\tau_{RSS} = \sigma_{app} m \tag{1.2}$$

Thus, the higher the Schmid factor (m), the lower the stress required to cause slip. For this reason, the primary slip system of a crystal will be the system with the highest Schmid factor. The graph in Figure 1.6 below, shows the extent to which the Young's modulus varies based on the crystallographic direction.

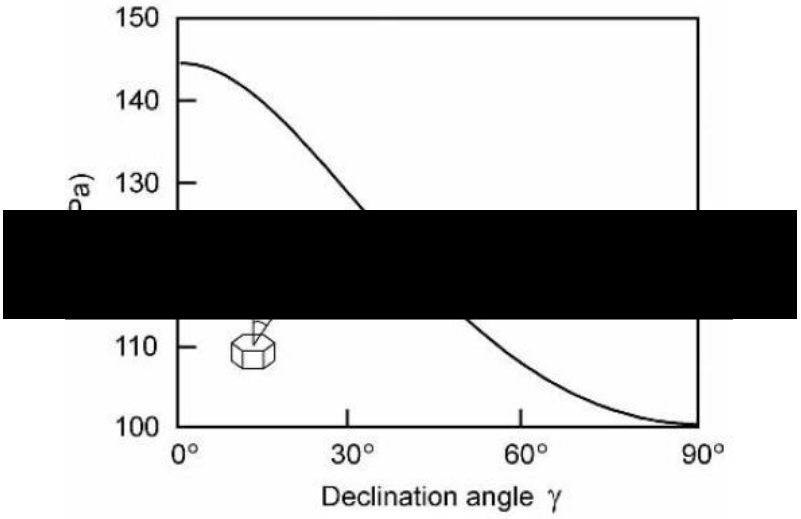

.

Figure 1.6: Relation between orientation of HCP titanium single crystal and Young's modulus [4].

In the case of two, randomly orientated grains under load, one grain will have a larger yield strength than the other. When the grains are subjected to load the weaker grain will yield first, and as it deforms a stress concentration will build up in the stronger grain near the boundary between the two grains. The stress concentration activates dislocations in the available glide planes. These dislocations are referred to as geometrically necessary dislocations (GND's) as they ensure that the strain in each grain is equivalent at the grain boundary [21].

In a polycrystalline material, once slip has initiated in certain grains, further deformation is accommodated plastically but little increase in load is supported by the yielded grains. Therefore, a greater proportion of the load is partitioned to the grains that are yet to yield. As the load is increased further, the difference between the grains that have and have not yielded further increase until slip is induced in all grains. At this point, release of the load gives rise to residual microstrains [22]. Dye et al showed that for FCC metals, representative of nickel and austenitic steels, at small plastic strains when few grains are yielding, intergranular microstrain accumulation is swift. The rate of strain accumulation decreases as more grains yield, until all grains have yielded. At this point strain hardening and texture evolution cause further intergranular microstress development. Neutron diffraction techniques were used to accurately evaluate the micro-strains and micro-stresses. J.R.Cho et al [23] used the same technique on Ti-834 to characterise the intergranular strains in the alpha phase of Ti-834 during tensile testing.

In crystal structures with fewer than five active slip systems, such as is the case for HCP crystals, the specimen will exhibit brittle failure instead of plastic deformation. Basal and prism slip alone (which provide two slip systems each), do not supply sufficient slip modes to satisfy the condition that every grain must be able to plastically deform to meet the shape changes imposed by its neighbours – the von Mises criterion. Slip on <c+a> systems provide the additional c-axis deformation required for titanium to be a ductile metal. The slip systems of HCP structures are shown below (Figure 1.7). These consist of the prismatic <a> type slip, basal <a> type slip, pyramidal <a> type slip and 1st and 2nd order pyramidal <c+a> type slip.

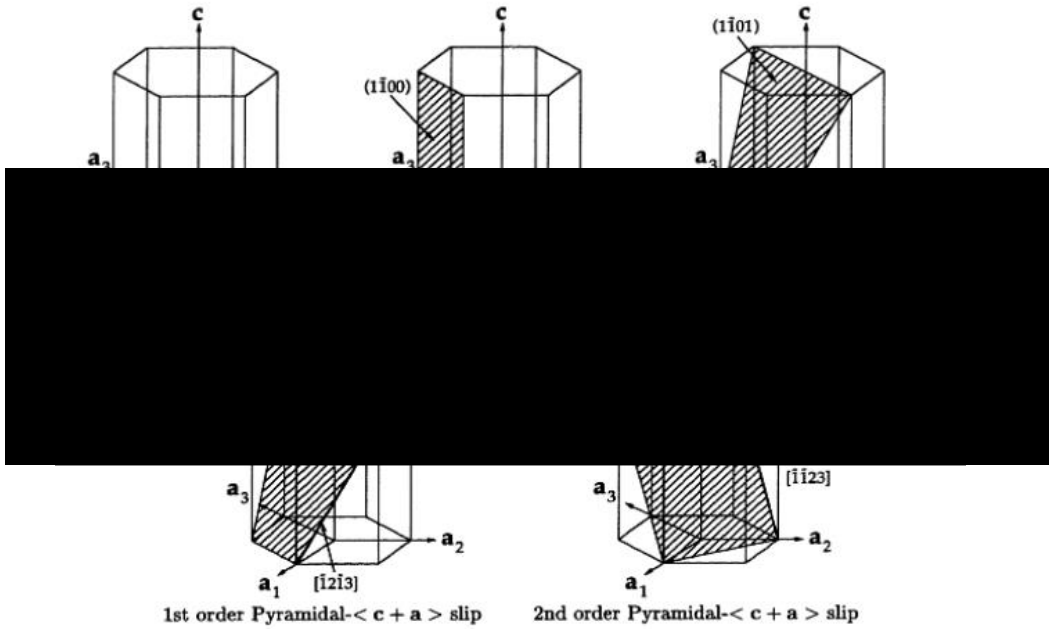

Figure 1.7: HCP slip systems for titanium [24].

As a rule, slip is most easily activated when the slip plane is parallel to both the plane of greatest atomic density and to the largest inter-planar spacing. Therefore, in the case of the HCP structure it is the basal slip modes that are the first to become active with the lowest CRSS [25]. Work has shown the critical resolved shear stress for prismatic slip to be roughly equivalent to that for basal slip [26], though the relative strength for slip activation does change with alloy chemistry as suggested above. However, it has been shown that the <c+a> pyramidal type slip systems are roughly three times harder to activate than <a> type systems [27].

Dislocation theory is a rather broad and complex topic [15]. A dislocation can be defined as the area between a slipped and unslipped region in a crystal structure. Dislocations provide a mechanism for plastic deformation. A dislocation has two main properties, a line direction and the Burgers vector. The Burgers vector describes the magnitude and direction of distortion to the lattice caused by the dislocation. The local

atomic structure of a dislocation is determined by the Burgers vector. The two most commonly observed dislocation types are edge and screw. For an edge dislocation the Burgers vector is perpendicular to the line direction. For a screw dislocation the Burgers vector is parallel to the line direction.

Dislocation density increases with increased plastic deformation. Common mechanisms for dislocation formation include grain boundary initiation and interfaces between the lattice and the surface. The interface between an oxide layer and a metal surface greatly increases the dislocation density as the oxide layer puts the surface of the metal into tension. This is because the oxygen atoms squeeze into the lattice so that the oxygen atoms are under compression.

1.6 Alloy Types

Titanium has very limited use in its pure form as it is too soft for the majority of industrial applications. In order to produce mechanical properties that can withstand the challenging conditions required within the jet engine it must be alloyed with other elements.

Titanium alloys can be described as alpha ($\propto$), beta (β) or alpha/beta ($\alpha + \beta$) depending on whether the alloying elements act to stabilise the HCP alpha phase or the BCC beta phase. The three groups get their names based on which phases are stable at room temperature. This is displayed schematically in the phase diagrams presented in section 1.6.1. Typical alpha stabilisers include aluminium, oxygen and nitrogen. Tin and zirconium are seen as neutral alloying elements as they have a small effect on the beta transus. The beta alloying elements include molybdenum, vanadium, chromium and niobium. Most alloys will contain both alpha and beta alloying elements, so the classification of the alloy depends on the relative proportions of each type. In order to categorise the elements it is common to express all the alpha stabilisers as aluminum equivalent and all the beta stabilisers as molybdenum equivalent. This is done through the two expressions given below given in equations 1.3 and 1.4.

$$\text{Al Equivalent} = \text{Al} + \frac{1}{3}\text{Sn} + \frac{1}{6}\text{Zr} + 10(\text{O} + 2\text{N} + \text{C}) \tag{1.3}$$

$$\text{Mo Equivalent} = \text{Mo} + 0.67\text{V} + 0.28\text{Nb} + 0.2\text{Ta} + 0.4\text{W} + 2.5\text{Fe} + 1.25\text{Cr} + 1.7\text{Mn} + 1.25\text{Ni} + 1.7\text{Co} \tag{1.4}$$

The various alloy types, their Al/Mo equivalence and application area are summarised in the table below. The near alpha and near beta alloy class reflect the fact that they contain only small amounts of beta phase and alpha phase respectively.

Table 1.2: Titanium alloy types.

Class	Aluminium Equivalent	Molybdenum Equivalent	Property/Application
Alpha	< 8	< 1	Low Strength, corrosion resistant
Near Alpha	8 to 10	< 2	High strength, elevated temperature
Alpha/Beta	5 to 10	2 to 8	General purpose high strength. Good toughness
Near Beta	< 8	10 to 15	High strength, high toughness, good forgeability
Metastable Beta	< 6	15 to 30	Very high strengths up to 1800MPa

Near alpha alloys such as Ti-834 and Ti-1100 [28] currently work near the limit of titanium's temperature capability at around 600℃ and are located in the HP compressor sections. Alpha alloys are able to retain their mechanical properties and creep resistance at high temperatures [29][30][31]. An important constituent of the high temperature alpha alloys is the α_2 intermetallic phase. The inclusion of Ti_3X precipitates (where X denotes a given alpha stabliser) have been shown to lead to significant reductions in ductility, due to promotion of slip band formation and inhomogeneous planar slip [32], as well as reduction in fracture toughness [33][18]. However, the intermetallic phase is much stronger than the alpha phase for high temperatures and studies have shown that in order to obtain high strength at temperatures of over 500℃ it is essential to include the α_2 phase. The work done by Roseberger and Ghonem [34] found Ti_3Al has a beneficial impact on the creep resistance of Ti-1100, which is increasingly important as component in service life times can be more than 100,000 hours. A feature of high temperature alpha alloys is exhausting the limits of solid solubility [35].

The well-established alpha/beta alloy, Ti-6Al-4V, the 'workhorse titanium alloy', is used for a large number of components within the engine, in part due to the range of microstructural forms produced via thermomechanical processing that can be tailored to specific applications. Ti-6-4 accounts for 50% of the total titanium production [36].

Beta systems are defined as alloys that contain enough beta stabilizer to retain 100% beta phase upon quenching from above the beta transus. The most common alloying elements, vanadium and molybdenum increase the strength of the alloy. Relative to alpha/beta systems, beta alloys tend to have higher yield and tensile strengths. Near beta alloys are used for the intermediate compressor stage owing to the good strength possessed by the alloy. Beta alloys, due to their combination of high strength, formability and toughness are used for aerospace fasteners and in dental applications. Wider adoption of beta alloys however is limited by cost due to both the expense of beta additions as well as processing expense due to the cost of casting them. This limits their use to niche applications.

The graph below (Figure 1.8) presents a selection of common titanium alloys moving from near alpha alloys on the left, through the alpha/beta alloys in the middle, to near beta alloys on the right.

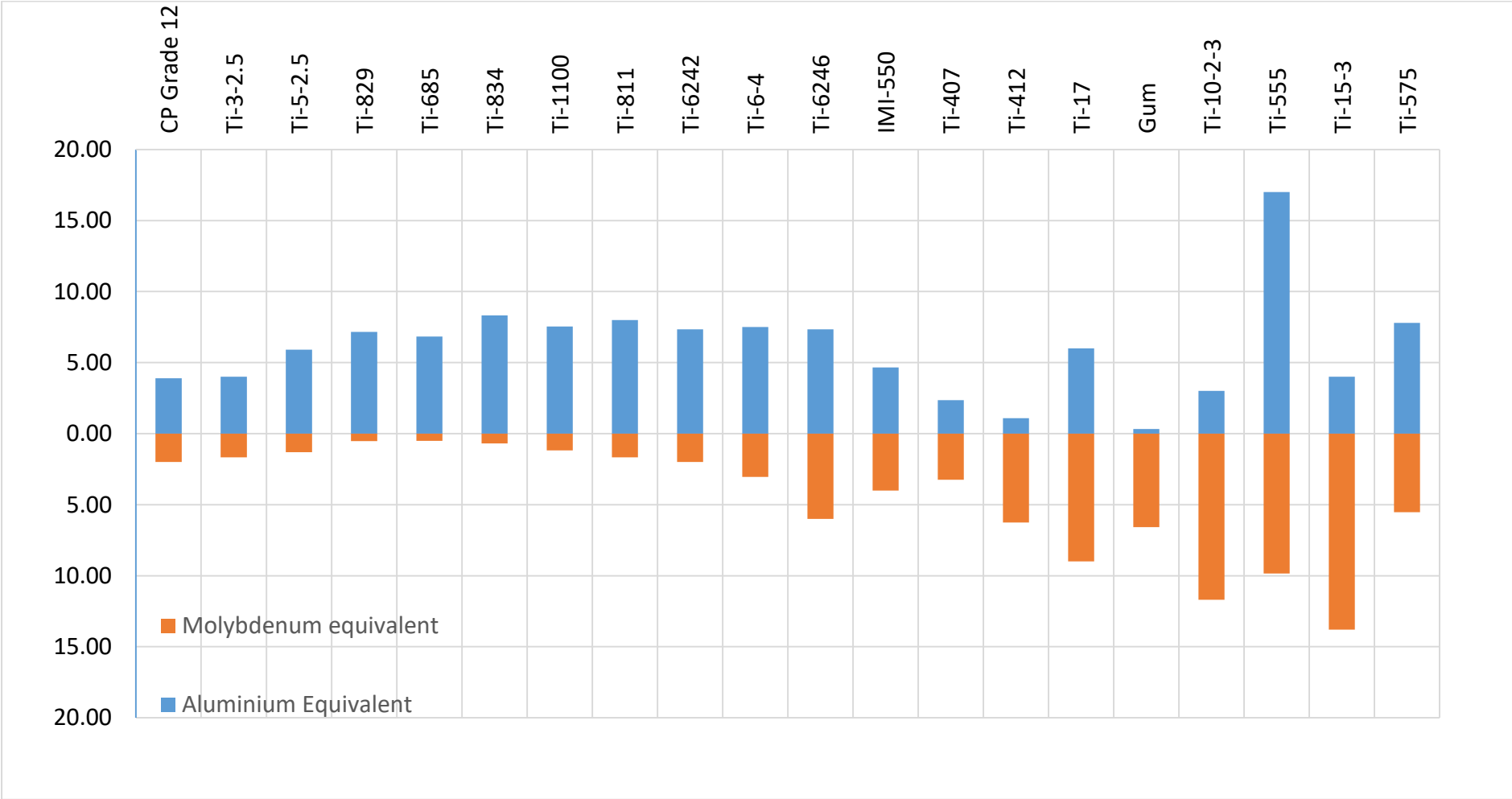

Figure 1.8: Common titanium alloys against their Aluminium and Molybdenum equivalent levels.

1.6.1 Phase Diagrams

The effect of alloying elements can be visualised using phase diagrams. Figure 1.9 below shows a typical example of an alpha stabiliser phase diagram.

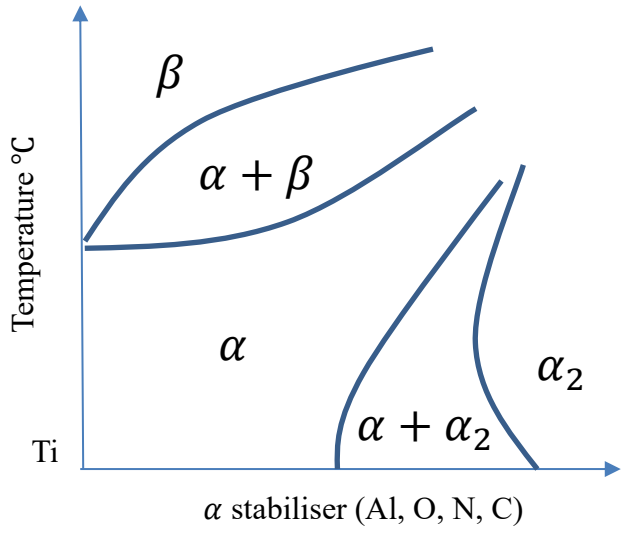

Figure 1.9: Alpha stabiliser phase diagram.

As the alpha stabiliser's proportion is increased a two phase field is opened up along with an increase in the temperature at which alpha phase is stable. However, beyond a certain limit, one enters the $\alpha + \alpha_2$ region. As α_2 is brittle, as mentioned above, it limits the amount of alpha stabilisers used. The aluminium equivalent equation given in 1.3 is useful because it can predict that α_2 will form if the aluminium equivalence is equal to or greater than 9.

The neutral alloys mentioned above, tin and zirconium, have very simple phase diagrams shown below.

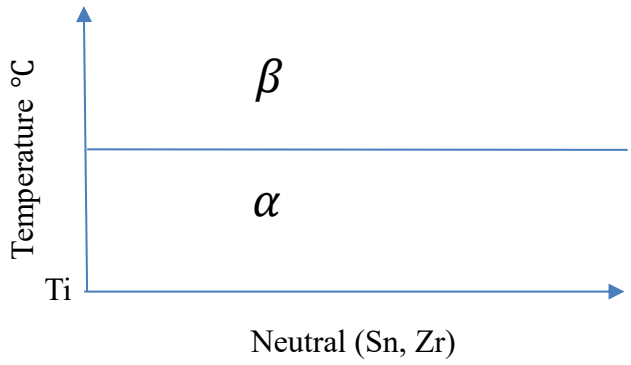

Figure 1.10: Neutral phase diagram.

There are two beta phase diagrams, one representing the effect of isomorphous stablisers, and the other the effect of eutectoid stabilisers. These two alloy types are referred to in a little more detail in section 1.6.3 below. These are displayed in Figures 1.11 and 1.12 below.

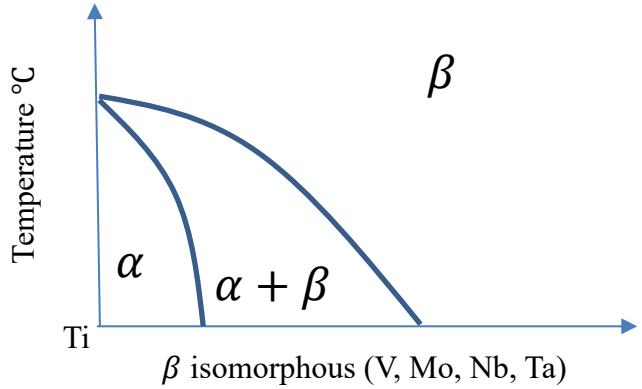

Figure 1.11: Beta isomorphous phase diagram.

Figure 1.11 shows that enough beta stabliser will give an alloy that is 100% beta at room temperature.

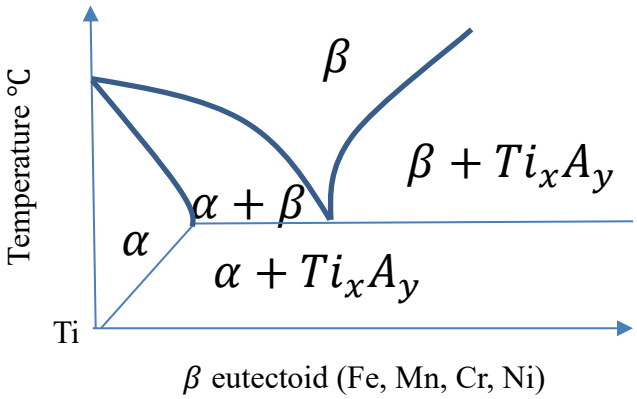

Figure 1.12: Beta eutectoid phase diagram.

As can be seen, eutectoids have the propensity to form intermetallic phases; these phases tend to be very strong, but also brittle. This is a consequence of the ordered crystal structure and their low symmetry nature. This leads to a combination of limited slip systems and high activation energy for dislocation motion. Similar to α_2, these intermetallic phases can have a detrimental effect on fracture toughness and ductility.

1.6.2 Alpha Stabilisers

As displayed in Figure 1.9, alpha stabilisers such as aluminium and oxygen increase the beta transus temperature, meaning the temperature at which the alpha phase is stable is increased. The basic mechanisms for strengthening alpha phase alloys are solid solution strengthening both by interstitials, where the alloying elements sit between the titanium matrix, and substitutional, where the alloying elements replace the titanium atom. The resulting disruption to the crystal structure impedes dislocation movement through the stress fields making plastic deformation harder. Interstitial alpha elements include oxygen, nitrogen and carbon and substitutional elements include aluminium, tin and zirconium.

Early alloys focused on the use of alpha elements in order to help with creep and strength requirements. It was found that if too high a proportion of alpha stabilising elements were used, i.e. the solid solubility limit was reached, fabrication becomes more difficult and the alloys become susceptible to embrittlement during processing or exposure to temperature owing to the formation of Ti_3x (α_2). Detail below is given of the specific alpha stabilisers.

1.6.2.1 Aluminium

Aluminium dissolves in the titanium matrix and acts to increase the strength of titanium for temperatures up to 550℃. Aluminium atoms are slightly smaller than titanium atoms (2.8:2.93 A) and therefore, their addition reduces both the ‘a’ and ‘c’ lattice parameters for the hexagonal unit cell. Aluminium is less dense than titanium so the simple binary alloy has a lower density than pure titanium. Aluminium content has also been shown to influence deformation mechanisms. High aluminium alloys tend to suppress deformation by twinning [25] as more aluminium increases the stacking fault energy, reducing the propensity for twinning to occur. Aluminium also tends to increase <a> type slip on the basal plane [37].

1.6.2.2 Tin and Zirconium

Tin and zirconium offer high temperature strength benefits to the alloy, going beyond the 550℃ limit of aluminium. However, they are very weak stabilisers with only 1/3 and 1/6 per unit of the effect of aluminium respectively, so can be considered as neutral alloys, having a near negligible effect on the beta transus temperature.

1.6.2.3 Oxygen and Nitrogen

Oxygen and nitrogen can offer low temperature strength benefits. However, it is important that the levels of each element are carefully controlled as they can form brittle nitride and oxide phases that are highly detrimental to the stability of the microstructure and the ductility of the alloy.

1.6.2.4 Carbon

Carbon is usually only unintentionally added during the manufacturing process. Carbon has the effect of reducing the solubility of aluminium in the α_p grains and increasing the concentrations of aluminium and molybdenum in the beta phase. The main effect of carbon is related to high temperature near alpha alloys with a bimodal microstructure. Whilst it has little effect on α_2 precipitation for fully lamellar microstructure (because there is no partitioning of elements), for bimodal structures carbon reduces the α_2 particle size and increases the inter-particle spacing of the primary alpha grains, reducing and delaying α_2 related embrittlement due to the decreased concentration of aluminium in alpha grains [38].

Carbon also allows for more tolerance when processing near alpha alloys during heat treatments, allowing for better control of the microstructure. It has been found that carbon addition in the range of 0–0.23wt% helps to slow down the change of primary alpha volume fraction with temperature. Zhang et al [39] investigated microstructural changes in an alloy containing different amounts of carbon and found that the beta transus temperature increases rapidly with the carbon content increased through the range of 0–0.32wt%. The amount of carbon must be limited as beyond the saturation limit a brittle carbide is formed.

1.6.3 Beta Stabilisers

Beta stabilisers such as vanadium and molybdenum lower the beta transus temperature and result in the beta phase being stable at a lower temperature. The effect is to increase the amount of beta phase retained in the alloy at room temperature.

There are two categories of beta stabilisers, these being isomorphous and eutectoids. In the case of isomorphous stabilisers, the alloying elements and beta titanium phase are mutually soluble. For eutectoid stabilisers, there is a solid state reaction in which two new phases are precipitated over a range of compositions. These are usually a

matrix rich alpha phase and an intermetallic phase. Detail below is given of common beta stabilisers.

1.6.3.1 Molybdenum

Molybdenum is an isomorphous beta stabiliser. It provides corrosion resistance and is therefore found in most high temperature alloys [5]. It can also be used to provide additional strength and resistance to creep, up to the solubility limit of the alpha phase. However, beyond this limit the resistance to creep starts to fall. With a high density (10.2g/cm^3) the levels of molybdenum are kept relatively low.

1.6.3.2 Vanadium

Also isomorphous, vanadium offers a large strength increase at low temperatures and offers creep resistance up to its solubility limit within the alpha phase. This is reflected in the strength increase seen from Ti-412 relative to Ti-407 as will be seen later on in section 4.7.2. Vanadium also has a higher density than titanium (roughly 6.1g/cm^3), so as with molybdenum its use must be limited.

1.6.3.3 Iron

Iron is a beta eutectoid stabilising element. As with carbon, iron is not usually intentionally added to a titanium alloy and instead is found within the titanium matrix as an impurity picked up through titanium sponge production. However, providing just a small amount of the element is retained within the alloy it can offer benefits. It has been found that when iron is added with silicon to a titanium alloy, a FCC FeSi compound is formed [40]. Research using the SEM has led to the idea that this compound hinders dislocation movement. This potentially helps to increase tensile strength at elevated temperatures. Iron does, however, lower creep performance.

1.6.3.4 Silicon

As with iron, silicon is a beta eutectoid stabilising element. Silicon has a lower density than titanium so helps to reduce the weight of the alloy and can offer an increase in creep performance. It is believed that silicon precipitates on dislocations at elevated temperatures, thereby hindering crack growth [41]. Creep performance increases with further addition of silicon up to its solubility limit within the alpha phase. Beyond this the brittle Ti_5Si_3 compound is formed which has a detrimental impact on ductility.

1.7 Titanium Microstructures

1.7.1 Introduction

The primary consideration during the development of titanium alloys for specific applications are the mechanical properties. As mechanical properties are strongly dependent on the microstructure, substantial work has gone into assessing the sensitivity of grain size [42], grain morphology [43] and crystallographic orientation [44]. This drives a better understanding of the failure mechanisms and therefore allows for more accurate predictions of the service life of components.

Microstructures are developed through thermomechanical processing. Structures are determined by the heat treatment temperatures relative to the beta transus, the cooling rate and the alloy composition. In each case the fundamental controlling element comes from the fact that titanium experiences an allotropic transformation on cooling from above the beta transus temperature, β_t whilst the alloy is at the BCC beta phase, down to the alpha, HCP phase. The manner in which this transformation proceeds affects the morphology and resultant microstructure [1].

Commercially pure titanium and alpha alloys are non-heat-treatable meaning that the range of application of this class of alloy is somewhat limited. The following section concentrates on alpha + beta alloys, where considerably more manipulation of the microstructure is possible.

1.7.2 Microstructure Types

Three distinctly differently types of microstructure can be obtained depending on the thermomechanical processing route. These are:

- Fully Lamellar
- Fully Equiaxed
- Bi-modal

1.7.2.1 Lamellar Microstructure

Lamellar microstructures are produced by cooling from above the β_t. On cooling, once the temperature falls below the transus, the alpha phase nucleates at grain boundaries and then grows as lamellae into the prior beta grain. The cooling rate determines the width of the alpha lamellae and also the size of the secondary alpha colonies. A colony refers to a group of similarly orientated lamellae, demonstrated in Figure 1.14. Several alpha colonies can exist within a beta grain. The diagram in Figure 1.13 below, displays the process as the alloy is cooled from above the beta transus. The basket-weave structure referred to in the figure is discussed in more detail in section 1.7.4.2.

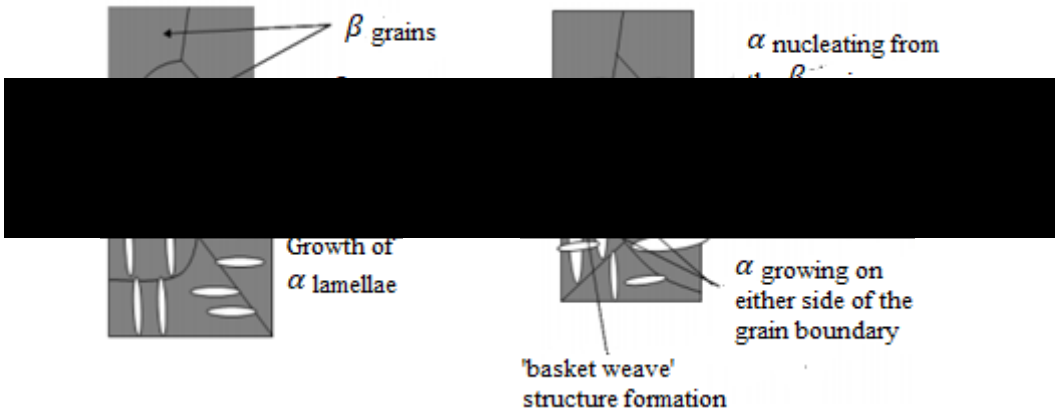

Figure 1.13: Cooling process from above the β_t to create a lamellar microstructure [45].

Work has shown that the most influential parameters on mechanical properties are the width of the alpha lamellae and the size of the alpha colonies [46]. These factors control the effective slip length in an activated system. Up to a limit, a coarser grain size is better for fatigue crack growth and fracture toughness. Figure 1.14 illustrates a typical lamellar microstructure.

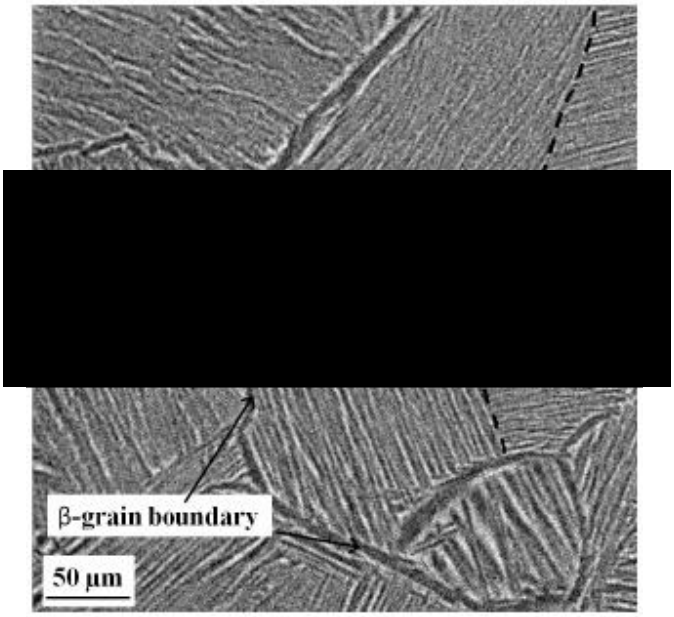

Figure 1.14: SEM secondary electron image of a lamellar microstructure [47].

1.7.2.2 Equiaxed Microstructure

Equiaxed microstructures are the result of a recrystallisation process. This means the alloy has to be highly deformed in the alpha + beta field to introduce enough cold work into the material. Upon the solution heat treatment at temperatures in the two phase field, a recrystallised and equiaxed microstructure is generated, consisting of primary alpha grains. Figure 1.15 illustrates a typical equiaxed microstructure. Equiaxed microstructures are known for high ductility as well as fatigue strength and are preferred for superplastic deformation.

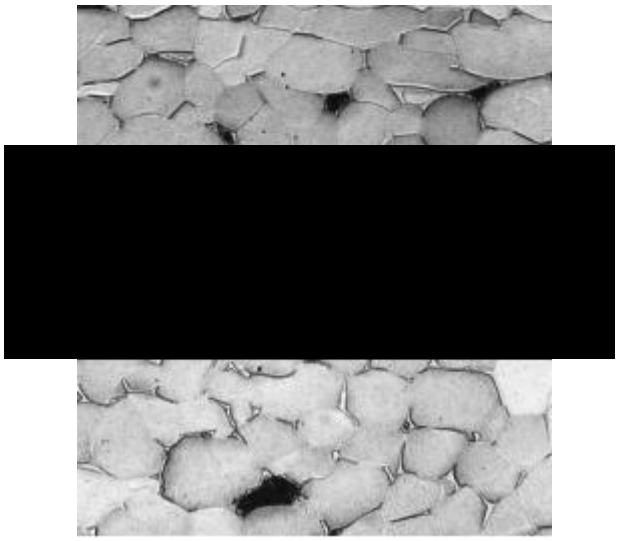

Figure 1.15: Optical microscope image of an equiaxed microstructure [45].

1.7.2.3 Bimodal Microstructure

Bimodal microstructures are a combination of lamellar and equiaxed microstructure. The solution heat treatment temperature determines the volume fraction of primary alpha. The nearer the solution treatment temperature to the beta transus, the lower the volume fraction of primary alpha. Solution heat treatment involves the heating of an alloy to a suitable temperature, holding at that temperature for sufficient time to induce one of more of the constituents to enter into solid solution and then cooling rapidly enough to hold these constituents in solution. The image below in Figure 1.16 shows a typical example of a bimodal microstructure.

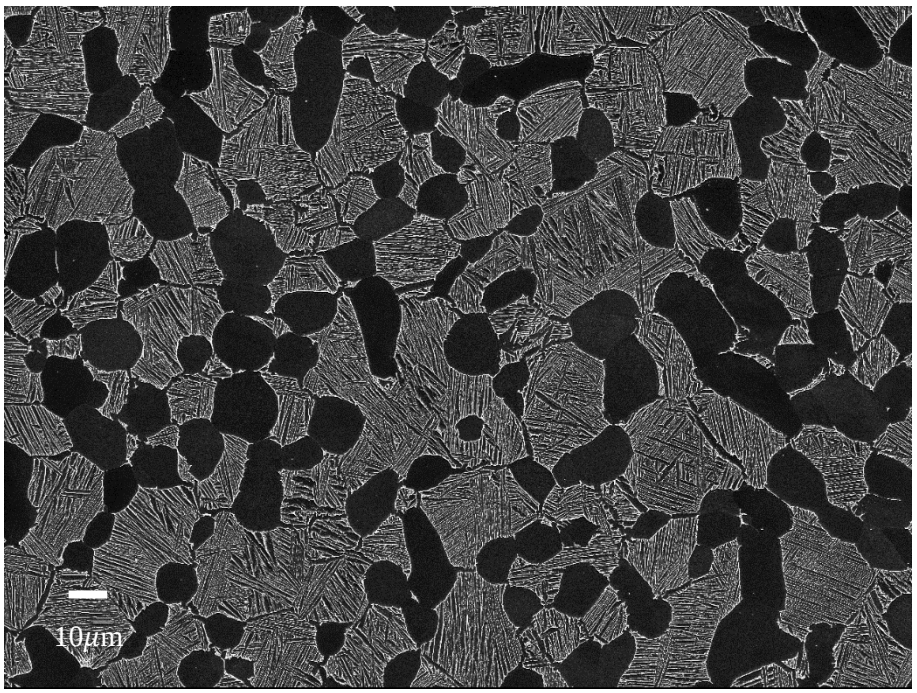

Figure 1.16: SEM secondary electron image of a bimodal microstructure.
The dark contrast represents the primary alpha grains and the whiter contrast, the alpha colonies within a beta matrix.

1.7.3 Microstructural Features

The section below discusses the effect of specific microstructural features. Isolating key microstructural features to develop a comprehensive understanding of the impact on mechanical performance is important. To this end, the use of computational modelling has become more common as it allows the study of complex microstructures with subtle variations, something difficult to achieve practically.

1.7.3.1 Primary Alpha Grain Size

A fine grain size will result in good tensile strength, ductility, resistance to fatigue crack initiation, super plasticity and oxidation resistance. Hall [48] and Petch [49] were the first to notice the dependence of strength on grain size and the equation linking these two properties, the Hall-Petch relationship, is shown in equation 1.5.

$$\sigma_y = \sigma_0 + \frac{k_y}{\sqrt{d}} \tag{1.5}$$

Here σ_y is the yield stress, σ_0 is the materials constant for the starting stress of dislocation movement (or the resistance of the lattice to dislocation movement), k_y is the strengthening coefficient and d is the average grain diameter. Grain boundaries impede dislocation movement, and the number of dislocations within a grain have an effect on how easily dislocations can cross grain boundaries. With a smaller grain size,

slip length is reduced. At a grain boundary pile up, the repulsive forces between each dislocation act as a driving force and helps to reduce the energy required for diffusion across the grain boundary, allowing further deformation in the material. Decreasing grain size decreases the number of dislocations in a given pile up which in turn increases the level of applied stress required to move a dislocation across a grain boundary. The higher the stress required to move the dislocation, the higher the material yield stress [50]. A coarse grain size is better for fracture toughness, fatigue crack propagation resistance and creep strength.

A study by Wu et al [51] collected together a large group of different HCF data sets on bimodal microstructures to access the correlations between specific microstructural features and fatigue performance. The results for grain size, plotted in Figure 1.17 show that decreasing grain size results in better fatigue performance. The same result was seen when looking at equiaxed microstructures.

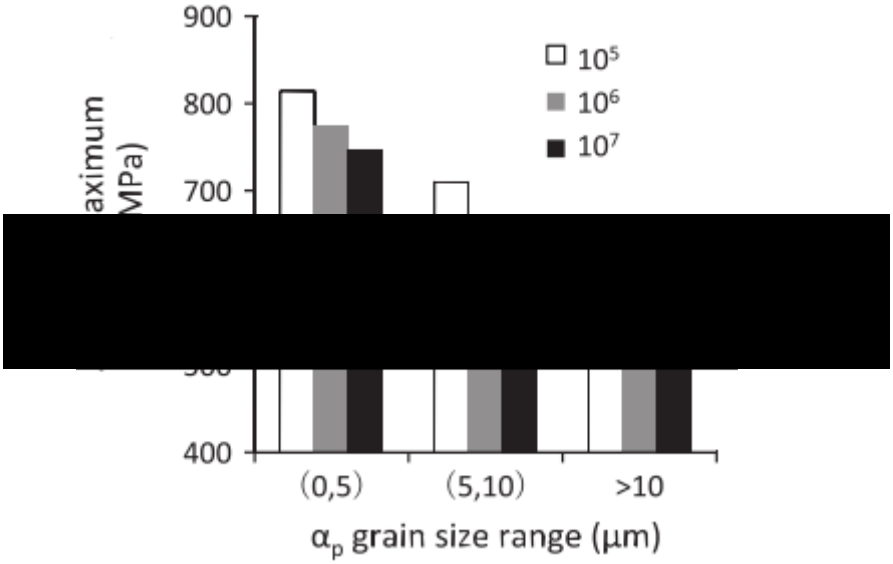

Figure 1.17: Relationship between primary alpha grain size (in a bimodal microstructure) and fatigue performance [51].

1.7.3.2 Volume fraction of primary alpha

It has been found that increasing primary alpha content increases tensile plasticity [52], refines the microstructure and helps to limit areas of common orientation or effective structural units (ESU's) to that of a single primary alpha grain [53]. Whilst primary alpha within a lamellar matrix does offer these advantages it has been suggested that the percentage volume should be carefully restricted as beyond a critical volume ductility ceases to improve and alloy element partitioning takes place. This degrades

the basic strength of the lamellar constituent of the microstructure, therefore resulting in a degradation of mechanical properties.

The exact percentage volume is alloy dependent. Figure 1.18 from Wu's study on the effect of microstructural features on HCF performance, shows that a primary alpha volume fraction of between 30–50% results in the best fatigue response.

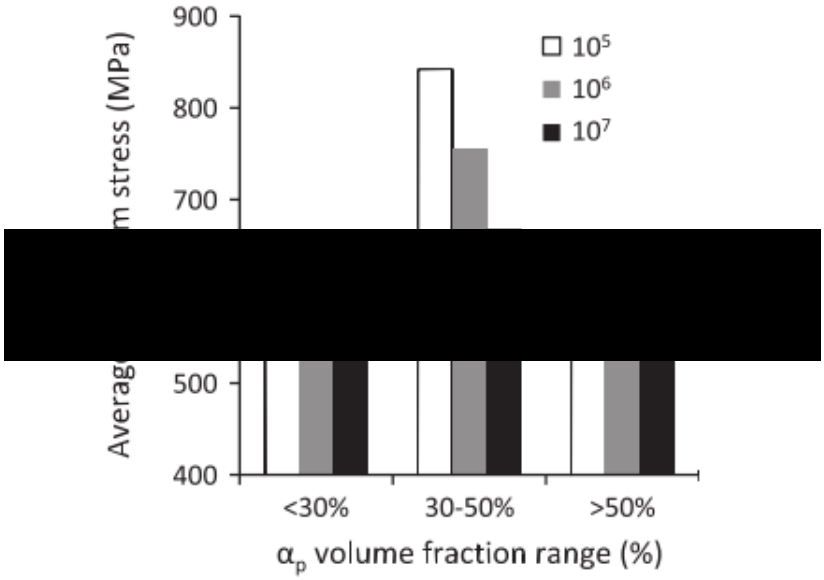

Figure 1.18: Relationship between alpha volume fraction and fatigue strength [51].

1.7.3.3 Secondary Alpha Lath Width and Orientation

Ashton et al [54] carried out a study to look at the effect of alpha lath width and orientation. Taking advantage of current modelling capabilities, lath widths of 1, 2 and 5 microns were tested using a crystal plasticity finite element model (CPFE). It was found that reducing width results in a stronger response. With decreasing lath width, there are a greater number of phase boundaries, resulting in more geometrically necessary dislocation (GND) hardening. Whilst a smaller lath width results in a higher monotonic strength, coarser alpha laths provide enhanced fracture toughness due to the increase in crack path tortuosity. A fine lath structure will resist crack initiation but will decrease crack propagation resistance [47].

Further to the lath width, the work of Ashton et al also looked at the effect of alpha phase crystal orientation with respect to the beta laths. Three different orientations were tested, the first with the primary slip direction perpendicular to the beta laths, the second with the primary slip direction parallel to the laths, and the third with the crystal c-axis parallel to the laths. A harder response was seen in the first case than the second

case as slip was inhibited by the beta laths. There was no barrier for dislocations in the case where the slip direction was parallel to the laths. The hardest response of all however was with the c-axis parallel to the long direction as <a> type slip systems are difficult to activate. In this case <c+a> type slip becomes active at a larger strains.

1.7.3.4 Secondary Alpha Colony Size

As mentioned in section 1.7.2.1, it is believed that the most influential microstructural feature on the mechanical properties of a fully lamellar microstructure is the alpha colony size as it determines the effective slip length. The colony orientation is also influential on material performance. The paper by Birosca et al. which looked at three dimensional characterisation of fatigue cracks in Ti-6246, suggests that cracks are diverted when large mis-orientations are observed between lamellae. These diversions can lead to secondary cracks and lamellae orientated for pyramidal or prismatic slip can even arrest the crack [55][56].

The experiment carried out by Li et al [57] looked at how three cooling rates affected the fatigue crack growth behaviour for a lamellar microstructure. Within both lamellar and bimodal microstructures the crack tends to propagate along the boundary of alpha colonies. Samples were water quenched, air cooled and furnace cooled. The microstructure resulting from the water quenched heat treatment was very fine, with fine alpha lamellae and small colonies. This meant the crack path was less tortuous and therefore the growth rate was higher relative to the other two specimens. The furnace cooled microstructure resulted in a weaker crack growth response than the air cooled microstructure. Whilst the structure contained the coarsest alpha lamellae and largest alpha colonies, because there were only a few colonies in a given beta grain, the fatigue crack growth resistance was limited. Therefore it was the air cooled microstructure with the best balance of alpha lamellae width and number of colonies contained within the beta grains that gave the best performance.

Colonies of alpha phase lamellae with different orientations hinder crack growth. When crossing the boundaries between colonies, the crack changes direction which can cause crack branching and secondary crack creation. This process requires additional energy and results in increased toughness and fatigue crack propagation resistance of the material.

1.7.4 Thermomechanical Processing

The different types of microstructures and effects of specific features have been discussed, but the way in which these structures are developed is explained in more detail below. Any thermomechanical step, whether that be a deformation process such as forging or rolling, a heat treatment process such as recrystallisation, or a final stage age or anneal will affect the microstructure and consequently the mechanical performance. Certain thermomechanical routes tend to generate regions of similar crystal orientation known as macrozones.

Macrozones are significant features within the microstructure and tend to have an adverse effect on mechanical properties. Care must be taken throughout a materials process route, to limit their introduction. Once introduced, it is possible to break macrozones up but it is far easier to avoid their introduction in the first place as discussed by Bache and Thomas [58].

1.7.4.1 Bimodal/ Fully Equiaxed Microstructure Processing Route

The graph below shows a typical route to generate a bimodal microstructure. Figure 1.16 above shows a typical example of such a structure [52].

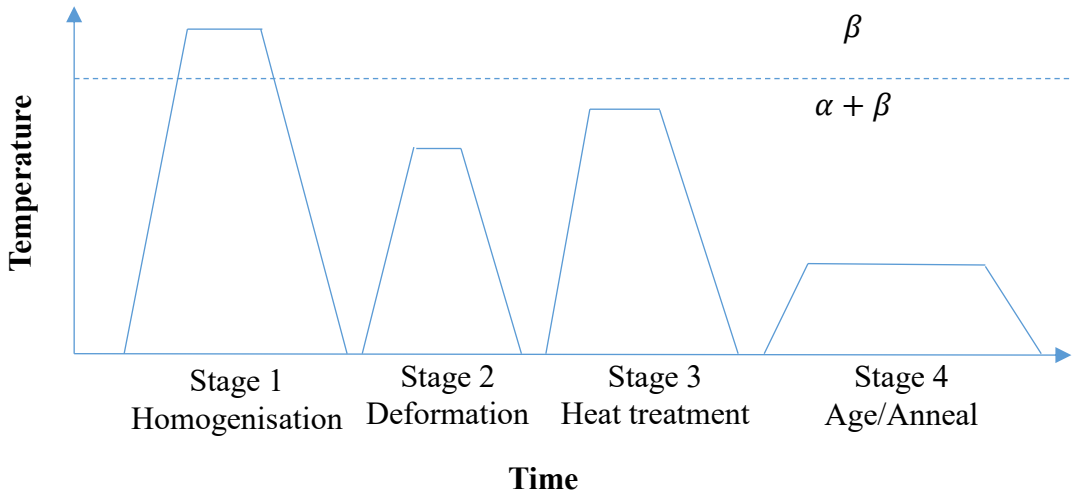

Figure 1.19: Typical thermomechanical processing route to generate a bimodal microstructure.

The primary alpha grain size is determined by the cooling rate from the beta phase field during the homogenisation step, which breaks up chemical segregation. A lamellar structure results after this first step, and the size of the individual lamella,

indicate the size of the primary alpha grains which form during the third stage heat treatment.

The deformation step will have a large influence on the texture of the material. The specific thermomechanical processes employed will determine the texture symmetry. These deformation modes include pancake forging, ring rolling, unidirectional rolling or cross rolling. The degree to which these processes deform the microstructure will determine the texture intensity and the deformation temperature will dictate the texture type [52]. Higher temperatures, or temperatures nearer the beta transus are preferred, as the increased number of slip systems available in the BCC structure results in less material cracking. It has been found that by varying the forging temperature of Ti-6-4 above and below the beta transus temperature, an improvement in fatigue strength of up to 20% can be achieved.

A range of options are available for the third stage heat treatment and fourth stage age or anneal. The specific treatment will be chosen based on the mechanical requirements that the component will face in service. The table below provides details of some common heat treatment processes used for Ti-6-4 [59].

Table 1.3: Example of heat treatment schedules and the resultant microstructure.

Heat Treatment Type	Schedule	Microstructure
Mill Anneal	1-4 hours at 700℃ - 790℃ air or furnace cool	Not a full anneal: traces of alpha + beta worked structure/partial recrystallisation/Widmanstätten alpha + beta
Solution Treat and Age	1 hour at 955℃ - 970℃ water quench, 4-8 hours at 480℃ - 595℃	Primary alpha, tempered alpha'/transformed beta.
Solution treat and overage (STOA)	1 hour at 955℃, water quench, 2 hours at 705℃, air cool.	Primary alpha, tempered α^1/ transformed beta.
Recrystallisation anneal	4+ hours at 925℃ - 955℃ furnace cool to 760℃ at <56℃/hr, cool to 480℃ at >370℃/hr, air cool.	Fully recrystallized alpha with some retained beta at grain triple points.
Beta Anneal	1 hour at 1010℃ to 1040℃, air cool to 650℃ at >85℃/min, 2 hours at 730℃ to 790℃, air cool.	Large grain, fully transformed structure.

If the cooling rate from the third step is sufficiently slow, the beta grains recrystallise into alpha leaving very little to no lamellae in the resulting structure leaving a fully equiaxed structure. This globular structure is also formed when the recrystallisation

temperature is sufficiently low. Figure 1.20 below compares an air cooled versus a furnace cooled microstructure.

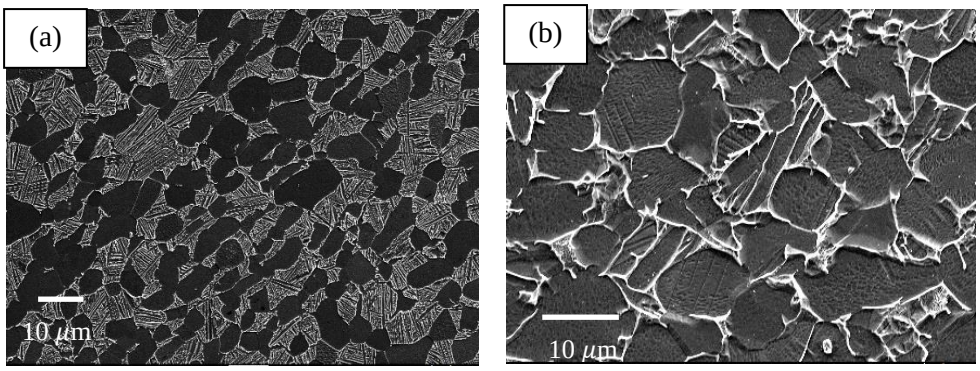

Figure 1.20: SEM SE images of a Ti-407 (a) Air cooled structure (b) Furnace cooled structure.

The fourth step is either an age or an anneal. An aging process is carried out below the Ti_3Al solvus temperature. Aging will precipitate Ti_3Al particles and harden the microstructure. For alpha + beta alloys, ageing has the potential to increase strength by around 30%. An anneal process is carried out above the solvus and will act as a stress relieving treatment.

1.7.4.2 Lamellar Microstructure Processing Route

The typical route for a fully lamellar structure is shown in Figure 1.21 [52].

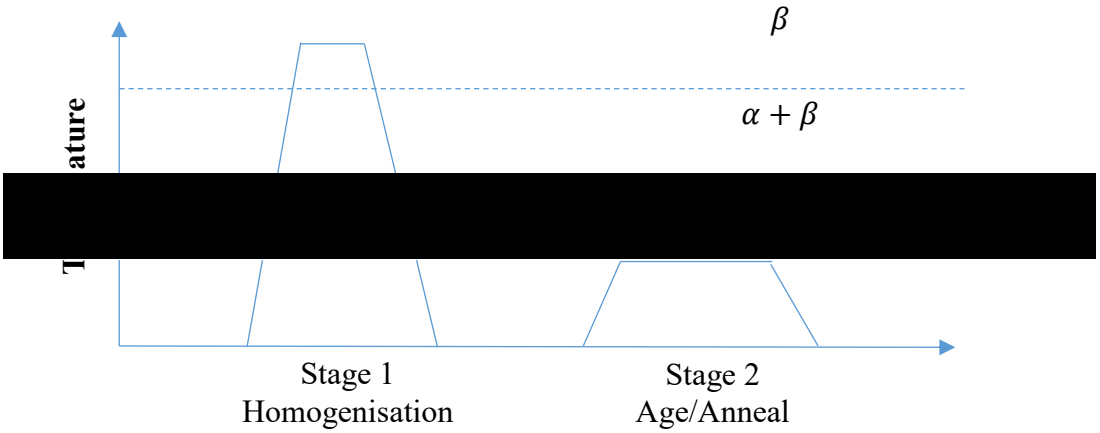

Figure 1.21: Process route for the generation of a fully lamellar microstructure.

Here the homogenisation treatment is carried out after the deformation process. Again the size of the alpha lath width is determined by the cooling rate from the homogenisation stage, with the faster the cooling rate the thinner the laths [57][60] [61]. With a low cooling rate, achieved through air or furnace cooling, the rearrangement process involves the diffusion of the atoms and takes place via a 'nucleation and growth' mechanism. The result is a widmanstattan microstructure,

exemplified in Figure 1.22(a). With faster cooling rates the transformation product has a more needle-like form. The needles are interwoven, and have what is termed a ‘basket-weave’ morphology, displayed in Figure 1.22(b).

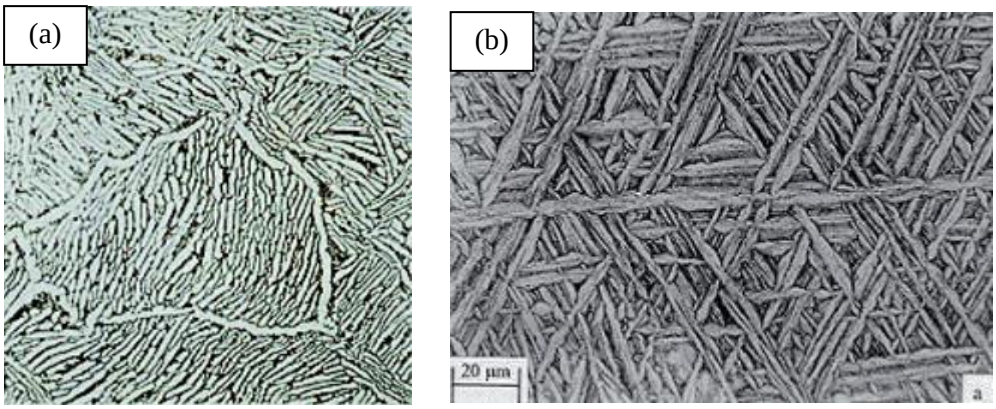

Figure 1.22: (a) Widmanstätten product (b) Basket-weave morphology.

If the cooling rate is reduced, the resultant microstructure is more plate-like in character and results in what is called an ‘aligned-alpha’ structure. The slower the cooling rate, or the higher the temperature the alloy is cooled from, the further the atoms can diffuse, leading to the development of larger grains. Important parameters dependent on the cooling rate are the size of the secondary alpha colonies, the width of the alpha lamellae and the grain boundary alpha layer.

Oil or water quenching result in much faster cooling rates. In this case there is not enough time for diffusion to occur, meaning the transformation process takes place by a diffusionless reaction to form a product called martensite. This is a shear process in which the atoms move less than the atomic spacing to form the product which has a pronounced needle form. The martensitic product is, in general, not desirable as it is hard and brittle and can often be associated with significant residual stresses. Martensite can be changed to a more effective product by a further age or anneal process which allows redistribution of atoms by diffusion. The images bellow displayed in Figure 1.23 help to illustrate martensite morphology.

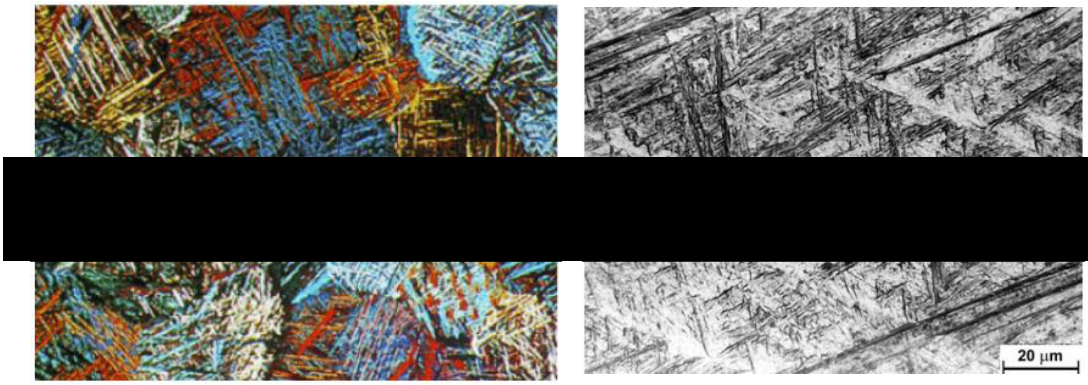

Figure 1.23: Example of martensite morphology [45].

1.8 Fatigue

1.8.1 Introduction

Since 1830 it has been acknowledged that a metal exposed to a fluctuating stress will fail at a level much lower than both the ultimate tensile strength (UTS) and the yield strength, defined by a standard tensile test. Failures that occur under conditions of a dynamic load are called fatigue failures as it is generally observed that they occur only after a considerable period of service [62]. The American Society for Testing and Materials (ASTM) definition of fatigue is given as: 'The process of progressive localised permanent structural change occurring in a material subjected to conditions that produce fluctuating stresses and strains at some point or points and that may culminate in cracks or complete fracture after a sufficient number of fluctuations' [63]. In other words it is the process of mechanical failure due to the initiation and growth of a crack under cyclic loading.

Fatigue has become a progressively more prevalent consideration and today accounts for 80–90% of all in-service failures. The fact that the original bulk design strength of the material is not exceeded, and the only indication of potential component failure is a crack which can be difficult to observe, means that fatigue is a dangerous failure mode. Therefore detailed understanding of crack initiation and growth mechanisms associated with fatigue are extremely important.

Fatigue is split into two regimes: low cycle fatigue and high cycle fatigue. Generally, when the number of cycles falls below 10^5, it is referred to as low cycle fatigue (LCF). When the number of cycles is greater than 10^6, it is referred to as high cycle fatigue (HCF). The frequency of high cycle fatigue can be in the range of 50–2KHz and in service can result from phenomena such as flutter and resonance. Within the LCF regime, one cycle could consist of an entire flight procedure from take-off to landing.

High cycle fatigue is of particular interest for Ti-407 where initial testing delivered results indicating similar performance to Ti-6-4, despite the significantly lower yield strength of Ti-407. A large proportion of the mechanical testing to be conducted during this project will be high cycle fatigue.

1.8.2 Fatigue Fundamentals

The following section defines the parameters that define a fatigue test when generating a stress versus cycles to failure (S/N) curve, and the stages of fatigue from crack initiation to final failure. S/N curves can also be referred to as Wh*ö*ler curves after August Wh*ö*ler, who in the 1850s was the first to carry out the systematic investigation of stress against cycles to failure [64].

Tests can either be load controlled where the maximum stress is kept constant, or strain controlled where the maximum strain is kept constant. Although the majority of S/N data uses load controlled tests, it is argued that the constrained conditions of critically stressed features seen in service is better simulated by strain controlled testing [65]. Strain controlled is also more representative for high elevated temperature fatigue testing, where a part or component will expand and contract in response to the operating temperature [66]. However, from a practical perspective, these are more expensive and time-consuming experiments to conduct.

1.8.2.1 Load Ratio

The load ratio, or R-ratio, is defined by the minimum and maximum stress applied to the test piece throughout a given cycle. The R-ratio is given by:

$$R = \frac{\sigma_{min}}{\sigma_{max}} \tag{1.6}$$

With regard to testing, the most common R-ratios are:

- R = -1. This is also known as fully reversed loading where the maximum and minimum stresses are equal but opposite, meaning the material will experience compression as well as tension.
- R = 0. The stress varies from 0 to some maximum load.
- R = 0.5. This refers to a high mean stress test. As the R-ratio is further increased the minimum stress becomes higher whilst the stress amplitude decreases for a given maximum stress.

1.8.2.2 Wave Form

As well as the R-ratio, when performing a fatigue test, selection of an appropriate waveform is also important. There are a number of different forms and some of the most common include:

- Sinusoidal – a continuous variation of the stress from minimum to maximum.

- Triangular - the load is applied at a constant rate and as soon as the peak load is reached the load begins to be taken off at the same constant rate.
- Square – can be used for dwell fatigue testing where the load is held at a maximum stress for a selected period of time. A square waveform involves the load being applied almost instantaneously.
- Trapezoidal – More commonly used for both LCF and dwell fatigue tests. The difference from the square waveform is that the load is applied and removed at a defined constant rate.

Graphical representations of the most common wave forms are given below in Figure 1.24.

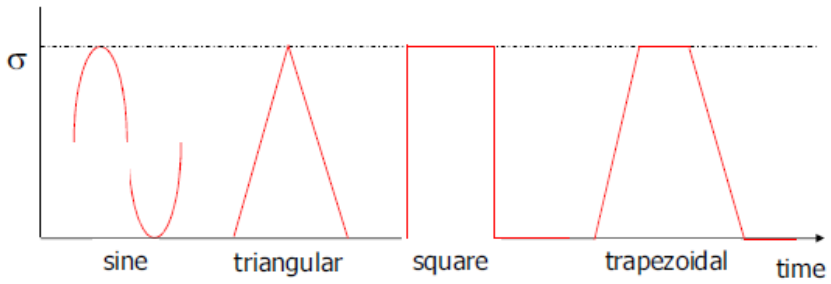

Figure 1.24: Common fatigue waveforms.

1.8.2.3 Stages of Fatigue Failure

Fatigue can be subdivided into four distinct stages.

- Crack initiation – this includes the early development of fatigue damage where cracks have been found to initiate from persistent slip bands [67] or at 'weak links' within the microstructure. Initiations will be located either at the surface, coincidental to the test piece circumference, or subsurface. The location of the initiation depends on several factors, such as test frequency, the occurrence of residual stresses from machining and 'weak links' within the microstructure where initiation may more easily occur.
- Stage I crack growth – this involves the deepening of the initial crack on planes of high shear stress. The crack grows along slip bands usually at 45 degrees to the tensile axis.
- Stage II crack growth – this involves the growth of a well-defined crack in a direction normal to the tensile axis.

- Overload or failure – this occurs when the crack reaches sufficient length so that the remaining cross section cannot support the applied load.

Figure 1.25 shows the fatigue fracture surface of one of the HCF tested Ti-407 specimens, demonstrating a subsurface initiation. This is manifested by the dark halo around the initiation site.

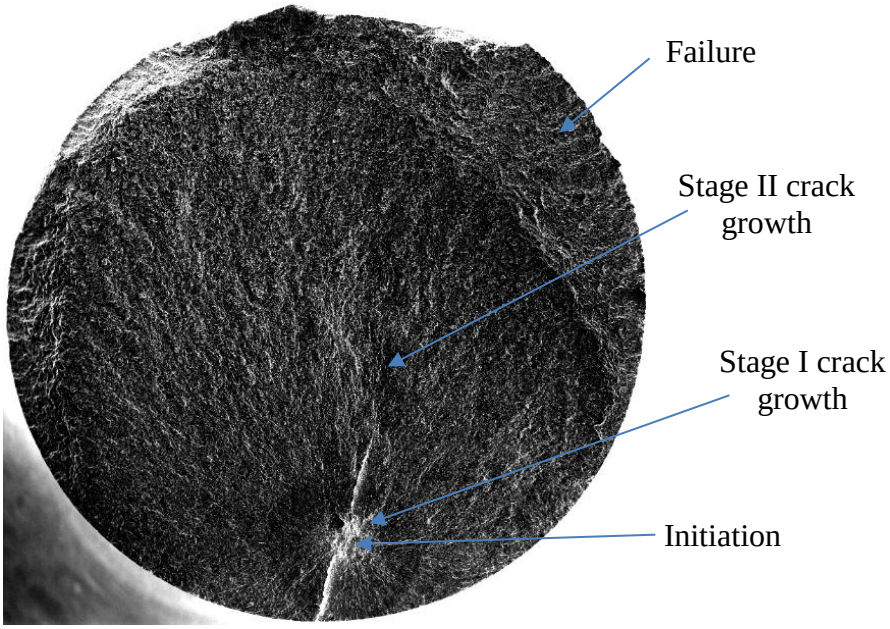

Figure 1.25: SEM fracture surface example of a subsurface initiation.

The graph below displays the variation of the crack growth rate with respect to the fatigue life of a given specimen.

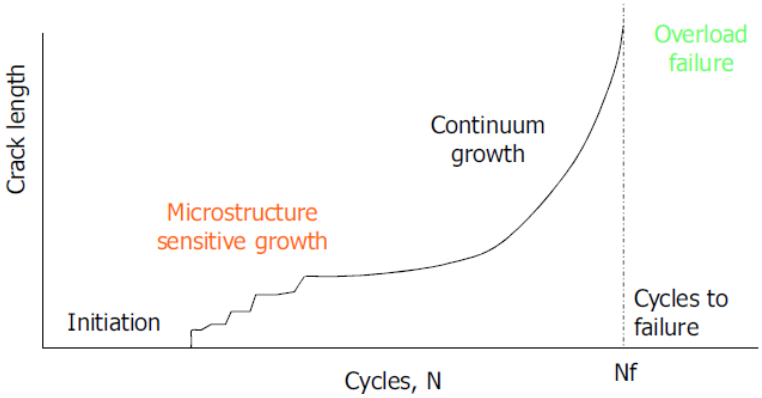

Figure 1.26: Graph showing crack length against number of cycles for a standard fatigue failure.

The test conditions and the material affect the relative proportions of the crack initiation life and crack propagation life. A fatigue crack can be formed before 10% of the total life of the specimen has elapsed under LCF conditions whilst 95% of the fatigue life could be taken by the crack initiation stage for HCF testing [68].

1.8.2.4 Crack Initiation and Stage I Crack Growth

Fatigue cracks develop as a result of localised plastic deformation accumulated during cyclic loading. Initiation usually occurs at the surface, as the stress concentration is highest here and grains slip more readily as they are less constrained. Dislocation glide caused by cyclic stresses leads to persistent slip bands, extrusions and intrusions developing in grains at the surface [69]. However, cracks may also initiate subsurface at weak points in the microstructure.

Classical fatigue initiation described by W.A. Wood explains the mechanism for producing slip band intrusions and extrusions [70]. Dislocations accumulate near a surface stress concentration and form structures called persistent slip bands. Persistent slip bands can either be an extrusion, an area that rises above the surface, or an intrusion, an area that falls below the specimen surface. These bands form due to the movement of material along slip planes. They are the result of a systematic buildup of fine slip movements, corresponding to movements of the order of less than 1nm rather than the steps of 100 to 1000nm, which are observed for static slip bands. Such a mechanism is believed to allow for the accommodation of the large total strain (summation of the microstrain in each cycle) without causing appreciable strain hardening.

Figure 1.27 below, illustrates the generation of slip band intrusions and extrusions.

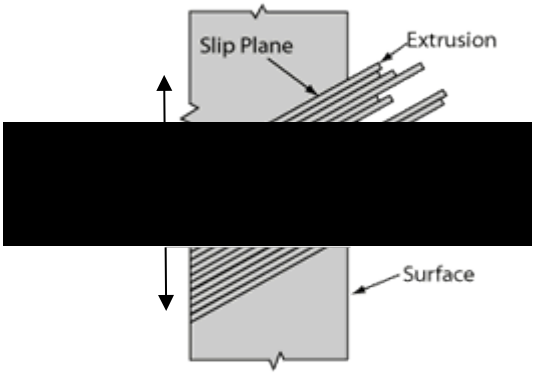

Figure 1.27: Crack initiating slip band intrusions and extrusions schematic [71].

The tiny steps left on the surface act as stress raisers from which microcracks can initiate. These microcracks nucleate along the persistent slip bands usually orientated at 45 degrees to the loading direction. In a polycrystalline material the crack may extend only a few grain diameters before the crack propagation changes to stage II. The rate of crack propagation in stage I is generally very low, in the order of nano-

microns per cycle which may be less than a lattice spacing. The plastic zones are smaller than the grain size and the fracture surface of stage I is practically featureless.

Further to the classical initiating mechanism, a mechanism specific to titanium LCF and dwell fatigue is described by a pile up model proposed by Stroh [72] and later developed by Evans-Bache [73][74]. The model describes a situation where a soft grain and a hard grain lie adjacent to each other. A soft grain refers to a grain where dislocations can move easily. They are orientated such that the basal or prismatic plane is subject to maximum shear stress, where the slip planes are at 45 degrees to the loading axis. In a hard grain, dislocation movement is much more difficult, with the basal plane perpendicular to the tensile axis. Slip in such grains will occur only on the pyramidal plane. With a maximum Schmid factor roughly a third that of the basal plane, a much higher stress is required for slip. In a situation where this grain combination occurs, a stress concentration develops ahead of the dislocation pile up in the soft grain. This cannot be relieved by slip in the hard grain which results in the initiation of a crack. The model is displayed through the diagram in Figure 1.28.

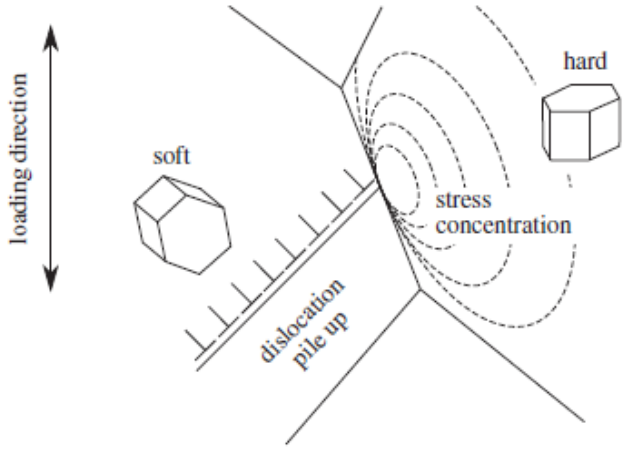

Figure 1.28: Stroh pile up model.

Understanding of this mechanism shows that developing the microstructure to avoid these rogue grain combinations through careful processing can help to increase the fatigue limit.

1.8.2.5 Stage II Crack Growth

Stage II crack growth commences when the growth direction becomes perpendicular to the tensile direction. The fracture surface of stage II crack propagation shows a pattern of ripples or striations illustrated in Figure 1.29 below. Each striation represents the succeeding position of an advancing crack and is formed from each single cycle of stress. The existence of a striation unequivocally defines that failure was produced by

fatigue but their absence does not necessarily mean fatigue did not occur. Failure to observe striations may be due to very small spacing, insufficient ductility at the crack tip to produce a ripple by plastic deformation large enough to be observed, or obliteration of the striations by some sort of damage to the surface.

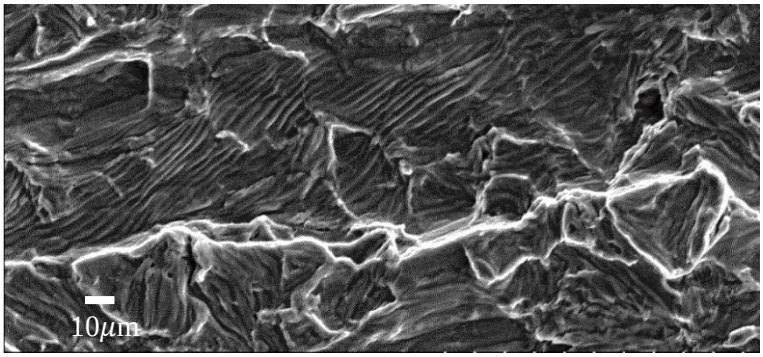

Figure 1.29: Example of fatigue striations.

Stage II crack propagation occurs by a plastic blunting process [75], displayed diagrammatically in Figure 1.30 [62]. At the start of the loading cycle the crack tip is sharp. As the tensile load is applied the small double notch at the crack tip concentrates the slip along planes at 45 degrees to the plane of the crack. As the crack widens to its maximum extension it grows longer by plastic shearing and at the same time the tip becomes blunter.

When the load is reduced, or changed to compression for a negative R-ratio, the slip direction in the end zones is reversed. The crack faces are crushed together and the new crack surface created in tension is forced into the plane of the crack where it partly folds by buckling to form a re-sharpened crack tip. The re-sharpened crack tip is then ready to advance and be blunted in the next stress cycle.

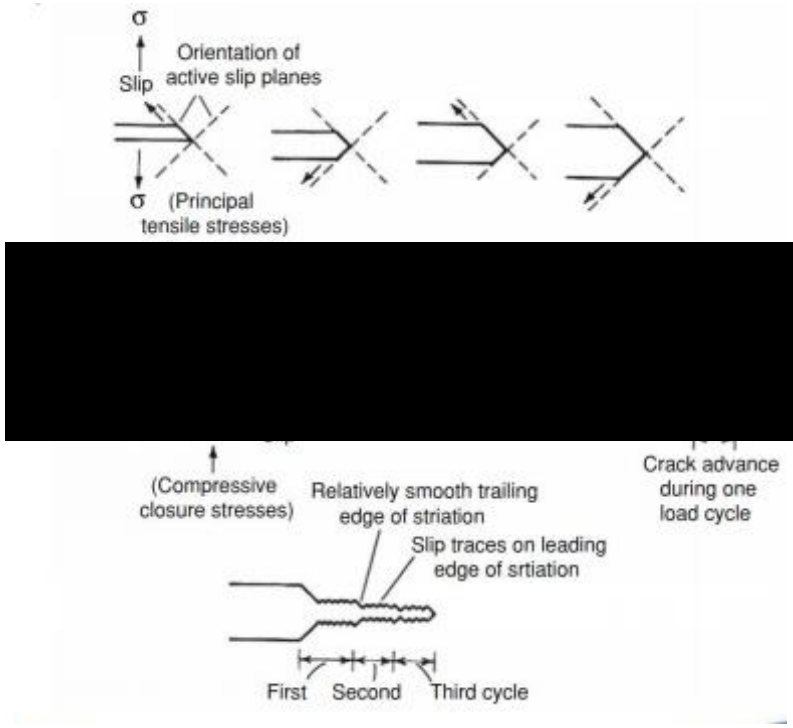

Figure 1.30: Plastic blunting process [76].

1.8.3 Factors Influencing Fatigue

In service, engine blade aerofoils can experience short bursts of low amplitude fatigue at high mean stresses and at frequencies greater than 1kHz [77]. The initiation for such conditions takes a significant proportion of the total life as the stress amplitude is usually much lower compared to that associated with LCF. Much research has been carried out to determine the way aspects such as microstructure, load ratio and test frequency effect the S/N curve.

1.8.3.1 Fatigue/Microstructure Relationship

The resistance to fatigue requires a trade-off between crack initiation and propagation performance. This is because fine equiaxed microstructures which help to impede crack initiation due to the shorter slip length, have a much poorer crack propagation resistance where a large grained lamellar microstructure is better suited [46]. When crossing the boundaries between colonies the crack changes direction which may cause crack branching and secondary crack creation. This process requires additional energy and results in increases in toughness, and fatigue crack propagation resistance of the material. The work by Wu et al [51] determined that bimodal offers the best overall HCF performance with lamellar the next best and equiaxed the poorest.

Generally with high cycle fatigue, the most influential factor for total fatigue life is the resistance against crack initiation and short crack propagation, which can take up to

95% of the total life [78]. Whilst the crack is microstructurally short, its behaviour is influenced by local microstructural features such as grain orientations, dislocation densities and sub-grain or phase boundaries.

The work of Knobbe [56] on Ti-6-4 forged material exemplifies how relatively subtle microstructural differences can affect fatigue performance. Two bimodal structures were tested, one in the mill annealed (MA) condition and the other in the solution heat treated (SHT) condition. Both had similar grain sizes (~10μm) and volume fractions (~65%) but the MA structure, which unlike the SHT structure, was not fully recrystallised, contained large misorienation variations in single primary alpha grains along with sub grain boundaries. This had the effect of reducing the slip length and resulted in a 10% higher fatigue limit at 6 x 10^6 cycles. Another interesting comparison between the two microstructures seen in the fatigue data was the greater scatter associated with the MA product. This can be explained by the residual stresses either impeding or enhancing crack initiation depending on crystallographic orientation, magnifying any scatter relative to the fully recrystallised SHT structure. The fatigue data from this report is displayed below in Figure 1.31 [56].

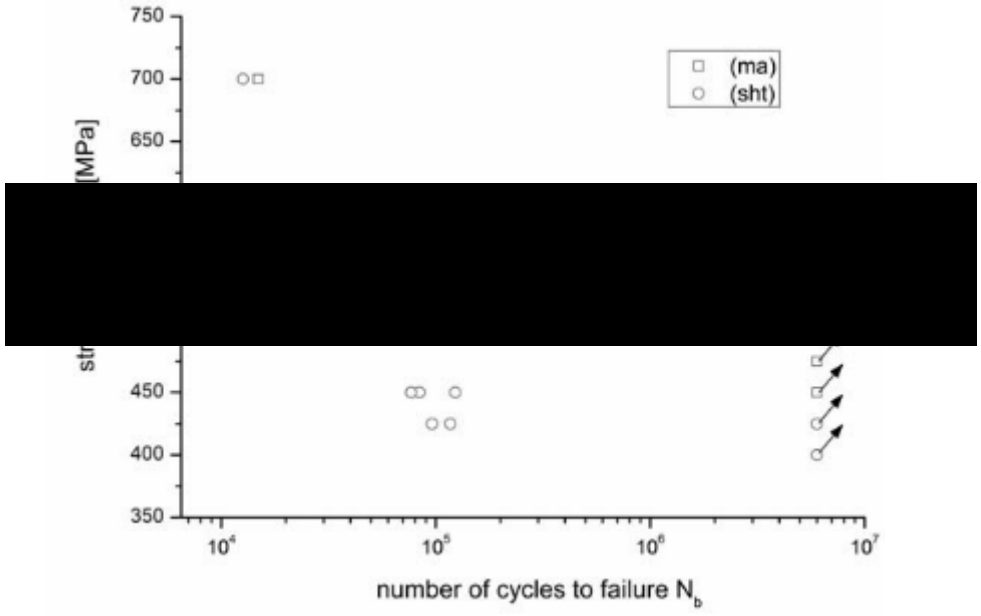

Figure 1.31: Fatigue data comparing solution heat treated vs mill annealed bimodal microstructures [56].

1.8.3.2 Effect of Frequency and Strain Rate

Fett et al performed tests on aluminium alloys in the low frequency range (0.2-20Hz) and found an increase in fatigue life as frequency is increased [79]. Another study by Mayer and Laird performing tests on polycrystalline copper produced the same results

testing in the same frequency range [80]. For low frequencies, increased slip band formation was observed while for higher frequencies greater amounts of hardening with lower levels of strain were seen. Among titanium alloys, the Stroh model requires time at maximum load to develop pile ups with enough stress concentration to form a crack. Further, the deformation mechanism is related to the strain rate. Higher levels of deformation twinning are overserved at higher strain rates in aluminium lean titanium alloys [81]. Therefore as the frequency is increased, initiation via the Stroh mechanism is less prominent so that the number of cycles to failure is likely to increase. For this reason, differences facet characteristics are observed when comparing LCF to HCF failures. Initiation sites generated by LCF failures tend to exhibit spatially flat facets, with the loading direction near perpendicular to the plane of the facet. Crystallographic measurements tend to reveal near basal (i.e. hard) orientated grains. Conversely, HCF initiated failure sites tend to revel higher spatial angles with the angle between the loading direction and the c-axis between 20–40°. Again, faceting is seen on or near the basal angle, meaning the facet is orientated for a relatively high Schmid factor allowing for basal slip to develop and initiate the crack.

A common interpretation on the strain rate effect is that, as the loading rate is increased, dislocations have less time to overcome obstacles via thermal activation, thereby reducing the amount of plastic strain accumulated. Therefore, higher frequencies will require higher loads to produce the same strain range. The effect is amplified at lower stress ratios where the dynamic amplitude is greatest. Fatigue is a plasticity induced phenomenon so the reduced plastic strain could explain the increased fatigue strength at higher frequencies.

It has also been suggested that crystal structure affects the level of frequency dependence. Research by Roth et al has shown that FCC materials are only slightly frequency dependent whereas fatigue of BCC materials are highly frequency dependent [82]. In an FCC structure, a total of twelve slip systems remain active at high frequencies. Five remain active in BCC structures. HCP structures contain only three primary slip planes (basal, pyramidal and prismatic) and at low temperatures only the basal slip system remains active limiting the amount of plastic deformation that can occur, therefore increasing frequency dependence.

1.8.3.3 Environment

The frequency effect is further exaggerated by the environment, where corrosive environments would have more time per cycle to introduce damage into the specimen.

Comparisons of HCF tests conducted in vacuum versus in air have shown that laboratory air can be regarded as rather corrosive [83]. The graph displayed below (Figure 1.32) shows a comparison of LCF data test in laboratory air and vacuum conditions. Laboratory air environments are more comparable to tests conducted in a 3.5% NaCl than to vacuum tests [84].

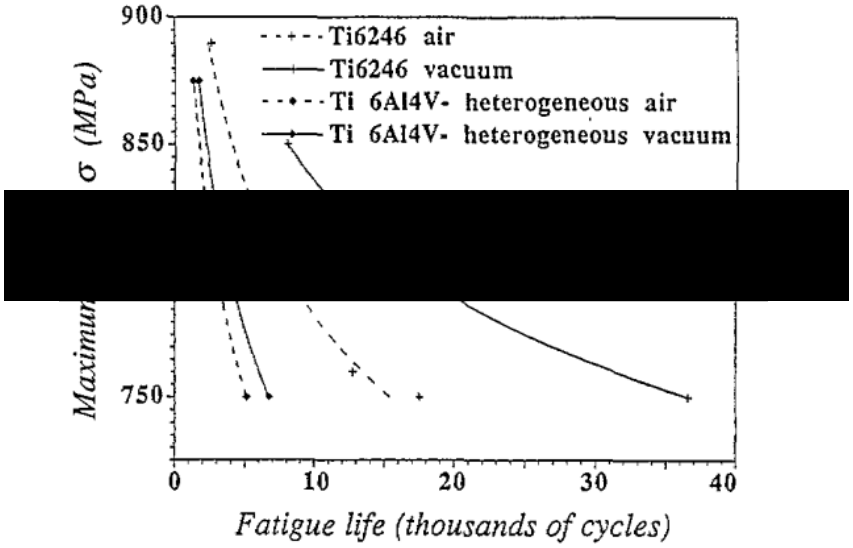

Figure 1.32: LCF plot demonstrating the corrosive nature of air relative to a vacuum [84].

1.8.3.4 Temperature effect

A consideration concerning frequency effect is the observed increase of the temperature of the test piece or the component as frequencies are increased through the hundreds, up to the KHz range, particularly at low stress ratios where the dynamic amplitudes are greatest. The concern would be that internal heating would produce more damage within the material reducing fatigue life, implying that higher frequencies would result in lower fatigue strengths. However, from all data obtained in this project, if heating did occur, it did not produce a significant effect.

1.8.3.5 Creep

Time dependent creep is important for stresses at or near the static yield. Research has shown that considerable static creep damage at room temperature can occur at stresses as low as 80% of the yield strength [85]. As the frequency is decreased, more time is spent at maximum stress, resulting in more creep damage and therefore a potentially reduced fatigue performance. Further to this, as the stress ratio is increased the material will become more susceptible to time dependent creep [86].

For the most part, the discussion of the frequency effect on fatigue suggests that higher frequencies result in longer lives for a given stress. This is due to the interaction of several mechanisms including strain rate effect on dislocation motion, diminished number of active primary slip systems at high frequencies in HCP and BCC materials, and reduced effect from environmental damage.

1.8.3.6 Effect of Foreign Object Damage on Fatigue

An evaluation was carried out by J.O. Peters et al [87] on the influence of bimodal versus lamellar microstructures and their susceptibility to HCF failure following foreign object damage (FOD). The FOD was simulated by firing high velocity 200-300m/s steel spheres at the test specimen. The main effect of the FOD damage was to induce preferred sites for the premature initiation of fatigue cracks on subsequent cycling. The result of the FOD damage was to significantly reduce resistance to HCF in both bi-modal and lamellar microstructures. However, the lamellar microstructure displayed a much higher crack growth resistance than bimodal microstructure in the presence of the induced large through thickness cracks. One factor associated with the faster growth rates of foreign object damage initiated microcracks is the microstructural changes associated with impact induced plasticity. This is evident from shot peening experiments. One of the main differences between the bimodal and lamellar reactions in this experiment was the fact that in the case of bimodal, the FOD induced microcracks were of comparable dimension to the fine grained bimodal microstructure. In the lamellar structure, however, such microcracks were far smaller than the average lamellar colony size, therefore resulting in a better resistance to fatigue following FOD damage.

1.8.3.7 Fatigue Crack Propagation

Understanding of the propagation characteristics of a given material is important. Plots of stress intensity factor range against fatigue crack growth rate are used to define this. The crack growth rate is defined as the extension of the crack per cycle. The stress intensity factor range, defined below in equation 1.7, is a function of the stress range ($\Delta\sigma$), the crack length, a, and a material geometry factor, Y.

$$\Delta K = Y\Delta\sigma\sqrt{\pi a} \tag{1.7}$$

An example of a crack growth rate plot is shown below in Figure 1.33.

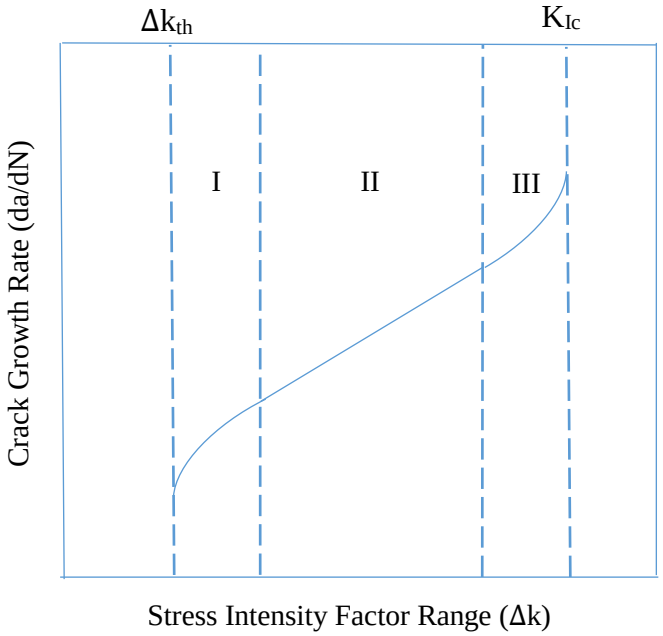

Figure 1.33: Example of a plot of stress intensity factor range against crack growth rate.

The curve can be split into three main regions.

In region I, at low ΔK values, the crack growth rate is extremely low. There is a stress intensity factor range threshold, ΔK_{th} below which the fatigue crack growth rate is too small to measure. The threshold is defined by ASTM as that value of K for which the crack growth rate is equal to or less than 1×10−10 m/cycle [88]. The fatigue threshold is influenced by a number of factors including loading frequencies, mode of loading condition, load history and environment [89].

In region II a linear growth is seen between ΔK and crack growth rate. This is commonly referred to as the Paris regime which is described by the relation in equation 1.8.

$$\frac{da}{dN} = C(\Delta K)^{n} \tag{1.8}$$

Here, C is the intercept constant and n is the slope of the line within the Paris regime. Components which are lifed using the damage tolerance approach, are lifed using region II of the crack growth rate curve.

Region III is defined by rapid, unstable crack growth to failure. The crack growth rate accelerates as the stress intensity factor approaches the fracture toughness, K_{1c} of the material [90].

1.8.4 Fatigue Life Prediction Methods

A number of titanium alloys are used in demanding applications where fatigue is the primary cause of damage. Over the years, extensive fatigue databases have been generated through both laboratory and test bed assessments in aid of titanium component design. These databases have been used to help generate fatigue life prediction methods.

1.8.5 Fundamental Approaches

When forming lifing approaches it is important to consider the statistical nature of fatigue. This is often accounted for using the +/- 3 sigma approach. For fatigue prediction, as the stress is decreased, the life variability increases. In order to effectively predict lives using fatigue data, each dataset must be interpreted with this in mind. In order to predict the fatigue response of components in service, the relation between fatigue behaviour to the applied stresses and strains must be known [91]. The three mains ways of testing are:

- Full scale component testing – This is by far the most expensive approach, meaning that only a very limited number of tests can be carried out. However, it is highly comprehensive in that factors such as stress concentration features, surface residual stresses and surface finishes influence the result. Therefore, the results from these tests are able to provide the most accurate information, closely simulating the actual in-service performance of the jet engine.

- Sub/Pseudo component testing – this approach scales components down so stress fields representative of those in service can be achieved.

- Uniaxial plain specimen testing – this is by far the most common method for fatigue testing as it is inexpensive, meaning large datasets can easily be compiled. They help to provide deeper insights into the cyclic deformation characteristics of materials. However, plain specimens are limited in that they show limited residual stresses and surface finish effects and almost no multiaxiality and volume effects.

In terms of predicating component lives there are three approaches that have gained widespread acceptance. These are outlined below.

1.8.6 Safe Life

The safe life approach works on the life to first crack criterion. It accounts for fatigue life variability. The benefit of this approach is that it is very safe and means that components will operate with little or no damage from fatigue, meaning the component is very unlikely to be in service with a crack. It is therefore suitable for critical components such as the discs. It also has low inspection costs. A component would be removed from service once the safe life has been exceeded or 'retired for cause' on the detection of a fatigue crack. The main drawback of this approach is that only working on the life to first crack means that very often components that are structurally sound are taken out of service, meaning that most of the life that the components are capable of achieving is wasted. This is costly as it means components are replaced unnecessarily. An assumption of this method is that components are defect free. Whilst is can be said that this assumption is reasonable thanks to the manufacturing and processing methods of today, it does not totally eliminate the possibility of defects arising, such as inclusions or foreign object damage. These can severely affect the life of a component [92].

1.8.7 Fail Safe

Fail safe is used where failure would not significantly impact continued operation of the engine, for example casing structures. The assumption is that the component will eventually fail, but when it does it will do so in a safe manner [93]. When a structure is designed such that cracks will easily be detected before they reach a critical length it can be considered as a fail-safe design. This method is more commonly associated with systems or processes, where back-ups can be employed in the event of a failure. This fail safe method reduces the expense associated with design and testing as well as reducing production costs. This approach requires regular maintenance inspections [94].

1.8.8 Damage Tolerance

Unlike the safe life approach, damage tolerance is based on crack propagation characteristics. It is used in cases where there are known pre-existing defects, or if no defects are detected, it is assumed that there are defects present that are below the non-destructive testing (NDT) threshold. In this case the defect size is assumed to be at the NDT threshold and the life calculated from there, (that being 0.3mm). Where there are known pre-existing defects, an approximate propagation life can be calculated based on the fracture mechanics approach. The drawback of this approach is that it ignores the initiation life of the component which can significantly underestimate the total life of the component.

1.8.9 Total Life Prediction Methods

The problem with the above approaches is that they can be inefficient and costly, lifing either based solely on either the initiation or the propagation life of the component. Recently, Rolls-Royce plc have begun to address this issue by taking a total life design philosophy which includes consideration of both initiation and propagation to generate a more accurate life estimation of components. This method allows for factors that are known to affect fatigue such as surface finish, residual stresses and other damaging deformation modes [95].

Gas turbine components are lifed so that they can be withdrawn from service or repaired before failure actually occurs. Peak elastic stress is an approach to this problem. This technique involves the consideration of design curves from notches and relevant component features, such as the dovetail stress concentration of the HP compressor disc. The notches are designed so they have a similar stress gradient, and therefore critically stressed volume as the component feature. The assumption is made that if the peak elastic stresses in the component and the stresses applied to a plain test piece are the same, they will develop cracks in the same number of cycles. However, this ignores the stress redistribution that can take place at the notch once yielding has occurred. Critical strain techniques are used to address such limitations.

Mean stress effects in HCF applications have received attention for years and many design methodologies focus on this issue. The most popular of these is the constant life Haigh diagram, more commonly known as the Goodman diagram [76].

1.8.10 Stress Life Methods

For any given stress ratio and given life, the effective stress amplitude can be determined. The derivation of this relationship came about when it was noticed that if the usual stress against cycles to failure curve was plotted on a log scale, a linear graph was produced. Basquin was the first to notice this and generated the Basquin relationship given below in equation 1.9.

$$\sigma_a = \sigma_f'(2N_f)^b \tag{1.9}$$

Here σ_f'is the fatigue strength coefficient and b is the fatigue strength exponent, the gradient of the log stress versus log cycles graph. Basquin's equation was modified by Morrow (equation 1.10) in order to take into account stress ratio. Basquin's initial equation assumed a fully reversed loading cycle (R = -1).

$$\sigma_a = (\sigma_f' - \sigma_m)\,(2N_f)^b \tag{1.10}$$

Here σ_m is the mean stress which acts to decrease the fatigue strength coefficient when it is positive and increase it when it is compressive.

1.8.11 The Goodman/Haigh Diagram

A large number of metals demonstrate a linear relationship between stress amplitude, σ_a, and mean stress, σ_m, on a constant fatigue life plot. This is commonly known as the Goodman diagram [96]. There is some debate in the literature as to who was the first to report the linear relation between stress range and mean stress [64]. Some sources state this is incorrectly attributed to Goodman due to his popular engineering book, as Fidler was the first to report the linear relationship and Haigh was the first to use straight line representation of constant life fatigue data [96]. An example of such a plot is shown below in Figure 1.34.

The graph can be quantified in terms of the Goodman relationship given in equation 1.11.

$$\sigma_a = \sigma_{FL} - (\sigma_{FL} / \sigma_{UTS})\,\sigma_m \tag{1.11}$$

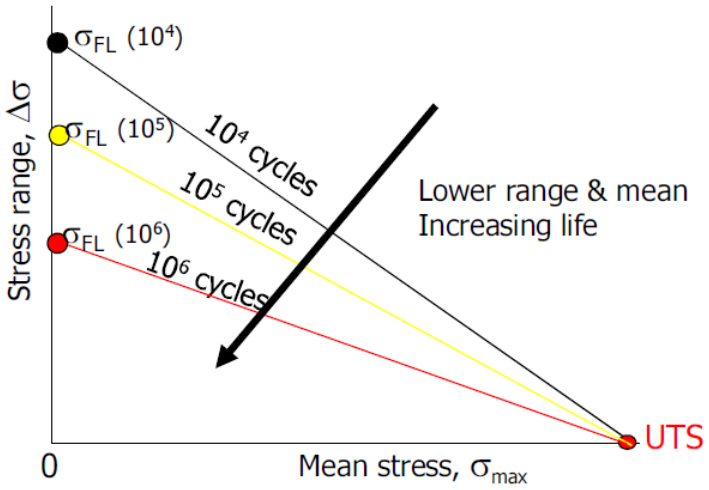

Figure 1.34: Example of a Goodman/Haigh diagram.

The Goodman diagram shows that for a given stress range, as the mean stress from zero (representative of a fully reversed loading pattern) increases the number of cycles to failure decreases. It can be used to define allowable stresses for a given lifetime by choosing a stress that sits below the line of constant life. Figure 1.35 gives an example of this approach [97].

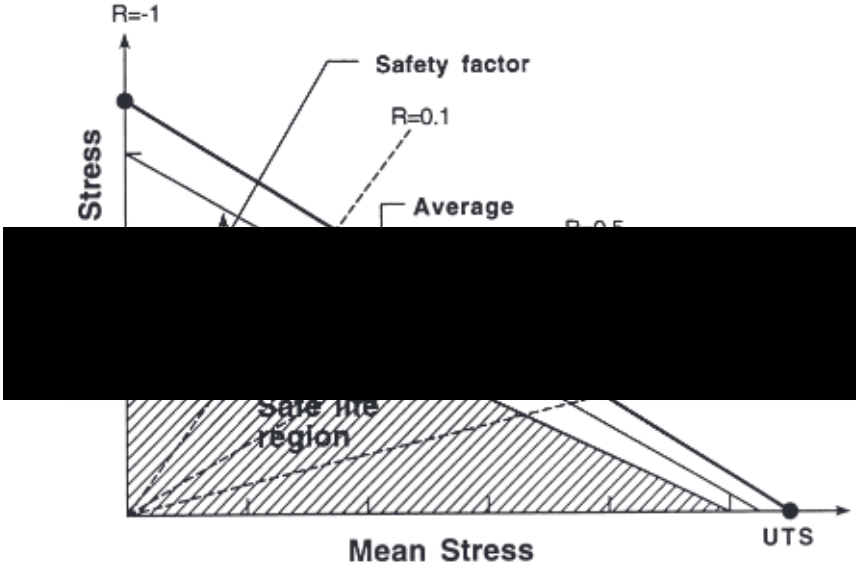

Figure 1.35: Representation of stress region a component can operate in up to a given number of cycles [97].

A line of constant life can theoretically be plotted by connecting a straight line from a data point corresponding to fully reversed loading (at R = -1) to the ultimate tensile strength of the material. However, experimental data shows the linearity of the Goodman relationship to be dependent on the microstructural condition for $\alpha + \beta$ titanium alloys. Ivanova et al reported a linear relationship for fully lamellar microstructures, but anomalous relationships for coarse grained bimodal and equiaxed

microstructures [98]. It was also found that the HCF strength at intermediate mean stresses was significantly lower than that predicated by the Goodman relationship.

Use of the relationship is subjected to further restrictions. First, high levels of scatter in the data are associated with high mean stresses. The fracture mode transitions from one of fatigue to one of creep. In the creep regime consideration of time should be given during which fatigue cycles occur. Therefore, the plot is highly dependent on the frequency. Another shortcoming of this approach is that it is based on initial material quality and does not account for a reduction in capability due to in-service induced changes such as FOD, fretting or fatigue [88]. The diagrams assume the same mechanisms are responsible for failure at all stress ratios which may not be the case.

1.8.12 The Effect of Texture on Fatigue

The limited number of slip systems available in the HCP phase of titanium alloys mean that mechanical properties are sensitive to the crystallographic orientation. The general trend found in the literature is a degradation of fatigue performance when loading perpendicular to the basal plane [99][100][101]. Part of the reason for this is attributed to the fewer slip systems available when loading in this direction. This reduces stress relaxation and results in a larger stabilised stress range as demonstrated by Bache and Evans [102]. Interestingly, the strongest fatigue orientation direction does not correspond to the strongest static direction, which is with the c-axis parallel to the tensile axis.

A study by Germain and Bache found that crack initiation and in particular the formation of facets at the initiation site, is related to areas of common crystallographic orientation[103]. When looking at optical images of the Ti-6-4 cross rolled structure that was tested, the grain size was quoted as roughly 30μm. However, EBSD revealed much larger regions of similar crystallographic orientation. These can be referred to as effective structural units (ESU's) and can strongly influence the fatigue response. In this study, the size of the ESU measured from the EBSD data corresponded to the size of the facet region seen on the fracture surface.

1.8.13 Dwell Sensitive Fatigue

A troublesome issue seen by the fan and compressor blades and discs is a considerable reduction in fatigue life due to the dwell effect. Dwell fatigue occurs when the maximum load is held for a significant period of time, at temperatures below 200℃. Alloy chemistry, microstructure and micro-texture are all major factors that affect the severity of dwell fatigue. Testing shows that near alpha alloys are more prone to the dwell effect than alpha + beta or near beta alloys [104]. Within the gas turbine, the dwell period occurs during take-off and cruise, when the titanium compressor discs and blades are exposed to a high mean stresses for an extended period, at a relatively low temperature. It has been found that cold dwell fatigue can reduce the time to failure of components by more than an order of magnitude [105]. The importance of dwell sensitive fatigue was first highlighted in 1972 when an uncontained failure of two IMI685 titanium alloy fan discs occurred on a Rolls-Royce RB211 engine which was powering a Lockhead Tristar [106][107]. After the incident it was confirmed that the LCF life of IMI685 was reduced due to a five minute hold on peak stress. Figure 1.36 below demonstrates the difference between the dwell fatigue response and fatigue response of IMI685 [73].

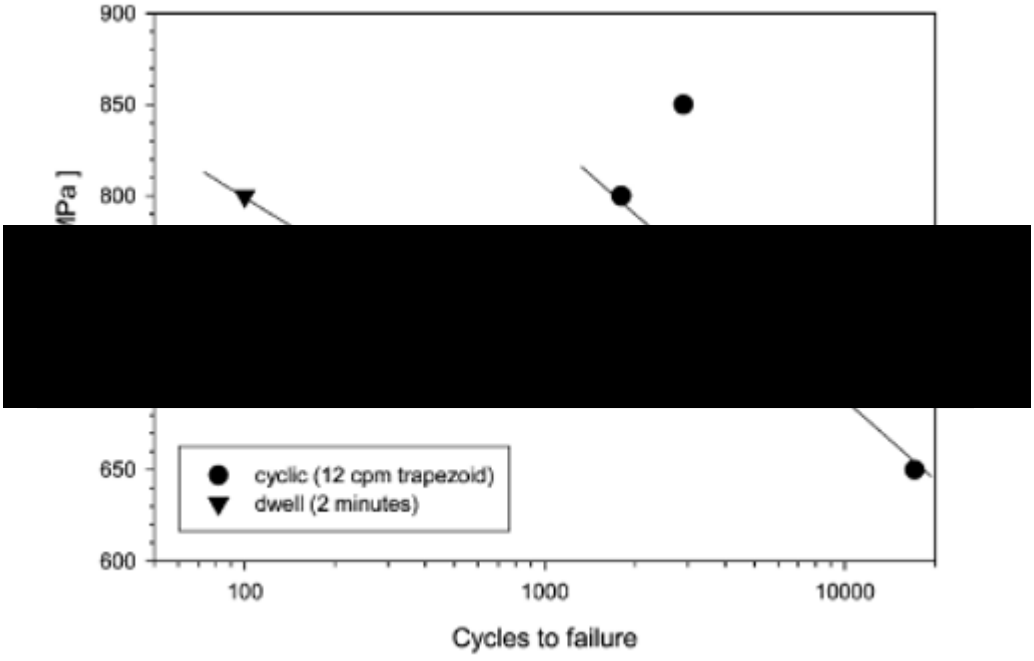

Figure 1.36: Effect of dwell period on fatigue life [73].

It is believed that dwell is a result of the accumulation of time dependent plastic strain on the local microstructural scale. Despite the fact that creep is usually considered as a high temperature failure mode, research has shown that titanium does accumulate

strain under static loads at room temperature. Ambient temperature strain accumulation results from planar slip damage [73]. The inherent anisotropic mechanical response of neighbouring grains leads to the formation of quasi cleavage facets on basal planes which are orientated at a favourable angle for subsequent crack propagation. The dwell effect is therefore considered to be an initiation, or at most a short crack dominated mechanism, and has minimal effect on crack growth rate [73].

The Stroh model, referred to in section 1.8.2.4 is particularly pertinent regarding dwell fatigue. During the stress dwell period, the dislocation density at the soft/hard grain boundary becomes greater than that during a normal fatigue cycle due to the continued source activation under sustained stress. A larger level of load shedding occurs resulting in higher localised stress in the hard grain, meaning earlier facet crack initiation [108].

The role of the effect of interstitial elements on dwell, in particular hydrogen has been investigated, mostly on the near alpha alloy Ti-685 but also on Ti-6242. Whilst abnormally high levels of hydrogen have been shown to be detrimental to dwell fatigue life, most likely owing to the resultant embrittlement [109], a study by Gerland et al [110], found that in the range of 30-300ppm, the higher the hydrogen content, the smaller the accumulated strain and better the dwell fatigue performance. Increasing hydrogen content in this range did increase the crack growth rate, but the improvement to crack initiation was more substantial. The apparent contradiction of results in various studies in terms of the precise optimum levels of hydrogen [111][112][113], suggest that the influence of hydrogen on dwell fatigue is very sensitive to stress level. This is in part due to the relative proportions of crack initiation and crack growth.

An attempt to explain the difference in dwell-fatigue life has been made through detailed examination of the crack initiation sites. For example Sinah et al [112] assessed the crystallography of faceted initiation regions for hydrogen contents of 49, 189 and 230ppm on a bimodal structure for Ti-6246. However the small differences observed between the three cases did not explain the improved life seen from the higher hydrogen content. Instead the difference in performance is explained by reduced levels of load shedding from the soft regions of the bimodal structure to the hard regions for higher hydrogen contents. Evans and Bache however did report a change in fracture mechanism based on content for Ti-685 of lamellar microstructure [114]. For 20-60ppm faceted cracking was seen, but for higher hydrogen content

(>100ppm), the mechanism changed to extensive cracking along α/β interfaces and at prior β grain boundaries.

1.9 Material Processing

Mechanical deformation operations such as forging or ring rolling are used to shape titanium billets towards their final component shape. Machining processes shape the components into the various complex geometries. Often the final machined component can weigh less than 10% of the initial forging weight, a parameter commonly referred to as the buy to fly ratio. Due to the large amounts of waste generated from the forge-machine process, near net shape processes such as investment casting, powder metallurgy, and laser forming have become attractive methods [62].

1.9.1 Forging

Forging is one of the most common metal shaping process and involves the application of thermal and mechanical energy to a workpiece to shape it into a desired geometry. Two major classes or equipment are used for forging operations: the forging hammer and the forging press. The forging hammer delivers rapid impact blows to the surface of the metal while the forging press subjects the metal to a slow speed compressive press [62]. For titanium operations, the compressive press is more commonly used.

Open die and closed die are the two main categories of forging. Open die forging is carried out between flat dies of simple shape. The process is used mostly for large workpieces where the number of parts produced is small. One of the first processes on titanium ingots is upset forging, where the cross sectional diameter is increased and the length is decreased.

In closed die forging the workpiece is completely enclosed within the die. Closed die forging is used to shape more complex geometries and multiple components. A slight excess of material is used when closed die forging, to ensure the entire cavity is filled. This excess metal comes out as a thin ribbon referred to as a flash. It is important to ensure that the pressure required to fill the most intricate areas of the cavity is less than the pressure required to eject the flash to ensure that the entire cavity is filled.

The images below display examples of open die forging (Figure 1.37a) [115] and closed die forging (Figure 1.37b) [116].

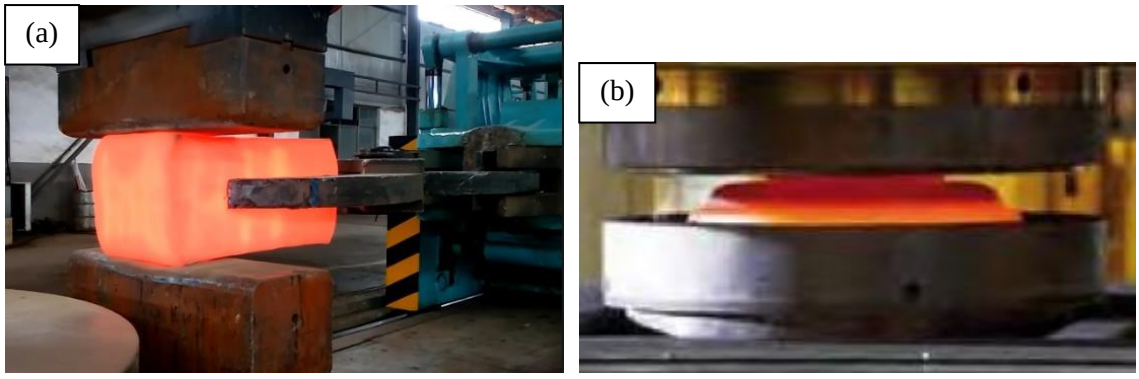

Figure 1.37: (a) Open die forging and (b) Closed die forging.

Titanium alloys have a relatively low thermal conductivity. This means that at high deformation rates the workpiece experiences significant adiabatic heating, as the heat is unable to dissipate away. This can lead to strain localisation. Intense shear bands cause inhomogeneous strain distributions and ultimately lead to non-uniform microstructures. Control of deformation rates during forging and ring rolling processing steps is therefore very important as it can have a significant influence on the microstructure and resultant mechanical response. Another important parameter to consider is the working temperature. The lower the temperature is the higher the flow stresses are, meaning more heat is generated in the active shear bands. In cases of extremely high deformation rates or low working temperatures, the critical strain for ductile fracture can be exceeded locally in these shear bands resulting in the formation of voids. These are referred to as strain induced porosity and have a detrimental effect on the fatigue life [4].

1.9.2 Ring Rolling

There are several ways to make an industrial grade metal ring including: casting; bending and seam welding; torch or saw cutting; and powder processes. However, round shaped components such as the fan and compressor casing are most easily formed from the ring rolling process. Advantages of this process include material savings, the reduction in corrective machining operations, the creation of smooth surfaces and favourable grain orientation and the inherent cost savings from the more efficient process. A review by Mamalis and Johnson found that the price of an RB211 jet engine in 1976 would be reduced by $100,000 (worth $430 000 or £330,000 today) if the rings were formed by ring rolling instead of being machined [117].

In order to create a ring rolled ring, a hole is pierced in the centre of a billet (using a hydraulic press), producing a thick walled cylinder. This is then heated and placed in

a ring rolling mill, an example of which is given in Figure 1.38(a) [118]. The preform billet is placed over the idle or mandrel roll and is forced towards the driven roll, plastically deforming the billet under high pressure in the radial direction, reducing the width of the section. The axial rolls which apply pressure parallel to the axis of the ring, reduce the height of the cross section. Radial-axial rolling mills are capable of producing rings of up to 6.4m in diameter. Ring rolling produces seamless rings and, depending on the application, can be seen as a near net shape process. A snap shot of the ring rolling process is shown in Figure 1.38(b) [119].

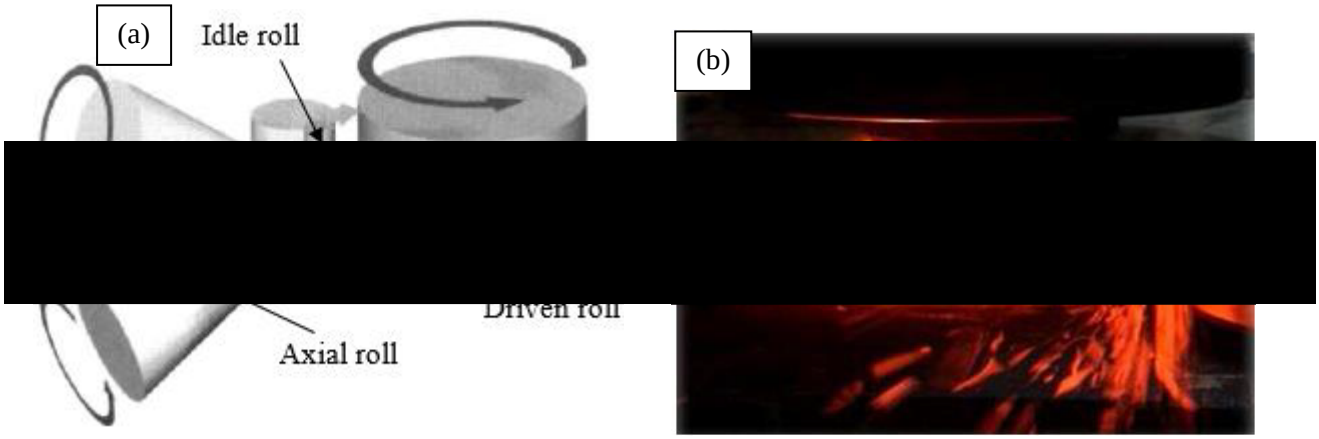

Figure 1.38: (a) Basic configuration of a radial-axial rolling mill (b) Snapshot of the ring rolling process.

Studies have been carried out to optimise the ring rolling process parameters on titanium alloys. Parameters to take into consideration include the rolling force of the dies, the angular velocity of the roll and the surface temperature of the dies used [120]. Higher ring rolling temperatures allow for more deformation, but the level of precision of the final geometry is reduced. Whilst less reduction is possible with cold rolling, on top of the increased geometrical accuracy, the work hardening helps to increase the strength and fatigue life of the component.

The aim of optimising the parameters is to achieve minimal forming loads, uniform distribution of strain and temperature and minimal defects. Defects associated with the ring rolling process include surface defects such as fish tailing and folder, flow localisation and shear bands. Form errors in the cross section can occur at the two free surfaces within a roll bite where unwanted deformation is generated perpendicular to the direction of the pressure. This is the origin of the fish-tail defect which is displayed below in Figure 1.39. Form errors in the ring itself are also a concern. These include: non circularity; conicity; dishing and waviness. As the spread of the deformation is

non-uniform a bulge is likely to appear at the edges of the unconstrained faces of a ring rolled ring in purely axial or radial directions. In a radial axial machine the effect is further exaggerated because the bulge is deformed twice per revolution leading to higher levels of strain in the ring corners [118].

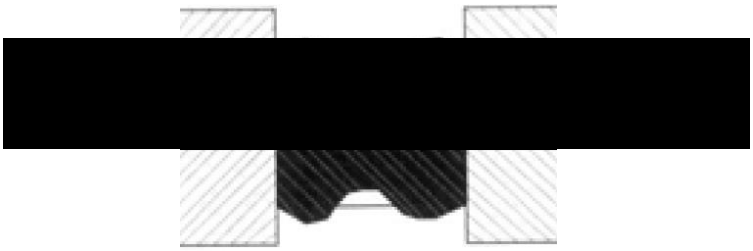

Figure 1.39: Fish tail defect associated with the ring rolling process [62].

Particular microstructures are achieved by attaining a certain temperature profile, generated rolling speed selection and temperature control. It is important to control temperature changes whilst rolling titanium alloys [121].

1.9.2.1 Cold Rolling versus Hot Rolling

It has been shown that cold rolling saves energy and material through increased precision meaning that waste can be reduced by 10–30%. Cold rolled material requires less machining and heat treatment after the process. A study found that cold rolled steel alloy had a 10% increase of both ultimate strength and ductility relative to hot rolling. However rolling a too low a temperature will result in surface cracking through the formation of shear bands.

1.9.2.2 Preform

The material that is initially placed on the ring rolled mill is referred to as the preform and its design influences the ease at which a specific cross section can be produced. Traditionally the preform is generated from a blank which is heated, upset, forged and then pierced. One area of research has studied how the level of waste generated from the pierced material can be reduced through a method referred to as ausrolling [122]. The preform is tower forged. This means that the material removed by piercing to form the outer ring is itself pierced and pre-shaped to become the inner ring. Figure 1.40 shows the difference between the traditional process and the ausrolling process.

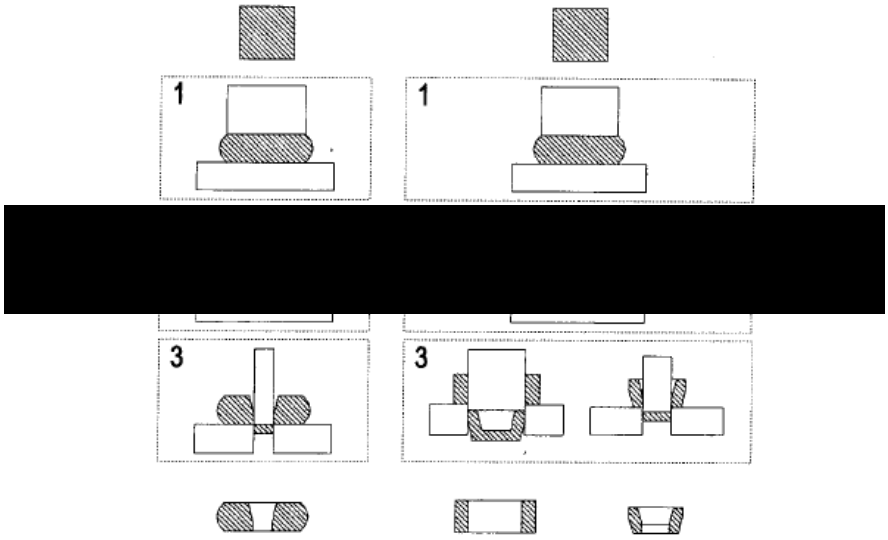

Figure 1.40: Manufacture of preform through the traditional process (left) and the ausforming process (right) [62].

1.10 Jet Engine

The final section of the literature review gives an overview of the components of the jet engine. First, however, some information is given on the current state of affairs regarding environmental targets, with closer public and media scrutiny leading to more careful consideration of environmental impact within the aviation industry.

1.10.1 Efficiency Trends

Between 1960 and 2014 the average fuel burn of commercial aircraft fell by 45%. Within this time there have been periods of rapid improvement due to the adoption of new technologies and more efficient aircraft design, and periods where little to no improvement was observed, demonstrated by the graph in Figure 1.41 [123]. Because fuel is an important factor to the overall operating costs of airline companies, aircraft and engine manufacturers have a strong incentive to improve efficiency. Historically, fluctuation in fuel prices has changed the level of drive behind efficiency improvements, but the continual increased demand for air travel and the International Civil Aviation Organisation (ICAO) fuel burn technology goals suggest an acceleration of improvement over the next 10 to 20 years.

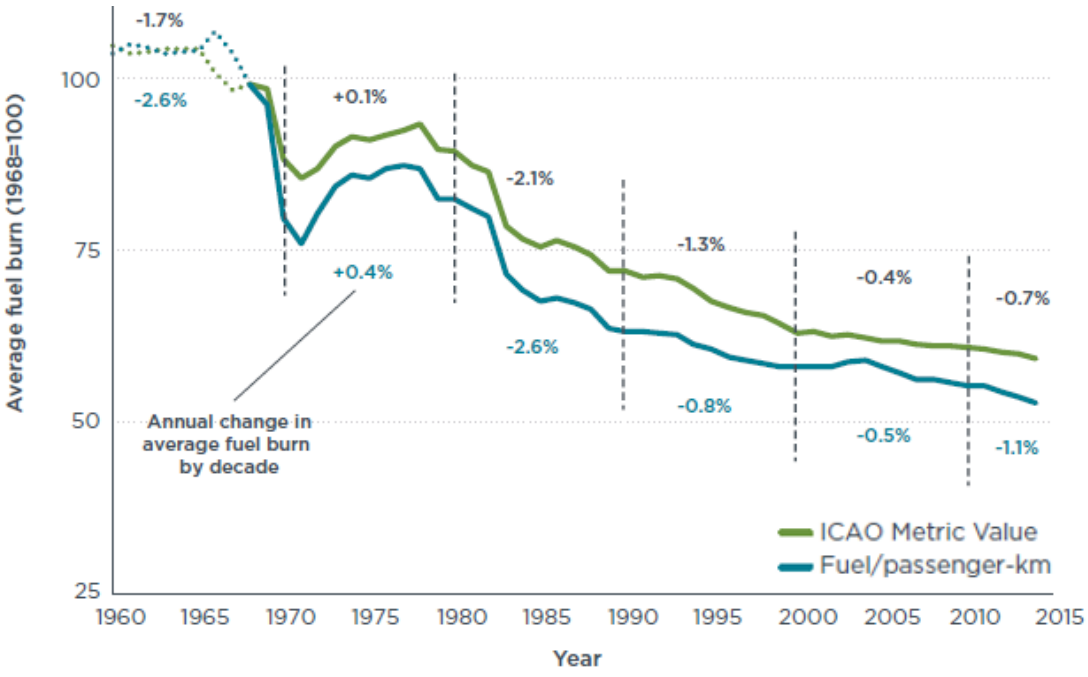

Figure 1.41: Average fuel burn for commercial jet aircraft from 1960 to 2014.

Despite the efficiency improvements that have been achieved, the perpetual increase in demand for air travel meant that CO_2 emissions quadrupled between 1960 and 2000. This trend is displayed graphically in Figure 1.42.

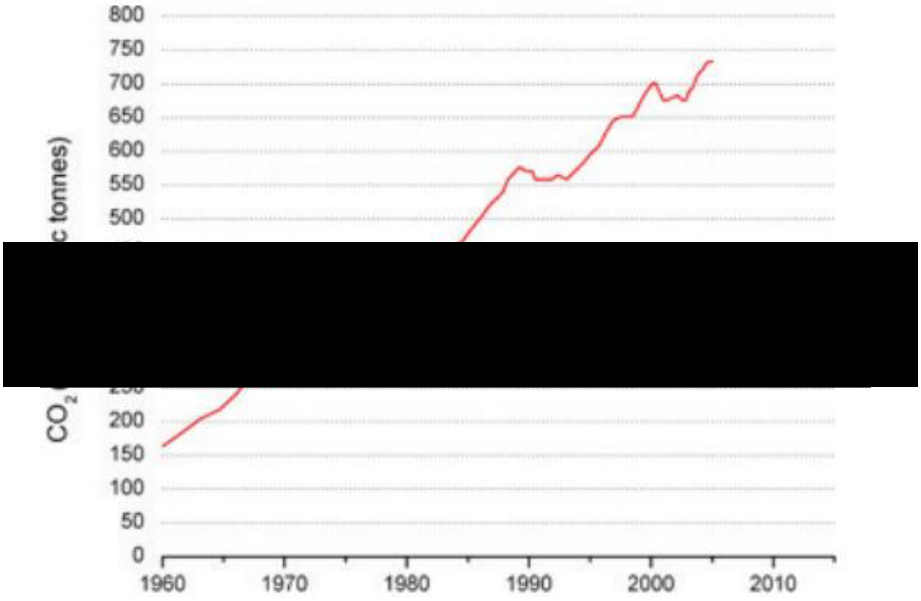

Figure 1.42: CO_2 emissions from aviation from 1960 to 2006 [124].

Aircraft manufacturers predicted that the global civil fleet could almost double, from 20,500 in 2006 to 40,500 in 2026 [125]. In 2010, the 37th session of the ICAO set the goal of achieving carbon neutral growth from 2020, by maintaining a 2% fuel efficiency improvement each year from 2021 to 2050. Andrew Macintosh and Lailey Wallace suggest however, that it is doubtful emissions will be stabilised at levels consistent with risk averse climate targets without restricting demand [126].

Because aircraft eject the majority of their emissions at high altitude (8–12Km), they have a magnified damaging effect on climate forcing, for example cloud formation and O_3 production. Climate forcing refers to the difference between the sunlight absorbed by the earth and energy radiated back into space. The microphysical and chemical properties of the upper atmosphere are altered as a result of the cloud effects and emissions from the gas turbine. The climate change effect resulting from this ultimately damages welfare and ecosystems. Figure 1.43 demonstrates the damaging effects of aircraft emissions [127].

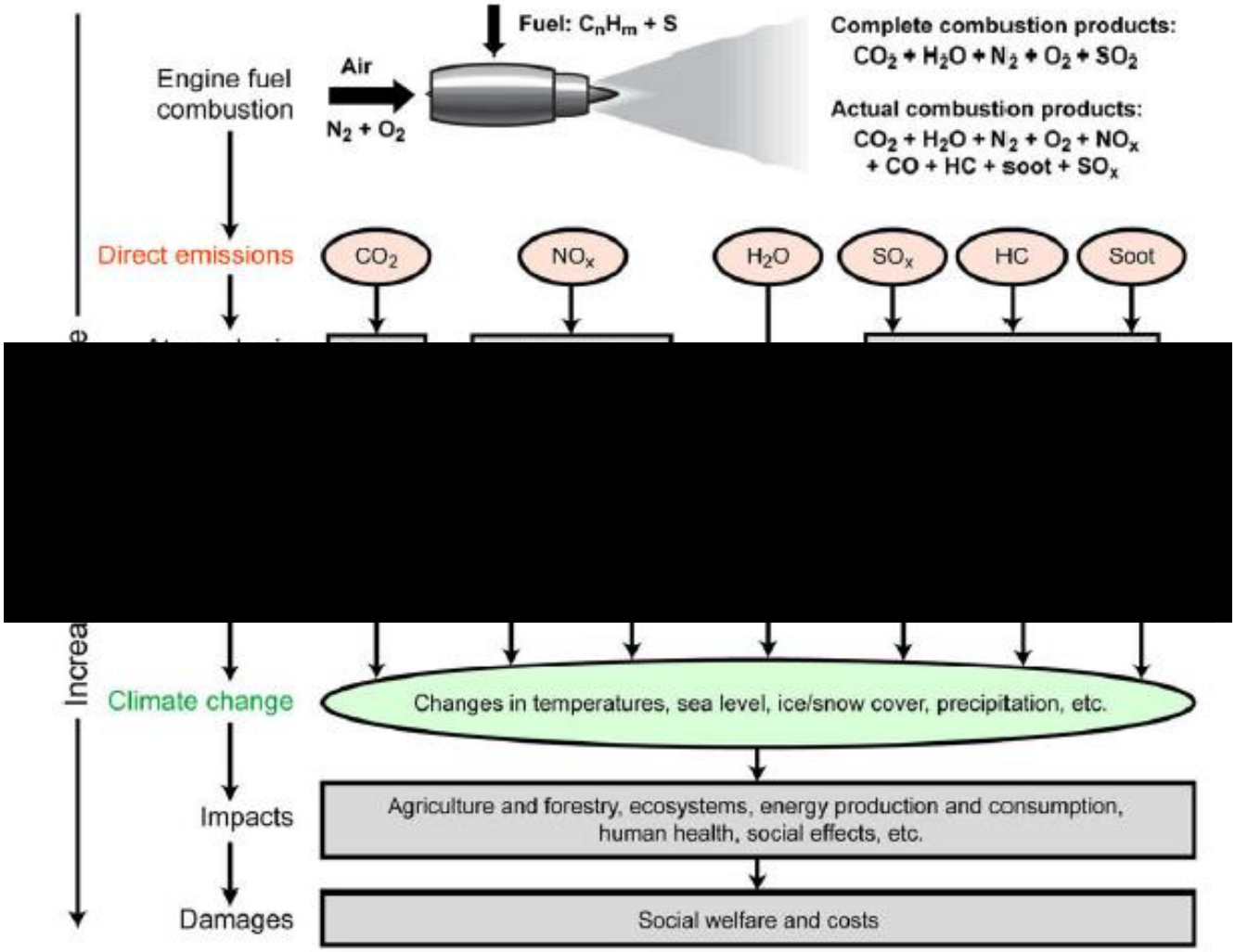

Figure 1.43: Impact of aircraft emissions on climate change.

Materials science plays an important role in helping to continue the trend of improved engine efficiency, developing lighter and higher temperature alloys. Efforts to improve the gas turbine engine have focused on three main areas: increasing the turbine entry temperature; increasing the efficiency of turbomachinery components such as blisks and blings; and adding modifications to the basic cycle, for example intercooling. Abradable coatings helped to further increase efficiency by optimising the aerodynamic performance through the engine. Performance improvements are gained by reducing clearance between blades and engine casing [128].

1.10.2 Engine Components

The main engine components are detailed below.

1.10.2.1 Fan

The fan compresses the bypass air and feeds supercharged air into the core of the engine. Large engines can draw in one tonne of air per second. The fan is driven by the low pressure turbine through a driveshaft. The components of the fan system are the blades, the disc, the containment casing and the front bearing housing.

1.10.2.2 Compressor

The compressor system consists of intermediate and high pressure compressors. The purpose of the compressor is to supply the combustor with as much energy as possible in order to maximise the amount of thrust that can be generated. Compression ratios of up to 40:1 are possible with temperatures at the exit greater than 700℃ [129]. The compressor section consists of a series of rotating and stationary blades, the rotating blades squeeze the air against the static blades increasing the pressure, temperature and energy of the air.

1.10.2.3 Combustor

Heat is created in the combustor by converting the chemical energy of the fuel into thermal energy. The superheated compressed air approaches the combustor at roughly 500mph where it is slowed down by the perforations in the casing. Fuel is mixed with the air and the mixture is burned at temperatures of up to 2000℃ forcing exhaust gases towards the turbine.

1.10.2.4 Turbine

The hot gases that leave the combustor expand to lower pressures and temperatures through the turbine, and the rapid expulsion of the gases produce force to power the aircraft. Energy is extracted as it travels through the turbine section to drive the fan and compressor. The turbine consists of alternate static vanes and rotating discs.

1.10.2.5 By-pass air

Thrust from bypass air can contribute more than half of the thrust produced by the engine, and more than 80% of the total thrust for some phases of flight [130]. Relative to the core, thrust is produced by a large mass flow of air being accelerated a relatively small amount compared to the core, where a relatively small amount of air is accelerated to high speeds at a high temperature. Bypass air helps to increase the overall efficiency of the engine because much of the energy from the air carried

through the core is used to spin the high and low pressure turbines that drive the fan and compressor sections of the engine. The sharp increase of efficiency seen in 1970 on the graph in Figure 1.41 can partly be attributed to the first high bypass engines on the Boeing 747-100 and Boeing 747-200. The cool bypass air also helps to reduce the noise of the engine. It is mixed with the much hotter air that travels through the core; this mixing cools the engine exhaust and reduces the jet engine noise resulting from the rapid expansion of the air once it leaves the engine. Further to this, the cool bypass air can be used for general engine cooling.

1.10.3 Use of Titanium

The engine components are made predominantly from titanium and nickel alloys. Titanium is lighter than nickel but its use is limited up to the HP compressor section of the engine due to its maximum operating temperature of around 600℃ [131]. Titanium accounts for roughly 30% of the engine weight. Ti-6-4 is used for a range of components including the fan blades and disc, and low pressure compressor disc and blades, and is used up to temperatures of approximately 450℃. Ti-6246 and Ti-17 are used in areas where high strength is necessary [132]. Near alpha alloys such asTi-834 and Ti-1100 are used in the HP compressor section where strength at high temperature is important.

1.10.4 Use of Nickel

Beyond the compressor, where the temperatures increase, nickel alloys are used. An important area of research is the increase of temperature capabilities of nickel alloys up to the stoichiometric temperature of approximately 2150℃. Engines operating at higher turbine inlet temperatures are thermally more efficient and have an improved power to weight ratio. Currently nickel blades operate at up to 1800℃. In the last 25 years this temperature has increased by roughly 300℃: 150℃ thanks to improved cooling design, with the blades operating in a gas stream far in excess of the melting point of the blade material, and 150℃ down to improved materials and casting techniques [19]. Figure 1.44 displays the distribution of titanium, nickel, steels and other materials within the jet engine [19].

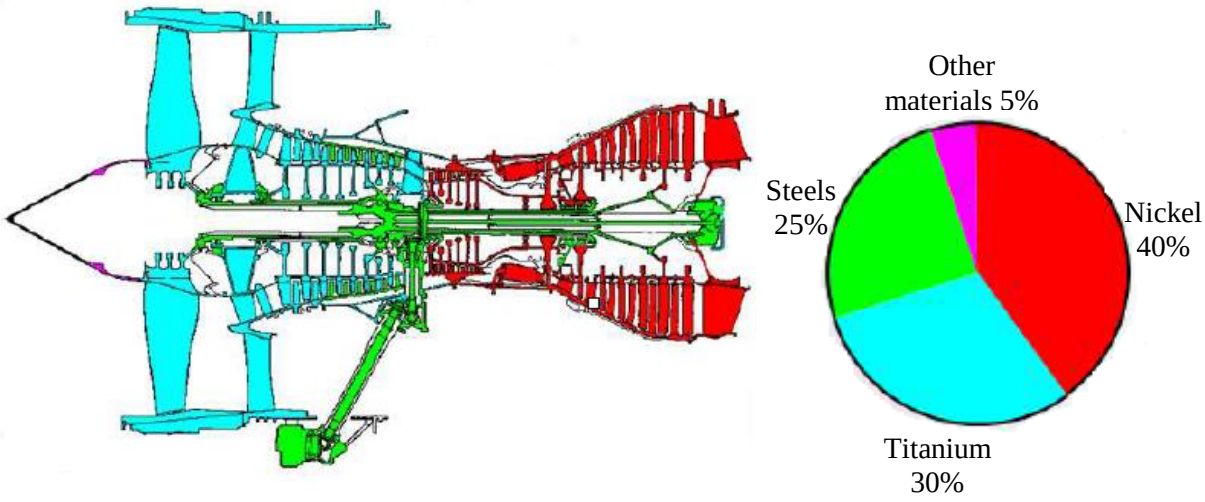

Figure 1.44: Typical distribution of materials within the gas turbine engine.

1.10.5 Component Classification

Components in the gas turbine engine are ranked in terms of the risk to the airframe if a given component were to fail. The part classifications are:

- Critical – Failure of a critical component would be a hazard to the airframe, as failed parts cannot be contained within the engine. Discs and shafts fall into this category. The required in service failure rate is less than one in a hundred million.
- Sensitive – Failure of sensitive components may result in engine shutdown. There should not be a risk to the airframe as no high energy debris would be released. Examples of sensitive components include blades, combustion chambers and outlet guide vanes
- Unclassified – Failure of unclassified parts present very little risk to the engine. Most static parts fall into this category.

Containment of blades is a major consideration in modern engines, particularly when one considers the energies associated with the large fan blades. The tip of the blade reaches speeds of up to 1000mph and experience centrifugal loads of 100 tonnes. The casing must be able to contain the blade if one or more are released either partially due to a bird-strike or some other kind of foreign object damage, or fully in the case of failure in the root due to fatigue.

1.10.6 Aircraft Engine Monitoring

Aircraft engine monitoring systems are used to check to health of the engine to prevent expensive repairs and the premature removal of engines from service.

The Trent 900 was the first Trent engine to be fitted with the advanced engine health monitoring (EHM) system based on QUICK Technology.

1.10.7 Current Aircraft Market

Boeing and Airbus are the main competitors within the aircraft manufacturing market and Rolls-Royce plc supply both with the following engines:

- RB200 Series used to power the Boeing 747 and 757
- Trent 500 series used to power the Airbus A340
- Trent 700 series used to power the Airbus A330
- Trent 800 series used to power the Boeing 777
- Trent 900 series used to power the Airbus A380
- Trent 1000 series used to power the Boeing 787
- Trent XWB used to power the Airbus A350

Other major engine suppliers include General Electric and Pratt & Whitney. Further to this, several joint ventures exist: CFM international, a joint venture between General Electric and Safran Aircraft engines; Engine Alliance, a joint venture between General electric and Pratt & Whitney; and International Aero Engines, a joint venture between Rolls-Royce plc, Pratt & Whitney, Japanese Aero Engine Corporation and MTU.

As of February 2019, it was announced that Airbus was going to end production of its largest model, the A380, as a result of Emirates reducing their order from 162 to 123 [133]. The A380 has 550m^2 of usable floor space, which is 40% larger than the next biggest airliner, the Boeing 747. In an all economy configuration it can carry 868 people. Initially the A380 was hailed as a technological marvel that would connect the world's crowded airport hubs. Indeed, the rationale in building a high capacity aircraft was the belief in the hub and spoke model of aviation. It was predicted that 1,500 would be built. However, following the decision to cease production, the final tally will be little over 250.

The A380 was aimed at the rapidly expanding Asian market where airlines were keen to fly more people per flight. After an initial spurt of orders when the model was first announced, demand for such a large aircraft dried up in favour of smaller, wide-body jets [134].

Long haul aircraft with two engines such as the Boeing 787 and 777, and airbus A330 and A350 are proving to be favoured over larger aircraft. Advances in engine technology mean aircraft no longer need four engines to fly long distance. Indeed, the efficiency of the A380 relative to the 787 is poor. The A380 has an efficiency of 72mpg per seat relative to 102mpg per seat of the 787. Also, the use of smaller aircraft mean passengers do not have to rely on travelling via 'hub' airports, making journeys from more rural areas easier and more direct. This point to point model is better suited for smaller aircraft which are more easily accommodated at smaller airports.

The whole program for the A380 is thought to have cost around £19.4bn but has never made a profit.

1.10.8 Future Possibilities for Engine Technology

SABRE (Synergetic Air Breathing Rocket Engine) is a new engine concept currently under development by Reaction Engines Limited. It would work as a jet engine up to Mach 5.5, before switching to rocket mode. Currently, rockets have to carry liquid oxygen and liquid hydrogen to power them, which is heavy and expensive. The SABRE engine is capable of creating its own liquid oxygen by rapidly cooling air entering the engine from 1000℃ to -150℃. It could reduce the time to travel to the other side of the globe to four hours.

2 Introduction

Following the literature survey, the depth of understanding derived from the mechanical data for each alloy highlighted the importance of an efficient testing matrix to successfully characterise the performance of Ti-407 and Ti-412. The initial work was focused on collating existing company data and external literature on Ti-407 and similar alloys. The second phase processed suitable material stocks for the extraction of mechanical test specimens. Thermomechanical processing experiments were carried out to fully understand the microstructural evolution of the alloy. A design of experiments was conducted to evaluate pertinent mechanical properties, i.e. monotonic tension, fatigue, fatigue crack propagation and threshold behaviour. An extended test matrix followed, generating fractured specimens for detailed fractographic inspection to identify key deformation and failure mechanisms. The large frequency effect observed from the initial HCF and LCF curves, led to the undertaking of dwell and strain controlled testing. Further to Ti-407 and Ti-412, fatigue testing was conducted on Ti-6-4 and Ti-834 to act as a comparison of both material and product form.

2.1 Initial Research & Development

The development of Ti-407 was motivated by the cost-saving opportunity available through improved workability. Titanium alloys have been employed extensively within the aero-engine sector since the 1950s. The high strength to weight ratio at low to intermediate service temperatures, good corrosion resistance and low density relative to that of competing metals, contribute to the production of lightweight and durable components, with applications ranging from the large-scale fan blades and supporting discs at the front of the engine, through to relatively small vanes and blades in the high pressure compressor section. The well-established Ti-6-4 (Ti-6Al-4V) is still used for many engine components such as the fan blades and discs, in part, due to the range of microstructural forms produced via thermomechanical processing that can be tailored to specific applications. Ti-6-4 accounts for 50% of the total titanium production [135]. This alloy is widely acknowledged as presenting a balance of mechanical properties including good fatigue performance with intermediate fracture toughness and moderately high tensile strength [136]. Over the years substantial work has been undertaken to optimise the manufacturing and production of Ti-6-4 components. However, economic competition is encouraging more cost-effective

production, leading to the development of bespoke alloys, better suited for specific components in terms of both mechanical performance and ease of manufacture.

Historically and in general, the machinability of titanium and its alloys was considered to be difficult. The term machining refers to metal removal and cutting proceses. These processes include turning, milling, end milling, drilling and reaming [4]. Early practitioners in the 1950s believed that ‘machining of titanium and its alloys will always be a problem, no matter what techniques are employed to transform this metal into chips’ [137]. More recent workers in the 1980s, when referring to the same issues, stated that ‘this is still true in so far as cutting tool materials are concerned’ [138]. The low thermal conductivity of titanium increases the temperature at the tool/workpiece interface, decreasing the tool life. When machining Ti-6-4, about 80% of the heat generated is conducted into the tool and is concentrated on the cutting edge and tool face.

Additionally, titanium is highly chemically reactive. This results in the material welding to the cutting tool during machining, leading to significantly shorter tool lives. The high strength of titanium which is maintained at elevated temperatures, and the relatively low elastic modulus decrease the machinability further. In fact, relative to nickel and steel alloys, the elastic modulus of titanium is roughly 50% lower. This is a problem because it can cause deflection of the workpiece if it is not sufficiently supported by tooling. Understanding of this issue is particularly important during final machining operations if tight dimensional tolerances are required. For these reasons, the improvements in machining of titanium alloys had fallen behind the progress seen by other materials in this area [139]. Other alloys such as steels and nickel-based superalloys have benefited from the advancement in the development of cutting tools. This progress includes the use of coated carbides, ceramics, cubic boron nitride and polycrystalline diamond [140]. These cannot be used with titanium however, because of a strict set of quality criteria driven by the aerospace and automotive industries. The tools need a high coefficient of thermal conductivity, good thermal resistance, high hardness, wear durability and hot hardness. Hence, tungsten carbide tools are used for the vast majority of titanium tooling processes.

Titanium alloys with lower aluminium content are more malleable. Increasing the Al content distorts the crystal lattice and therefore tends to impede dislocation movement, making the alloy stronger but less ductile. Figure 2.1 demonstrates how the reduction of the aluminum content increases cold rolling ability [141].

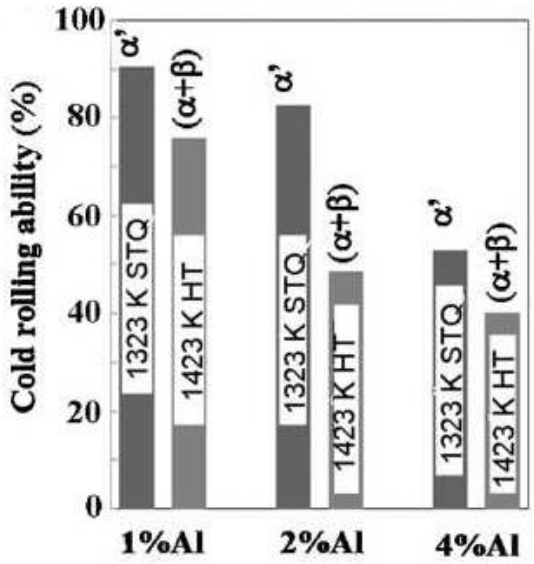

Figure 2.1: Effect of aluminium content on cold rolling ability.

At TIMET, an assessment of aluminum content, aluminum equivalent and alpha/beta ratio is carried out on alloys to be processed to determine the most suitable rolling route. Increasing the Al content increases the propensity for surface cracking and therefore dictates the use of lower strain rates during processing. Ti-834 is one of the most difficult alloys to process. It has found use in fighter jets, where the performance benefits of its high temperature capabilities of up to 600℃ outweighs the cost of manufacture. However, Ti-6-4, which can be used up to temperatures of 450℃ is preferred for commercial applications. The diagram below, in Figure 2.2, plots the aluminium equivalence as percentage of aluminium and molybdenum equivalence against a number of common titanium alloys. Metallurgists at TIMET agreed that the order in which the alloys are presented correlates with the most difficult (top left) to easiest (bottom right) to process. Maintaining a low aluminium equivalence percentage to enable cost effective production is clearly a key consideration. It is encouraging to note the positions of Ti-407 and Ti-412.

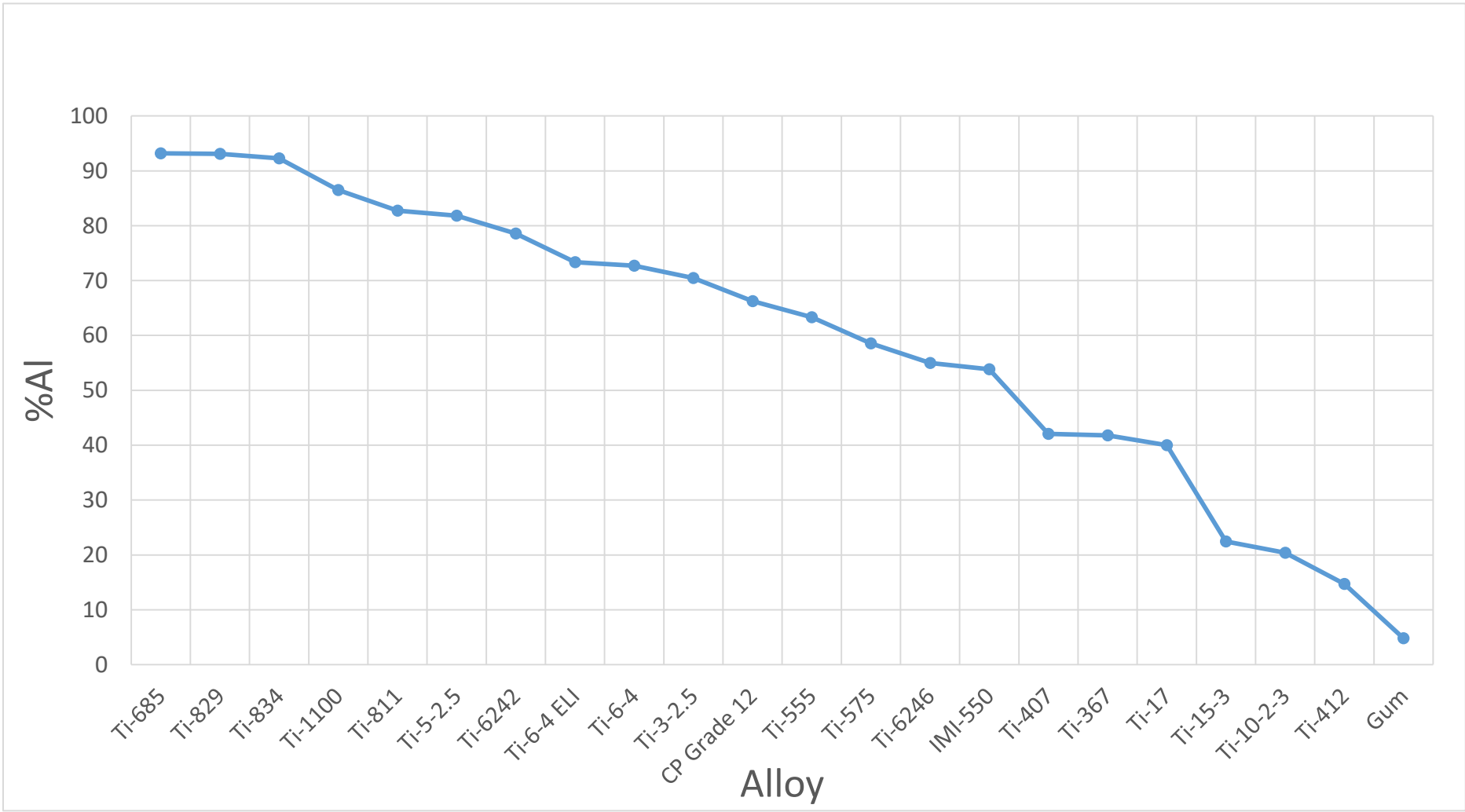

Figure 2.2: Plot of alloy vs aluminium equivalence percentage (Al equivalence / Al + Mo equivalence).

An important aspect during processing is the difference between the beta transus temperature and the rolling temperature. A bigger difference will result in more alpha phase, which, with fewer available slip systems than the more ductile BCC beta phase, will increase the amount of cracking. The alloys Ti-685, Ti-829 and Ti-834, which have the highest beta transus temperature due the large percentage of alpha phase, are particularly difficult to process and require more heat treatments, extra processing steps such as plaining and more complicated machining steps. Despite the increased cost of these alloys, the still have demand in areas of the engine that require good creep resistance.

Previously it has been shown that the alloy Ti-1Al-4V has a UTS of roughly 650MPa and an elongation to failure of 25% (6). This was taken as the starting point for the development of Ti-407. During the development of the alloy it was important to show a viable and economical solution which considered factors such as the availability of raw materials, the preferred melting method, the effect of industrial conversion routes and the properties of heavy forging sections. More than 100, 200g buttons of various chemistries were melted during the development of the alloy. These buttons were rolled, heat treated and tensile tested. Multiple linear regression and neural network modelling was used to help optimise the most promising chemistries. The table below shows the composition and physical properties of the final Ti-407 and Ti-412 chemistry relative to Ti-6-4 and Ti-3-2.5 [142].

Table 2.1: Chemistry and physical properties comparison.

Attribute	**Ti-407**	**Ti-6-4**	**Ti-3-2.5**	**Ti-412**
Al, wt%	0.85	6	3	1.1
V, wt%	3.1	4	2.5	6.9
O, wt%	-	0.15	0.1	0.15
Si, wt%	0.31	-	-	0.15
Fe, wt%	0.22	0.15	-	0.8
ρ g cm^{-3}	4.53	4.42	4.48	~4.55
Tβ °C	877	996	935	832

Ti-407 displayed more than double the tool life than that of Ti-6-4 based on V15 tests. V15 testing is a standardised machining test that allows comparison between alloys and other materials. The test finds the maximum cutting speed for 15 minutes tool lifetime. The reduction in tool wear and the lower forces required allow for faster,

more efficient machining. Compared to Ti-6-4 the low flow stress, greater malleability and wide process window of Ti-407 should allow it to be processed with fewer reheats, while exhibiting less surface cracking and giving a consistently good surface finish [142]. Optimised Ti-407 manufacturing processes should favour nearer net shape giving higher yields and requiring less machining to finished components. However despite the improved machinability as far as tool wear and cutting force are concerned, the increased ductility of Ti-407 does also present some problems. Firstly, chip formation is less optimal when compared to Ti-6-4. The higher thermal conductivity of Ti-407, which is almost double that of Ti-6-4, is one of the contributing factors towards the more continuous and much more difficult to manage chip formation. Secondly, due to the greater strain accommodated in the chip, serve plastic deformation and mechanical twinning are retained in the machined surface [143]. These subsurface features could have a detrimental effect of the mechanical performance.

A large database of processing yield performance is available at TIMET. This database expresses the yield as a plus or minus percentage relative to the average yield across all alloys. For Ti-407 this is +6%. Data is not yet available for Ti-412 but based on Figure 2.2, which shows a 25% decrease in aluminum equivalence relative to Ti-407, it would be expected that its processability would be superior to that of Ti-407.

Initial HCF data on Ti-407 carried out at TIMET's Witton plant in Birmingham, is presented in Figure 2.3. Run-out at 20 million cycles was found at 500MPa.

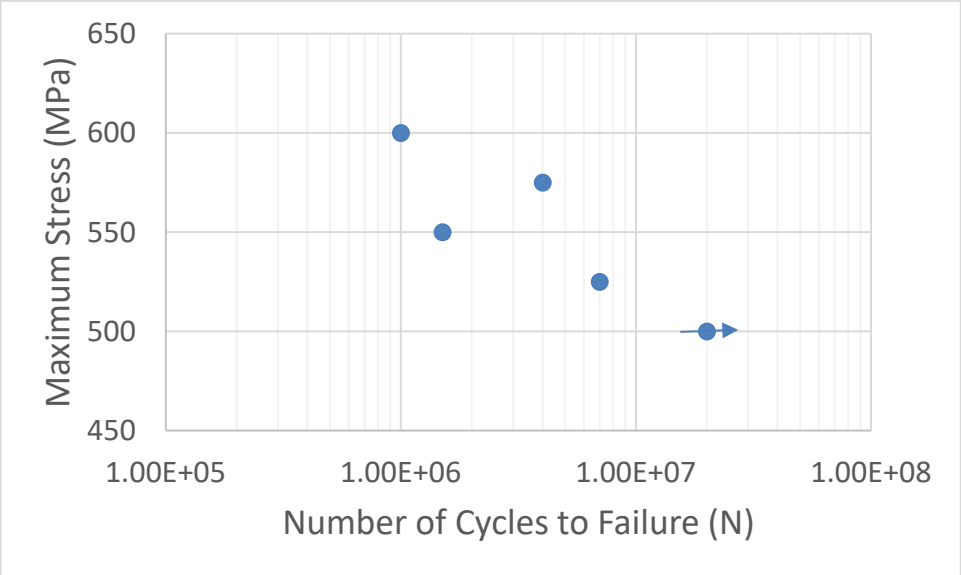

Figure 2.3: Initial HCF fatigue tests results on Ti-407.

Of particular interest, Ti-407 can replace Ti-6-4 in applications where the key design criteria are energy absorption during fracture and HCF endurance limit. The most relevant applications within the gas turbine are, therefore, the engine fan and

compressor casings. Due to its relatively low strength, Ti-407 may not be able to replace all Ti-6-4 components but as mentioned, promisingly Ti-407 demonstration casings have shown 2.5 times the lateral expansion and absorbed more than twice the impact energy when compared to Ti-6-4. Whilst Ti-407 is slightly denser, its superior energy absorption means that less material will be required for the same component and therefore weight savings can still be made. Further weight savings again may be possible from the stronger Ti-412 alloy, with less material required for a given component to provide the same performance.

3 Experimental Methods

The following section describes how the data was generated through the testing processes themselves, and the analysis of the fractured specimens. First, the origins of the material used for the testing are given. Secondly, an explanation of test piece manufacture is provided. For the pancake material, part of this process included determining a suitable heat treatment program to generate a desired microstructure; the heat treatment trials carried out for this purpose are described. Thirdly, a description of testing methods are provided. Finally an explanation the post-test analysis is given.

3.1 Testing Material

Throughout the course of the project a large amount of testing was carried out. The majority was completed on Ti-407 material. As a means of comparison, tensile data and fatigue curves were generated from Ti-6-4 test pieces. Towards the end of the project some further HCF, LCF, dwell and tensile data was generated for Ti-412, a slightly stronger variant of Ti-407. Finally, some supplementary Ti-834 HCF testing was carried out for further comparison. The test product forms were either ring rolled, or pancake forged, apart from the Ti-834 test pieces which originated from bar stock.

Ring rolled product from two different companies were used. In order to keep the companies anonymous, they will be referred to as manufacturer 1 and manufacturer 2.

3.1.1 Ti-407 Manufacturer 1 Ring Rolled Material

First, two ring rolled blocks from the same original ring were tested. These were machined at manufacturer 1. The first block was used to generate the initial HCF and LCF curves and the second to investigate dwell and test-piece orientation sensitivity. Images of the two blocks are shown below in Figure 3.1.

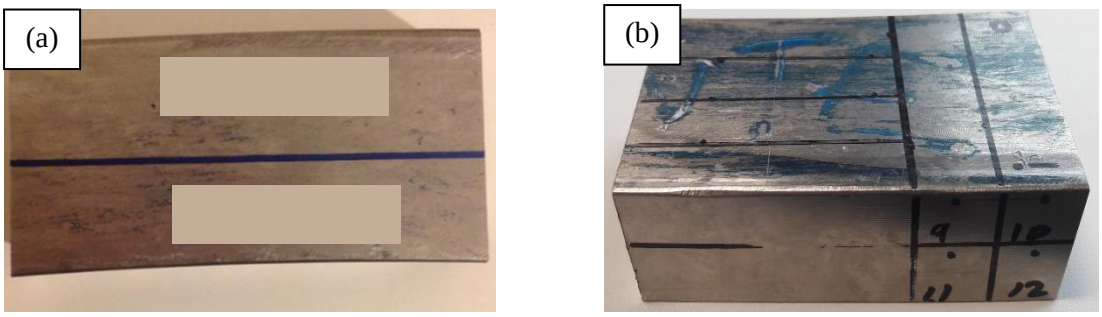

Figure 3.1: The two Ti-407 ring rolled blocks from manufacturer 1 (a) Used for the initial HCF and LCF curves and (b) For dwell and orientation effect testing.

3.1.2 Ti-407 Manufacturer 2 Ring Rolled Material

A third ring rolled block from manufacturer 2 was tested to provide a more detailed study on test piece orientation effects and testing frequency. This was rolled from an original alpha/beta forged billet of 26 inches into a ring of 125 inches in diameter, shown below in Figure 3.2(a) along with the ring rolled block used to extract the test pieces, Figure 3.2(b). Roughly marked on the block in Figure 3.2(b) is the rolling direction.

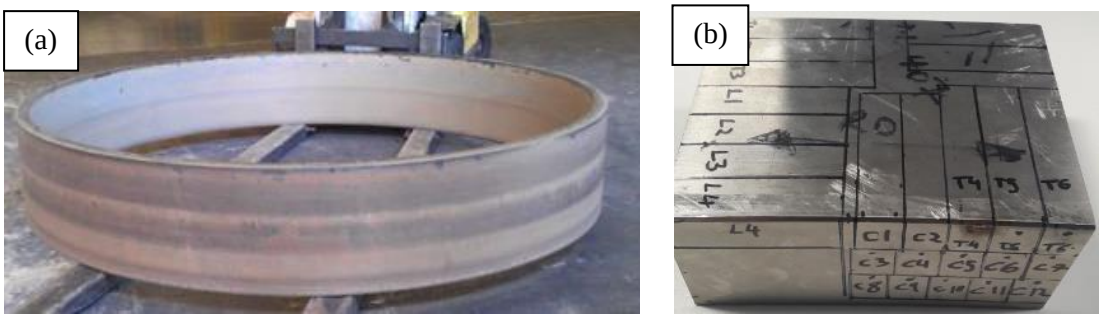

Figure 3.2: (a) The original TI-407 manufacturer 1 125 inch ring, and (b) The block from which testing specimens were extracted.

For the ring rolled material of both manufacturers, specimens were manufactured directly from the blocks, with no additional heat treatments carried out.

3.1.2.1 Orientation directions

At this point it is worth defining the directions referred to when discussing orientation. The radial direction points from the middle of the ring towards the outer edge following the length of the radius. The tangential direction follows the circumference of the ring and is perpendicular to the radial direction. Finally, the axial direction runs along the axis of rotation of the ring. The image presented in Figure 3.3 displays these directions [144].

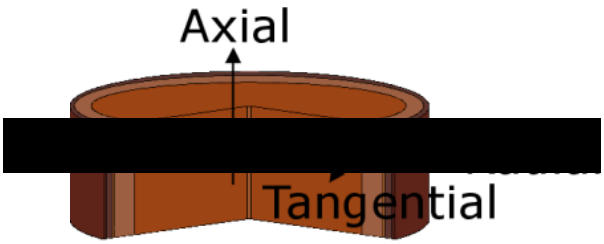

Figure 3.3: Directions associated with the ring rolled product form.

In Figure 3.2(b), ‘L’ refers to fatigue specimens in the tangential direction, ‘C’ to fatigue test pieces in the axial direction and ‘T’ to tensile pieces in their respective directions.

3.1.3 Ti-407, Ti-6-4 and Ti-412 Forged Pancake Material

The process used to generate the forged pancake testing material is a standard TIMET procedure, designed to roughly mimic a secondary forging operation. A cross section is cut from a billet and cut up into a set number of slices. These slices are then forged into the final pancake form. In each case specimen blanks were extracted from the pancakes before heat treatments with the exception of the Ti-412 pancake, which was heat treated prior to blank extraction.

3.1.4 Ti-407 Pancakes

Pre-production Ti-407 pancake material (Ti-0.85Al-3.9V-0.15O-0.25Si-0.25Fe) was produced by TIMET via electron beam single melting (EBSM) in a cold hearth furnace to create an ingot. Billet sections were cut into four, 90° segments. A proprietary sequence of thermomechanical processing was carried out to produce component representative pancake forgings for this work. Mechanical test specimen blanks were extracted from the central regions of each pancake to deliberately avoid sampling the extremities of the material. Extraction was carried out through electrical discharge machining (EDM), a machining process that allows hard material to be worked to very close tolerances, allowing for the maximum use of the material available [145]. Figure 3.4 shows the four Ti-407 pancakes, and Figure 3.5 shows the extraction of the blanks.

Figure 3.4: The four Ti-407 pancakes, roughly 20cm in diameter.

Figure 3.5: Extraction of specimen blanks from central regions of pancakes.

3.1.5 Ti-6-4 Pancakes

Ti-6-4, being a well-established and prominently used alloy, as well as the alloy that Ti-407 will potentially replace, provided a good comparison to the Ti-407 HCF fatigue data. For this purpose, blanks were extracted from three similarly forged Ti-6-4 pancakes. The first two pancakes came from the same original billet. Unfortunately, the original billet identity has been lost and therefore the billet diameter and forging temperature are unknown. The first two pancakes with blanks extracted are shown below in Figure 3.6.

Figure 3.6: First two Ti-6-4 pancakes with blank extraction.

The third pancake originated from billet DRA4400, which had an 8 inch diameter. It was forged at 960℃ with a minimum soak time of 90 minutes. This pancake is shown below in Figure 3.7.

Figure 3.7: Third Ti-6-4 pancake from 8 inch diameter billet.

3.1.6 Ti-412 Pancake

Initial tensile data, HCF, LCF and dwell fatigue curves were generated from pancake forged Ti-412 material. The plan in Figure 3.8 shows the location of the fatigue test pieces (RLH8001_001 – RLH8001_016), and of the two tensile tests (RLH10004_001 and RLH10004_002). Whilst in general, extraction of test pieces near the extremities of the pancake was avoided, in this case one tensile piece was extracted from the middle and the other from the edge of the pancake, to check for effects of location on mechanical properties.

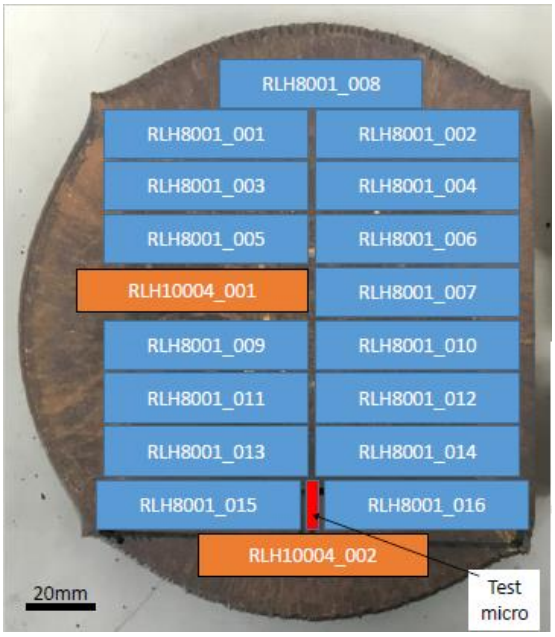

Figure 3.8: Cut up plan for the Ti-412 fatigue and tensile test pieces

3.1.7 Ti-834 Bar Stock

Finally, Ti-834 material originating from bar stock was tested. The remaining material from a previous work package [146] was tested under HCF loading conditions to see the position of the HCF curve relative to the already tested LCF and Dwell curves.

3.2 Pancake Forged Product Microstructure Development

Heat treatment trials were conducted in order to establish a solution treatment temperature that would generate a bimodal microstructure with approximately 30–40% primary alpha (α_p) volume fraction. This goal was based on results from early stage research and development [142] which suggested that this specific volume fraction provided the optimum fatigue performance. Increasing content has been shown to increase tensile plasticity [147], refine the microstructure and limit the formation of areas of common crystallographic orientation [148]. Whilst α_p within a lamellar matrix does offer these advantages, the percentage volume must be carefully restricted since beyond a critical volume, ductility ceases to improve, and alloy element partitioning takes place [149]. This degrades the basic strength of the lamellar constituent of the microstructure, therefore resulting in a decrease in fatigue life. A SNOL 1.8 Kw electric furnace was employed for microstructure trials, with two calibrated N type thermocouples in contact with the specimens (15x15mm cubes). The temperatures were constantly monitored throughout the duration of the heat treatments using calibrated Fluke thermometers.

3.2.1 Ti-407 Forged Pancake Heat Treatment Trials

For the case of the Ti-407 pancake material, samples were subjected to three different solution heat treatments, each for a two-hour period followed by an air cool. The results were:

- 820℃ producing 50% α_p volume fraction
- 840℃ producing 30% α_p volume fraction
- 860℃ producing 20% α_p volume fraction.

Figure 3.9 shows the resultant microstuctures and their volume fractions, measured using Mipar image analysis software [150].

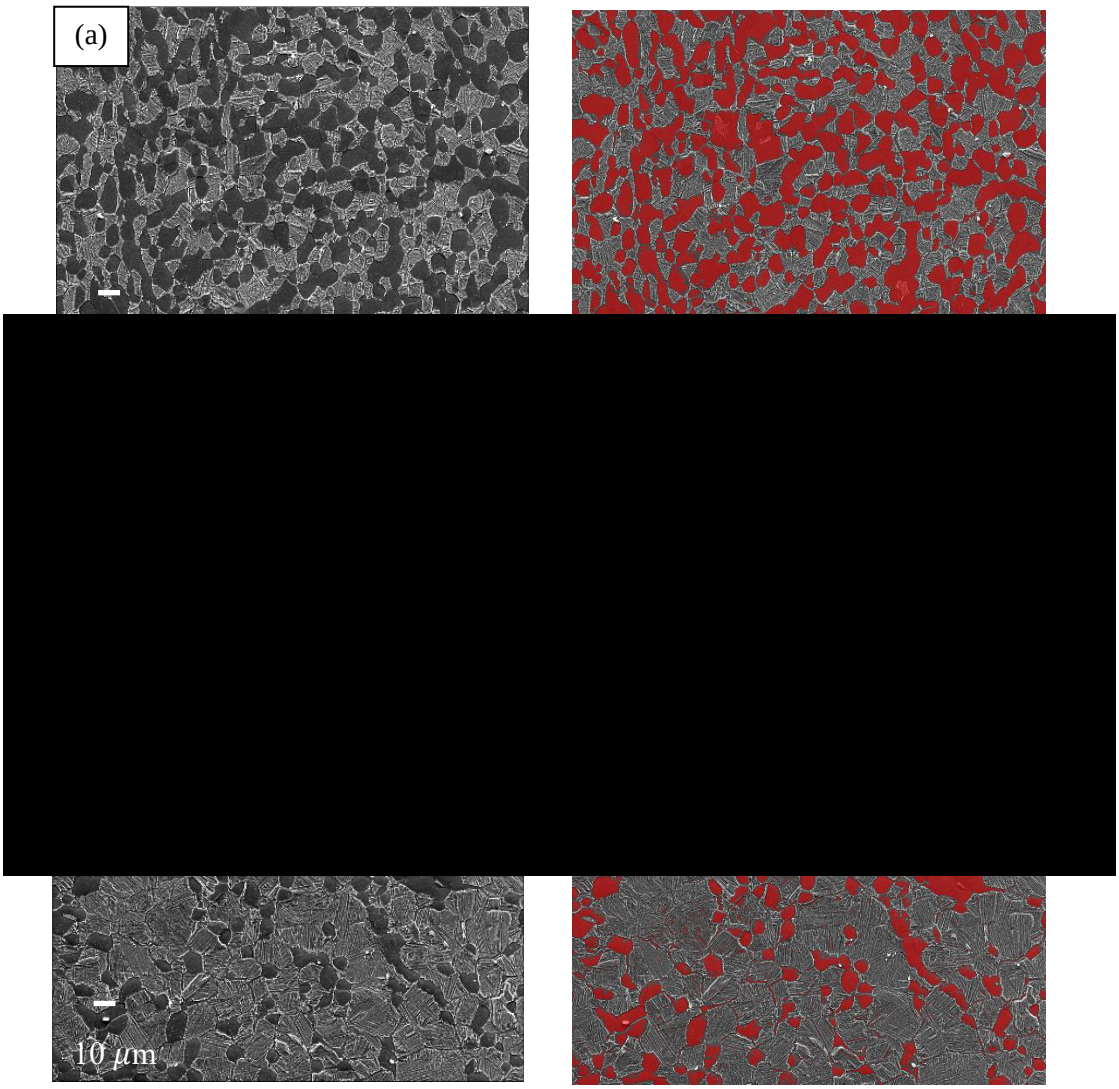

Figure 3.9**:** Bi-modal microstructures of the Ti-407 pancake material generated under three solution heat treatment temperatures (a) 820℃, (b) 840℃ and (c) 860℃. SEM image to the left, corresponding image analysis to identify α_p volume fraction percentage to the right.

At this point the effect of a water quench and furnace cooling were also investigated. Specimens were solution treated for two hours at 840℃ and then cooled at the different rates. The resultant microstructures are displayed below in Figure 3.10.

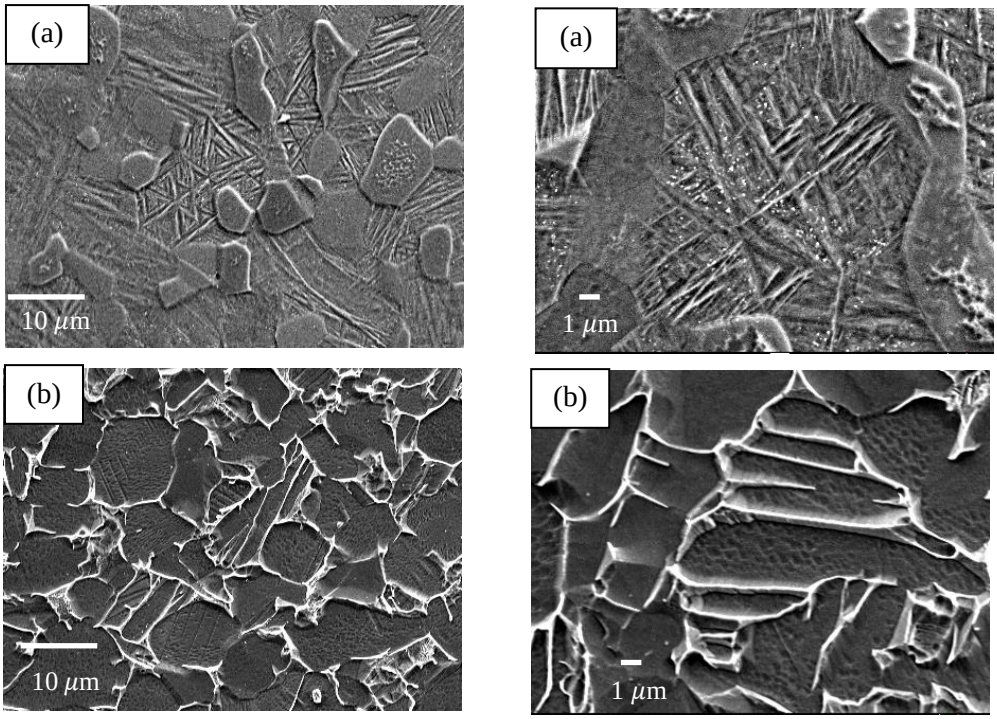

Figure 3.10: Secondary electron SEM images showing the effect of (a) Water quench and (b) Furnace cool on etched Ti-407 microstructure.

Water quenching resulted in a sharp plate-like form for the transformation product. The fast cooling rate of water quenching allows for tighter control of primary alpha volume fraction as it prevents the recrystallisation of primary alpha grains within beta regions, possible during a slower cooling period. Water cooling is preferred when high strength is the driving requirement but does result in a loss of ductility. Oil quenching is more commonly used within an industrial setting which offers a slightly slower cooling rate relative to a water quench.

Much coarser secondary alpha is seen from the furnace cooled microstructure. The slow cooling allows time for the beta grains to recrystallise out into alpha. Furnace cooling results in higher ductility but lower strength. It was decided that air cooling provided the most suitable microstructure for the subsequent mechanical testing.

All mechanical specimen blanks were heat treated at 840℃ for two hours and air cooled, followed by an eight-hour aging treatment at 500℃ and again air cooled. The 30% volume fraction of α_p grains demonstrated an average α_p grain diameter of 10 microns.

3.2.2 Ti-6-4 Forged Pancake Heat Treatment Trials

In total, three Ti-6-4 forged pancakes were machined into test pieces. The third pancake underwent a different heat treatment process to the first two pancakes, detailed below.

First, the same method was employed to determine a heat treatment temperature that would produce a α_p volume fraction of approximately 30%. Two temperatures were trialed, again with the samples subject to a two-hour solution treatment:

- 950℃ producing ~42% α_p volume fraction.
- 960℃ producing ~34% α_p volume fraction.

The resultant microstructures are displayed in Figure 3.11 along with image analysis based on measurements of the α_p volume fraction percentage.

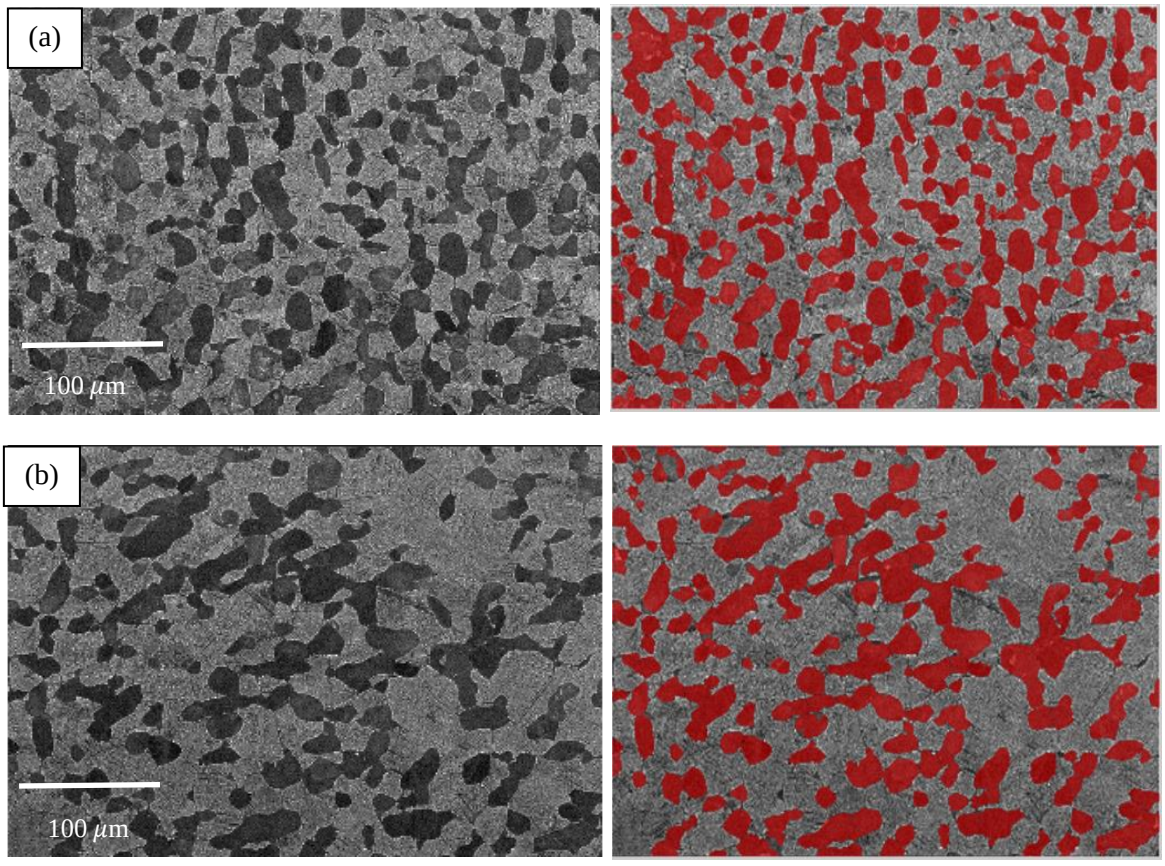

Figure 3.11: Secondary electron SEM images of etched Ti-6-4, solution treated for two hours at (a) 950℃ (b) 960℃.

It is emphasised that the 960℃ heat treatment ultimately employed provided a bespoke microstructure, i.e. non-standard for typical aero-engine casing applications. This offered an academic comparison to be made with the Ti-407 processed to the same 30% α_p content.

As with Ti-407, the two pancakes from the first billet, underwent an eight-hour aging treatment at 500℃ following the solution treatment. However, the third Ti-6-4 pancake from the second billet was subjected to a two-hour anneal at 700℃ following the 960℃ solution treatment. Figure 3.12 below compares the microstructures of the two different billets (i.e. pancakes 1 and 2 vs pancake 3).

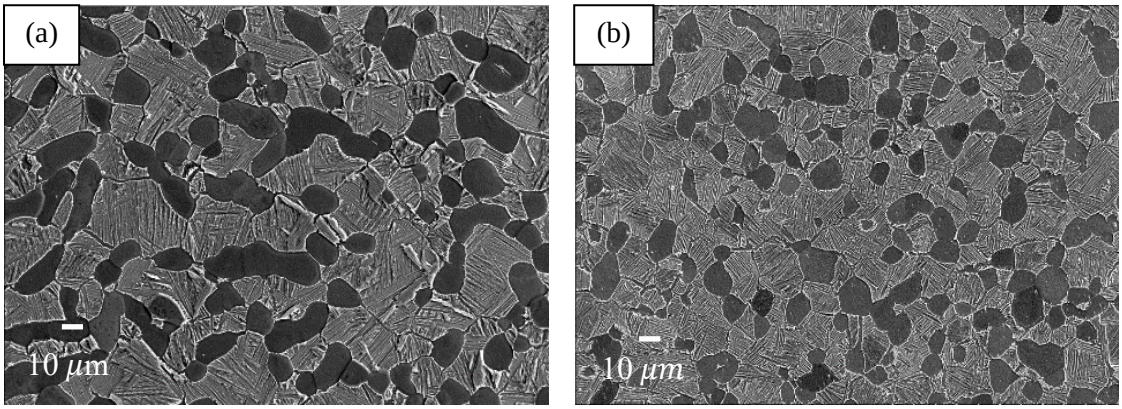

Figure 3.12: SEM image of Ti-6-4 pancake forged microstructure from (a) First billet and (b) Second 8 inch diameter billet.

In the aged Ti-6-4 microstructure from the first billet, the average diameter of the primary alpha grains varied between 20–30 microns. For the Ti-6-4 annealed test pieces from the second billet, the typical diameter of the primary alpha grains was moderately smaller at 10–20 microns. This is most likely due to the size of the first billet being larger than the second billet, meaning slower cooling after forging resulting in the growth of larger grains.

3.2.3 Ti-412 Forged Pancake Heat Treatment

Contrary to the Ti-407 and Ti-6-4 pancakes where the test piece blanks were extracted from the pancakes before they were heat treated, the Ti-412 pancake was heat treated before specimen extraction. A solution treatment temperature of 795℃ was applied for one hour followed by an air cool, and then an aging temperature of 500℃ for 8 hours was employed, again followed by an air cool. Figure 3.13 below shows microstructural images from (a) Tensile test piece 1 located at the centre of the pancake and (b) Tensile test piece 2 located at the edge of the pancake.

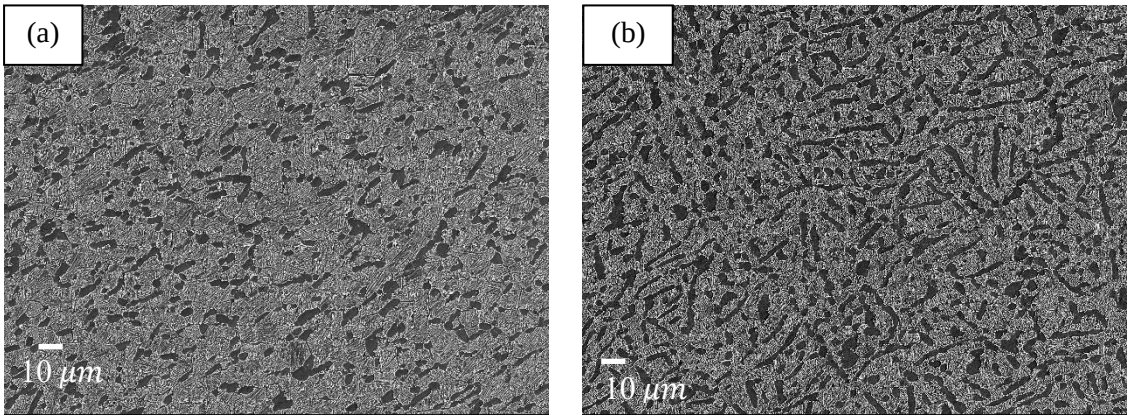

Figure 3.13: Ti-412 microstructure images: (a) Test piece RLH10004_001 and (b) Test piece RLH10004_002.

Clearly the test piece extracted from the edge of the pancake has a much higher primary alpha volume fraction. Further to this, relative to Ti-407 the grain size of Ti-412 is significantly smaller, the equiaxed grains measuring between 5–8 microns in diameter. The grains have an aspect ratio of up to 1:5, with pronounced elongation. As a general comparison, some slight elongation of the Ti-407 grains are observed but the Ti-6-4 grains have a much more equiaxed morphology.

3.2.4 Heat Treatment Summary

The heat treatments for each of the pancakes are summarised below in Table 3.1.

Table 3.1: Heat treatment schedules for forged pancake products.

Alloy/ (Pancake Number)	**Solution Treatment**	**Final Treatment**
Ti-407 (1-4)	840 ℃ 2 hours	500℃ 8 hours age
Ti-6-4 (1 and 2)	960℃ 2 hours	500℃ 8 hours age
Ti-6-4 (3)	960℃ 2 hours	700℃ 2 hours anneal
Ti-412 (1)	795℃ 1 hour	500℃ 8 hours age

3.3 Final Test Piece Machining and Measurements

Following the heat treatments for the pancake material, and following their extraction from the blocks for the ring rolled material, the blanks were then machined using CNC turning operations into plain cylindrical specimens suitable for tensile and fatigue experiments (Figure 3.14 and Figure 3.15). For the fatigue test pieces, the final step

included a longitudinal polish to reduce surface roughness and ensure that if any scratches were introduced into the specimen, they were parallel to the loading axis to limit any effect on crack initiation. Tests pieces were machined at PS Marsden and GTG Engineering. Precise characterisation of the test piece topography could be obtained using the Nanovea 3D profileometer and was used to quantify the surface roughness. This was found to be 0.9μm based on the measurement of five separate test pieces. There were no significant differences between Ti-407, Ti-6-4 or Ti-412 test pieces. The image below in Figure 3.16 exemplifies the final longitudinal finish.

Prior to testing, a non-contacting shadowgraph was employed to measure the co-axiality of the test pieces and the critical dimensions of the parallel gauge section according to the guidance of aerospace-based fatigue test standards [151].

Figure 3.14**:** Examples of post heat treated blank, CNC machined cylinder and final fatigue test piece.

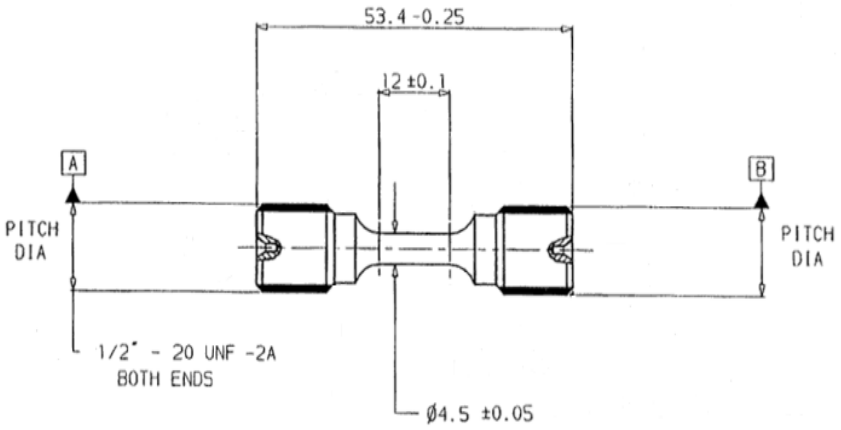

(a) RLH8001 axial fatigue test piece geometry.

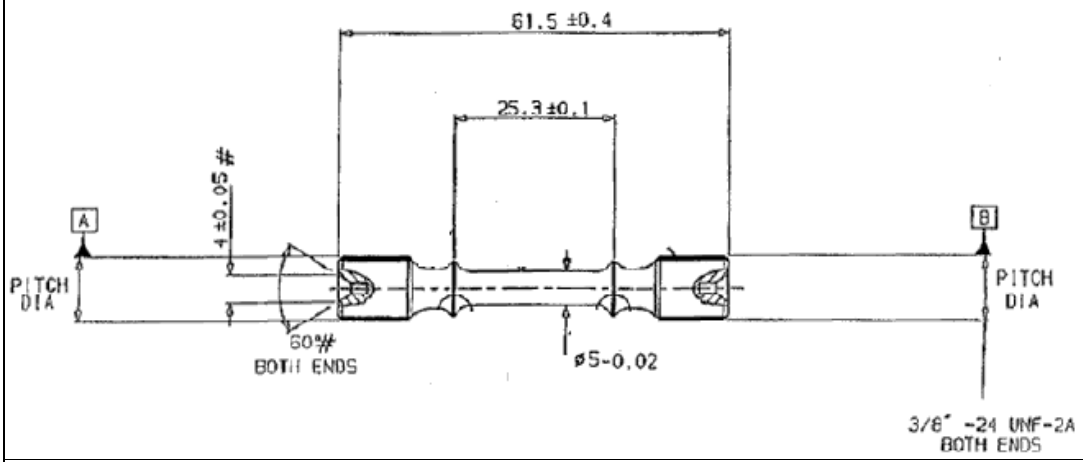

(b) RLH10004 pipped tensile test piece

Figure 3.15: Test piece geometries (a) Axial fatigue and (b) Pipped tensile

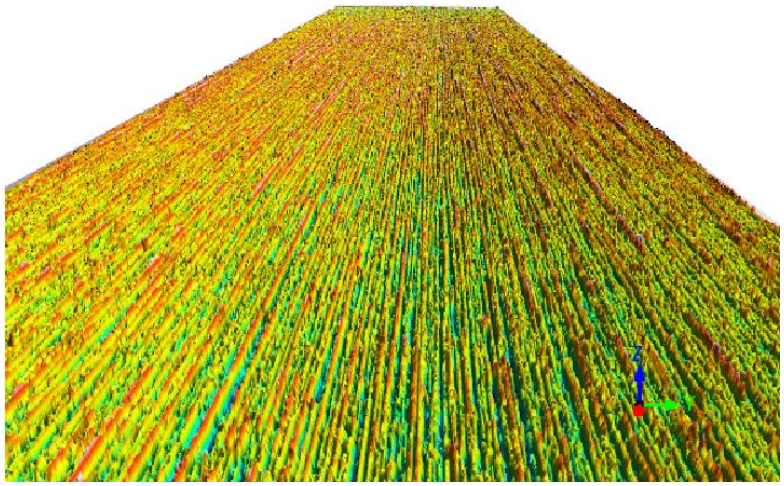

Figure 3.16: Final surface finish on a fatigue test specimen following a longitudinal polish.

3.4 Testing

Testing was carried out at the Swansea Materials Research & Testing (SMaRT) facilities according to the SMaRT quality system which is accredited to ISO17025 (UKAS7772).

Figure 3.17: Some of the SMaRT mechanical testing facilities in 'The Universal Lab'.

3.4.1 Tensile Testing

Key mechanical properties of the material were measured through room temperature tensile testing. Following the guidelines of BS EN ISO 2002-1:2005 [152], a strain rate of 0.002/min was applied to define yield, increasing to a rate of 0.01/min to induce fracture. The tensile tests were performed on a Schenck RMC100 electric screw machine with a load capacity of +/- 100kN and a stroke range of 100mm. An MTS extensometer with a gauge length of 12mm was attached to the specimen to record the

specimen extension through to fracture. The measured load and extension values were translated into stress and strain based on the specimen geometry, allowing for stress versus strain curves to be plotted.

3.4.2 Hardness Testing

Hardness testing is popular in industry because it is a cost-effective and non-destructive method, sometimes used to estimate a material's strength through empirical relationships linking strength and hardness [62].

In general, there are three types of hardness measurements:

- Scratch hardness – various minerals and other materials are rated based on their ability to scratch one another, measured according to Moh's scale. This scale consists of 10 standard minerals: 1 is talc and 10 is diamond. Most metals fall in the range of 4–8 on this scale, though it is not widely used because the intervals are very narrow in the high hardness end.
- Rebound or dynamic hardness
- Indentation hardness: there are several different types of indentation hardness tests such as Brinell, Meyer, Rockewell and Vickers.

The Vickers hardness method was used for the testing carried out within this project. This method is popular as it provides a continuous scale for hardness for a given load from soft to hard materials. With other testing methods such as Brinell or Rockwell it is necessary to change the load or the indenter at some point in the hardness scale meaning that measurements at one end of the hardness scale cannot be strictly compared with measurements at the other end.

Hardness testing was carried out using a Struers Duramin-40 A3 machine. The tests were carried out according to ASTM Standard E92-72 [153]. A square base diamond pyramid is used as the indenter. The measured diamond pyramid hardness number (DPH) or Vickers hardness number (VHN) is defined as the load divided by the surface area of the indentation calculated from the measurements of the lengths of the diagonals of the indentation. The DPH is determined from equation (3.1) below.

$$\mathrm{DPH} = \frac{2\,P\sin(\frac{\theta}{2})}{L^2} \tag{3.1}$$

Here, P is the applied load, L is the average length of the diagonals and θ is the angle between opposite faces of the diamond. This is usually taken as 136° as it defines a desirable ratio of indentation diameter to ball diameter in the Brinell hardness test.

In general, the measured hardness is independent of load. However, if the applied load is too low elastic recovery becomes appreciable which introduces error into the results. Furthermore, with the very small indentations produced from the lighter loads, the error in locating the ends of the indentation becomes greater. Further to the possible human error associated with locating the end of the indentation, Vickers hardness testing requires careful surface preparation and is slow relative to other techniques.

3.4.3 Fatigue Testing

All mechanical testing was conducted at a laboratory temperature of 22^{o}C and followed appropriate international standards for fatigue experimentation [154]. In all fatigue tests, complete rupture of the specimen was induced (i.e. no 'run-outs' were generated).

3.4.3.1 High Cycle Fatigue Testing

High cycle fatigue (HCF) tests were conducted on either a 100kN or 20kN Amsler vibrophore resonance machine at a load ratio of R=0, using a sinusoidal waveform with a frequency at or very near 100Hz. The tests were carried out in accordance with BS EN 3987:2009 [155]. Based on the precise gauge measurements recorded for each test piece using the shadow graph, the required load based on the stress was determined. The results were plotted on a stress against cycles to failure (S/N) curve. A schematic of the HCF waveform is displayed in Figure 3.18 below.

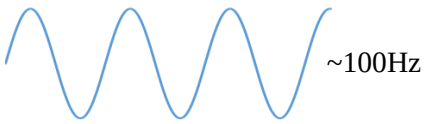

Figure 3.18: Schematic of HCF test waveform

3.4.3.2 Low Cycle and Dwell Fatigue Testing

Low cycle fatigue (LCF) tests, again under R=0 load conditions were performed on ESH servo-hydraulic test rigs with a load capacity of 50kN. Fifteen cycle per minute trapezoidal waveforms were employed, comprising one second linear rise and fall ramps with a one second hold at both peak and minimum load. Dwell tests were also carried out on servo-hydraulic test rigs, with a 120 second hold at peak stress. The tests were carried out in accordance with BS 6072:2010 [156]. A small number of tests with

higher frequencies (1 and 10Hz sine) were also carried out on the servo-hydraulic test rig to observe the effect of eliminating the hold period on number of cycles to failure. A schematic of the LCF and Dwell waveforms are shown below in Figure 3.19.

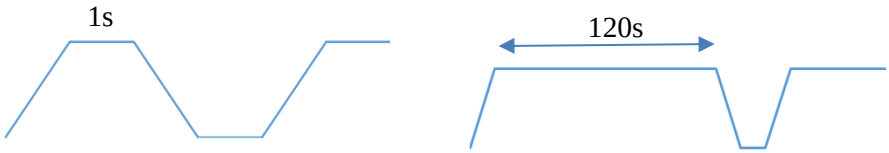

Figure 3.19: Schematic of (a) LCF and (b) Dwell waveform.

3.4.3.3 Strain Controlled Fatigue testing

Strain controlled testing, conducted to conventional British standards [157], was carried out initially to define the cyclic yield of Ti-407 pancake forged material. The first set of testing was carried out using a trapezoidal waveform. A constant strain rate was applied from minimum to maximum strain, and the minimum and maximum strain levels were held for one second. The trapezoidal waveform was applied under the control of a side-mounted strain gauge bridge extensometer. For the first test, the strain was stepped up every 10,000 cycles beginning at a strain of 0.4% rising to 0.8% in steps of 0.05. The test piece then broke early on during the 0.85% strain cycles.

Different frequency tests were carried out to observe the effect on stress relaxation. The highest frequency carried out was 3Hz. This test was conducted in a similar manner to the trapezoidal low cycle fatigue test, with an initial maximum strain of 0.4% being stepped up every set number of cycles under failure, which occurred at a strain of 0.6%. This time however, the strain was stepped up every 100,000 cycles to ensure that each strain step ran over roughly the same length of time. Initially the test had to be tuned to ensure that the minimum and maximum strains requested were accurately reached. There was some uncertainty as to whether it would be possible to control a higher frequency test, but after careful set up the test was completed successfully.

Finally, a dwell strain controlled test was attempted. As described above, a 120 second hold at maximum stress was employed. The test was stepped up every 300 cycles, running for a similar time as the 0.25Hz and 3Hz tests.

A schematic representation of the waveform with respect to the yield stress is plotted below for the LCF trapezoidal and 3 Hz sinusoidal waveform.

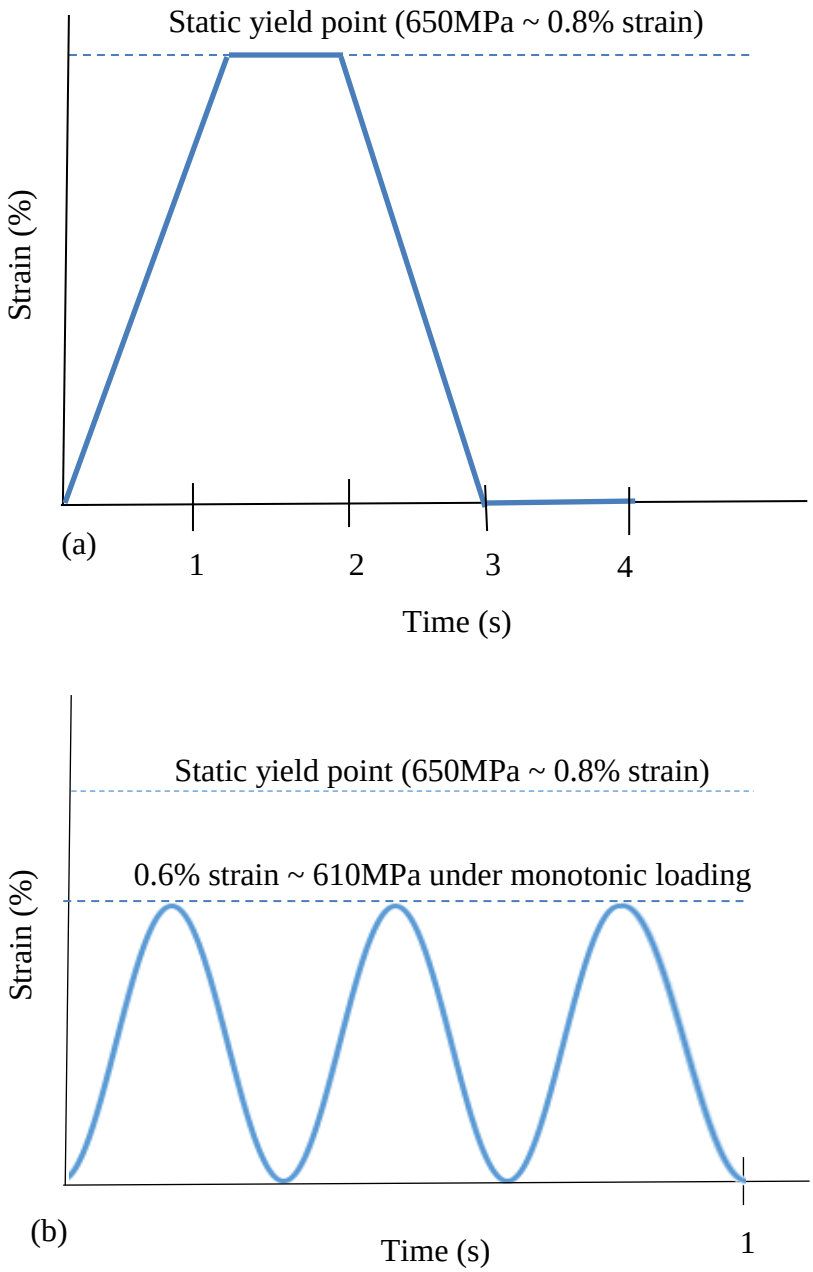

Figure 3.20: Schematic of the Ti-407 strain controlled waveforms with respect to the yield stress for (a) The 15 cycles per minute trapezoidal waveform and (b) The 3 Hz sinusoidal waveform.

3.4.4 Ti-407 Fatigue Crack Growth Testing

Fatigue crack growth (FCG) testing was carried out on Ti-407 material from pancake forgings. In total 12 FCG tests were carried out, to conventional British standards [158]. The table below summarises the heat treatments and R ratio used for each test piece.

Table 3.2. Test piece heat treatments and R ratios.

Specimen	Heat treatment	R Ratio
1	820℃ Air cooled	0.05
2	820℃ Air cooled	0.7
3	840℃ Air cooled	0.05
4	840℃ Air cooled	0.7
5	870℃ Air cooled	0.05
6	870℃ Air cooled	0.7
7	820℃ Vermiculite cooled	0.05
8	820℃ Vermiculite cooled	0.7
9	840℃ Vermiculite cooled	0.05
10	840℃ Vermiculite cooled	0.7
11	870℃ Vermiculite cooled	0.05
12	870℃ Vermiculite cooled	0.7

The solution heat treatments were followed by an aging treatment at 500℃ for 8 hours. The six resultant microstructures are displayed below in Figure 3.21.

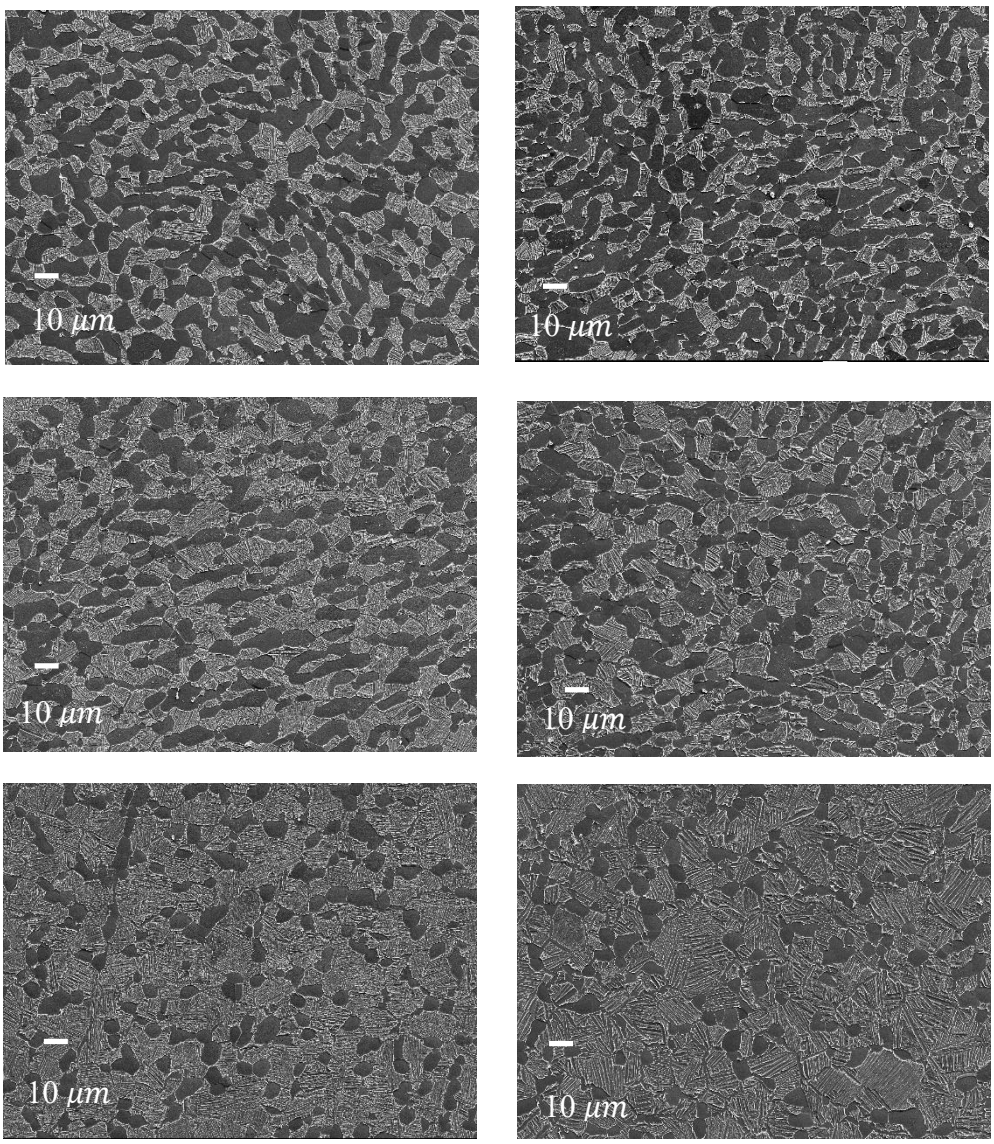

Figure 3.21: Ti-407 FCG microstructures. Top left to bottom left: 820℃, 840℃ and 870℃ then air cooled. Top right to bottom right: 820℃, 840℃ and 870℃ then vermiculite cooled.

Specimens experienced a significantly slower cooling rate when quenched in the vermiculite material which resulted in the wider alpha laths seen in Figure 3.22. The widths of air-cooled laths were measured between 0.5–0.8 microns whilst the width of vermiculite-cooled laths were roughly 0.8–1 micron.

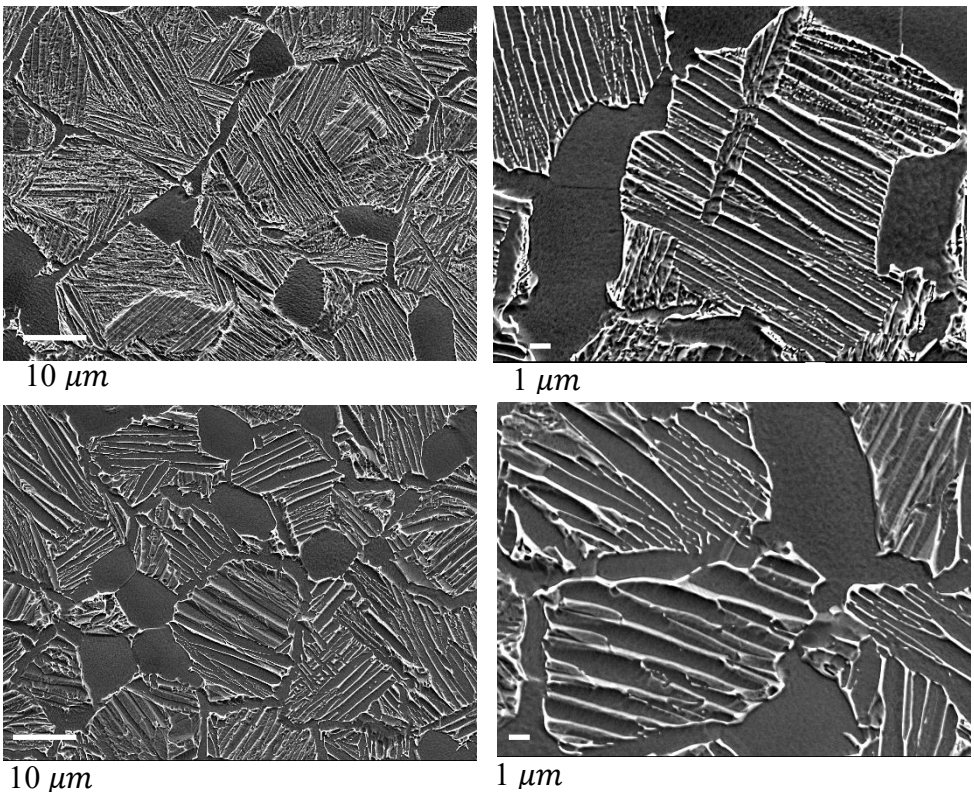

Figure 3.22: Ti-407 air-cooled laths (top) and vermiculite-cooled laths (bottom), cooled from 840℃.

The rationale behind the use of vermiculite cooling as a means of comparison to air cooling, was that cooling in vermiculite is more representative of the typical cooling rates seen in the centre of a billet. Therefore, the fatigue crack growth rates measured under these different cooling rates gives confidence that the conditions experienced under thicker sections are understood.

Following their extraction from the pancake, the specimens were sent off to PS Marsden Precision Engineers Ltd, where they were machined into corner notched FCG test pieces. The RLH5325 specimen geometry is shown below in Figure 3.23.

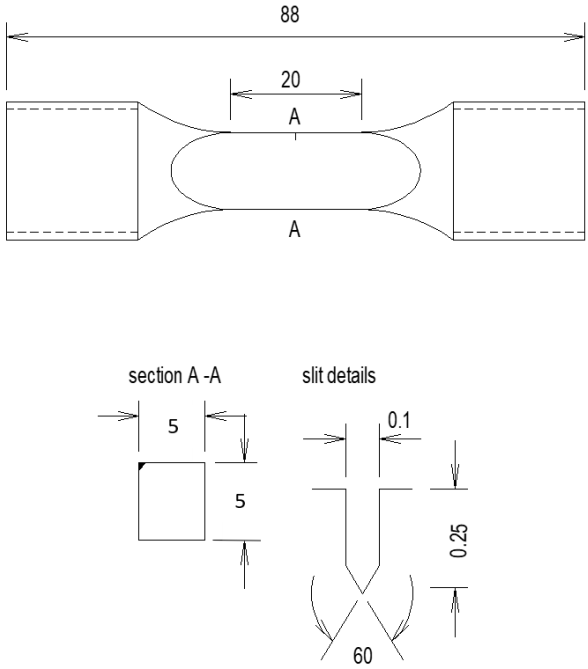

Figure 3.23: RLH5325 Corner notched specimen geometry used for FCG testing.

As with the LCF and HCF tests, the shadow graph was used to measure the gauge section width of the test piece. Further to this, each side of the slit length was measured using the Keyence, an optical microscope. The slit measurement was recorded as the initial crack length. Tests were carried out on servo-hydraulic test rigs which were connected to an automated and calibrated Dirlik crack growth monitoring package [159].

Prior to loading the test piece into the rig, platinum wires were welded across the notch. Platinum is generally used in this type of testing for two main reasons: it has a high oxidation resistance so can be used for high temperature tests, and it is highly conductive.

It is important that the welds are located as near to either side of the notch as possible to ensure a linear relation of the voltage (v) against crack length (a). This is particularly important for measurements whilst the crack is short. For a badly welded specimen a tail would be visible at the start of a log log da/dN vs dK plot. The further apart the weld locations are the more pronounced this tail would be. A reference is also welded at least 5mm away from the notch so the base conductivity and resistance of the material are known. A pre-cracking procedure using a sine waveform at 5Hz was carried out before moving to a 1-1-1-1 trapezoidal waveform. A target voltage is set, and once this is reached, the test is automatically stopped. It is important to ensure that the final voltage, i.e. the final crack length is not so large that the specimen ruptures.

Tests were terminated at a maximum final length of approximately 2.0mm equating to a crack length (a) over gauge (W) ratio of roughly 40% (a/W ~ 0.4).

On completion of the test, the crack was tinted by placing the test piece in the furnace at 550℃ for one hour, in order to allow for measurement of the final crack length. The average crack length was generated from nine measurements at specific angles from 0 to 90°, Figure 3.24. The initial and final crack length against the initial and final voltages were put into the Dirlik software in order to compile the da/dn versus dk graphs.

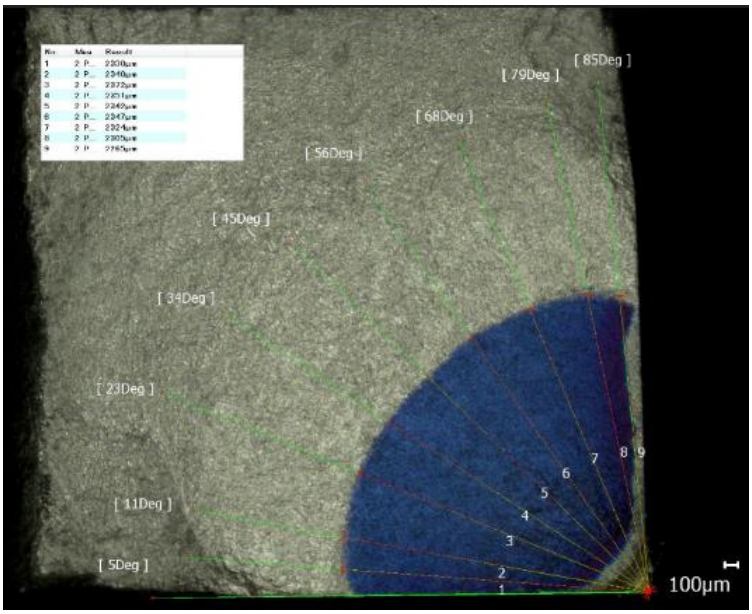

Figure 3.24: Measurement of final crack length under optical microscopy.

Images of the crack path around the microstructure were taken on selected test pieces by sectioning the test piece transversely above and below the crack, and then mounting the section in Bakelite. For these specimens the final crack length was measured viewing crack under the scanning electron microscope (SEM). Test pieces were polished and etched using the standard procedure for titanium. These were imaged using the Keyence and SEM.

3.5 Metallurgy and Observation

3.5.1 Metallographic Preparation

Sections of the test pieces were cut using a silicon carbide cut-off wheel on a Struers secotom -10 and later on an ATA Brilliant 200 cut-off machine. A feed rate of roughly 0.05mm/sec was used at an RPM of around 2,300. Increasing the RPM of the wheel reduced the load on the disc for a given feed rate but introduced more heat into the

specimen and wheel. It was necessary to use enough coolant during the cutting process to ensure the introduction of heat damage was prevented.

In order to observe the microstructure and perform both energy dispersive spectroscopy (EDS) and electron backscatter diffraction (EBSD) analysis following the sectioning of samples into suitable sizes, pieces were mounted in conductive bakelite; a thermosetting resin. Thermosets are polymers that are irreversibly hardened by curing from a soft solid. A temperature of around 200℃ was used and a force of around 250 bars applied during the embedding of the specimen. Water cooling is applied to allow for the shortest possible mounting time. Following the application of heat and pressure, extensive cross linking between polymer chains is produced to form an insoluble polymer network [160].

Following the mounting process, material was polished on a Struers Labopol-5 auto polisher according to the procedure presented below in Table 3.3.

Table 3.3: Standard polishing procedure for titanium.

Step	Polishing Cloth	Media	Force (N)	RPM	Time (min)
1	Piano 220	Water	25	300	1
2	MD Plan	Dia Pro Plan	30	150	5
3	MD Chem	OP-S Suspension (0.04μm)	20	150	8

The first polishing stage, carried out on a 220 grit finish, removes the damaged layer of material caused during the sectioning process. The second stage, using a 9μm diamond suspension on a woven non-nap silk cloth, removes coarse scratches. The third stage removes trace amounts of damage and the surface scratches introduced during the grinding operations, to produce a highly polished specimen. Between each polishing step the specimen was rinsed, cleaned using acetone and dried using ethanol. This was particularly important after the final polishing step to ensure that OP-S particles were removed from the specimen surface.

To observe the microstructure of the specimens it was necessary to etch the surface of the sample. Krolls reagent was used (1.5ml HF, 4mL HNO_3, 94mL H_2O) and is the most common etchant used on titanium as it brings out the general microstructure of alpha-beta alloys. The process of etching consisted of swabbing the specimen surface, and then rinsing and drying. The time between applying the etchant and washing it off

was a compromise between the level of detail and the contrast and varied depending on the alloy. Shorter times show more detail whilst longer times show more contrast [160]. Etched for too long and the surface will tend to burn.

Microstructures were initially observed under the Reichert MeF3 microscope in conjunction with Nikon imaging software. Following this, more detailed examination was carried out using a Hitachi SU3500 SEM and the JEOL JSM 7800F Field Emission Gun (FEG) SEM microscope. Secondary electron (SE) signals were used to generate the images.

3.5.2 Microstructural Measurements

Measurements of grain sizes and alpha lath width sizes were carried out using the measurement tool on Mipar [150]. Twenty to thirty measurements were taken across the surface of the samples to ensure an accurate value was defined. In order to measure the primary alpha volume fractions, image analysis was carried out using Mipar. This program enables accurate measurement of different phases on an 8-bit image. Areas can be removed based on morphology and pixel area which helps to differentiate between primary alpha grains and secondary alpha laths. Volume fraction measurements were carried out on images of 500x to 600x magnification to allow for a suitable sample size with accurate capturing of primary alpha grain areas.

3.5.3 Electron Backscatter Diffraction (EBSD)

For best results from EBSD mapping, the sample surface should be as smooth as possible, without any residual stresses from sectioning. Titanium can be difficult to prepare because it is a relatively soft material. This means that the surface can quite easily be roughened during preparation. Surface roughness is further increased due to the different metal removal rates of the alpha and beta phase [56]. Successful indexing is also dependent on the number of phase and grain boundaries. The pattern quality is worse near boundaries because patterns begin to overlap. For this reason, fine grained microstructure are more difficult to index. Another factor that plays a role in determining the pattern quality is the dislocation density (presence of elastic and plastic strains) in the specimen. Higher dislocation densities result in poorer indexing [161]. Microstructures from a Mill Annealed heat treatment are likely to have higher dislocation densities due to the partial recrystallisation of the primary alpha grains.

Whilst for most nickel alloys a 10 minute polish is usually sufficient for a well indexed map, preparation of titanium requires a more stringent preparation procedure. Initially a longer final stage polish was tested of between 20 minutes to half an hour. However, this did not produce favourable results, with relatively low indexing. An etch-polish-etch process was therefore trialed. The sample was polished using a mixture of colloidal silica and hydrogen peroxide (10:1) and etched using Krolls solution. This polishing method had been successfully employed in a study by Britton et al during their investigation into dislocation content in macrozones using EBSD [161] and provided better results in the present study. It was found that the more times the sample was etched and polished, the better the results were. Etching removes any surface damage and polishing reduces surface topography. The only problem with this method was that it was rather difficult and time-consuming. On a couple of occasions scratches were introduced onto the sample surface when re-loading it into the auto polisher. However, this method was found to produce the most favourable results. A third method that was also tested was the vibratory-polisher. The sample is placed on a short nap-woven synthetic cloth in a shallow pool of OP-S with a weighted holder placed on top of the specimen. The sample is then left for anything up to 12 hours. This was the most straightforward process, but in general the indexing wasn't quite as good as that achieved from the polish-etch method.

EBSD was carried out using the AZtec software, integrated with the SEM [162]. Typically when generating representative texture maps of fractured test pieces, the polished plane was prepared approximately 5mm sub-fracture. Crystallographic orientation maps extending across the entire specimen gauge section, or as much of the gauge section as time would allow, were captured. In order to generate the large maps needed to accurately characterise the texture of the different product forms tested, the montage feature was used. Between 40 to 70 individual fields were stitched together. Each field was roughly 500 x 500 microns with a step size of between 2–3 microns. On the inverse pole figure (IPF) maps presented throughout the results section, every color represents an orientation according the legend.

3.5.4 Chemical Analysis

Chemical analysis was carried out through Energy-Dispersive x-ray Spectroscopy (EDS) integrated with the SEM. The reflection of the electron beam with the sample under observation produces a range of emissions including x-rays. An energy

dispersive detector is used to separate the characteristic x-rays of different elements into an energy spectrum and EDS software is used to analyse the spectrum and determine the elements to which the energies are attached. An EDS detector contains a crystal that absorbs the energy of the x-rays by ionisation, emitting free electrons in the crystal that become conductive and produce an electrical charge bias [163]. The x-ray absorption converts the energy of the individual x-rays into electrical voltages of proportional size. The electrical pulses correspond to the characteristic x-rays of the elements. A standard EDS spectrum is commonly presented as x-ray count against energy in keV. The energy peaks correspond to the elements of the sample.

Chemical analysis was carried out for each of the product forms tested over a 500 by 500 micron area. An example of the setup is shown below in Figure 3.25. Measurements from primary alpha grains (spectrum 1–5), transformed beta areas (spectrum 6–10), and the average across the entire area (spectrum 11) are presented in the results.

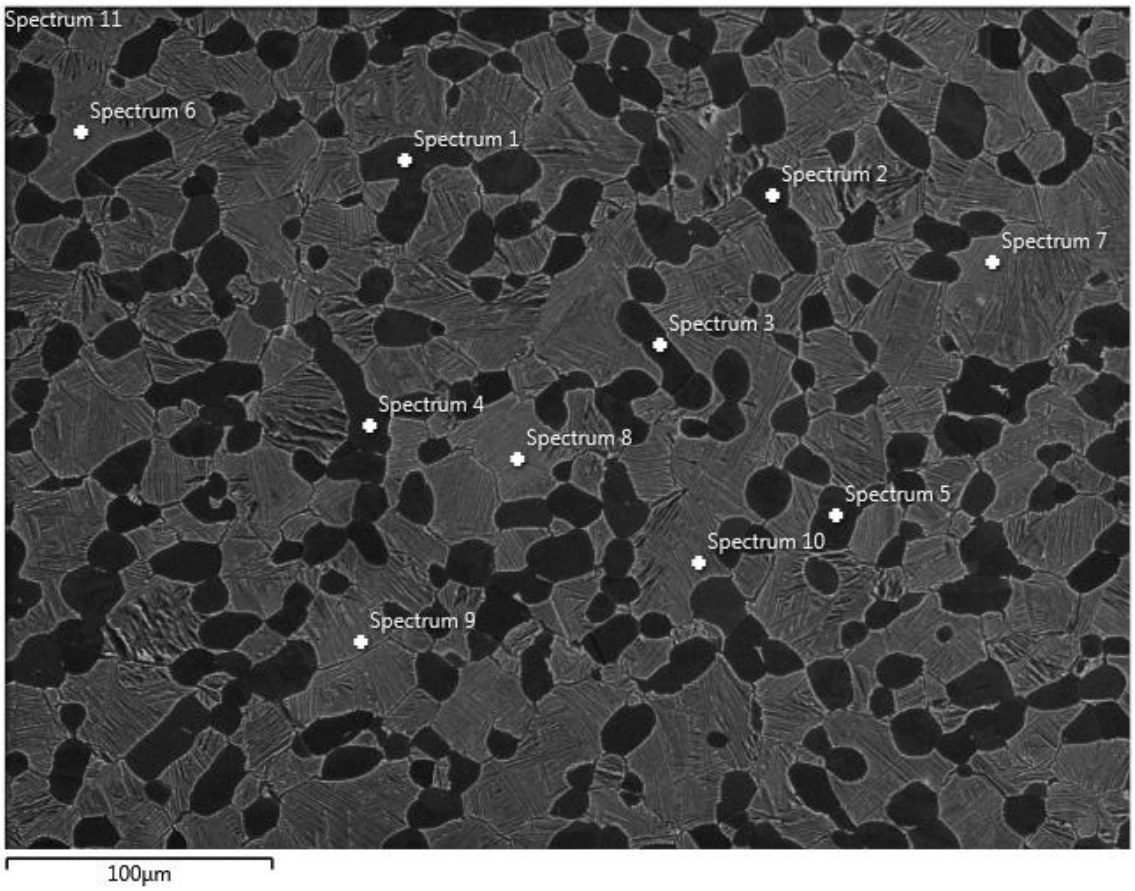

Figure 3.25: Example of chemical measurements across the primary alpha grains, transformed beta region and average area.

One thing to note is that whilst Figure 3.25 shows an etched sample for demonstration purposes, within the results EDS was carried out on polished un-etched samples, as measurements on an etched surface can significantly differ from the bulk chemistry.

3.5.5 Observation of Fracture Surfaces

Fractured surfaces were mounted from the base of the specimen on a metal mount and attached using either silver DAG or carbon adhesive tabs. Silver DAG provided a better and stronger attachment to the metal stub, eliminating the problem of drift during SEM analysis. However, several hours were needed for the silver DAG to dry so when large numbers of fracture surfaces were to be imaged in a single SEM session the most efficient method was to stick several fracture surfaces onto a single mount using carbon adhesive tabs. Before observation, fractured specimens were cleaned in an ultrasonic bath. They were placed in a vial of acetone in a bath of water and vibrated at high frequency for 20 minutes.

Observation of fracture surfaces was an important part of the project as it enabled detailed characterisation of the initiation sites, with initiation lives intimately controlling total fatigue life, particularly in the HCF regime. Interpretation of the possible initiating mechanisms, in part from the SEM images, helped to better understand the fatigue data generated. In order to capture the detailed images required for this, comprehension of use of the SEM was important. The main user inputs were the accelerating voltage and the aperture.

The higher the accelerating voltage the faster the electrons travel down the column and the more penetrating power they have. With more surface penetrating, surface detail is obscured so better results were obtained from lower accelerated voltages when viewing the fracture surfaces.

Aperture helps to increase image resolution while reducing the probe current. Before aperture however, decreasing the working distance helps to increase image resolution. An important process when focusing an image is ensuring that the apertures are centred to the beam. If this is not the case the image will move when the user tries to focus it. Further to this, an important check is the astigmatism. This is seen as streaking of the image if not corrected.

3.6 Facet Characterisation

In order to fully characterise the facets of fractured specimens, two key pieces of information were required: the facet spatial angle, and the crystallographic orientation of the facets. The way in which these pieces of information were obtained is explained below.

3.6.1 Quantitative Tilt Fractography

The Quantitative Tilt Fractography (QTF) technique was used to determine the facet spatial angle relative to the loading axis; an angle of 0° would describe a flat facet and 20° would define a facet 20° from flat (Figure 3.26).

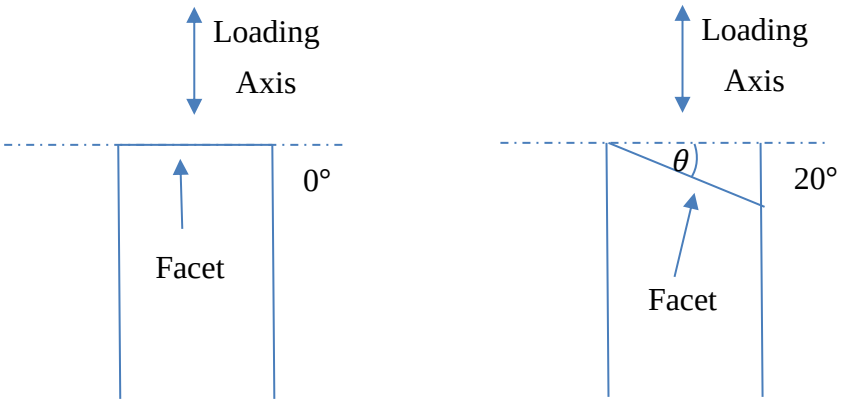

Figure 3.26: Example of interpretation of measured facet angles using QTF.

The measured angle dictated the appropriate tilt angle to generate EBSD measurements directly from the facets. The implementation of QTF consists of measuring the coordinates of three non-collinear points across the facet of interest, relative to a set origin at two different tilt angles.

Figure 3.27(a) and 3.27(b) show a measured facet at 0° and 30° SEM tilt. A two by two grid system was used to accurately measure the position of the selected points relative to the origin.

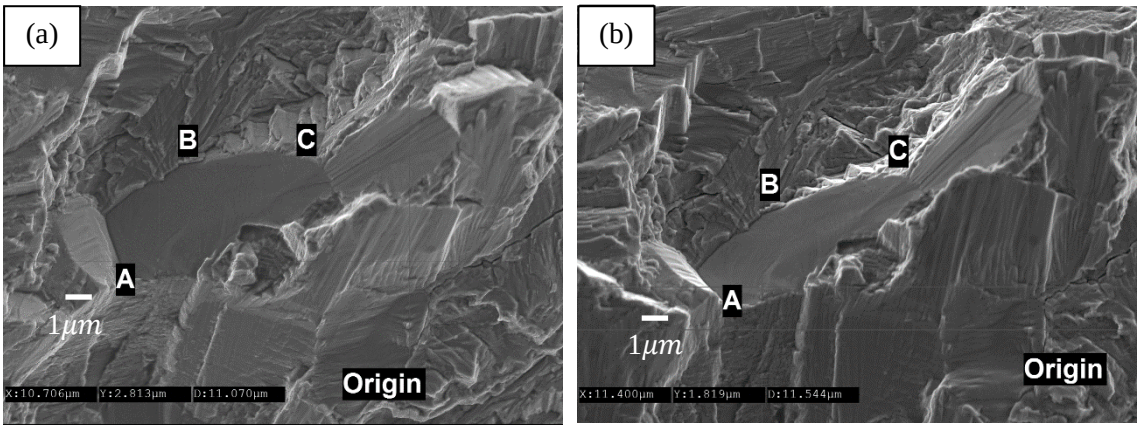

Figure 3.27: Images of a measured facet (a) At 0° tilt and (b) At 30° tilt.

Full derivation of the equations used can be found in the paper by Themlis et al [164]. The coordinates of a given feature, A, are calculated using equations 3.2–3.4 below. In these equations θ_1 and θ_2 are the two tilt angles and x_1^A and x_2^A, and y_1^A and y_2^A are the coordinates of feature 'A' at the two tilt angles; x_1^A and y_1^A correspond to the first tilt angle (0°) coordinates and x_2^A and y_2^A to the second tilt angle (30°) coordinates.

$$X^A = x_1^A . \sin \theta_2 - x_2^A . \sin \theta_1 / \sin(\theta_2 - \theta_1) \quad (3.2)$$

$$Y^A = y_1^A = y_2^A = y_1^A + y_2^A / 2 \quad (3.3)$$

$$Z^A = (-x_1^A . \cos\theta_2 + x_2^A . \cos\theta_1) / \sin(\theta_2 - \theta_1) \quad (3.4)$$

Here X^A, Y^A and Z^A give the coordinates of point A in the SEM stage axis system. Coordinates for features 'B' (X^B, Y^B and Z^B) and 'C' (X^C, Y^C and Z^C) are calculated in the same fashion as 'A'. The cross product of vectors $\overrightarrow{AB}$ (3.5) and $\overrightarrow{BC}$ (3.6) gives the vector representing the facet plane normal (3.7b).

$$\overrightarrow{AB} = (X^B - X^A)\,\mathbf{i} + (Y^B - Y^A)\,\mathbf{j} + (Z^B - Z^A)\,\mathbf{k} \quad (3.5)$$

$$\overrightarrow{BC} = (X^C - X^B)\,\mathbf{i} + (Y^C - Y^B)\,\mathbf{j} + (Z^C - Z^B)\,\mathbf{k} \quad (3.6)$$

$$\vec{n} = \begin{vmatrix} \mathbf{i} & j & k \\ (X^B - X^A) & (Y^B - Y^A) & (Z^B - Z^A) \\ (X^C - X^B) & (Y^C - Y^B) & (Z^C - Z^B) \end{vmatrix} \quad (3.7a)$$

$$\vec{n} = [(Y^B - Y^A).(Z^C - Z^A) - (Z^B - Z^A).(Y^C - Y^B)]\,\mathbf{i} - [(X^B - X^A).(Z^C - Z^B) - (Z^B - Z^A).(X^C - X^B)]\,\mathbf{j} + [(X^B - X^A).(Y^C - Y^B) - (Y^B - Y^A).(X^C - X^B)]\,\mathbf{k} \quad (3.7b)$$

Here **i**, **j** and **k** are the unit vectors along X, Y and Z, the SEM stage axis system. The X direction points to the top of the SEM image, Y to the left of the image and Z

parallel to the direction of the electron beam. Because the tilt axis is parallel to the y direction, the x coordinates change with tilt angle but the y coordinates remained the same.

Once the facet plane normal has been determined, the angle between the loading axis (Z) and the facet plane normal ($\vec{n}$) is determined from equation 3.8.

$$\alpha = \cos^{-1}\left(\frac{\vec{n}.\boldsymbol{k}}{|\vec{n}|}\right) \tag{3.8}$$

This is simply the **k** component of the facet plane normal divided by the square root of the sum of terms **i**, **j**, and **k** squared.

When using the technique it was important to understand sources of error. Thanks to the good resolution of the field emission gun (FEG) SEM, very small features could be selected as the coordinate location, keeping any error introduced by the placement of the measurement crosshair to a minimum. Increasing the tilt angle difference helped to increase the accuracy of the measured facet angle since the difference in the measured points increased. Therefore, the result of the error in the measured coordinates was reduced. However, as the angle was increased, features between the two images become less recognisable, or were even completely obscured owing to the topology of the fracture surface. The second possible source of error arose from the fact that the facets were not necessarily perfectly planar.

In order to confirm the accurate implementation of the QTF technique, the spatial angle of a grain on a flat polished specimen was measured. This was found to be 1.32°.The images and coordinates associated with this measurement can be found in Appendix B.

3.6.2 Crystallographic Orientation Measurements

Between the two steps of determining the spatial orientation of the facet and measuring the crystallographic orientation, it was important not to rotate the stage, to make sure that the orientation was the same, so the facet was tilted at 70° to the electron beam, to make indexing as strong as possible. Incidentally, the effect of the measured crystal orientation based on the SEM stage tilt angle was checked to observe the effect. It did not change the results but simply led to weaker indexing. These results are presented in Appendix C.

The SEM used for this study was the JEOL JSM 7800F with a field emission gun (FEG) as the emission source. Due to the rough topology of the facets to be measured, facet indexing could be challenging. Other research has measured crystallographic orientation of FIB'ed sections, which would reduce the problem of shadowing and other features on the fracture surface blocking the path of electrons to the phosphor screen. Whilst a FIB was not readily available at Swansea University, selected specimens have been sent off to Ohio State University (OSU) where FIB'ing and TEM is possible.

4 Results and Preliminary Interpretation

The following section presents the results generated over the course of the project with initial interpretation of the data. The findings are discussed in more detail and in a more holistic perspective in Chapter 5. Due to the number of different product forms, for each section, before presentation of the mechanical data itself, the microstructure and chemistry is characterised. Fractography and EBSD analyses, associated with the tested specimens, are also contained within this section. A number of more detailed images of the microstructure for each product form is provided in Appendix A including grain size and primary alpha volume fraction measurements.

4.1 Ti-407 Manufacturer 1 Ring Rolled Data

The first batch of testing was carried out on Ti-407 ring rolled material processed at manufacturer 1. The following section displays the tensile and fatigue results from the two blocks tested, following the characterisation of the microstructure and chemistry.

4.1.1 Microstructural and Chemical Characterisation

Figure 4.1 below displays a representative image for the microstructure of the manufacturer 1 ring rolled material. Table 4.1 presents the key microstructural parameters and Table 4.2 the chemical composition.

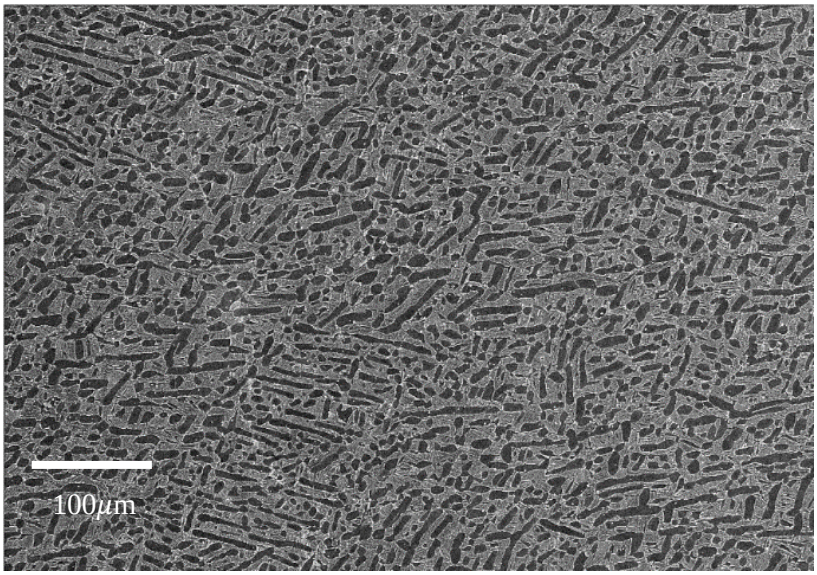

Figure 4.1: Representative microstructure from manufacturer 1 ring rolled Ti-407 material.

As mentioned in the experimental methods section, no heat treatments were carried out on the ring rolled material. A relatively elongated primary alpha morphology is seen, with the grains measuring up to 100 μm in length and 5–10 μm in diameter. Using the image analysis techniques described in section 3.5.2, a primary alpha volume fraction of 42% and lath widths of between 0.5–1 μm were measured.

Table 4.1: Key microstructural parameters for manufacturer 1 ring rolled material.

Primary alpha volume fraction (%)	42
Primary alpha grain width (μm)	10
Primary alpha grain length max (μm)	100
Primary alpha grain length min (μm)	10
Secondary alpha lath width (μm)	0.5 - 1

Table 4.2: Chemical measurements for manufacturer 1 ring rolled material.

Man 1 Ring Rolled Material	**Bulk chemistry (wt %)**	**Primary alpha grain (wt %)**	**Beta grain (wt %)**
Al	0.92	1.08	0.77
V	3.34	0.98	4.65
Si	0.35	0.32	0.32
Fe	0.27	0.03	0.37

4.1.2 Tensile Data - Ti-407 Manufacturer 1 Ring Rolled

A single tensile test from the manufacturer 1 ring rolled material was carried out to measure the key mechanical parameters of the material, summarised below in Table 4.3.

Table 4.3: Key data from tensile test.

Room Temperature Tensile Test on Man 1 ring rolled material		
Young's Modulus (GPa)	0.2% Proof Stress (MPa)	UTS (MPa)
106	616	714

The test piece came from location 10 of the material shown in Figure 3.1(b). As the fatigue results showed very little difference across the two different orientations, only one tensile test was conducted.

The stress strain curve is displayed in Figure 4.2 below. The strain rate is increased once the yield has been defined according to standard practice for tensile testing [152]. Due to limited material, this tensile test was conducted using a fatigue test piece. Because the RLH8001 test piece is not pipped, once the yield was defined the extensometer had to be removed to protect it from being damaged. Therefore during the second strain rate, the strain is calculated from the machine stroke data.

The point at which the strain rate is stepped up from 0.002/min to 0.01/min is manifested on the stress strain curve at the point where there is a jump in stress at 5% strain.

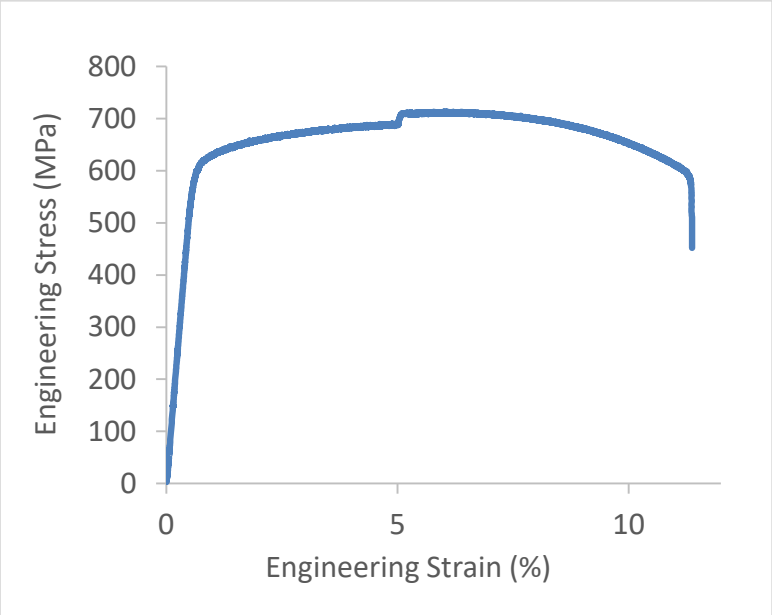

Figure 4.2: Stress-strain curve for Ti-407 manufacturer 1 ring rolled material.

4.1.3 Fatigue Data - Ti-407 Manufacturer 1 Ring Rolled

Two ring rolled blocks from the same ring were tested under HCF, LCF and dwell conditions. The graph in Figure 4.3 plots the initial HCF and LCF results from the first ring rolled block. This shows a distinct gap, almost two orders of magnitude at the low end of the stress range, between the LCF and HCF curves, which as seen throughout the fatigue results, is a recurring characteristic of the alloy in the tested product forms.

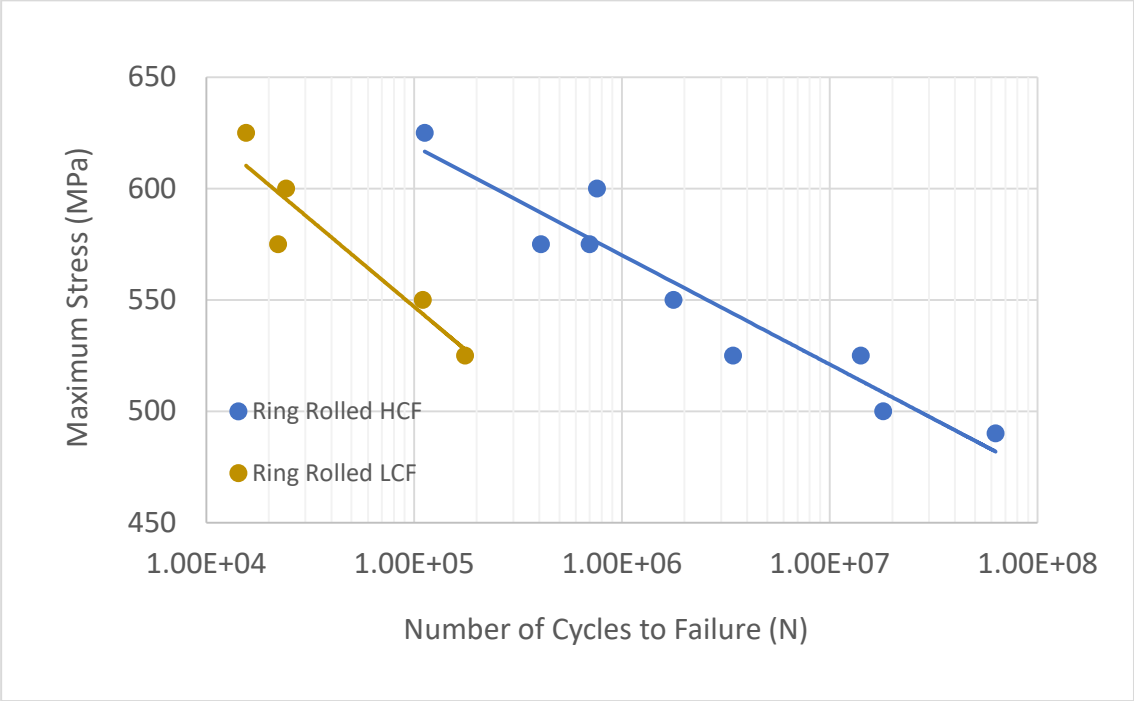

Figure 4.3: Manufacturer 1 Ti-407 HCF and LCF data from the first block.

The second ring rolled block was used for dwell sensitivity tests based on the observed knockdown in cycles to failure from HCF to LCF from the first block. The second block was also used to determine if radial and tangential orientation affected the mechanical performance. Figure 4.4 shows the dwell curve along with the additional LCF points from the second block.

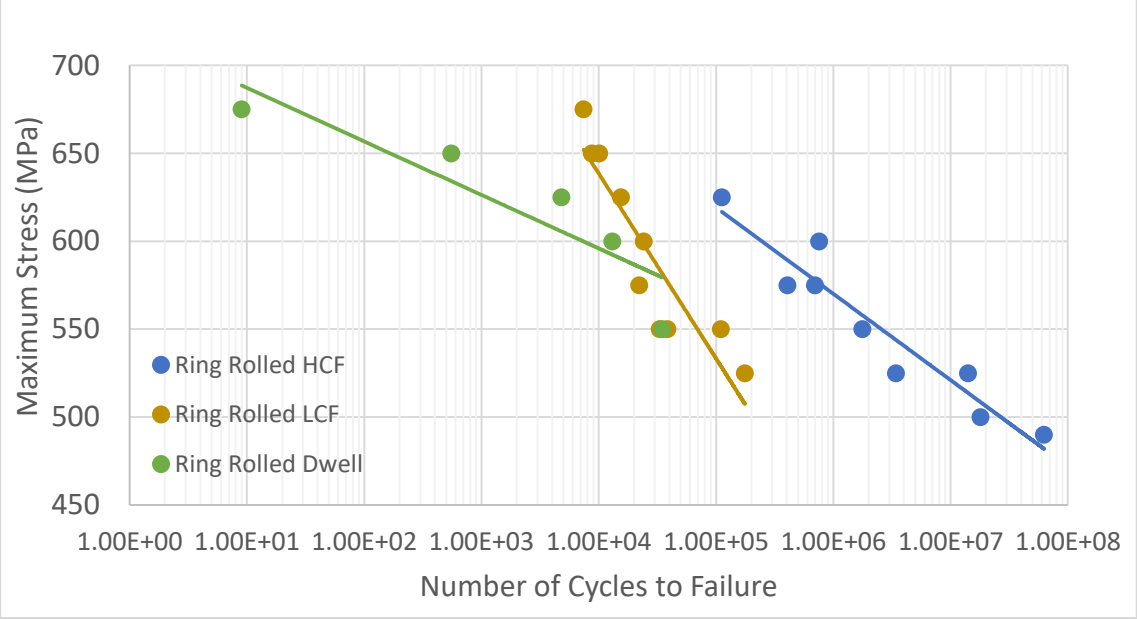

Figure 4.4: Ti-407 HCF, LCF and Dwell data from the two manufacturer 1 ring rolled blocks.

As shown in the specimen cut up plan (displayed overlaid to Figure 4.5) of the twelve pieces extracted from the second block, eight specimens were orientated in the tangential direction and four in the radial direction. The effect of the orientation on fatigue performance was examined by comparing the fatigue lives of differently orientated pieces at the same stress levels at both the top (650MPa) and bottom (550MPa) end of the stress range used to define the HCF, LCF and dwell S/N curves. Figure 4.5 below shows the points from the second ring rolled block which compare the orientation effect on life.

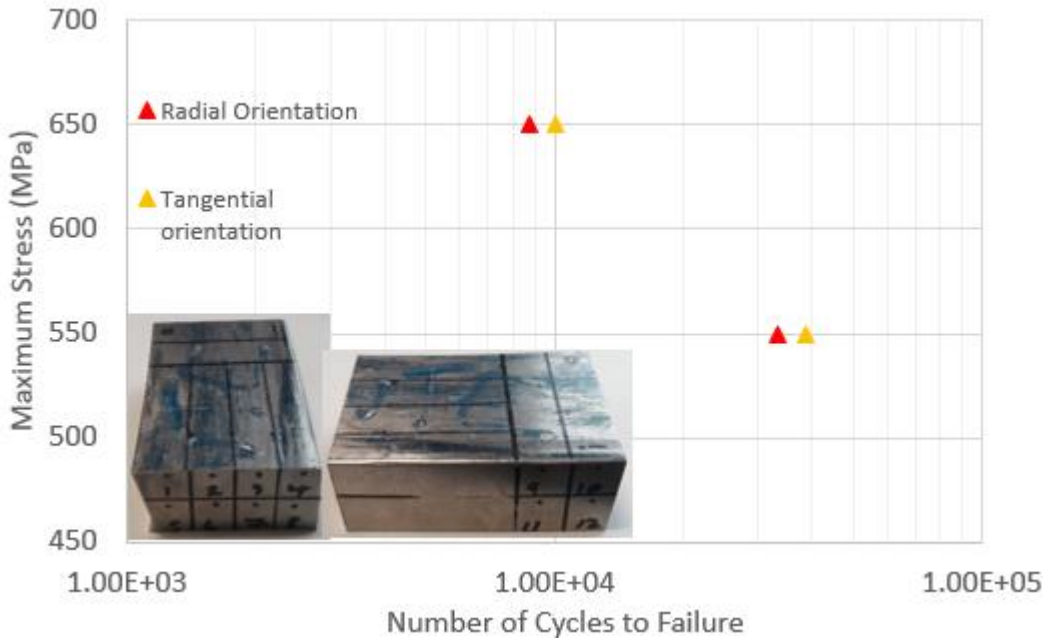

Figure 4.5: Ti-407 manufacturer 1 radial vs tangential lives at the high and low end of the fatigue curves shown above (in Figure 4.4).

Based on these results, it can be said that there is very little orientation effect from this material. Whilst the tangential direction was slightly stronger for both stress levels, in the case of the 650MPa test there was a difference of just 1358 cycles, and in the 550MPa test just 4913 cycles. In both cases this equates to a 15% difference, well within the scatter observed on a standard S/N curve.

4.1.4 Ti-407 Manufacturer 1 Fractography

The resultant test piece fracture surfaces from the fatigue testing are displayed below.

4.1.4.1 HCF Fractography

The HCF fractography results are displayed in Figure 4.6 and show a mixture of surface and subsurface crack initiation sites. The subsurface initiation sites are highlighted within the blue circles.

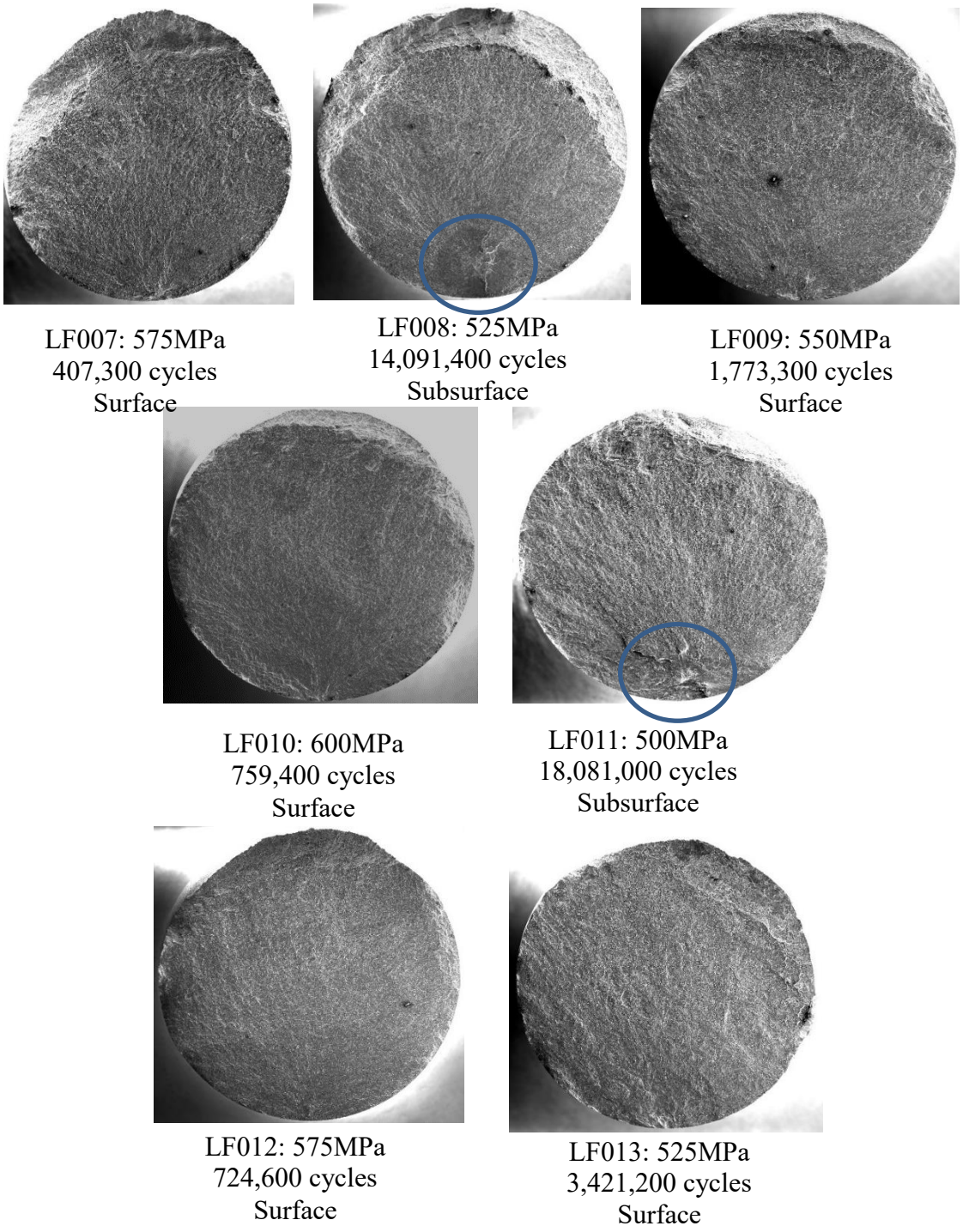

Figure 4.6: HCF fracture surfaces from manufacturer 1 ring rolled testing.

The HCF curve displayed in Figure 4.4 shows relatively little scatter, apart from the two tests at 525MPa where there is almost an order of magnitude difference between the two. The major difference between the two was that the longer life specimen (LF008) initiated subsurface, whilst the shorter life (LF013) initiated from the surface. The initiation sites of the two test pieces are displayed below in Figure 4.7.

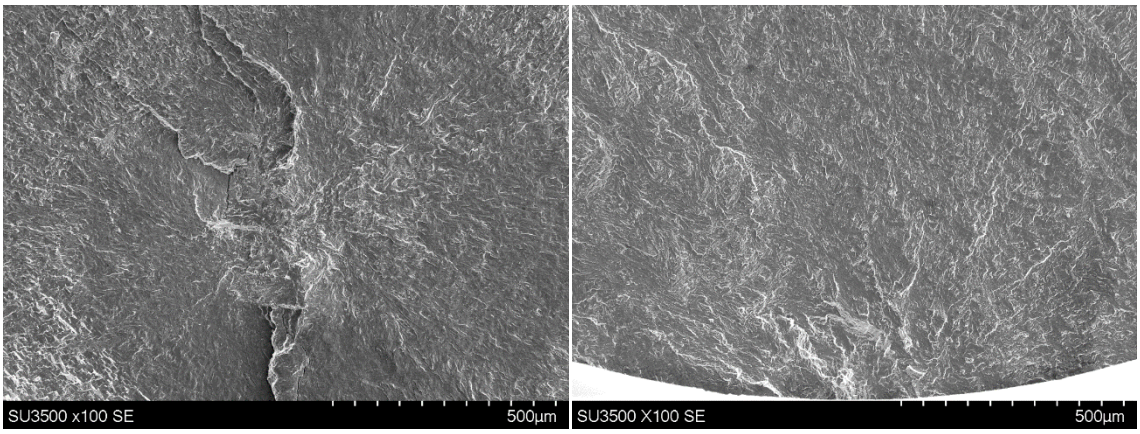

LF008: 525MPa	LF013: 525MPa
14,091,400 cycles	3,421,200 cycles
Subsurface	Surface

Figure 4.7: Ti-407 manufacturer 1 subsurface and surface initiation site for the two HCF tests at 525MPa.

4.1.4.2 LCF Fractography

For all of the LCF and dwell specimens, the cracks initiated from the surface, and tended to manifest a number of isolated equiaxed facets. A representative example of the fracture faces is shown below in Figure 4.8.

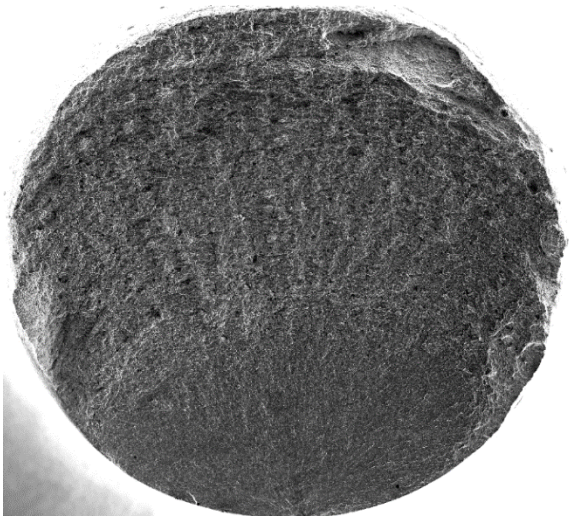

Figure 4.8: LCF fracture surface of a Ti-407 specimen from manufacturer 1.

4.1.4.3 Texture Characterisation

Texture characterisation for the ring-rolled material was carried out by performing a large area EBSD scan 3–4mm below the fracture surface of a failed test piece (LF012). The resultant IPF texture map is displayed in Figure 4.9. The corresponding pole figure maps are displayed in Figure 4.10.

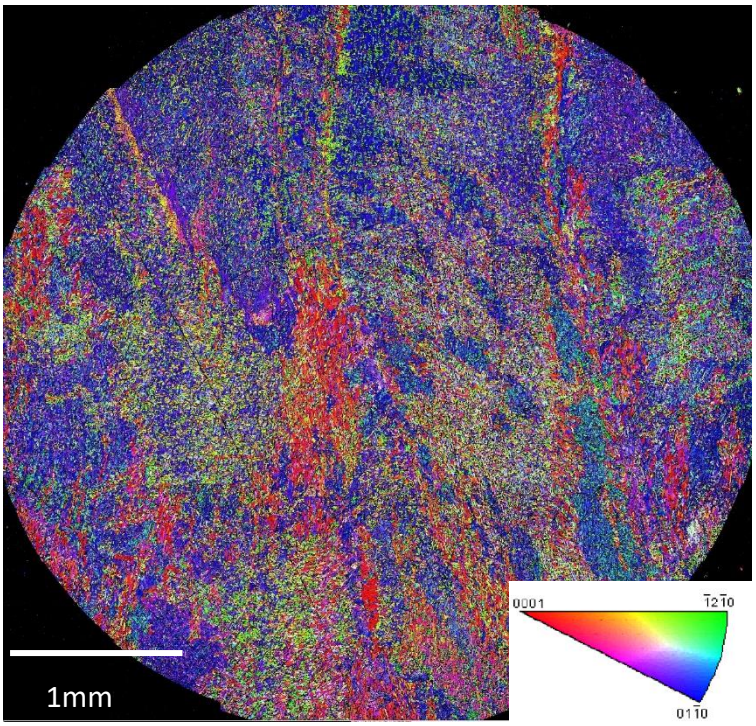

Figure 4.9: Ti-407 manufacturer 1 inverse pole figure (IPF). Specimen LF012 tested at 575MPa lasting for 724,600 cycles.

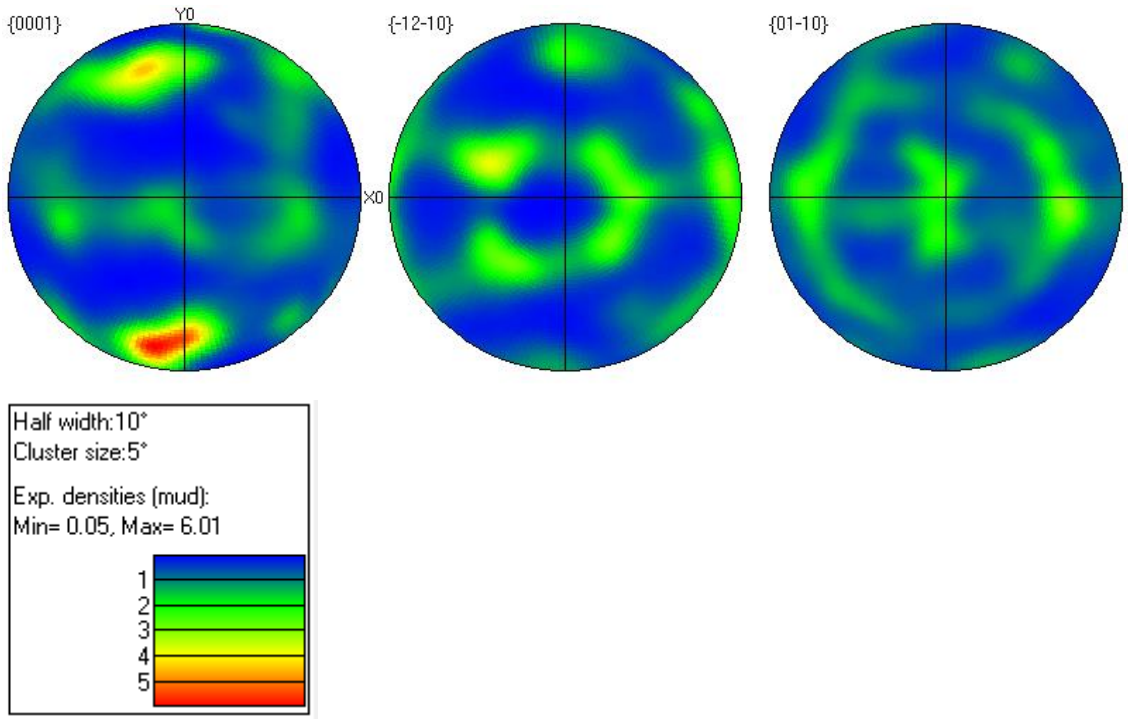

Figure 4.10 Pole Figures associated with Figure 4.9, showing a maximum texture intensity of 6.01.

4.2 Ti-407 Manufacturer 2 Ring Rolled Data

The following section presents the data generated from the Ti-407 ring rolled block of manufacturer 2. A total of 42 specimens were machined as shown in Table 4.4.

Table 4.4: Ti-407 manufacturer 2 ring rolled specimens.

Number of Specimens	Design	Orientation
3	Tensile (RLH10004)	Axial
12	Fatigue (RLH8001)	Axial
3	Tensile (RLH10004)	Tangential
22	Fatigue (RLH8001)	Tangential

4.2.1 Ti-407 Manufacturer 2 Microstructure and Chemical Characteristation

A representative image of the microstructure is shown in Figure 4.11. The key microstructural parameters are displayed in Table 4.5 and the chemical composition in Table 4.6.

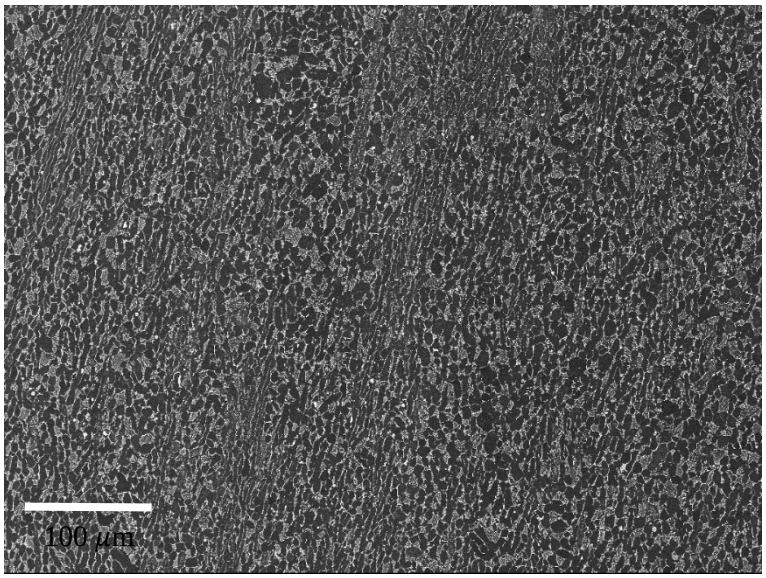

Figure 4.11: Representative SEM image of the Ti-407 ring rolled microstructure of manufacturer 2.

The volume fraction of primary alpha grains was measured at roughly 50%. Prevalent throughout the microstructure were bands of high aspect ratio, elongated grains. These had an average width of 3 μm and a maximum length 40 μm. The rest of the microstructure was made up of more equiaxed primary alpha grains with an average diameter of 9 μm, broken up by transformed beta and secondary alpha laths. The width of the secondary alpha laths was measured at between 0.9–1.2 μm.

Table 4.5: Key Ti-407 manufacturer 2 microstructural parameters.

Primary alpha volume fraction (%)	69
Primary alpha grain diameter μm (equiaxed area)	9
Primary alpha grain length max μm (elongated area)	40
Primary alpha grain width μm (elongated area)	3
Secondary alpha lath width μm	0.9-1.2

Table 4.6: Ti-407 manufacturer 2 chemical composition.

Man 2 Ring Rolled Material	**Bulk chemistry (wt %)**	**Primary alpha grain (wt %)**	**Beta grain (wt %)**
Al	0.79	0.97	0.74
V	3.14	0.96	4.58
Si	0.32	0.28	0.27
Fe	0.21	0.04	0.7

4.2.2 Tensile Data - Ti-407 Manufacturer 2 Ring Rolled

The results of the tensile tests are summarised in Table 4.7 below. Three tests in the axial and three in the tangential direction were conducted.

Table 4.7: Summary of Tensile results.

Manufacturer 2 Ring Rolled Block. Room Temperature Tensile Test Data					
	Young's Modulus (GPa)	0.2% Proof Stress (MPa)	UTS (MPa)	Elongation after Fracture (A %)	Reduction in Area (%)
Tangential Orientation					
1	95	575	705	19.48	57
2	92	573	705	20.57	60
3	94	573	704	20.6	62
Average	93.7	573.7	704.7	20.2	59.7
Axial Orientation					
1	106	665	753	19.19	55
2	109	665	753	19.48	57
3	108	662	755	19.75	55
Average	107.7	664.0	753.7	19.5	55.7

The results show that there is indeed a large difference in monotonic tensile properties, based on orientation. The axial tensile tests demonstrated a 15% higher proof stress and modulus of elasticity, and a 7% higher tensile strength. The ductility and reduction of areas between the two orientations are similar.

A comparison of the stress-strain curve between the axial and tangential direction is displayed in Figure 4.12.

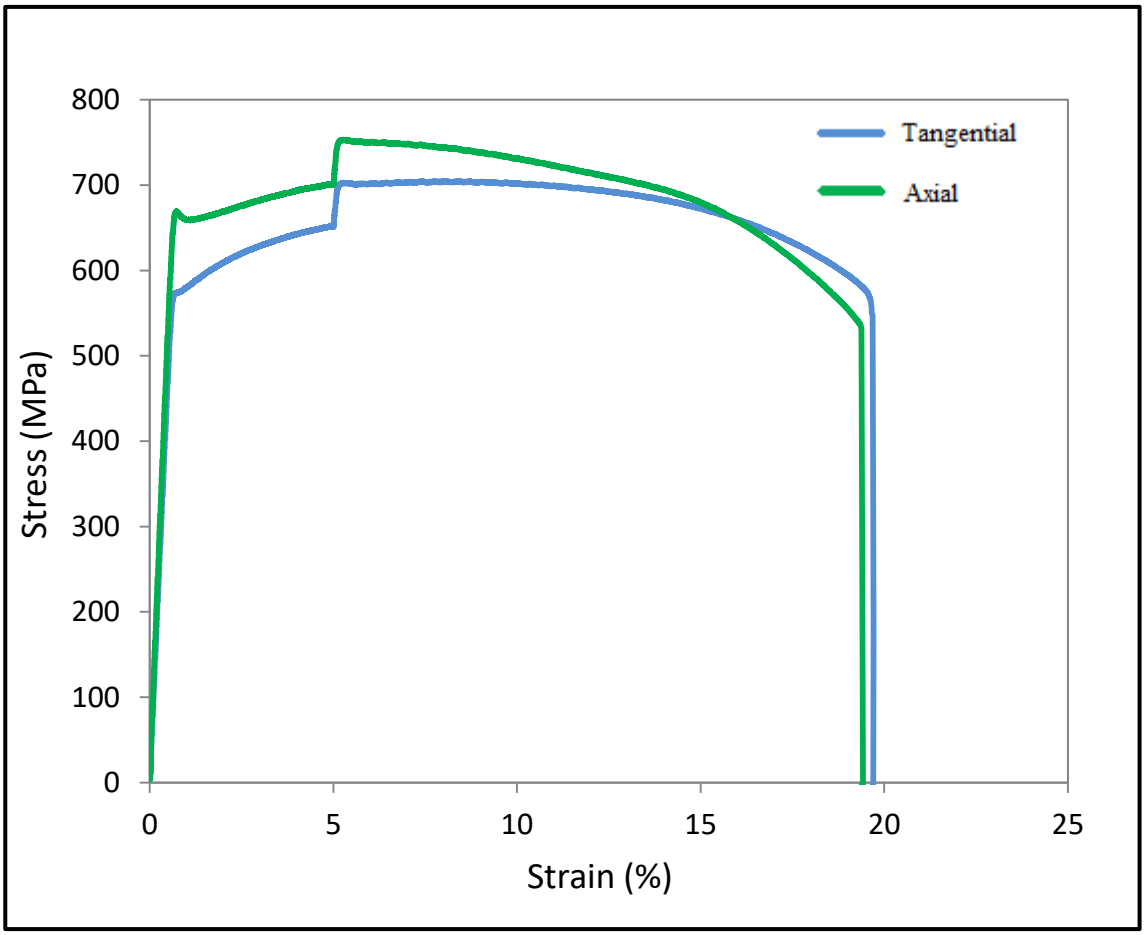

Figure 4.12: Stress strain curve comparing Ti-407 manufacturer 2 ring rolled axial against tangential orientation.

4.2.3 Fatigue Data - Ti-407 Manufacturer 2 Ring Rolled

The fatigue results below compare the orientation effect under both high cycle and low cycle fatigue conditions. The HCF and LCF curves are also plotted together for the axial and tangential orientation to observe the relationship between the two regimes. For the axial orientation, an additional 1Hz sine waveform test was completed to examine the effect of removing the one second hold time seen under a 1-1-1-1 trapezoidal loading waveform.

4.2.3.1 Ti-407 Manufacturer 2 Low Cycle Fatigue Orientation Comparison

The low cycle fatigue results for both orientations are plotted in Figure 4.13. The gradients of the slopes for both orientations are similar. However, the stress to cause failure at 100,000 cycles for the tangential orientation is roughly 525MPa, and for the axial direction, 590MPa. This 12% superior strength seen from the axial direction is relatively consistent across the range of stresses tested and correlates with the 15% higher proof stress seen from the tensile testing. The low number of axial tests was due to the limited material and whilst not ideal, they do appear to sit on the same straight line and at a similar gradient to the tangential curve which was plotted from more tests.

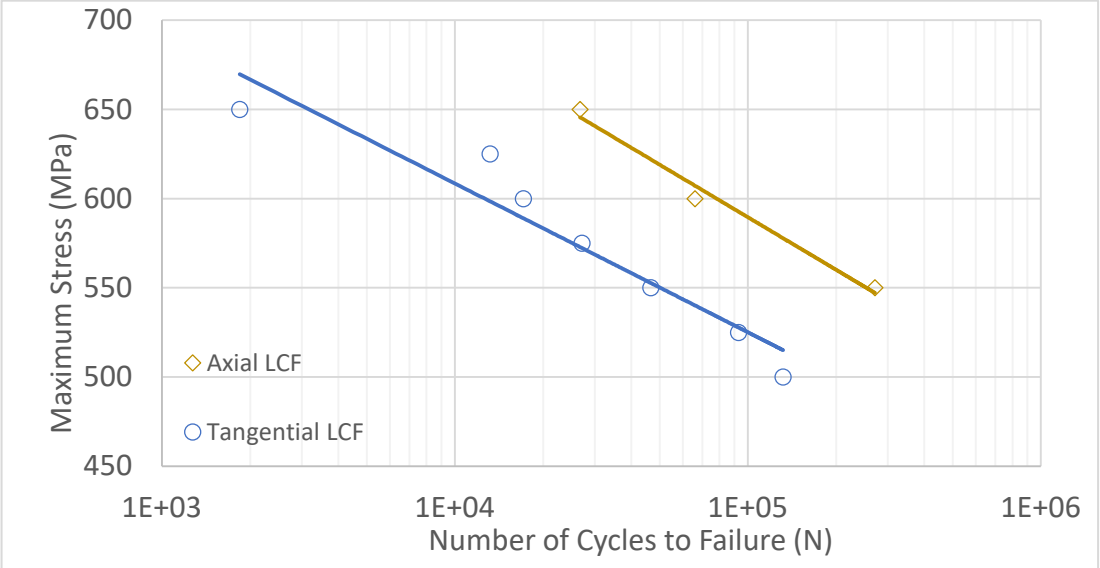

Figure 4.13: Ti-407 manufacturer 2 LCF comparison between axial and tangential directions.

4.2.3.2 Ti-407 Manufacturer 2 High Cycle Fatigue Orientation Comparison

Figure 4.14 plots the high cycle fatigue responses for both specimen orientations. Again, based on the limited number of tests for the axial orientation test pieces, the curves have a similar gradient. Comparing the stress required to cause failure at ten million cycles, a 17% superior strength for the axial orientation is seen relative to the tangential direction.

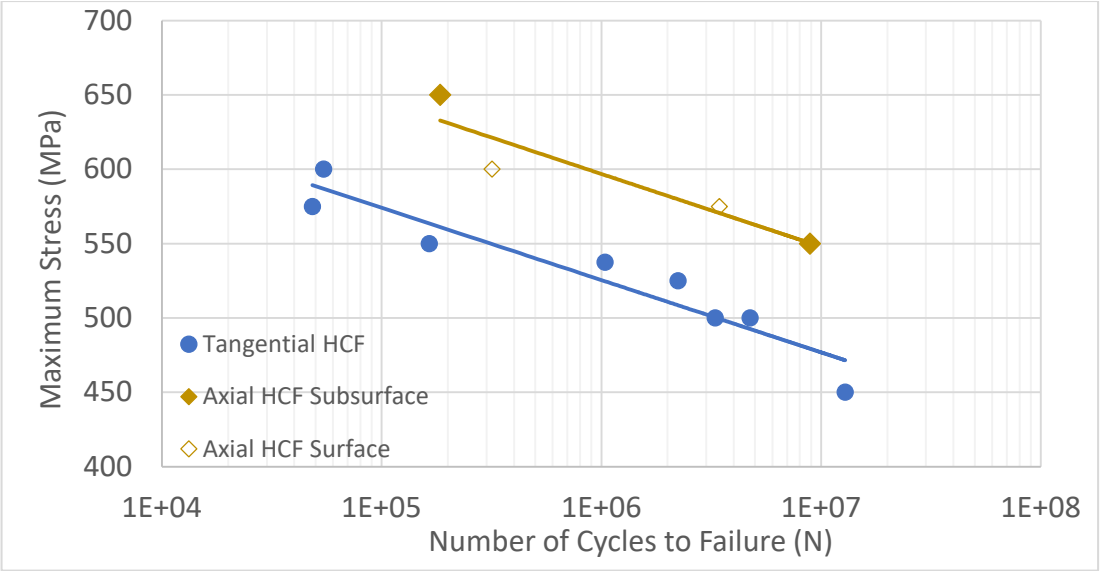

Figure 4.14: Ti-407 manufacturer 2 comparison of axial and tangential direction HCF.

4.2.3.3 Combined Fatigue Data for Axial Orientation

The characteristic gap between LCF and HCF is seen for the combined axial fatigue data plotted in Figure 4.15. More than 1.5 orders of magnitude difference in lives is seen at the lower end of the curve and roughly an order of magnitude difference at the highest stresses.

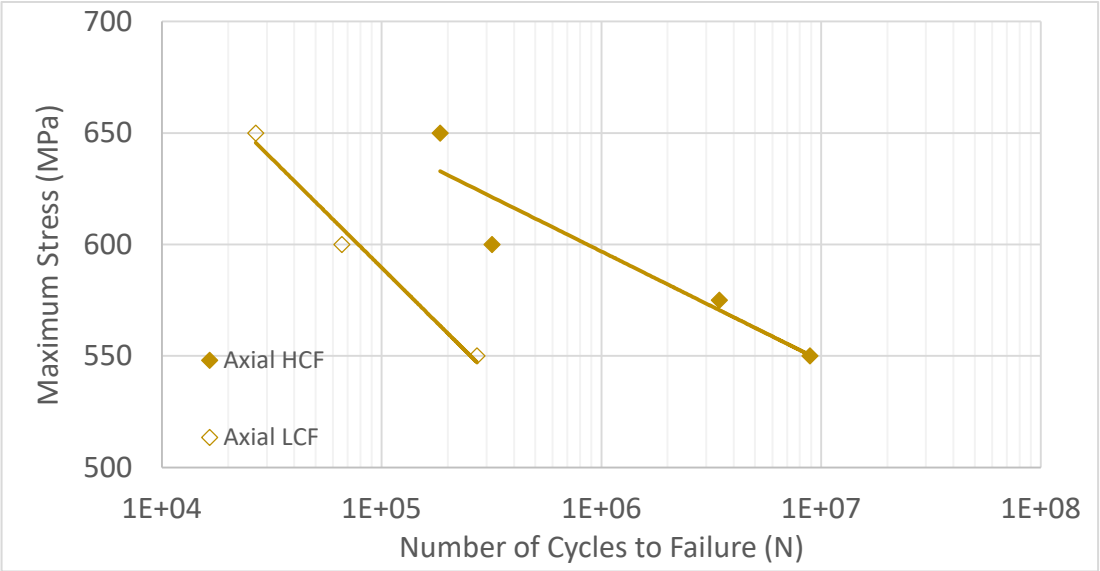

Figure 4.15: Ti-407 manufacturer 2 combined LCF and HCF data for the axial direction.

An additional 1Hz sine wave test was completed to test the effect of the 1 second hold seen under the trapezoidal waveform. As can be seen in Figure 4.16 the cycles to failure under 1Hz approaches the HCF curve.

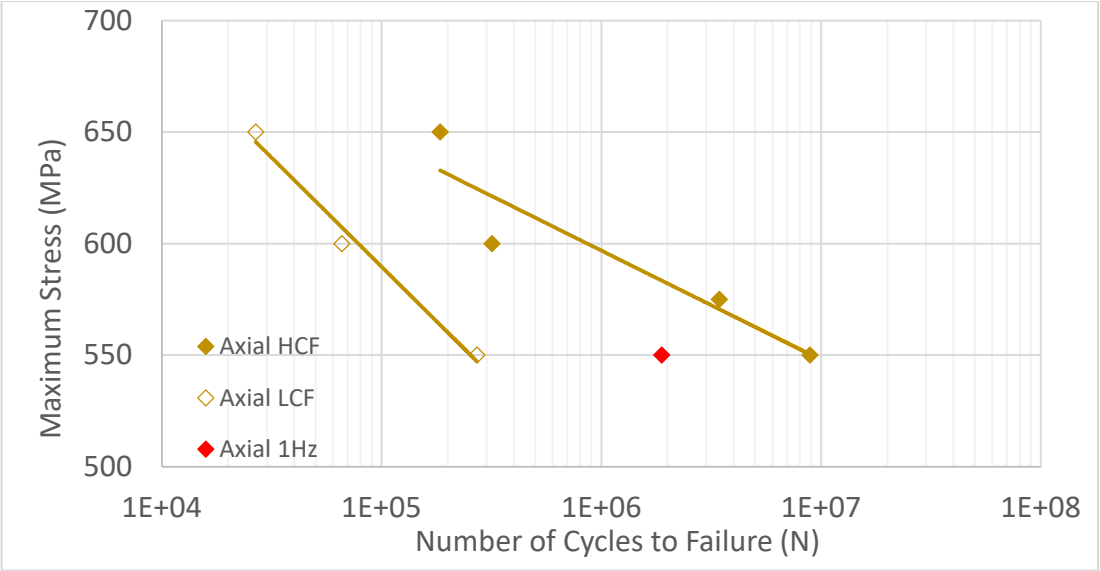

Figure 4.16: Combined data for axial HCF and LCF with additional 1Hz frequency.

4.2.3.4 Ti-407 Manufacturer 2 Combined Fatigue Data for Tangential Orientation

Figure 4.17 plots the combined fatigue data for the tangential orientation. Here the gap between the two regimes is not as prominent as has been seen previously. There is still a gap of more than an order of magnitude at the bottom of the tested stress range but the HCF curve approaches the LCF curve at roughly 575MPa, which is in the middle of the stress range.

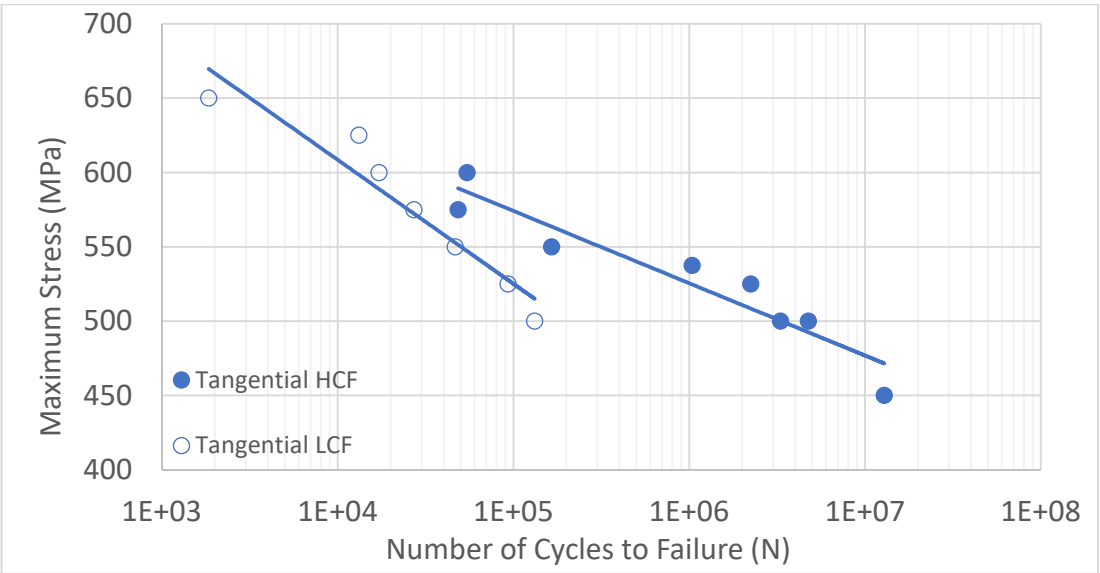

Figure 4.17: Combined LCF and HCF data for the tangential direction.

4.2.4 Manufacturer 2 Ring Rolled Fractography

4.2.4.1 Tangential LCF Fractography

Figure 4.18 shows a selection of fracture surfaces from the LCF tests. All were surface initiations.

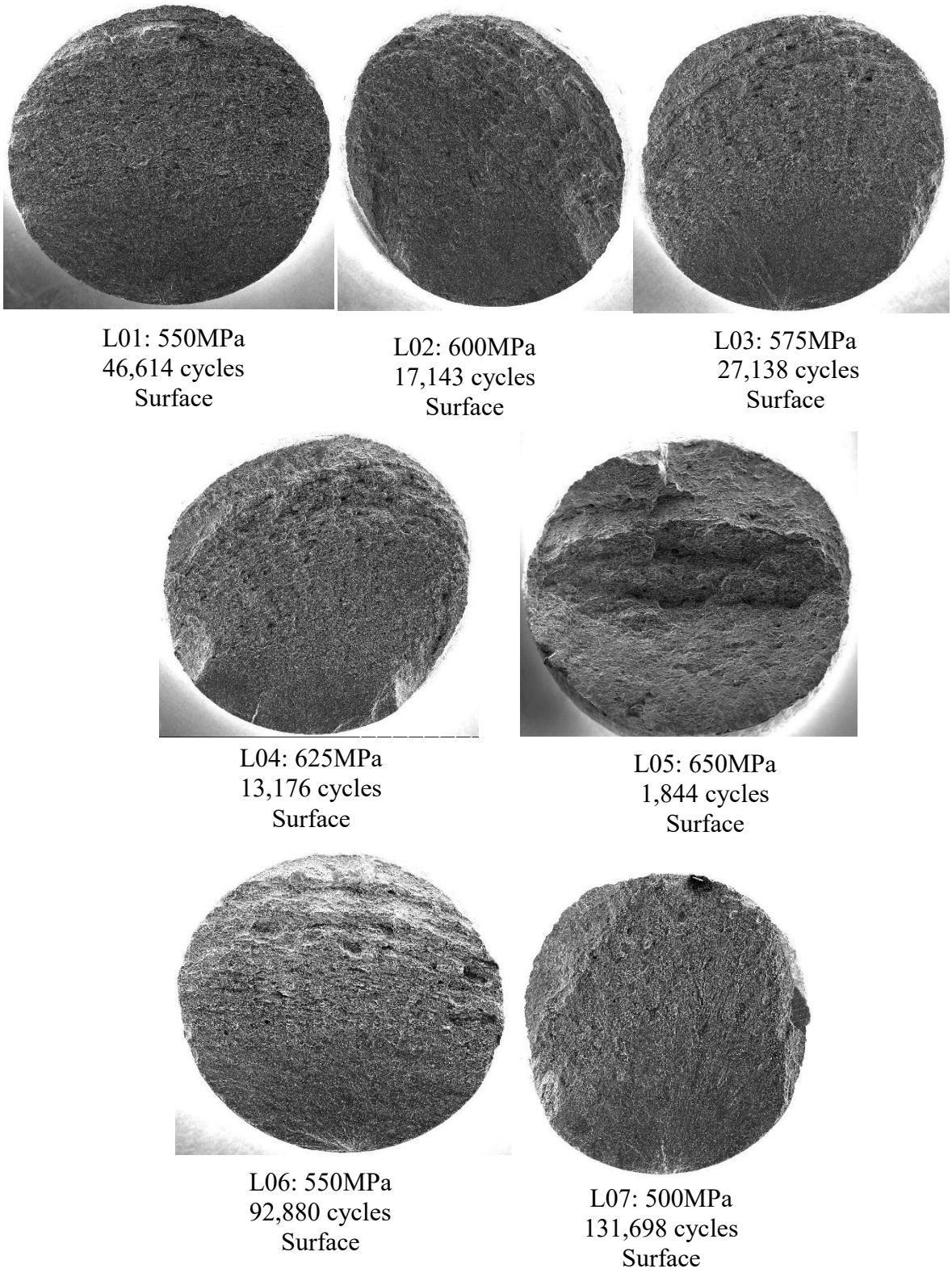

Figure 4.18: Fracture surfaces of the LCF tangential test pieces.

4.2.4.2 Tangential HCF Fractography

The HCF tangential fracture surfaces are included in Figure 4.19. Unlike the axial and manufacturer 1 HCF curves, no subsurface initiation sites were seen.

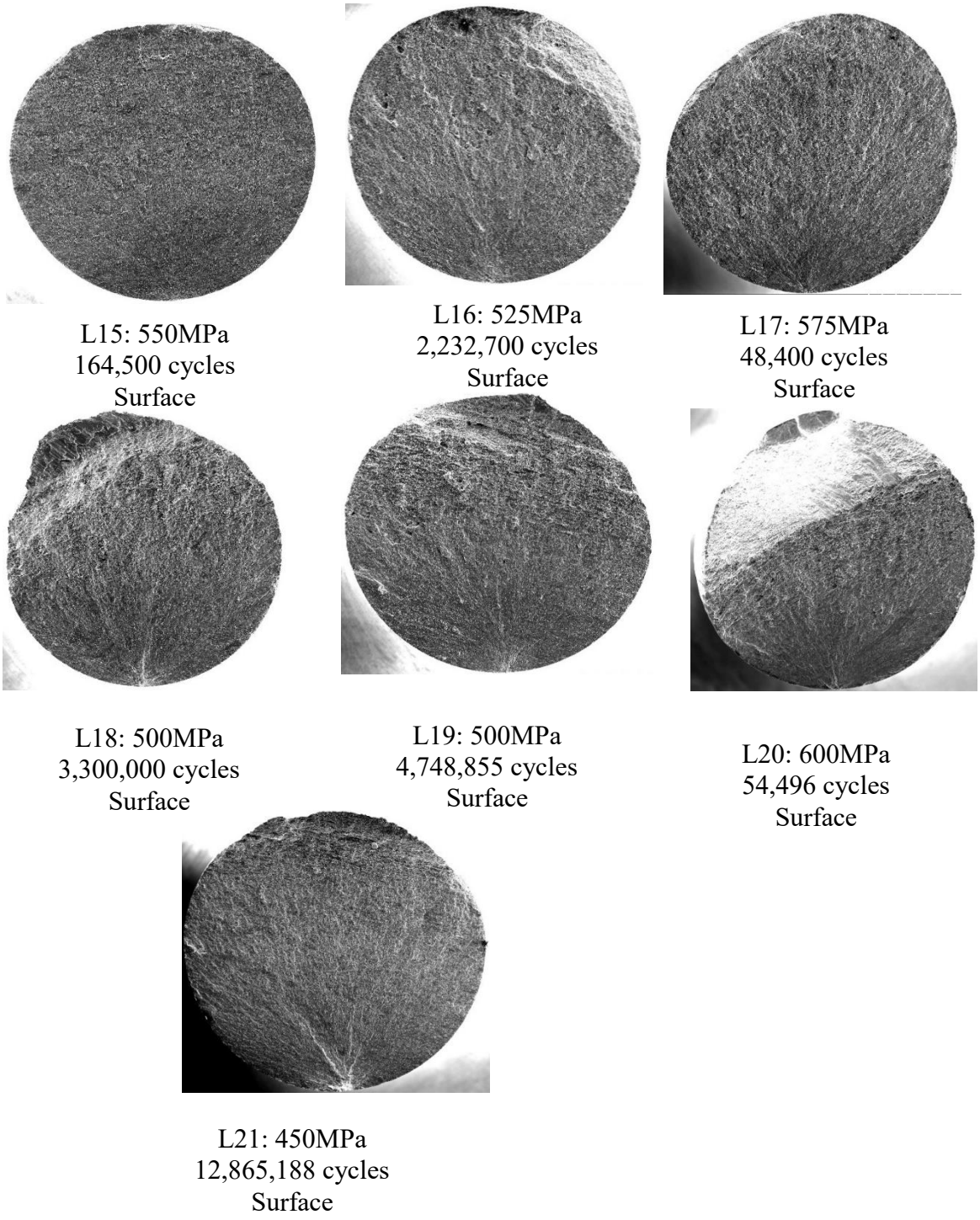

Figure 4.19: Fracture surfaces of the Ti-407 manufacturer 2 HCF tangential test pieces.

4.2.4.3 Axial LCF Fractography

Fracture surfaces representative of the axial fractures are shown in Figure 4.20. Again all cracks initiated at the surface.

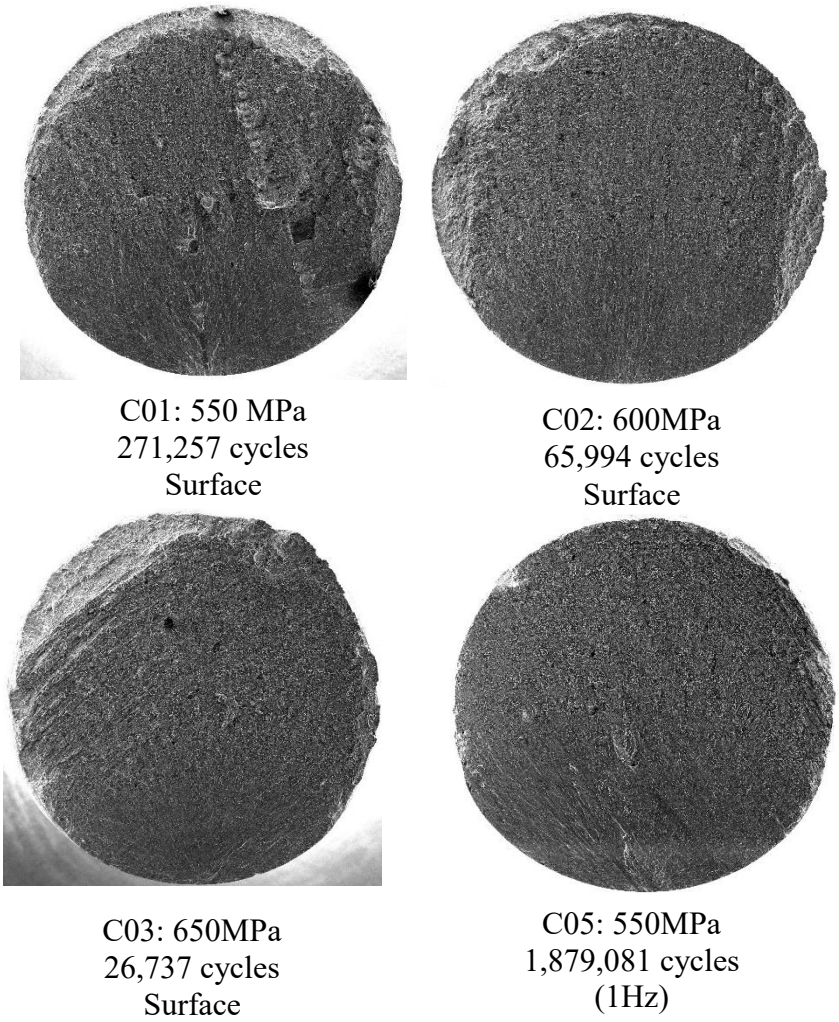

Figure 4.20: Fracture surfaces of the LCF axial test pieces.

4.2.4.4 HCF Axial Fractography

Figure 4.21 shows HCF fracture surfaces from axial test pieces. In this case two of the initiation sites were surface, and two of the sites subsurface. The subsurface sites are highlighted inside the circles.

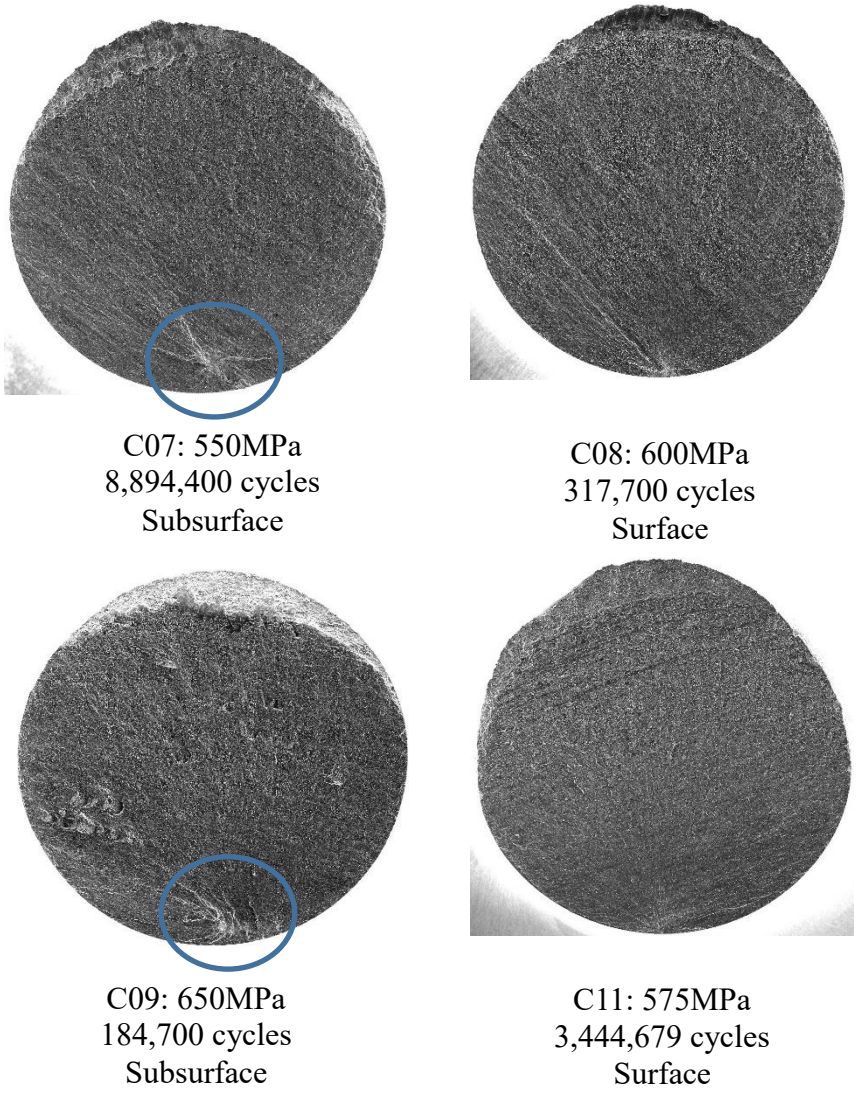

Figure 4.21: Fracture surfaces of the HCF axial test pieces.

4.2.4.5 Ti-407 Manufacturer 2 Ring Rolled Texture Analysis

The inverse pole figures and pole figures of a tangential and axial test piece cross section, 3–4mm below the fracture surface, are presented below. Figure 4.22 shows the IPF mapped from a tangential test piece and the corresponding pole figure in Figure 4.23. Figure 4.24 shows the IPF map from an axial test piece and the corresponding pole figure in Figure 4.25.

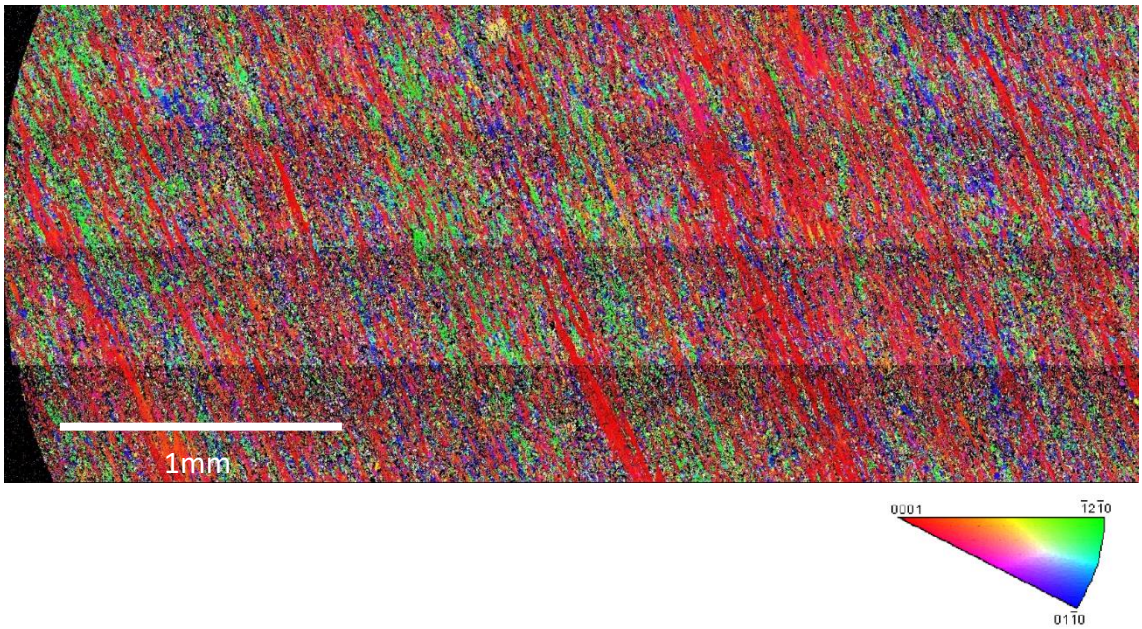

Figure 4.22. Ti-407 manufacturer 2 inverse pole figure of test piece L01 (tangential) tested at 550MPa under LCF conditions completing 46,614 cycles.

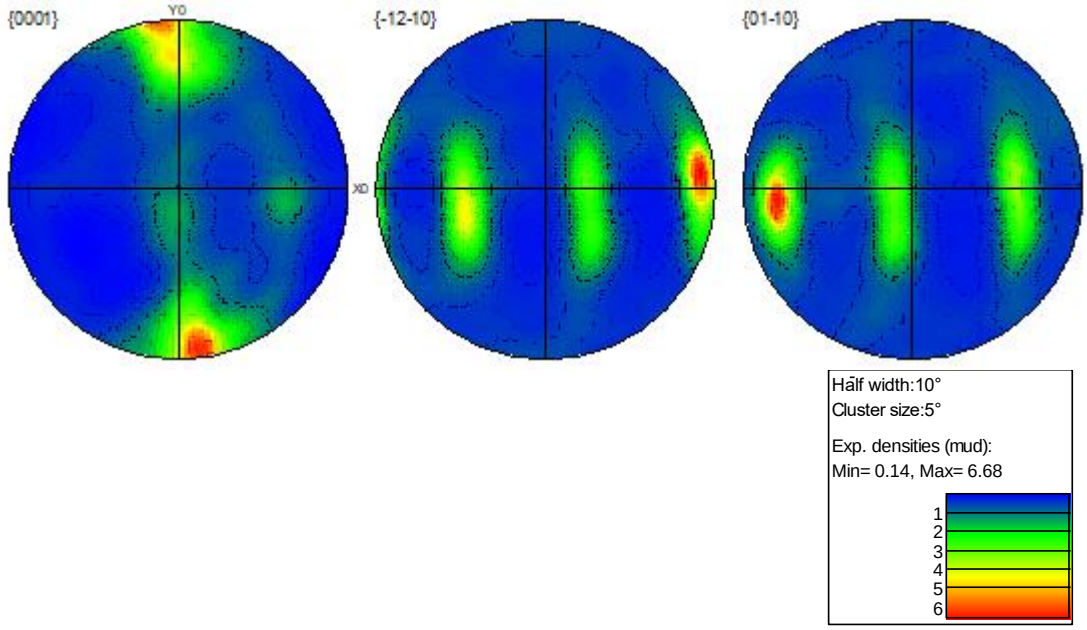

Figure 4.23: Pole figures corresponding to Figure 4.22.

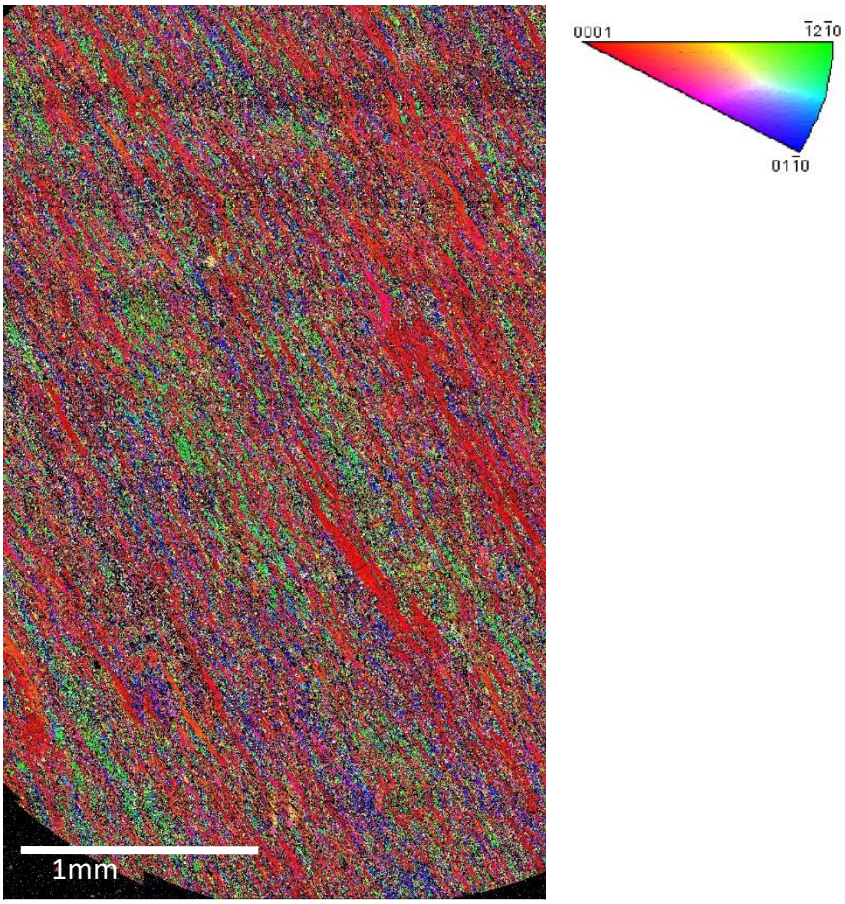

Figure 4.24: Ti-407 manufacturer 2 inverse pole figure of test piece C01 (axial) carried out under LCF conditions at 550MPa completing 271,257 cycles.

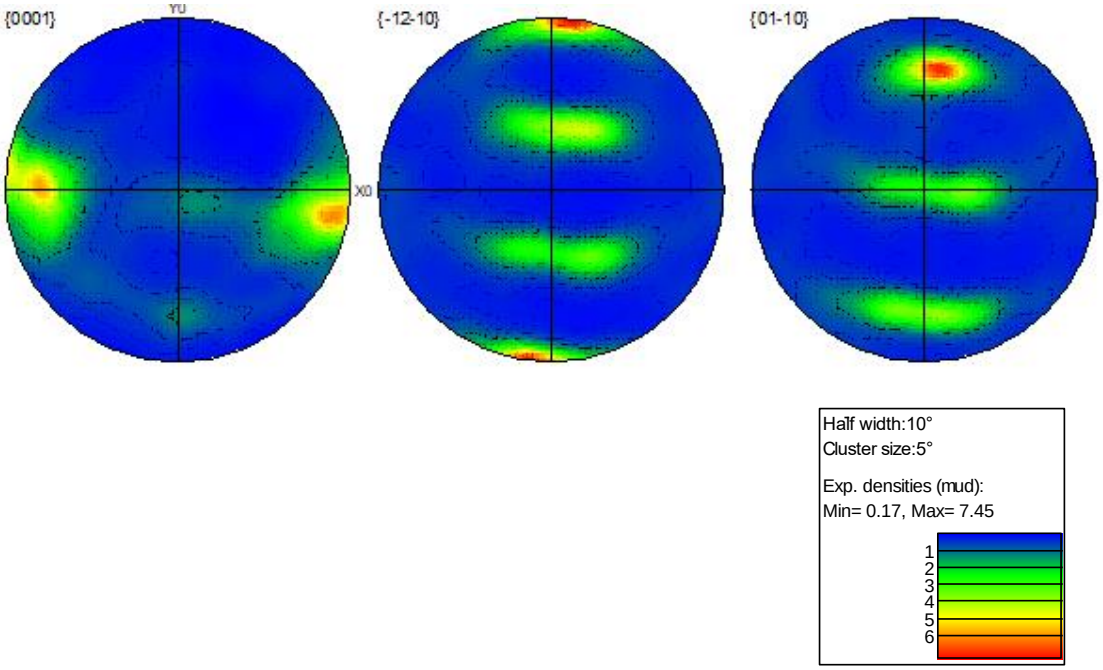

Figure 4.25. Pole figures associated with Figure 4.24.

The pole figures show a maximum texture intensity of 6.68 under the tangential orientation and 7.45 under the axial orientation. For both the tangential and the axial specimens, the inverse pole figure maps show long thin bands of basal orientated grains consistent with the bands seen in Figure 4.11. From the IPF maps it would appear that the bands of high aspect ratio grains are predominantly of basal orientation. For ease of reference another example of the microstructure is shown below in Figure 4.26.

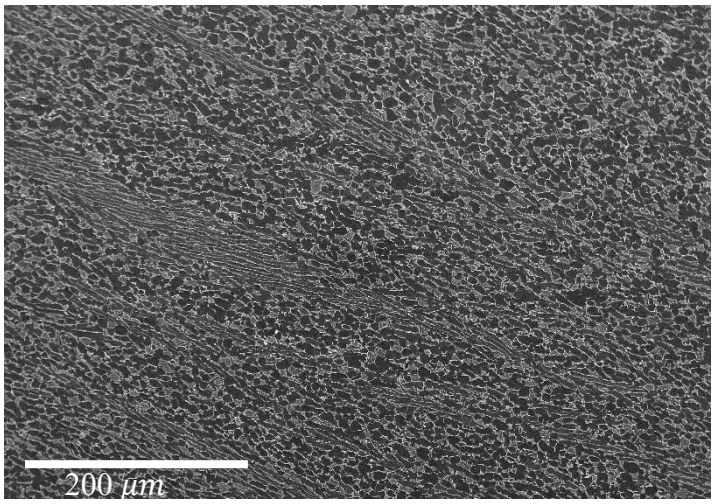

Figure 4.26. Microstructure image of the ring rolled product of manufacturer 2.

Further to the bands seen in the microstructure, some of the fracture surfaces displayed long thin features near the initiation sites, again similar in morphology and size to those seen from the texture maps and the microstructure images. Examples of these fracture surfaces are shown in Figure 4.27.

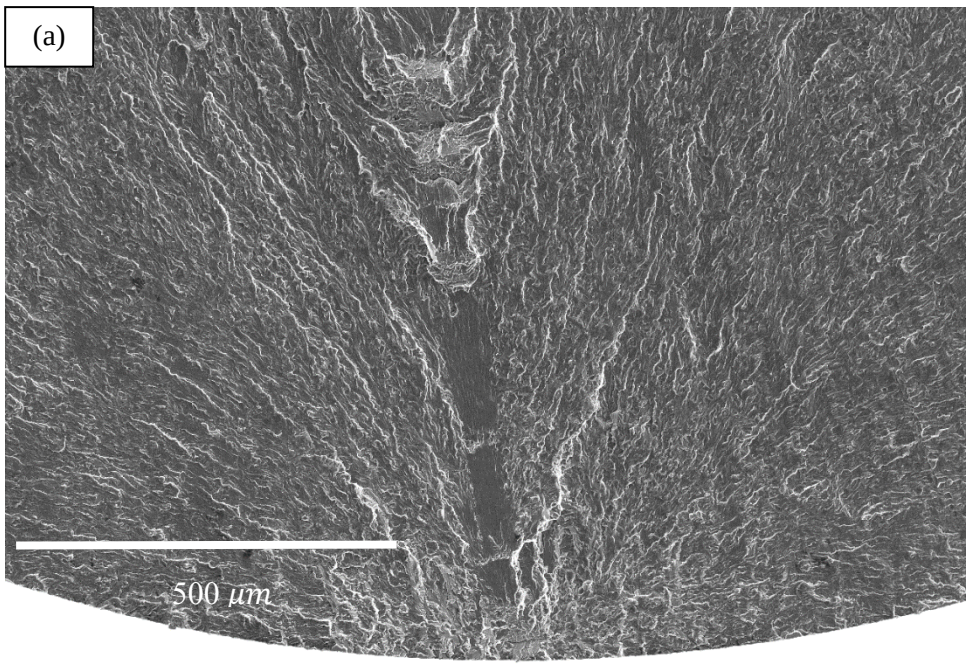

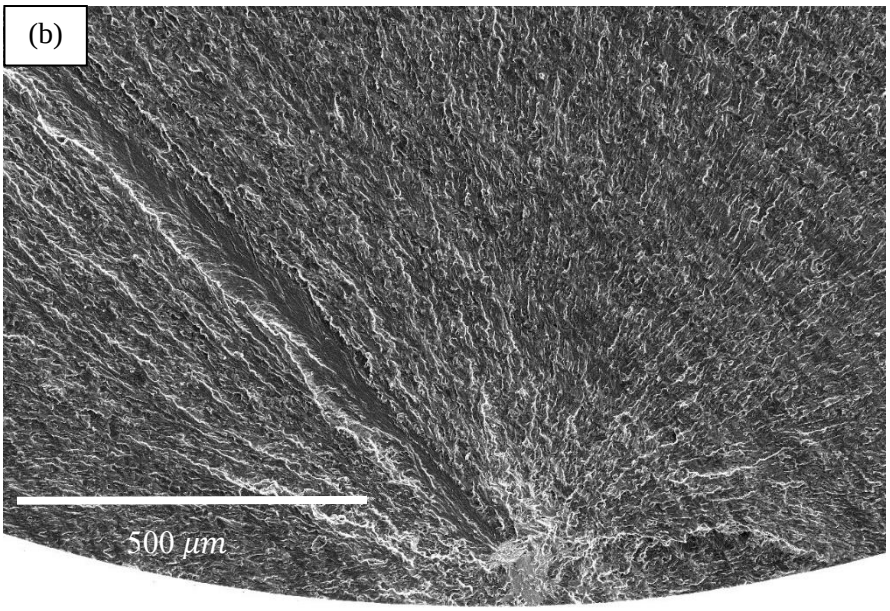

Figure 4.27: Example of fracture surfaces with elongated facets near the initiation site (a) Test piece C01 (axial) tested at 550MPa under LCF conditions, achieving 275,257 cycles and (b) Test piece C08 (axial) tested a 600MPa under HCF conditions achieving 317,700 cycles.

4.3 Comparison of Combined Ring Rolled Fatigue Data

The graphs below compare data from all of the ring rolled results.

4.3.1 Comparison of Manufacturer 1 against Manufacturer 2 Tangential Orientation

Figure 4.28 below compares the fatigue data from the test pieces of manufacturer 1 against the tangentially orientated data from the ring rolled block from manufacturer 2. Comparing both LCF and HCF data, the manufacturer 1 material displays a slightly stronger response, although the difference is more pronounced under HCF compared to LCF.

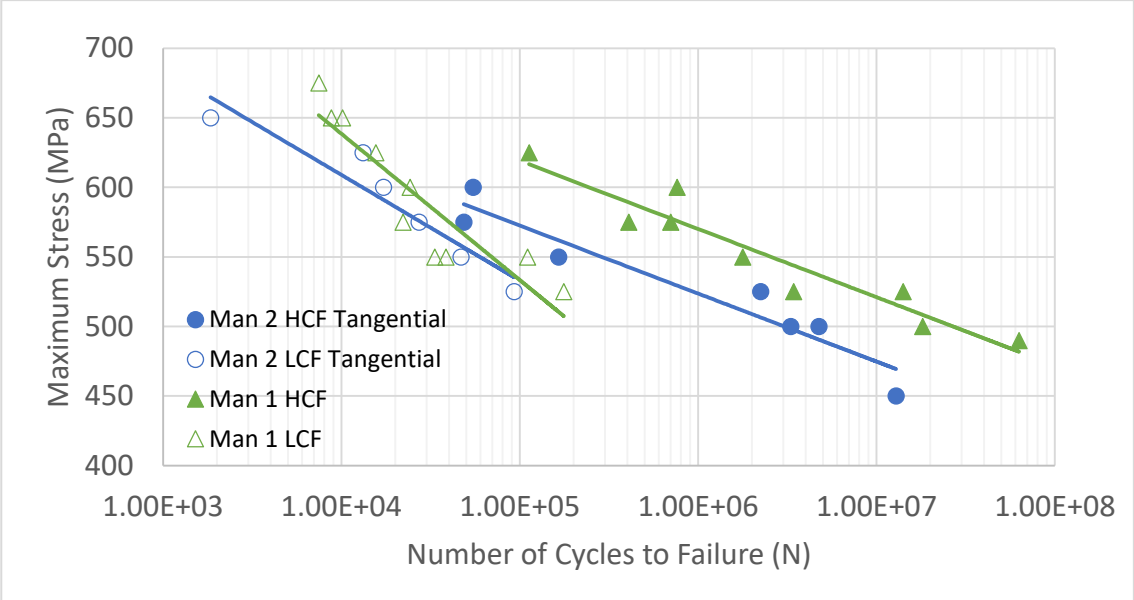

Figure 4.28: Plot of manufacturer 1 data against manufacturer 2 tangential.

4.3.2 Comparison of Manufacturer 1 against Manufacturer 2 Axial Orientation

Figure 4.29 compares axial orientation manufacturer 2 and manufacturer 1 LCF and HCF tests. This time it can be seen that for both cases the manufacturer 2 results appear superior to the manufacturer 1 results, although it is under LCF condtions where this difference is a little more pronounced.

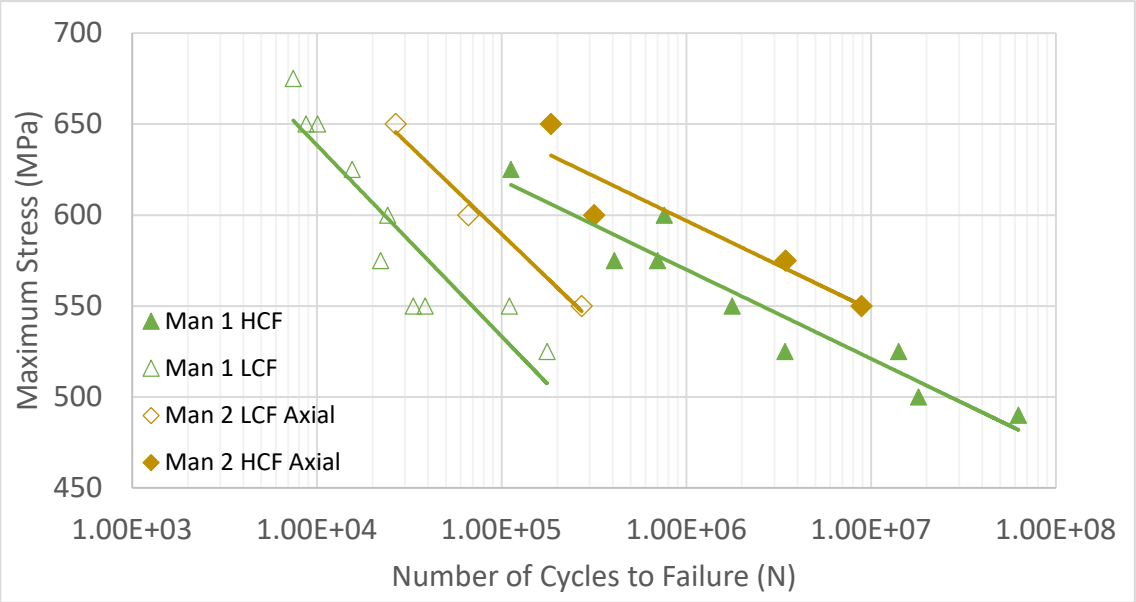

Figure 4.29: Plot of manufacturer 1 data against manufacturer 2 tangential material.

4.4 Ti-407 and Ti-6-4 Pancake Forged Data

The next section presents the tensile and fatigue data for Ti-407 and Ti-6-4 from the pancake forgings. As mentioned in the experimental section, the pancakes originated as a cross section from a billet, were cut into ‘cheeses’ (segments) and then forged into the final pancake form.

4.4.1 Microstructural Characterisation

The pancake heat treatment processing schedule has already been described in section 3.2. Details of microstructural parameters and chemical analysis (summarised in Table 4.7 and 4.8) are presented below to provide a comprehensive comparison of the individual product forms, before presentation of the mechanical data itself.

4.4.1.1 Ti-407 forged pancake microstructure

The average primary alpha grain width in the Ti-407 pancake material is roughly 9μm with a volume fraction of 34%. The presence of high aspect ratio elongated grains is still significant, although not as concentrated or prevalent as is seen in the ring rolled product forms. The secondary alpha lath width was measured between 0.5–0.8μm.

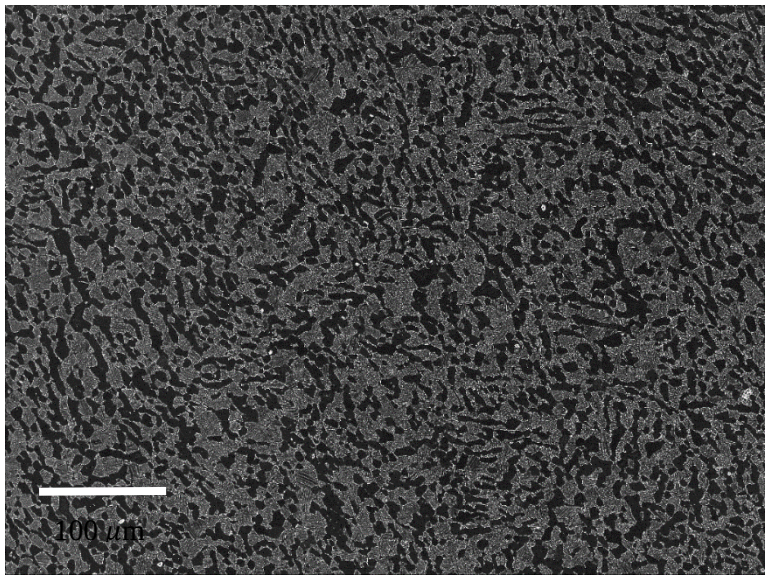

Figure 4.30: Ti-407 pancake forged microstructure.

4.4.1.2 Ti-6-4 Aged Microstructure

The aged Ti-6-4 microstructure had an average primary alpha grain size of 20 μm and a much more equiaxed morphology compared the Ti-407 material. The volume fraction was measured at 36%. The secondary alpha lath width was between 0.5–1 μm.

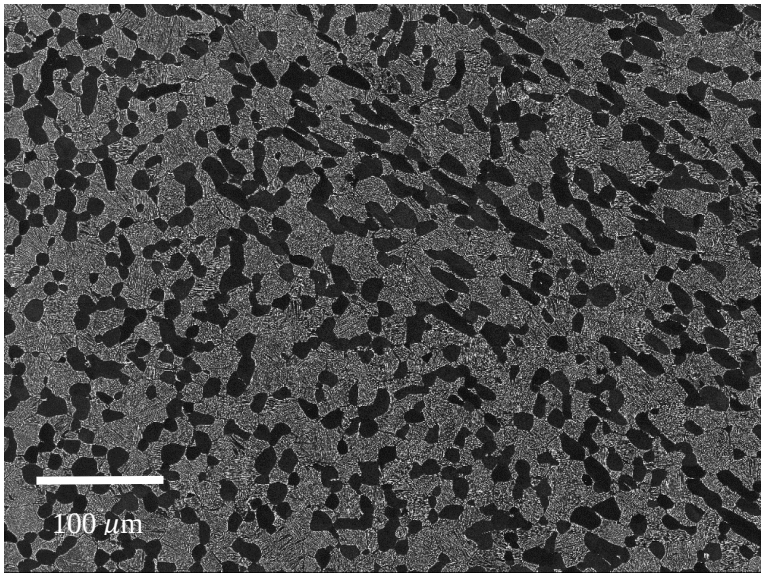

Figure 4.31: Ti-6-4 pancake forged aged microstructure.

4.4.1.3 Ti-6-4 Annealed Microstructure

The annealed primary alpha grain size was marginally smaller than that of the aged material, measured at 13 μm. A relatively equiaxed grain morphology is seen with a volume fraction of 34% and secondary alpha lath width of 0.5–0.8 μm.

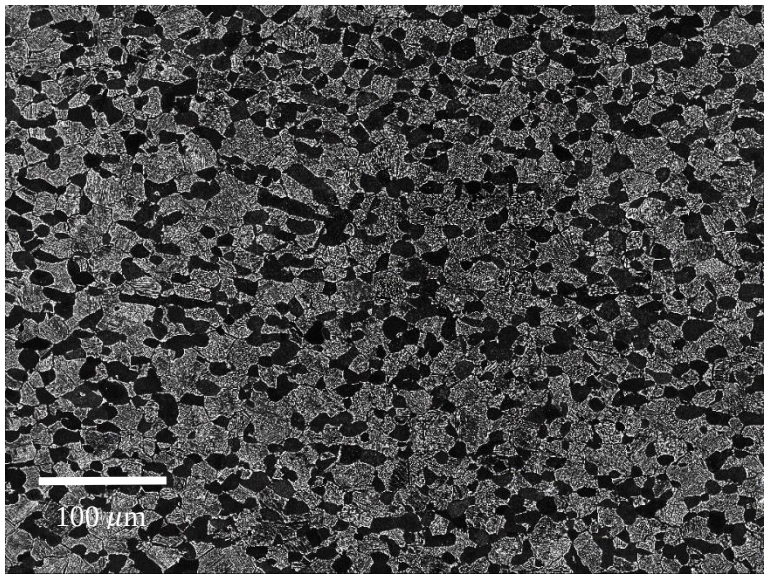

Figure 4.32: Ti-6-4 pancake forged annealed microstructure.

4.4.1.4 Summary of Microstructure and Chemistry

Tables 4.7 and 4.8 summarise the microstructure and the chemical composition of the Ti-407 and the two Ti-6-4 variants.

Table 4.7: Key microstructural parameters.

	Ti-407	**Ti-6-4 aged**	**Ti-6-4 annealed**
Primary alpha volume fraction (%)	34	36	34
Primary alpha grain diameter (μm)	9	20	13
Primary alpha grain length max (μm)	50	40	40
Secondary alpha lath width (μm)	0.5-0.8	0.5-1	0.5-0.8

Table 4.8: Material chemical composition.

Element	Bulk chemistry (wt %)	Primary alpha grain (wt %)	Beta grain (wt %)
Ti-407 Pancake material			
Al	0.83	1.08	0.73
V	3.03	1.17	4.23
Si	0.27	0.28	0.28
Fe	0.29	0.02	0.33
Ti-6-4 Aged			
Al	5.85	6.62	5.32
V	3.69	1.46	4.54
Fe	0.14	0.01	0.21
Ti-6-4 Annealed			
Al	5.97	6.83	5.66
V	3.80	1.43	4.34
Si	0.05	0.02	0.05
Fe	0.17	0.04	0.23

4.4.2 Tensile Data - Ti-407 and Ti-6-4 Pancake Forged

The results of the tensile tests are summarised in Table 4.9. Three tests on Ti-407 and four on Ti-6-4 were conducted. Due to the limited specimens from the annealed variant Ti-6-4 pancake, tensile tests were carried out only on the aged variant. The assumption was made, for the purpose of normalising the fatigue graphs, that the tensile strength of both variants are similar.

Table 4.9: Tensile results from Ti-407 and Ti-6-4 forged pancake product form.

Room Temperature Tensile Tests on Pancake Material					
	Young's Modulus (GPa)	0.2% Proof Stress (MPa)	UTS (MPa)	Elongation after Fracture (A %)	Reduction in Area (%)
Ti-407					
1	114	647	764	18.06	62
2	114	651	718*	19.63	57
3	114	646	714*	20.16	55
Average	114.0	648.0	764	19.3	58.0
Ti-6-4 aged					
1	117	915	1035	12.28	33
2	114	914	1037	12.65	54
3	115	912	1031	13.67	33
4	118	917	1040	13.04	38
Average	116.0	914.5	1035.8	12.9	39.5

*UTS invalid as strain rate not increased after 5% strain.

As mentioned in section 3.4.1, the strain rate was stepped up from 0.002/min to 0.01/min at 5% strain, once the yield point had been defined. However, due to incorrect test set-up this was not the case for the second and third Ti-407 tests where they remained at the lower strain rate until fracture, resulting in the lower UTS relative to the first test. This mistake was unfortunate but the Ti-6-4 results, and the results of the manufacturer 2 ring rolled material are relatively precise giving confidence in taking the one UTS value obtained with the strain rate step up, as being accurate. This does highlight the strain rate sensitivity of Ti-407, commonly seen in materials science.

The Young's moduli of the two alloys are similar but the UTS of Ti-6-4 is 35% higher than Ti-407 and the yield stress stronger by roughly 40%. One of the motivational factors behind the development of Ti-407 was increased ductility allowing for better toughness and therefore impact strength. The ductility (elongation after fracture) is measured at roughly 6% higher than that of Ti-6-4.

Figure 4.33 shows the stress strain curve of Ti-407 against Ti-6-4.

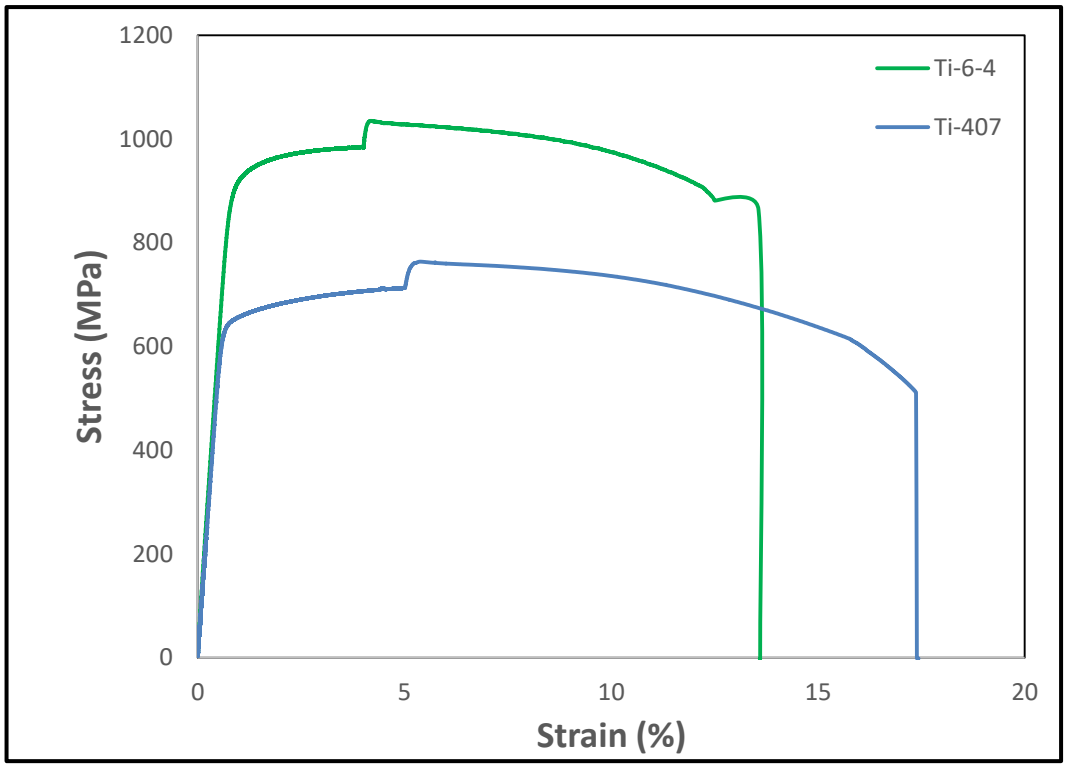

Figure 4.33: Stress strain curve of Ti-6-4 against Ti-407 pancake forged material.

4.4.3 Hardness Testing

The tensile results were reflected through the hardness testing carried out on Ti-407 and Ti-6-4, presented in Figures 4.34 and 4.35. Hardness measures the resistance of the material to localised surface deformation. Measurements were taken from primary alpha grains and transformed beta regions to see how the hardness differed. An average was calculated from 10 point measurements.

The measurements of the Ti-6-4 microstructure fall in line with the commonly reported 350 Vickers hardness observed in the literature [165].

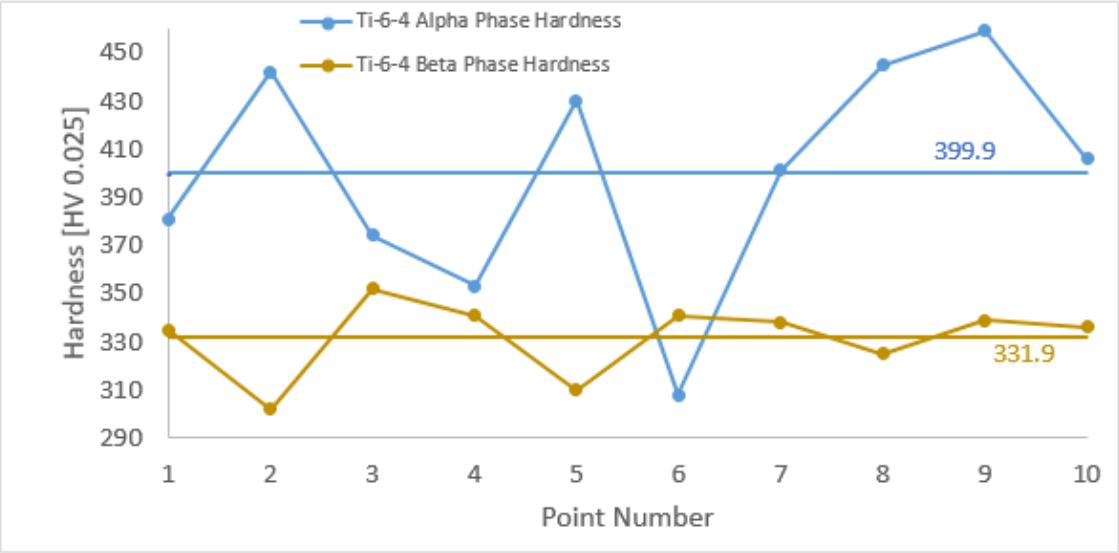

Figure 4.34: Hardness testing results for alpha and beta phases of Ti-6-4.

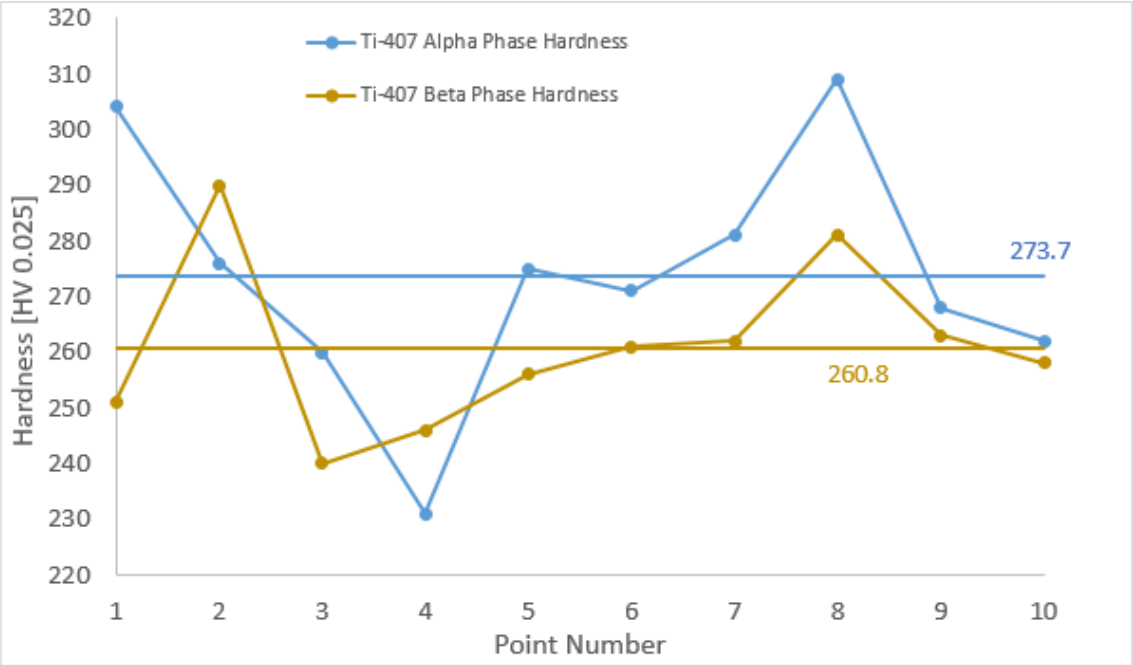

Figure 4.35: Hardness testing results for alpha and beta phases of Ti-407.

The 30% harder alpha phase of Ti-6-4 is roughly in line with the 35% higher tensile strength; both are indicators of a metal's resistance to plastic deformation. An interesting observation when comparing the two results is the much higher difference in hardness between the alpha and beta phase seen for Ti-6-4 compared to Ti-407. The alpha phase is roughly 20% harder in Ti-6-4 but just 5% harder in Ti-407. This is probably explained by the aluminum deficiency in the alpha phase of Ti-407.

4.4.4 Ti-407 vs Ti-6-4 High Cycle Fatigue Performance

Figure 4.36 presents the high cycle fatigue performance comparison of Ti-407 versus the aged and annealed variants of Ti-6-4.

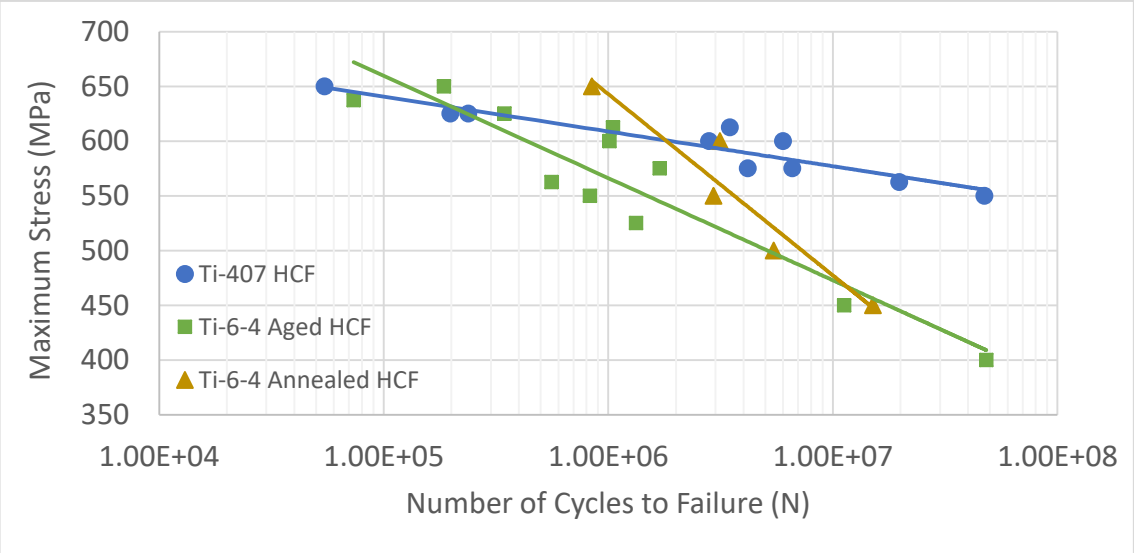

Figure 4.36: Comparison of Ti-407 HCF vs Ti-6-4 HCF in both an aged and annealed variant.

Despite the 40% lower yield strength of Ti-407, it is interesting to note the significantly stronger response of the new alloy, particularly at the lower end of the stress range. At a life of 10 million cycles, Ti-407 requires a stress of 575MPa to cause failure, roughly 100MPa more than that for both variants of Ti-6-4. Both variants of Ti-6-4 demonstrate similar strength at the lower end of the stress range, but the annealed variant is slightly stronger at the higher end, perhaps reflecting the finer grain size. Interestingly, the difference in Ti-6-4 performance is effectively opposite to that generated by Knobbe et al, where the HCF lives of two bimodal structures were roughly equivalent at higher stresses but differences in the fatigue performance became more apparent moving down the stress range towards the fatigue limit [56].

The HCF comparison plot is displayed again in Figure 4.37, but this time normalised by the yield strength. This further emphasises the stronger performance of Ti-407, which in fact still achieves a significant number of cycles above its yield strength, defined as 648MPa from the tensile tests. For Ti-407, 10 million cycles are achieved at roughly 90% of the yield strength, whilst for both variants of Ti-6-4, 10 million cycles are achieved at 55% of the yield.

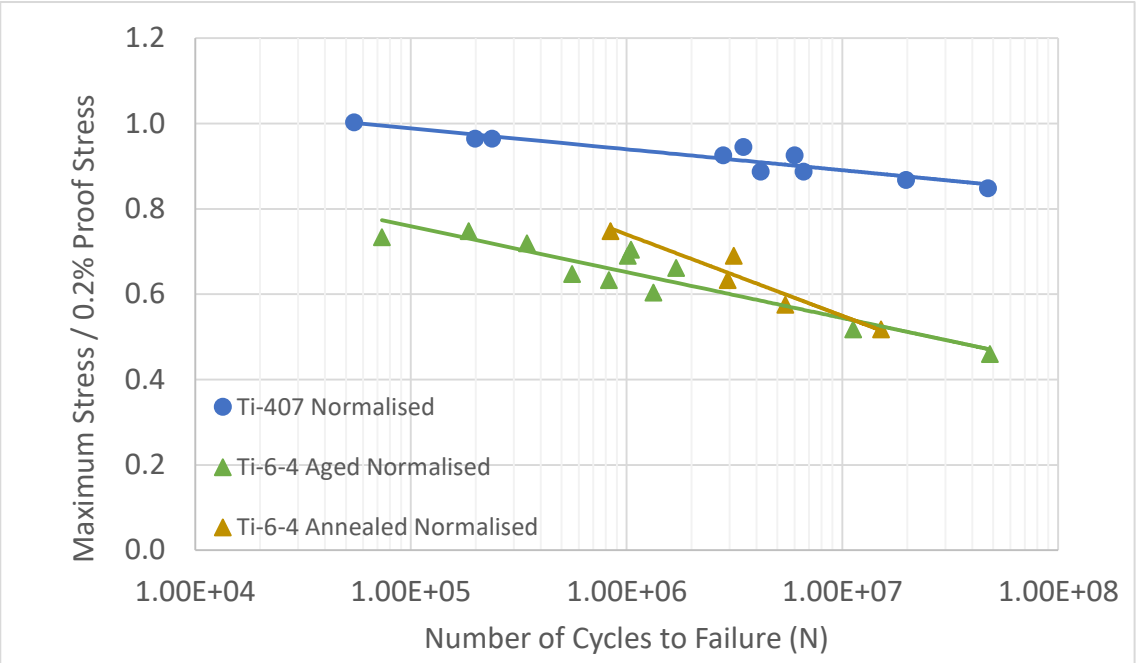

Figure 4.37: Ti-407 and Ti-6-4 HCF performance as a function of 0.2% proof stress. Normalised data from Figure 4.36.

4.4.5 Combined Fatigue Data

Figure 4.38 plots the combined Ti-407 fatigue pancake data in isolation. Similar to the manufacturer 1 and axial manufacturer 2 material, there is a large gap between the HCF and the LCF curves, more than two orders of magnitude at the bottom end of the stress range. A further knockdown is seen when pieces were subjected to a dwell cycle, though the debit is not as large as the knockdown from HCF to LCF particularly at the lower end of the stress range. The tests at 650MPa are at the material yield strength.

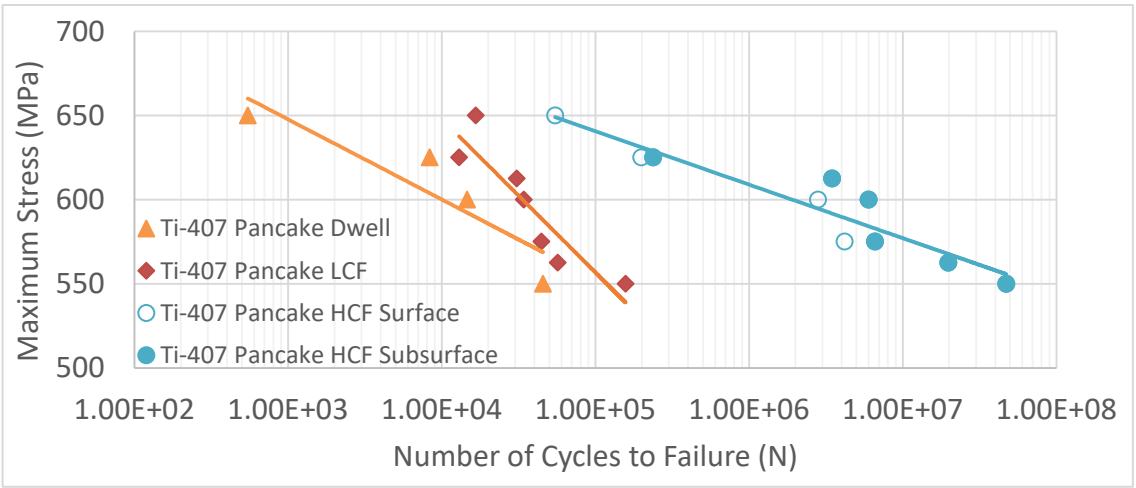

Figure 4.38: HCF, LCF and dwell fatigue data for pancake Ti-407.

An oversight during testing was the lack of a generation of an LCF Ti-6-4 curve to observe the relationship between the two fatigue regimes. However, a single remaining annealed Ti-6-4 test piece was tested under LCF conditions, and this single result, with the HCF curve is plotted below. Also plotted is a Ti-6-4 data set generated at the start of the project. The precise origins of this material are unknown, but are comparable to the result of the single annealed point.

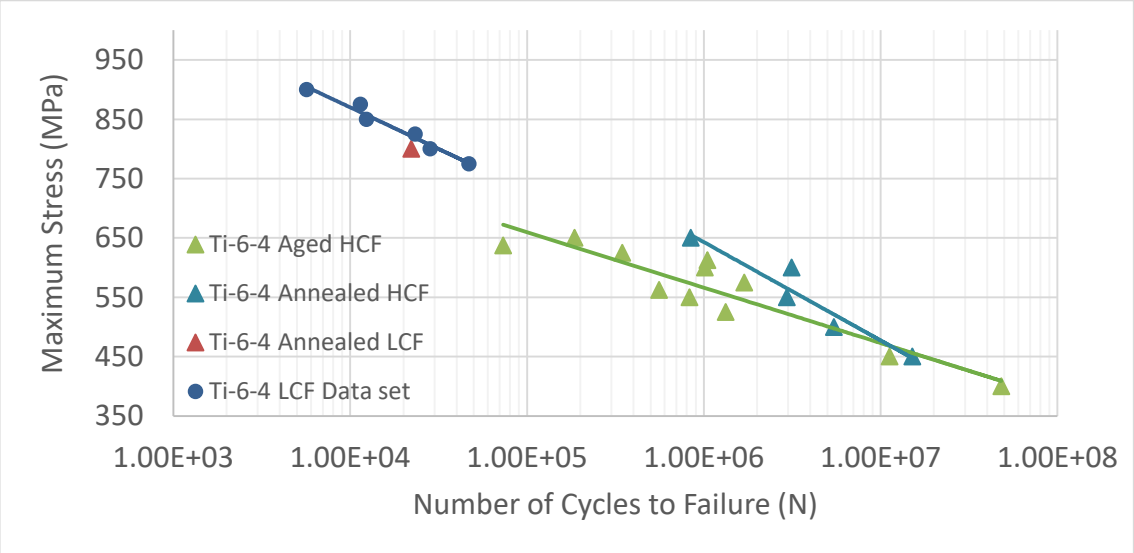

Figure 4.39: Ti-6-4 HCF and LCF fatigue data.

Clearly, there is a stark difference between Ti-407 and Ti-6-4, with the Ti-407 LCF and HCF fatigue data sitting alongside each other throughout the same stress range, and the Ti-6-4 LCF annealed point and additional data set sitting above and moving down towards the HCF curve in a more continuous transition between the fatigue regimes, as is more commonly seen in the literature [165]. Again considering the normalised data, the Ti-6-4 annealed 800MPa LCF point corresponds to stress of 92% of the yield, and the Ti-407 612.5MPa point (having completed 30749 cycles, which is nearest to the 22135 cycles completed by the Ti-6-4 annealed LCF point) corresponds to 94.5% of the yield. This is obviously much more comparable than the HCF data.

4.4.6 Pancake Forging Fatigue Fractography

The fracture surfaces from the fatigue tested pancake forgings of Ti-407 and Ti-6-4 are displayed below.

4.4.6.1 Ti-407 HCF Fractography

The Ti-407 HCF fracture surfaces displayed a mixture of surface and subsurface initiation sites (the subsurface sites highlighted inside the circles). The subsurface initiated failures were easily identified by the circular shaped dark halo formed during subsurface crack propagation, effectively within a vacuum environment. The fracture surface surrounding the halo, formed after the crack broke through at the surface and now open to oxidation, had a lighter appearance.

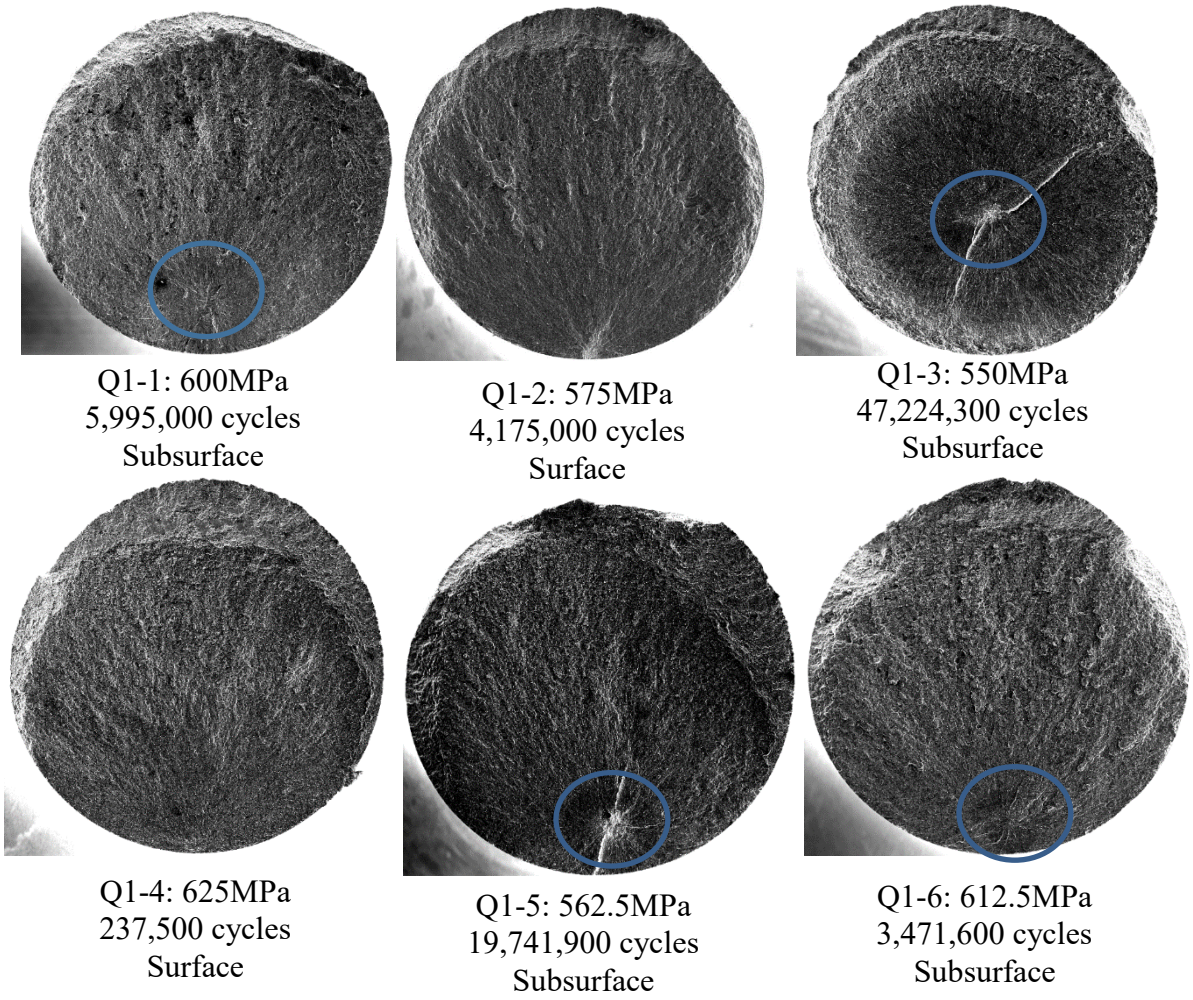

Figure 4.40: HCF Ti-407 forged pancake fractography.

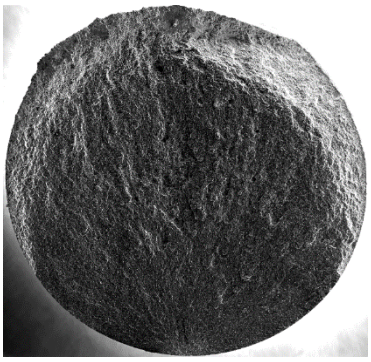

Q1-7: 600MPa
2,804,500 cycles
Surface

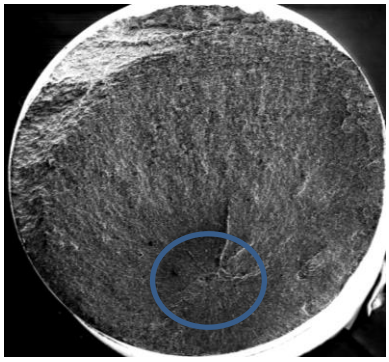

Q1-8: 575MPa
6,602,300 cycles
Subsurface

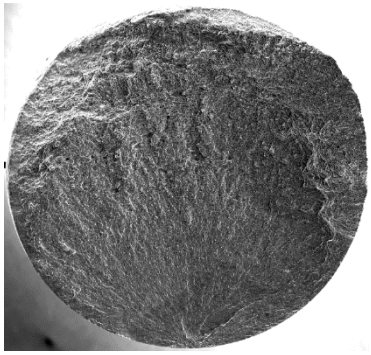

Q1-9: 625MPa
198,100 cycles
Surface

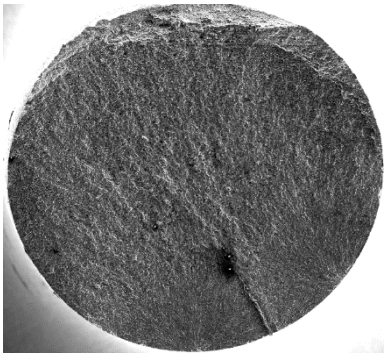

Q2-17: 600MPa
54,500 cycles
Surface

Figure 4.40 (continued): HCF Ti-407 forged pancake fractography.

Higher magnification images focused at the centre of the initiation sites are shown below. Quasi-cleavage facets were invariably revealed at the centre of the halo, marking the precise site of fatigue crack initiation.

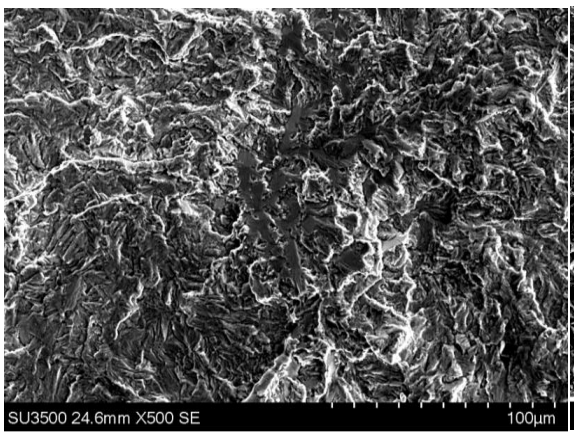

Q1-1: 600MPa
5,995,000 cycles
Subsurface

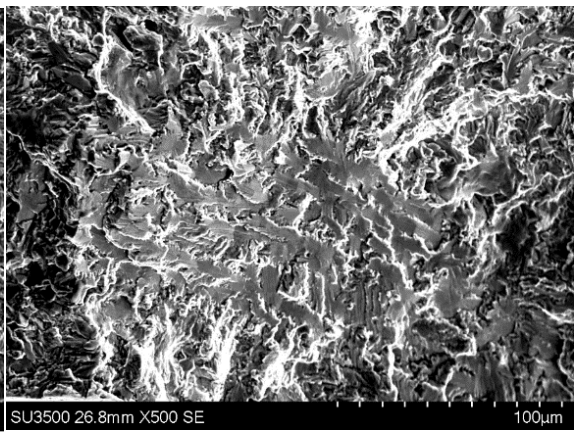

Q1-2: 575MPa
4,175,000 cycles
Surface

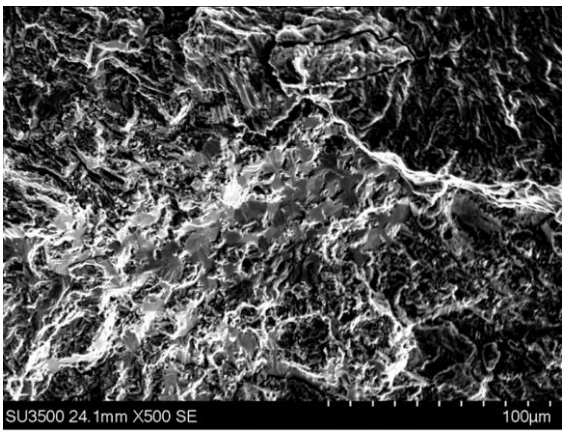

Q1-3: 550MPa
47,224,300 cycles
Subsurface

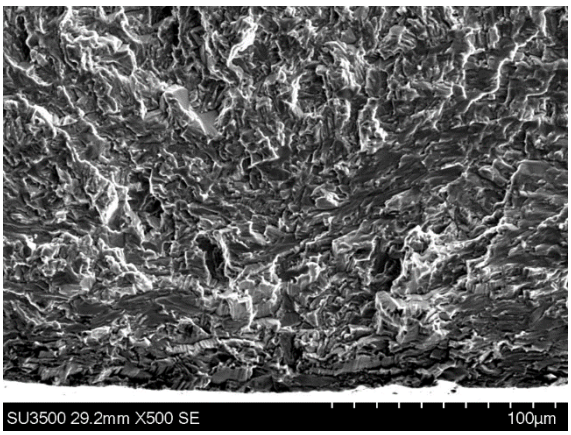

Q1-4: 625MPa
237,500 cycles
Surface

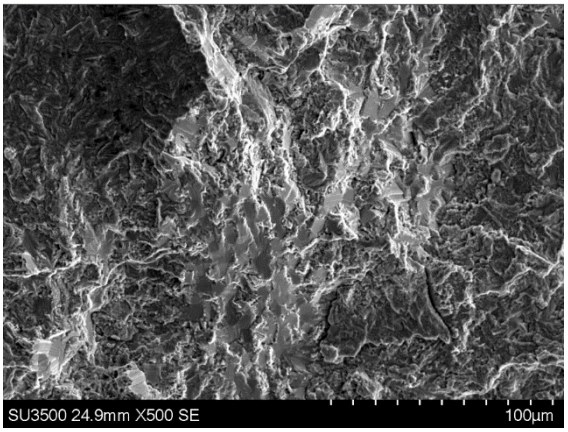

Q1-5: 562.5MPa
19,741,900 cycles
Subsurface

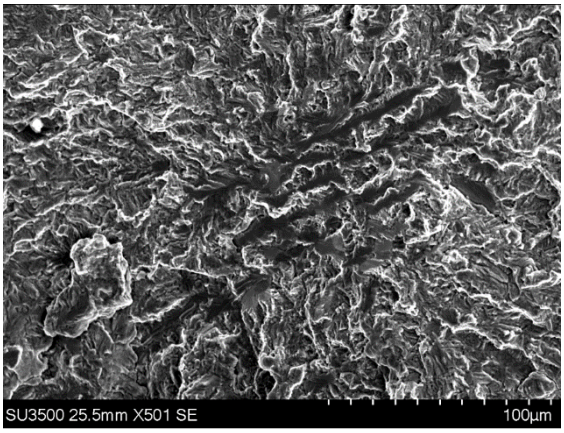

Q1-6: 612.5MPa
3,471,600 cycles
Subsurface

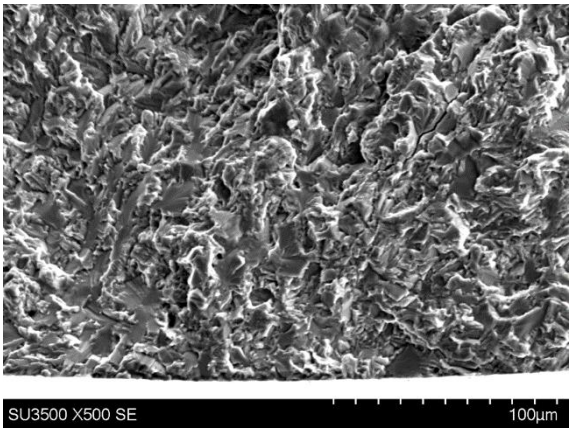

Q1-7: 600MPa
2,804,500 cycles
Surface

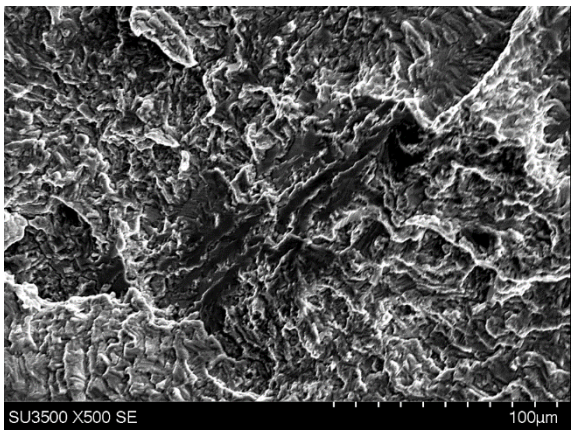

Q1-8: 575MPa
6,602,300 cycles
Subsurface

Figure 4.41: Initiation centers for pancake forged Ti-407 fracture surfaces.

4.4.6.2 Ti-6-4 HCF

For the Ti-6-4 HCF fractured test pieces, all initiation sites were found to be surface. The fractography is shown in Figure 4.42.

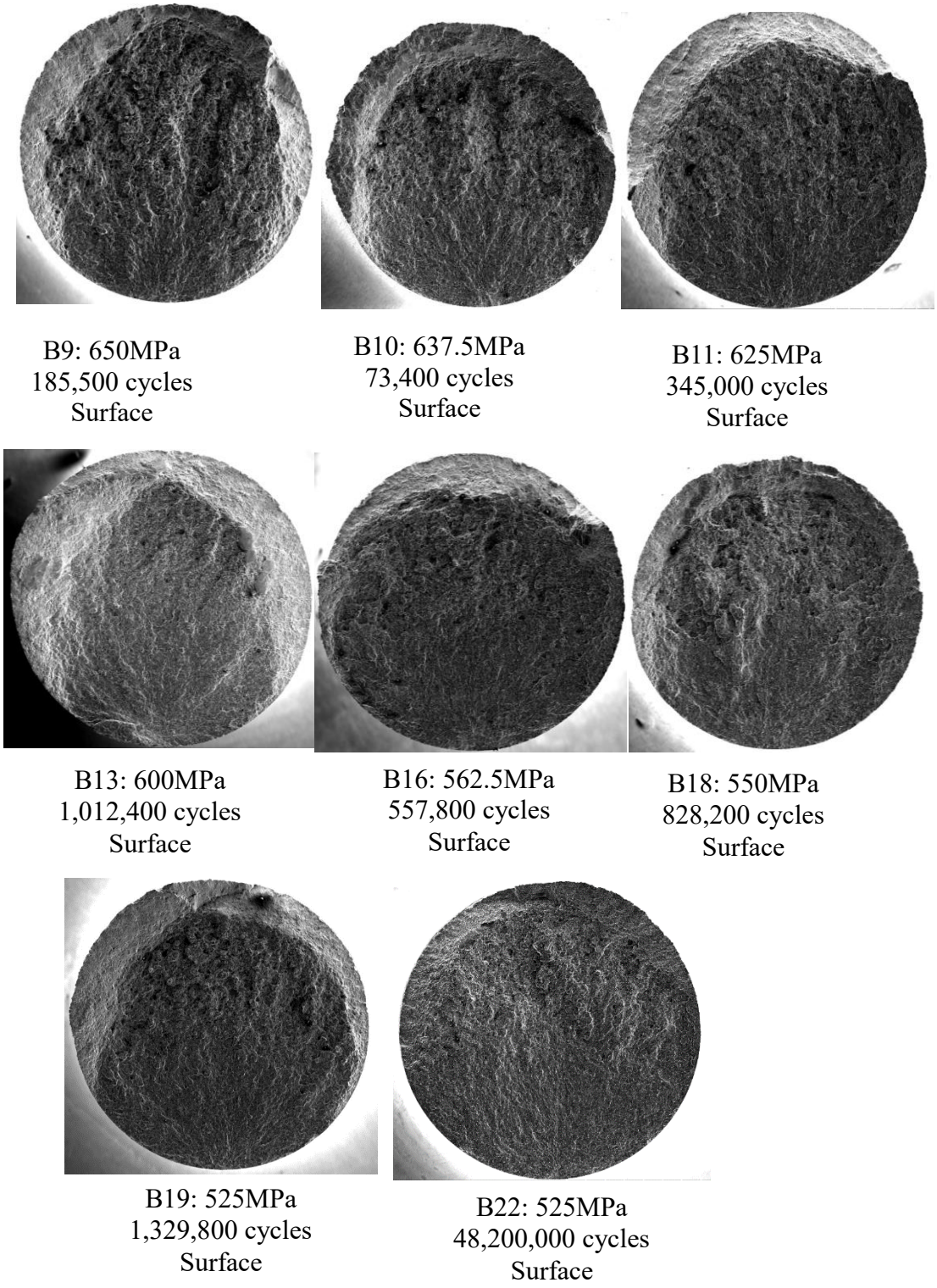

Figure 4.42: Ti-6-4 pancake forged HCF fracture surfaces.

Higher magnification images focused at the centre of the crack initiation sites are displayed below.

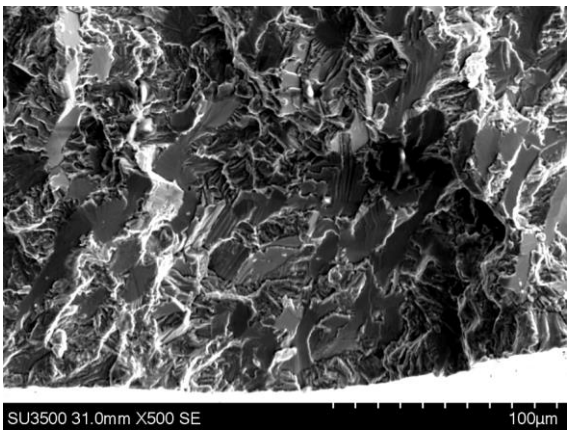

B10: 637.5MPa
73,400 cycles
Surface

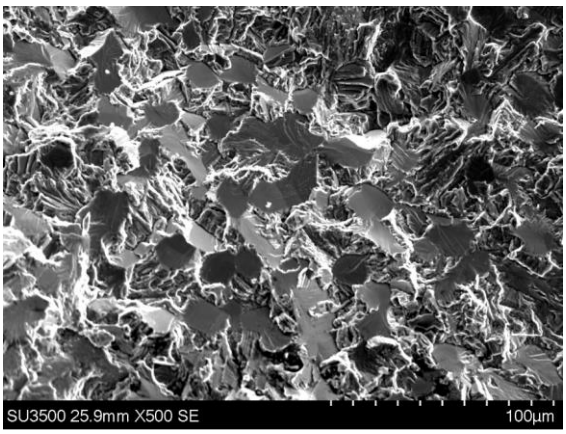

B13: 600MPa
1,012,400 cycles
Surface

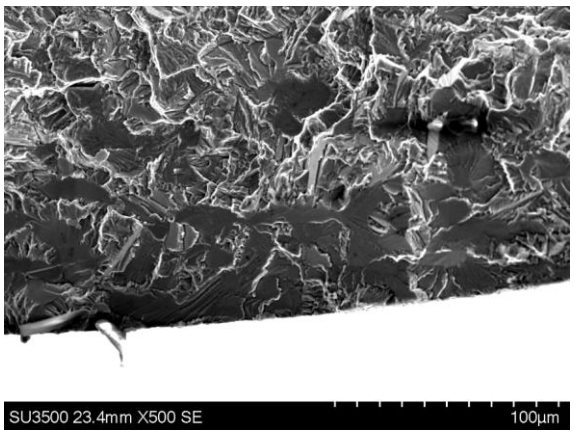

B16: 562.5MPa
557,800 cycles
Surface

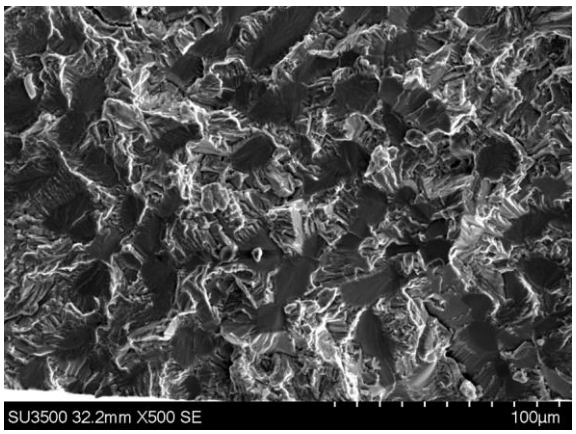

B18: 550MPa
828,200 cycles
Surface

Figure 4.43: Ti-6-4 HCF crack initiation sites.

4.4.6.3 Ti-407 LCF

The images in Figure 4.44 show the fracture surfaces from the Ti-407 LCF testing. All initiation sites were surface.

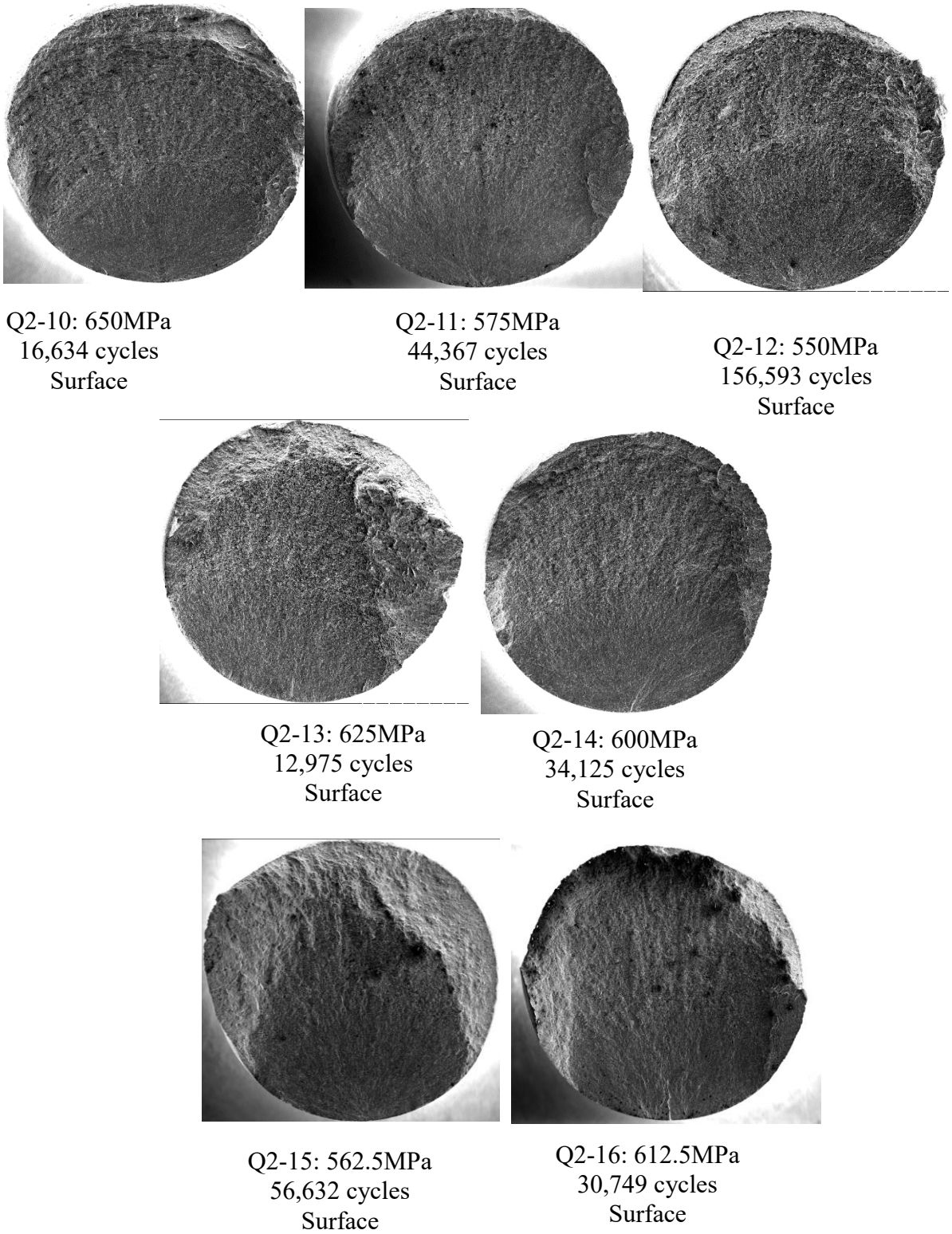

Figure 4.44: Ti-407 LCF fracture surfaces.

4.4.6.4 Ti-407 Dwell

The images in Figure 4.45 show fracture surfaces from two of the dwell tested specimens.

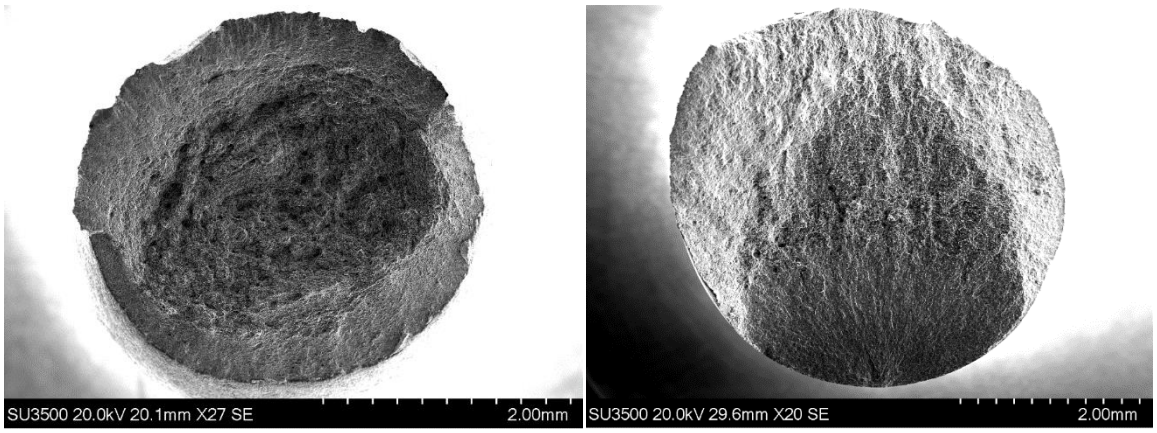

A1: 650MPa
547 cycles

A3: 550MPa
45,409 cycles

Figure 4.45: Dwell tested fracture surfaces

The fracture surface of A3 looks more standard for a fatigue test, but a high level of deformation is seen on fracture surface A1. This was tested at 650MPa, just above the measured yield of this material. Figure 4.46 below helps to emphasise this level of deformation. Referring to Figure 4.38, the very short life compared to the points tested at lower stress levels below the yield strength can be explained by the high levels of plastic deformation, resulting in a gradual increase in the applied true stress.

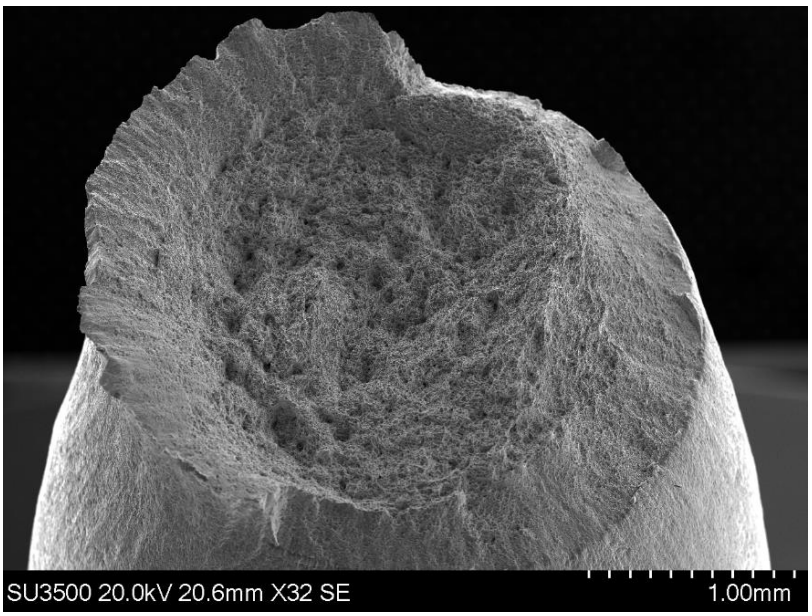

Figure 4.46: Test piece A1: 650MPa completing 547 cycles under dwell loading.

4.4.1 Texture Characterisation

The following section displays the texture measured from the Ti-407 and Ti-6-4 forged pancake material.

4.4.1.1 Ti-407

Figures 4.47 and 4.48 show IPF texture maps across the cross section of two Ti-407 pancake test pieces. The corresponding pole figures are displayed in Figure 4.49 and 4.50, respectively

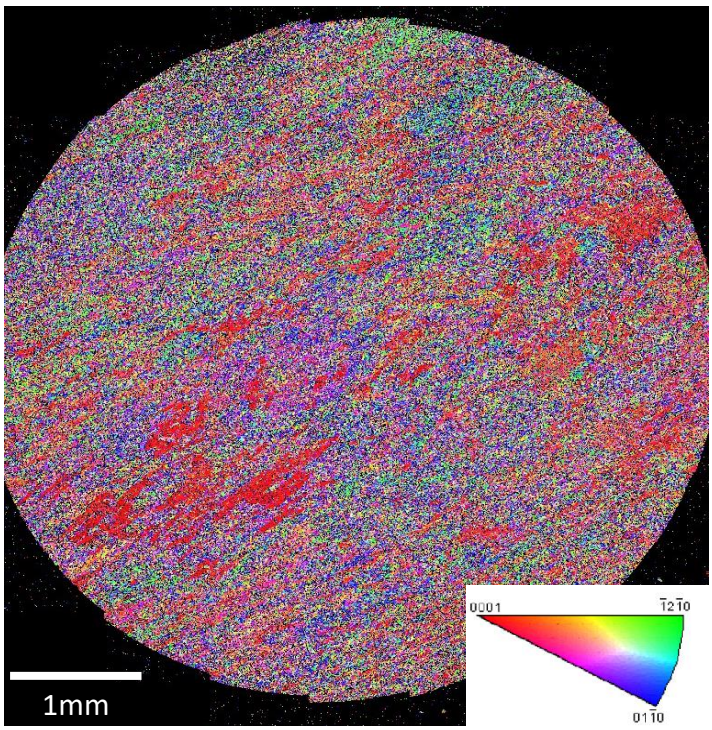

Figure 4.47: Inverse pole figure (IPF) map for Ti-407 forged pancake material. Test piece Q2-14 tested at 600MPa under LCF conditions completing 34,125 cycles.

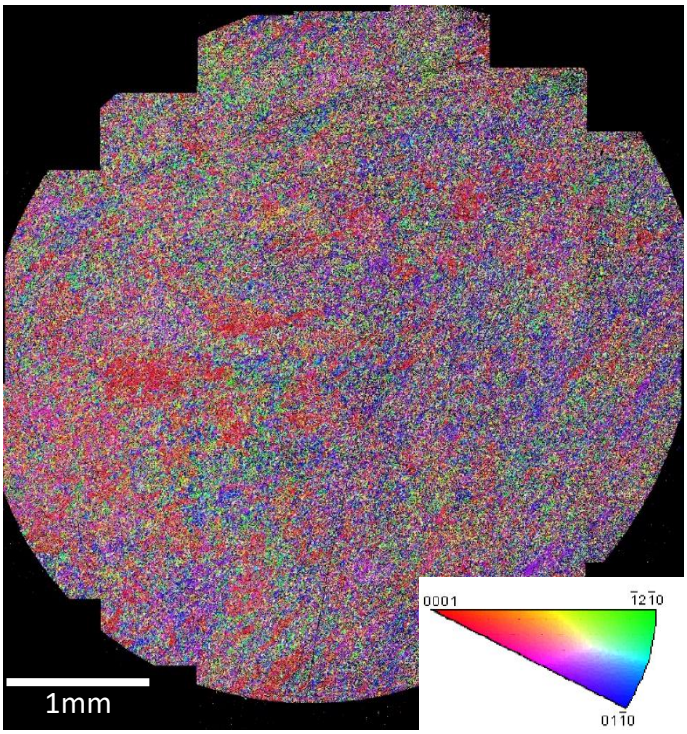

Figure 4.48: Inverse pole figure (IPF) map for Ti-407 forged pancake material. Test piece Q1-2 tested at 575MPa under HCF conditions completing 4,175,000 cycles.

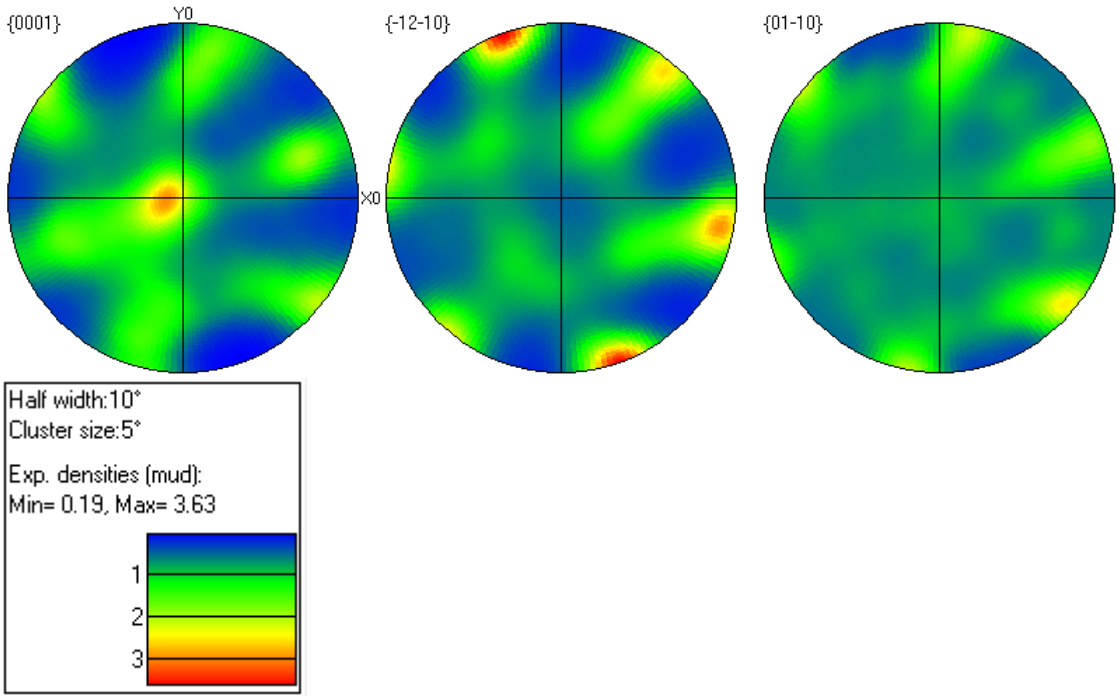

Figure 4.49: Pole figure associated with Figure 4.47.

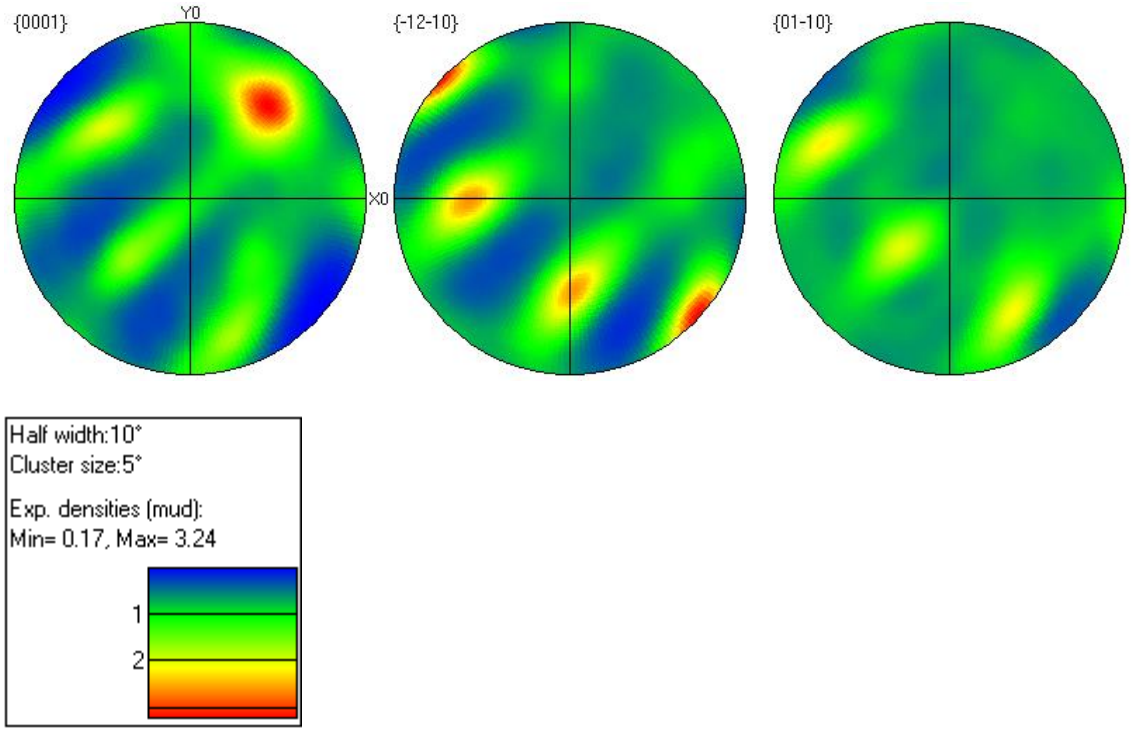

Figure 4.50: Pole figure associated with Figure 4.48.

4.4.1.2 Ti-6-4

A texture comparison was generated through EBSD on the Ti-6-4 material. The resulting IPF map is shown in Figure 4.51 and the corresponding pole figure in Figure 4.52.

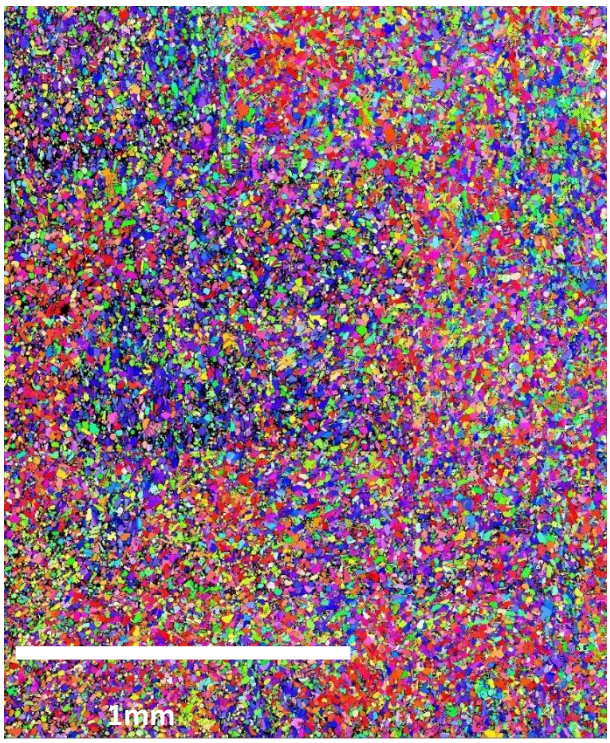

Figure 4.51: Ti-6-4 forged pancake material IPF map.

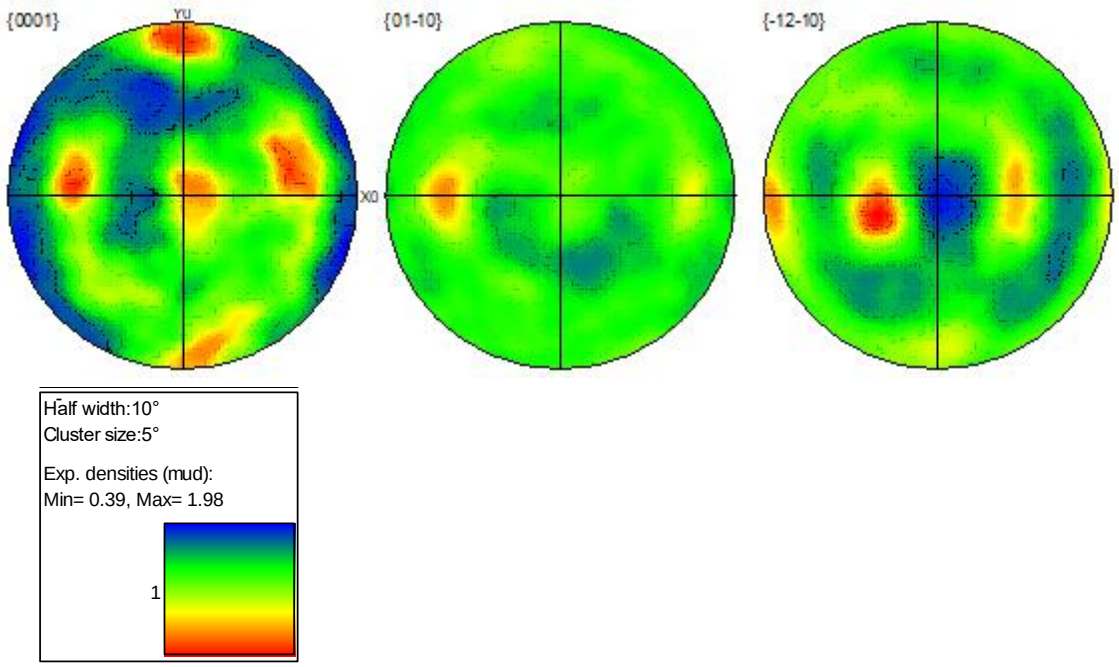

Figure 4.52: Pole figure associated with Figure 4.51.

As can be seen by comparing maximum texture intensities, Ti-6-4 shows a lower texture level than Ti-407.

4.4.2 Ti-407 Forged Pancake Material Strain Controlled Testing

The following results show the response of the stress during strain controlled testing. Strain controlled testing was carried out using three different frequencies, 0.25Hz trapezoidal, 3Hz sine and 0.008Hz 120s dwell, in order to determine if there were any differences in response based on frequency.

4.4.2.1 0.25Hz Trapezoidal waveform strain controlled step test

As mentioned is section 3.3.3, the strain range was stepped up every 10,000 cycles in order observe the response of the stress as the stain is increased, and also to enable a cyclic stress strain curve to be plotted, shown in Figure 4.55. Figure 4.53 below displays the results from the 0.25Hz strain controlled test.

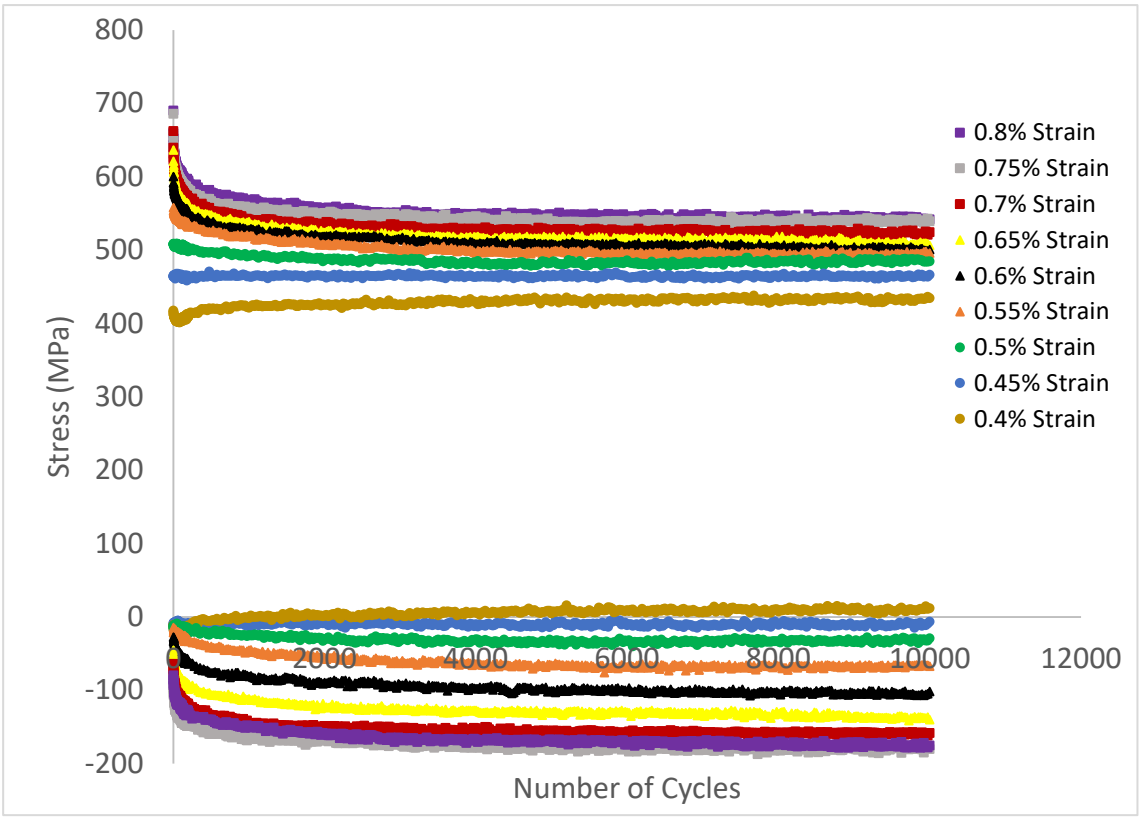

Figure 4.53: Plot of maximum and minimum stress versus cycles for Ti-407 - stepped strain controlled test using a 0.25Hz trapezoidal waveform

Figure 4.54 is replotted below focusing on just the maximum stress

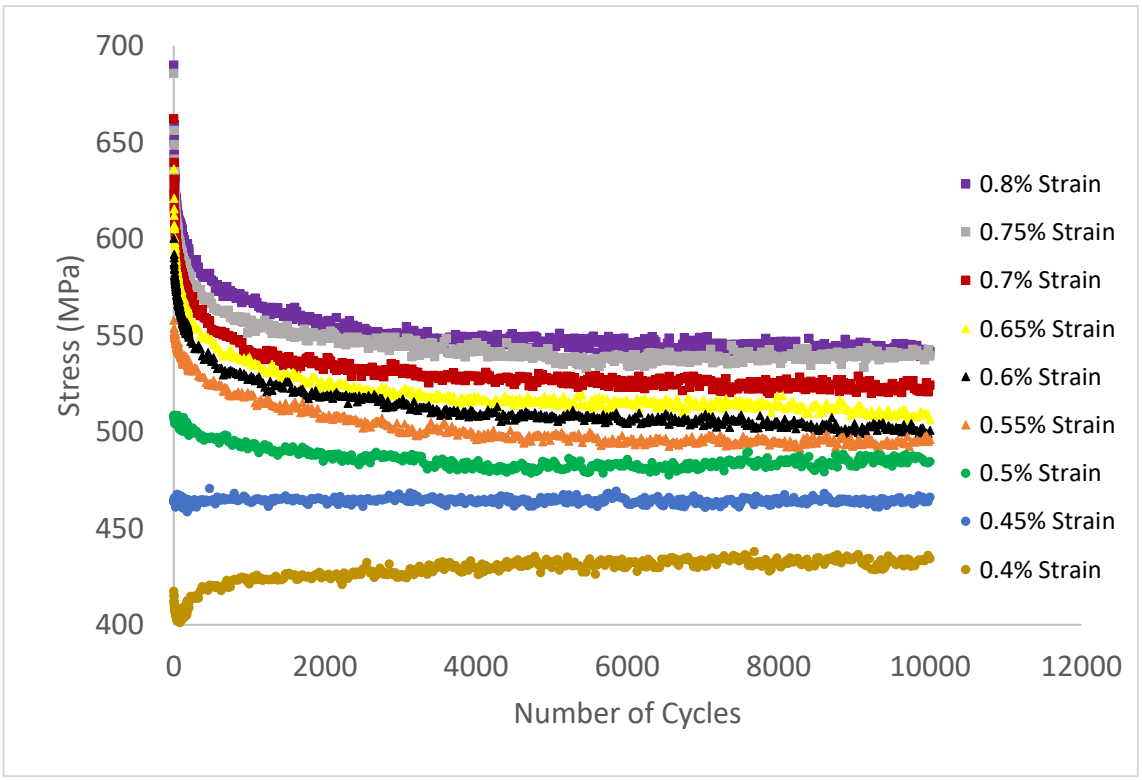

Figure 4.54: Maximum stress against cycle number for the stepped strain controlled test.

In general, the higher the strain, the more stress relaxation, but the more the specimen went into compression.

From this data the monotonic versus cyclic stress strain curve was plotted. The stress used for a given strain was taken at 6,000 cycles where the stress had stabilised.

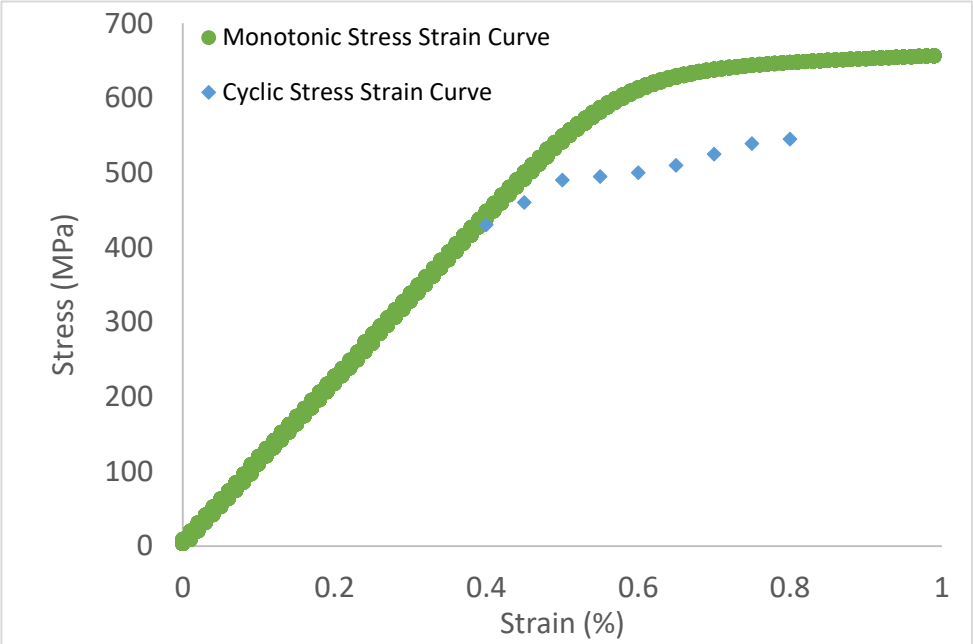

Figure 4.55: Ti-407 monotonic stress strain curve vs cyclic stress strain curve based on the trapezoidal 0.25Hz strain control stepped test.

Of note in Figure 4.54 is the hardening effect seen for 0.4% strain. For this reason, a further three steps on a second test piece, under the same waveform was conducted examining more closely strains of 0.3%, 0.35% and 0.45%. This was to see whether the alloy tended to harden at lower strains (Figure 4.56).

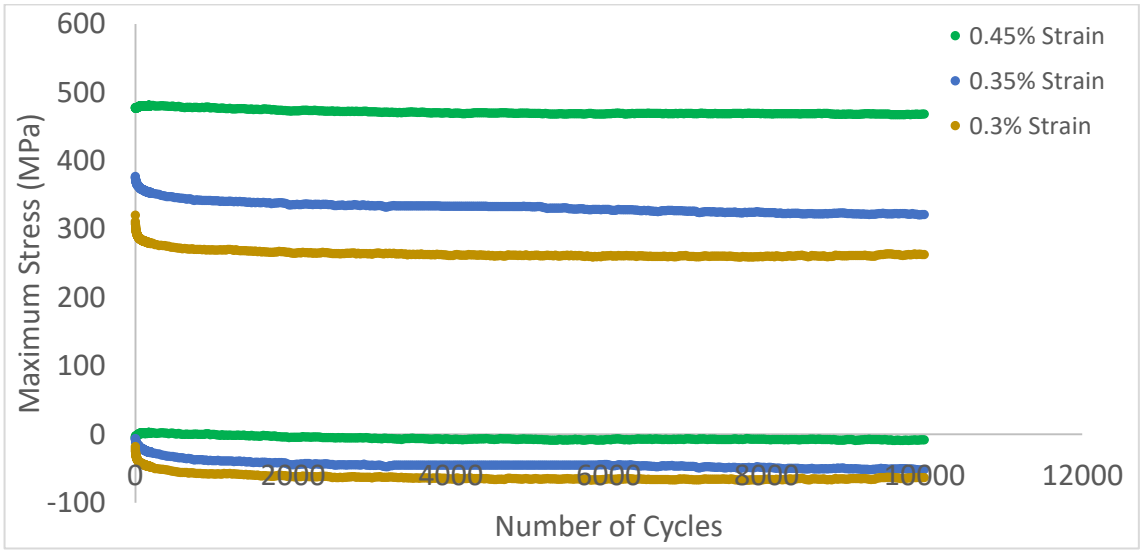

Figure 4.56: Ti-407 stress against number of cycles for low strains - 0.25 Hz trapezoidal waveform.

4.4.3 3Hz Strain Controlled Step Test

The graph below plots the stress level against cycle number for a 3Hz sine wave. This time the tests were run for 100,000 cycles so that the test time was similar to that of the 0.25Hz tests.

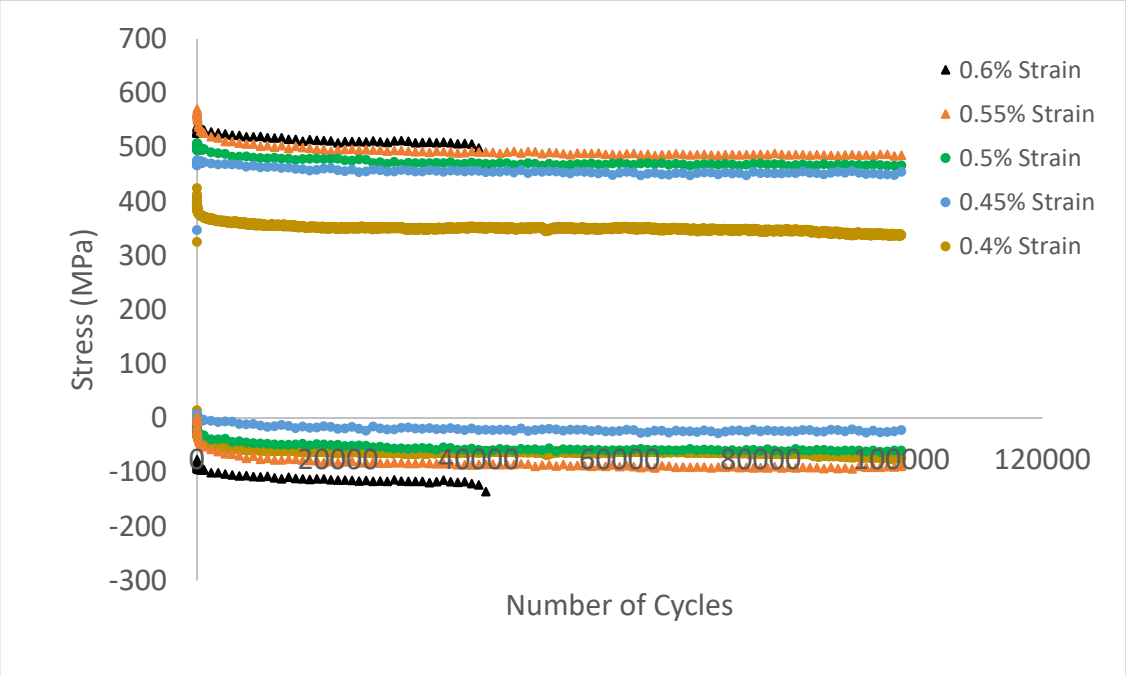

Figure 4.57: Ti-407 3 Hz sine waveform strain controlled step tests. Plots of stress against number of cycles.

Again the graph is replotted with just the maximum stress to pick up more detail on the response of the stress, Figure 4.58.

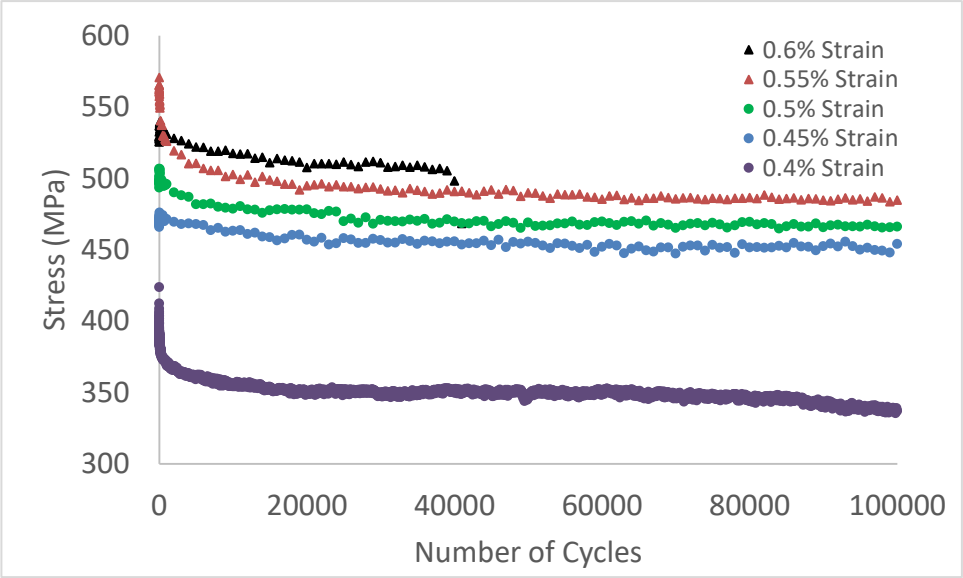

Figure 4.58: Maximum stress against cycle number for the 3 Hz sine wave stepped strain-controlled test.

4.4.4 Dwell Strain Controlled Step Test

Dwell strain controlled tests were also conducted to examine the effect on stress relaxation with a 120 second hold at maximum strain. Unfortunately, the extensometer kept slipping during this set of testing which meant it was difficult to generate reliable data. However, from the data generated, cyclic softening was observed from the first cycle.

4.4.5 Fatigue crack growth results

The combined fatigue crack growth data measured from Ti-407 specimens are plotted in Figure 4.59. This illustrates a relatively consistent response for cracks growing under the Stage II Paris regime. This would suggest that the fatigue crack growth rate of Ti-407 is insensitive to heat treatment temperature, associated microstructure and mean stress. Indeed, the data set can be described by a single power law fit, with the Paris coefficients m=2.934 and C=5e^{-11} respectively.

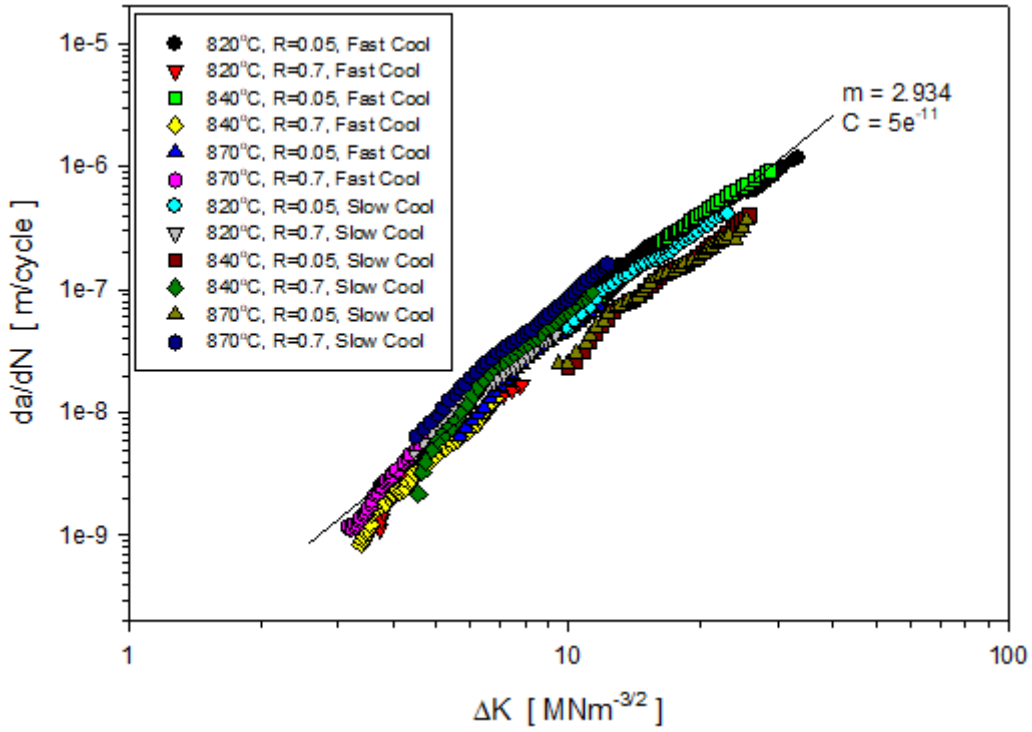

Figure 4.59: Combined fatigue crack growth data for Ti-407 assessed in six different microstructure conditions and two R-ratios.

Whilst combined fatigue crack growth data plotted together shows no correlation in crack growth rate against microstructure of R-ratio, the individual microstructural conditions (for example fast cool versus slow cool for the same heat treatment temperature) were compared to see if any more sensitive relationships could be found. These are displayed below.

4.4.5.1 Effect of Cooling Rate on Crack Growth Rate

The plots in Figure 4.60 compare more closely the cooling rate for the same primary alpha volume fraction and stress ratio to see if there is any discernable correlation between the thicker alpha laths generated from the slower cooling and crack growth rate.

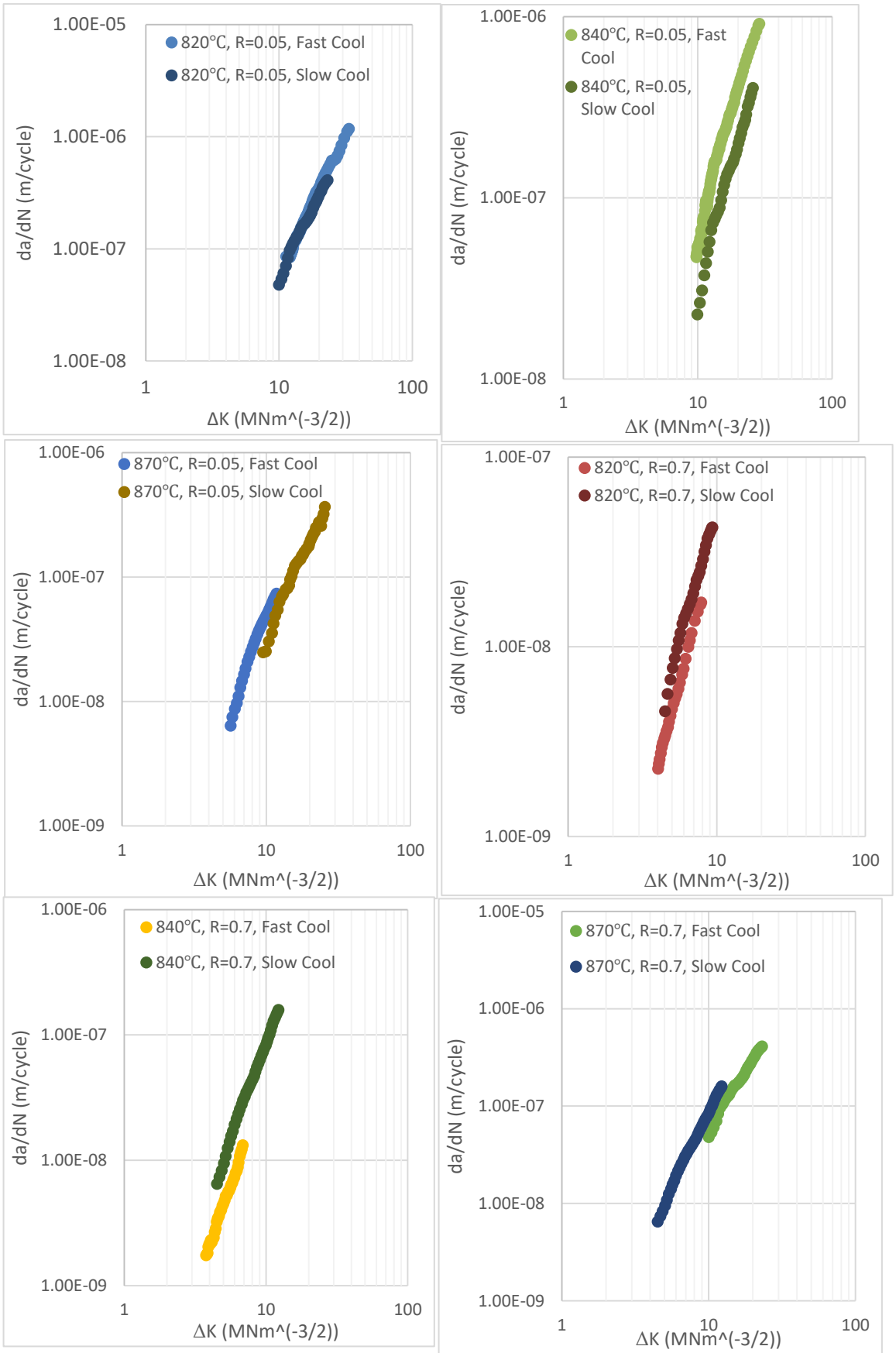

Figure 4.60: Fatigue crack growth rate plots comparing the effect of cooling rate for a constant primary alpha volume fraction and stress ratio for pancake forged Ti-407.

In two out of the six cases the slow cool demonstrated a marginally slower crack growth rate. In three of the six cases the fast cool demonstrated a slightly slower growth rate. In the R=0.05 820℃ case, the points were effectively on top of one another. There is no obvious correlation among these results.

4.4.5.2 Effect of Primary Alpha Volume Fraction

In the next four plots the effect of primary alpha volume fraction on crack growth rate, for the same cooling rate and same stress ratio, is displayed.

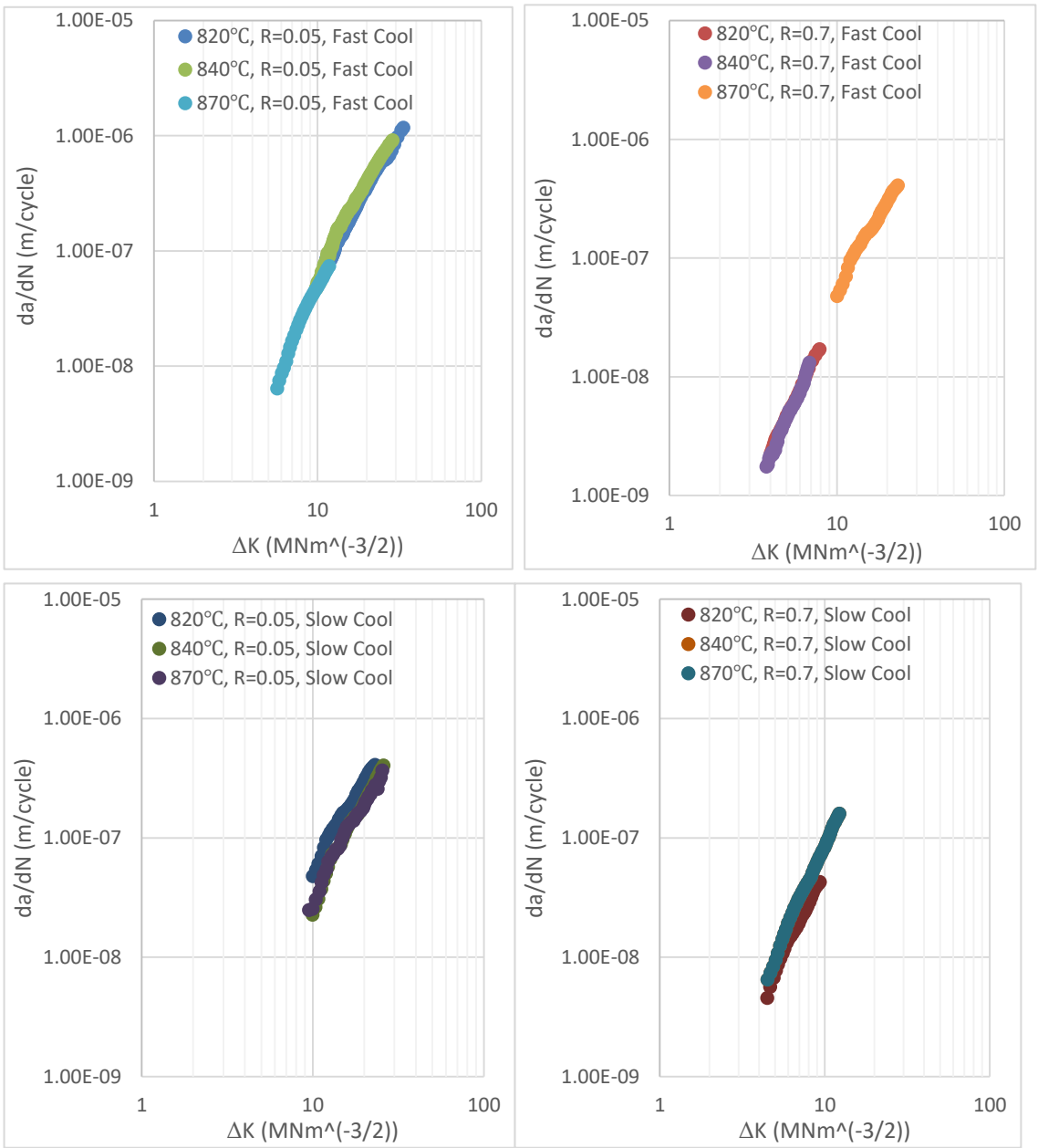

Figure 4.61: Plots of fatigue crack growth rate comparing the effect of primary alpha volume fraction for pancake forged Ti-407 material.

For the plots above, 820℃ correlates to 50% primary alpha volume fraction, 840℃ to 30% and 870℃ to 15%. Images of the microstructures were displayed in Figure 3.18.

Once again, no correlation is found when comparing the effect of primary alpha volume fraction in the range of 20–50%. Relative to the comparison of the effect of secondary alpha lath width, the data seems to sit even more closely together, implying that of the two parameters compared, it is the alpha lath width that crack growth rate would be most sensitive to.

4.5 Ti-407 Pancake Data vs Manufacturer 2 Ring Rolled Data

Figures 4.62 and 4.63 compare the pancake fatigue behaviour to the ring rolled manufacturer 2 data. Relative to the tangentially orientated specimens, the pancake offers superior strength under both LCF and HCF loading directions, though this difference is more pronounced under HCF loading conditions.

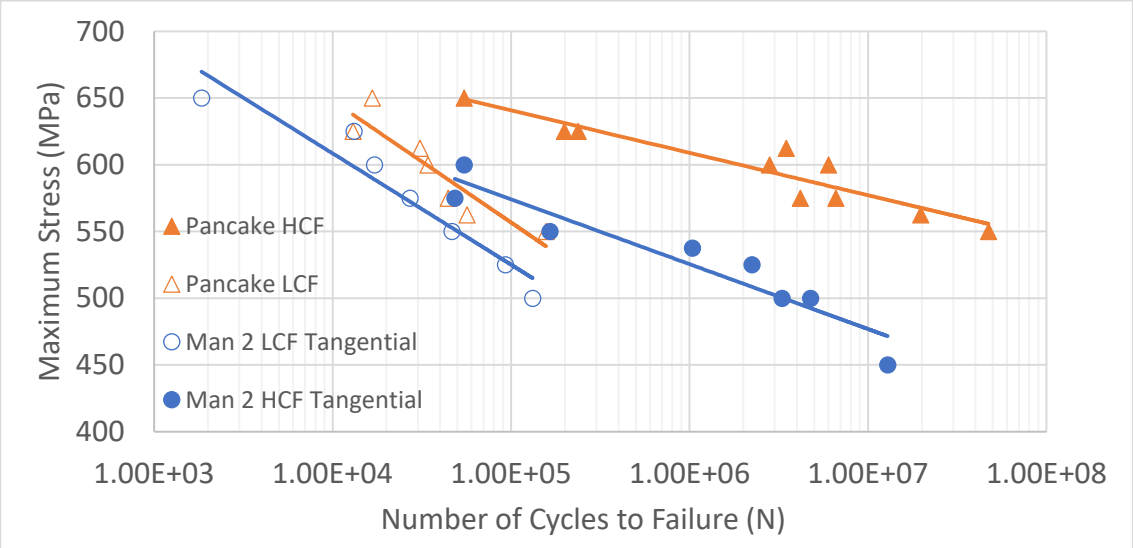

Figure 4.62: Ti-407 pancake data vs tangential manufacturer 2.

The axially orientated specimens from the manufacturer 2 ring rolled block actually offer a slightly superior performance under LCF loading conditions but the pancake and axial results under HCF loading sit on the same curve.

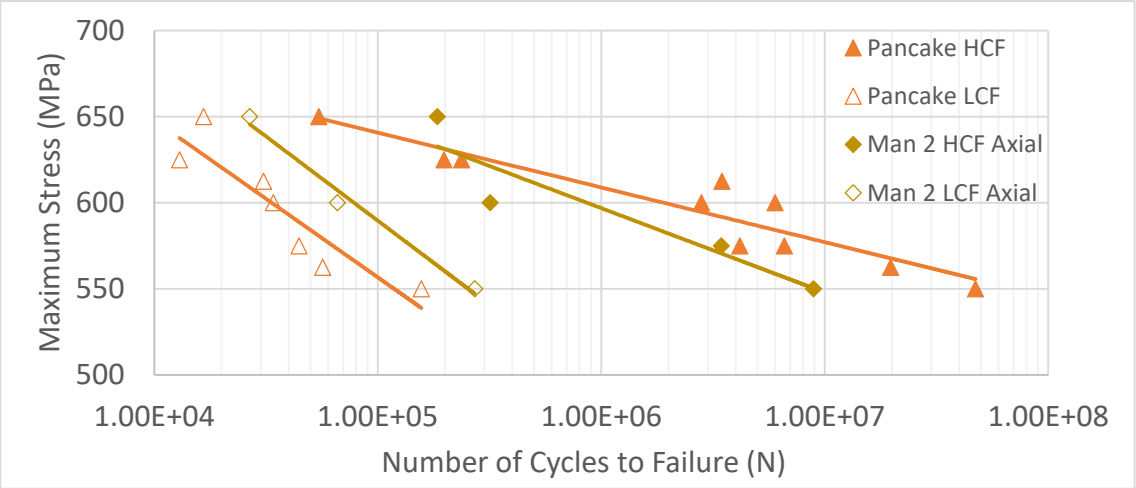

Figure 4.63: Ti-407 pancake vs axial manufacturer 2.

4.6 Ti-407 Pancake vs Manufacturer 1 Ring Rolled Data

Figure 4.64 compares the combined fatigue data from the pancake material against the manufacturer 1 ring rolled material. Under both HCF and LCF loading conditions, the pancake forged test pieces display slightly superior strength but this is more pronounced under HCF loading where there is a 50MPa difference for lives to 10 million cycles.

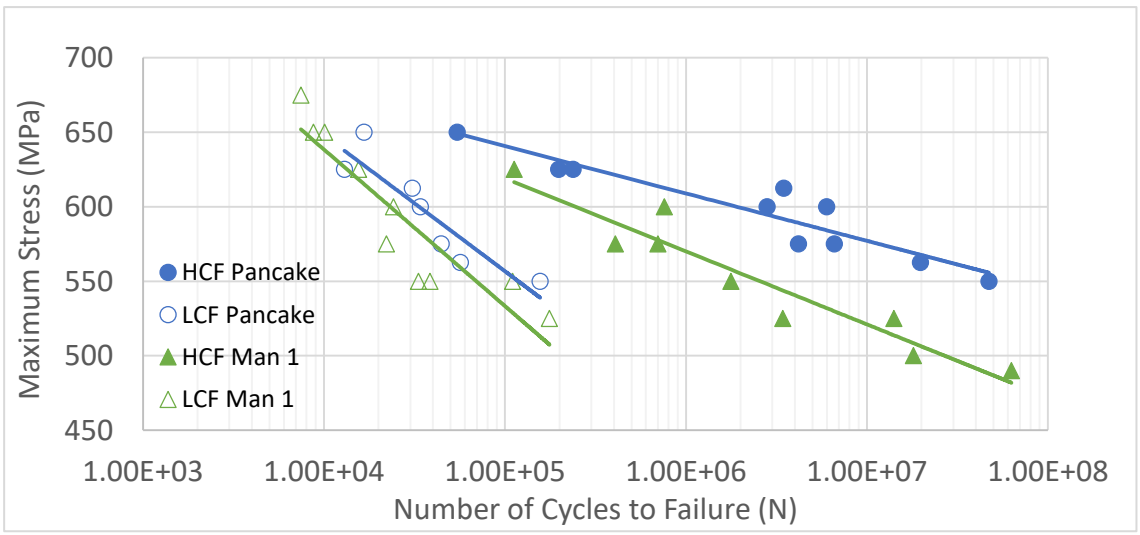

Figure 4.64: Comparison of Ti-407 pancake fatigue data against manufacturer 1 ring rolled data.

4.7 Ti-412 Pancake Forged Data

The final main batch of testing was carried out on Ti-412, a derivative of Ti-407 with a 100MPa strength increase coming from an increased vanadium content. In section 3.2.3 it was mentioned that contrary to the Ti-407 heat treatments, the Ti-412 pancake was heat treated prior to the extraction of the blanks. This resulted in a difference in the microstructure between the centre and the edge.

4.7.1 Ti-412 Microstructure and Chemistry Characterisation

Figure 4.65(a) displays a representative image of the Ti-412 microstructure, at the same scale as the other material products previously discussed. Due to the increased vanadium content, see Table 4.11, the primary alpha grain size is significantly smaller than Ti-407. In order to define the detailed morphology of the individual grains, a higher magnification image is presented in Figure 4.65(b). Key microstructural parameters are summarised in Table 4.10 and compared with the Ti-407 pancake parameters. The chemical composition is defined in Table 4.11.

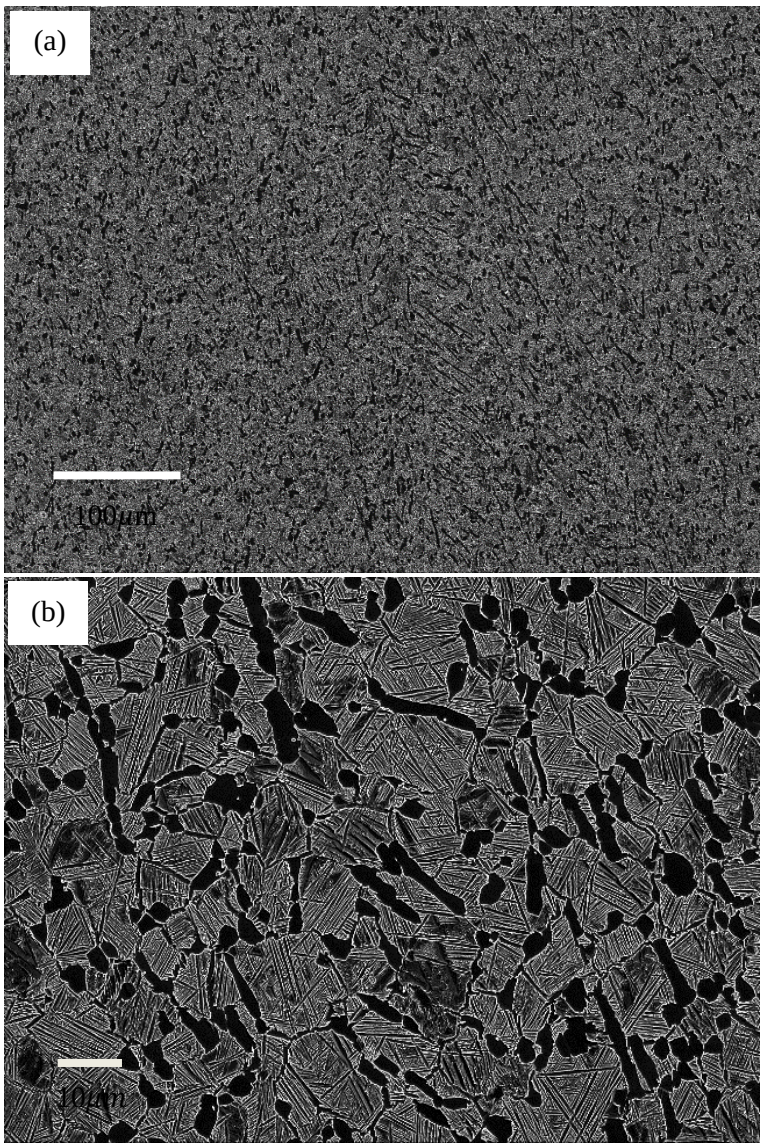

Figure 4.65: SEM secondary electron images of etched Ti-412 microstructure (a) Same magnification as previously displayed material (b) Higher magnification to observe grain morphology.

There was a relatively even split across the microstructure between equiaxed and elongated primary alpha grains. The elongated grains had a diameter of between 2.5–5 μm and the elongated grains had a width of 1–3 μm and a length of up to 40 μm. Relative to the other material seen so far, the secondary alpha laths were slightly finer with an average width of roughly 0.4 μm. The volume fraction was a little lower than the other forms with roughly 20% primary alpha.

Table 4.10: Key microstructural parameters of the Ti-412 material

	Ti-412	Ti-407
Primary alpha volume fraction (%)	20	30
Primary alpha grain diameter μm (equiaxed area)	3	10
Primary alpha grain length max μm Elongated area	40	-
Primary alpha grain width μm (elongated area)	2	-
Secondary alpha lath width μm	0.4	0.5-0.8

Table 4.11: Chemical composition of Ti-412

Ti-412 forged Pancake	**Bulk chemistry (wt %)**	**Primary alpha grain (wt %)**	**Beta grain (wt %)**
Al	1.03	1.51	0.99
V	6.8	1.54	7.47
Si	0.18	0.15	0.28
Fe	0.7	0.03	0.76

4.7.2 Tensile Data

Two tensile tests were conducted from the Ti-412 pancake. The data is presented in Table 4.12, along with the pancake data for Ti-407 and Ti-6-4 for a comparison.

Table 4.12: Tensile data for Ti-412 along with the tensile data for Ti-407 and Ti-6-4.

Tensile results					
	Young's Modulus (GPa)	0.2% Proof Stress (MPa)	UTS (MPa)	Elongation after Fracture (A %)	Reduction in Area (%)
Ti-412					
1	107	744	864	18.5	67
2	102	788	875	14.67	63
Average	104.5	766.0	869.5	16.6	65.0
Ti-407					
1	114	647	764	18.06	62
2	114	651	718	19.63	57
3	114	646	714	20.16	55
Average	114.0	648.0	764.0	19.3	58.0
Ti-6-4					
1	117	915	1035	12.28	33
2	114	914	1037	12.65	54
3	115	912	1031	13.67	33
4	118	917	1040	13.04	38
Average	116.0	914.5	1035.8	12.9	39.5

Ti-412 has a 14% stronger UTS compared to that of Ti-407 and yet maintains a similar ductility. The Young's modulus is actually slightly lower than that of both Ti-407 and Ti-6-4. There is an 11MPa difference in the UTS of the two Ti-412 tensile specimens, and a 44MPa difference in the yield. In section 3.1.6 it was mentioned that the first specimen came from the centre and the second from the edge, so the difference in mechanical properties is likely related to this. This difference is examined is slightly more depth in the discussion section. The stress strain curve is displayed in Figure 4.66 below.

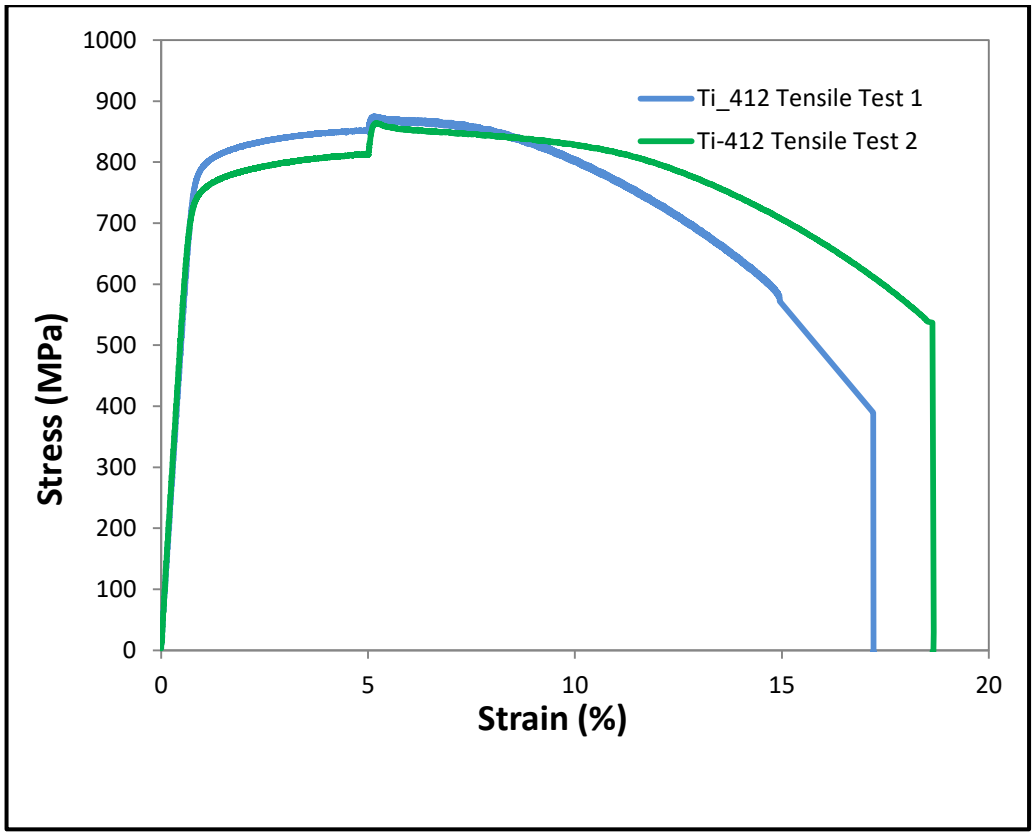

Figure 4.66: Stress strain curve of the two Ti-412 tensile tests.

4.7.3 Fatigue Data

Figure 4.67 below plots the combined HCF and LCF fatigue data of Ti-412 alongside the Ti-407 data. As can be seen, the Ti-412 data has superior fatigue strength but shares the same characteristic as the Ti-407 data with more than an order of magnitude difference at the low end of the LCF and HCF curve. For the high cycle fatigue data, surface (hollow points) and subsurface (filled points) initiations are differentiated showing half of the Ti-412 points to have initiated subsurface. Comparing Ti-412 and

Ti-407, the HCF curve indicates a 125MPa superior strength at 10 million cycles and the LCF curves indicate a 160MPa increase for Ti-412 at 100,000 cycles. Ti-412 dwell testing was also carried out. As can be seen, the inclusion of a 120 second hold has little effect on the specimen life. It should be noted that the Ti-412 test at 675MPa was terminated early due to a fault with the fatigue test rig, the test piece did not fail.

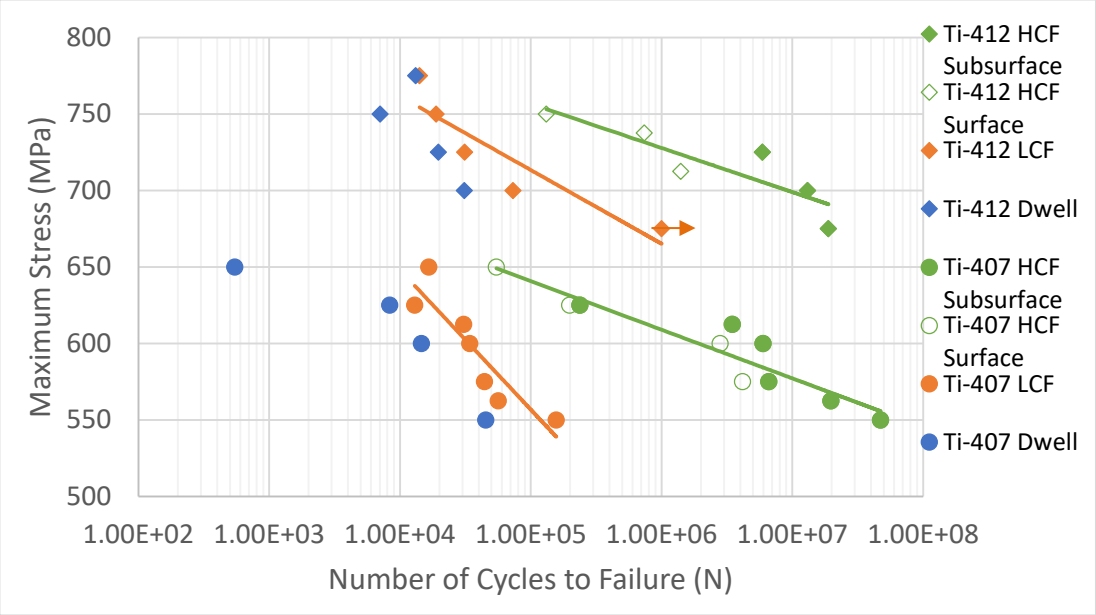

Figure 4.67: Ti-412 HCF and LCF and dwell data plotted with the Ti-407 pancake fatigue data.

Figure 4.68 compares the HCF and LCF data of Ti-407, Ti-412 and Ti-6-4. This highlights the difference in fatigue characteristics between Ti-6-4, and Ti-407 and Ti-412 across the two regimes.

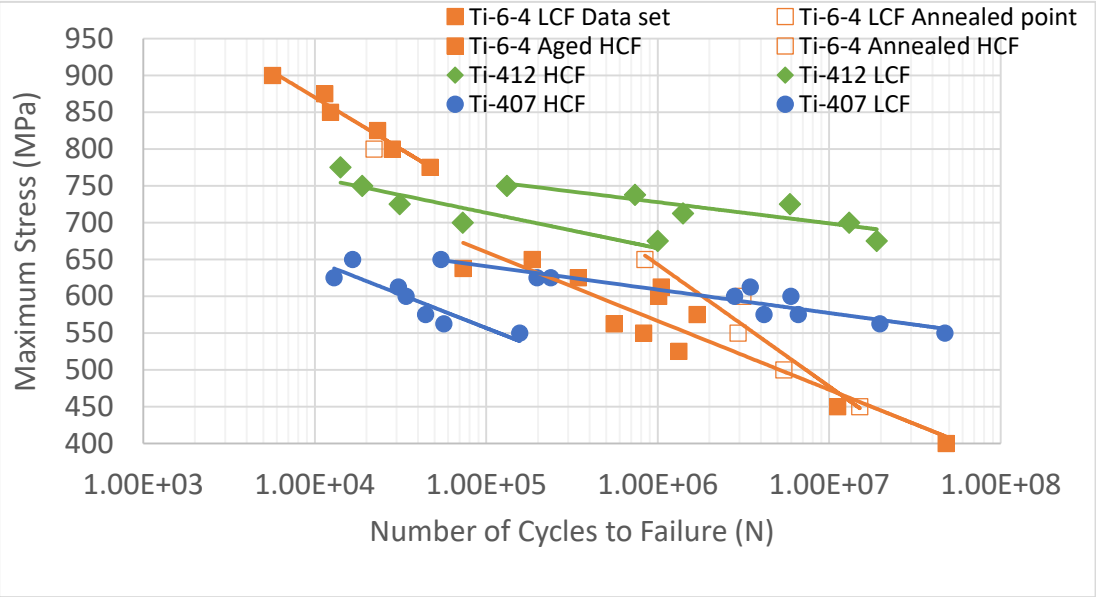

Figure 4.68: Combined plot of Ti-6-4, Ti-412 and T-407 pancake fatigue data.

4.7.4 Ti-412 Fractography

The fractography results for the HCF test pieces are presented in Figure 4.67. Similar to the Ti-407 pancake fracture surfaces, a mixture of surface and subsurface initiation sites are seen for the HCF fracture surfaces. For LCF and dwell tests, surface initiations were exclusively seen. Images are not included.

4.7.4.1 Ti-412 HCF Fractography

The Ti-412 HCF fracture surfaces are displayed below in Figure 4.69. Subsurface initiations are highlighted inside the circles.

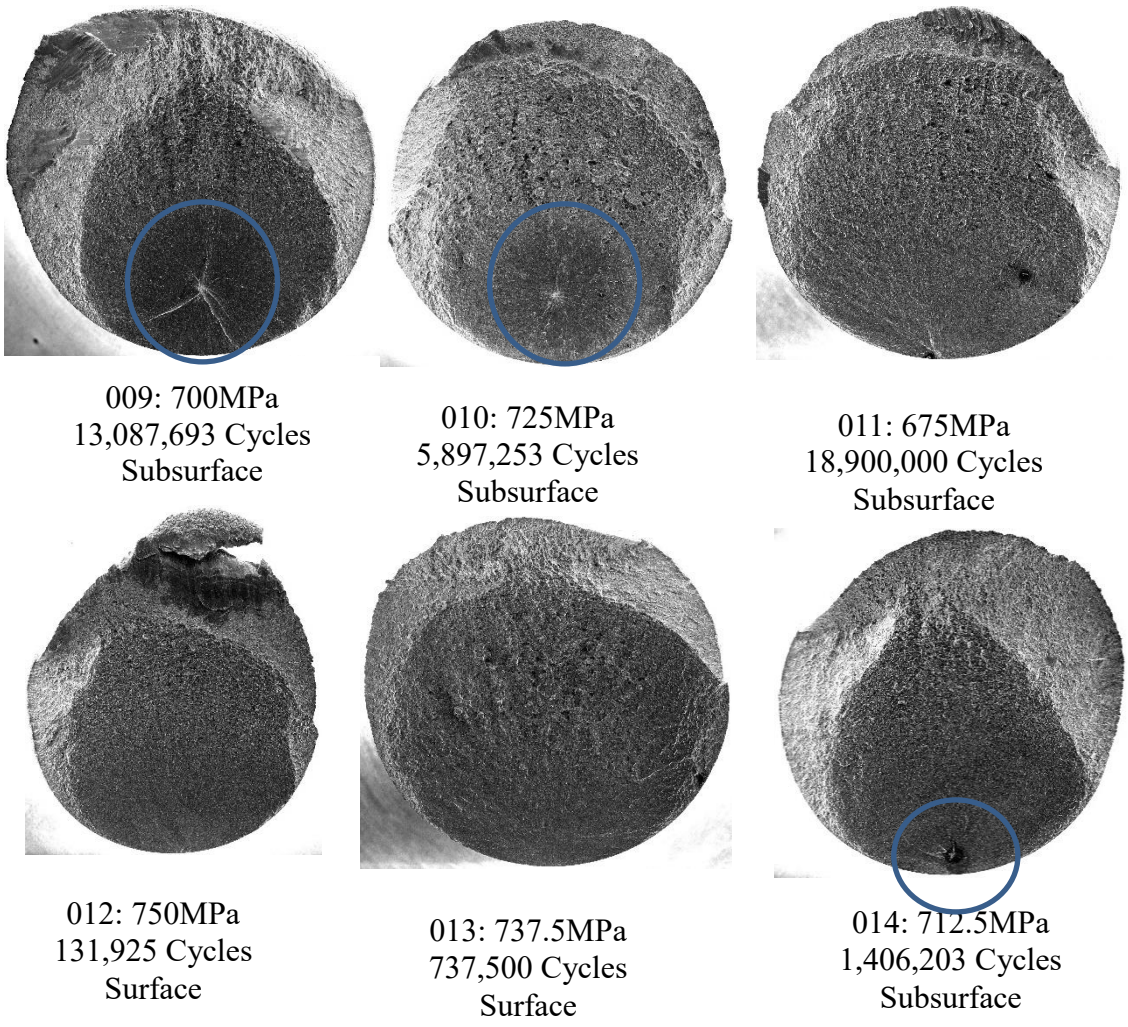

Figure 4.69: Ti-412 HCF Fractography

4.7.5 Ti-412 Texture

An IPF texture map and pole figure are displayed below in Figures 4.70 and 4.71. Unfortunately, due to time limitations the whole cross section was not captured. However, the area displayed was large enough to capture the general texture.

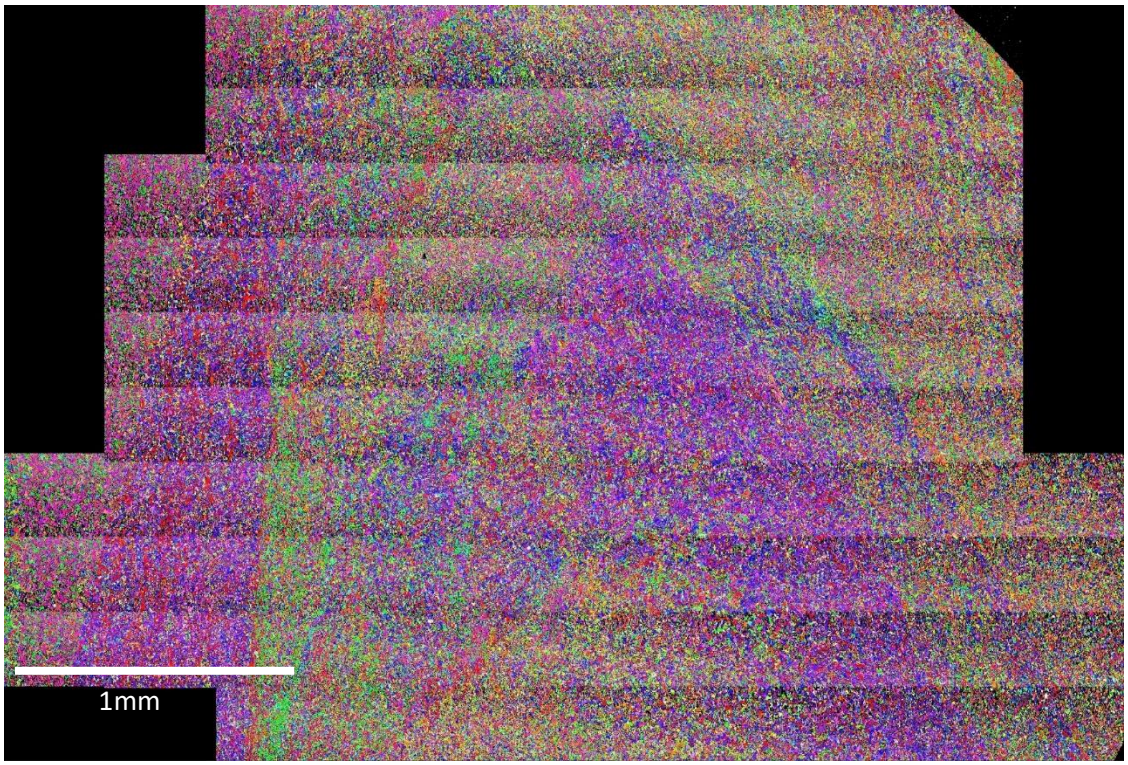

Figure 4.70: Ti-412 IPF texture map.

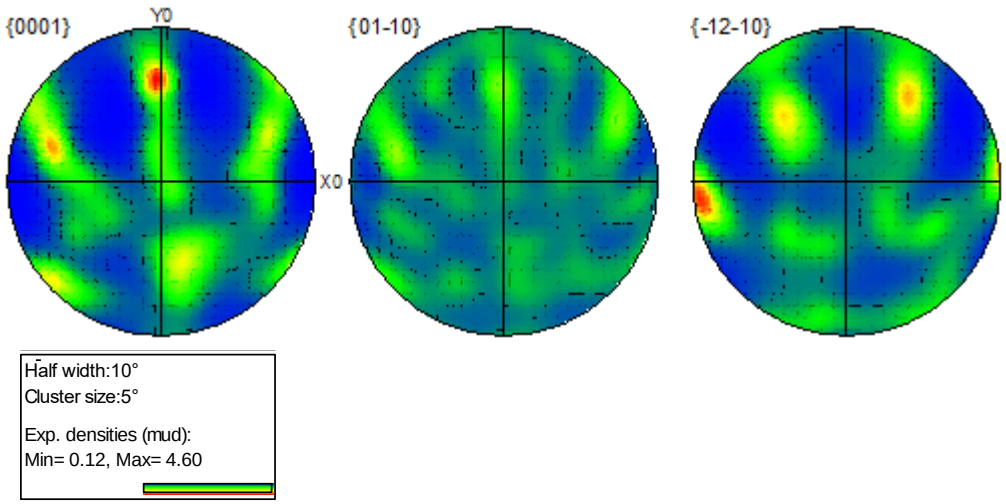

Figure 4.71: Pole figures corresponding to Figure 4.70.

The measured maximum texture intensity of 4.6 is about 28% higher than that for the Ti-407 forged pancake.

4.8 Comparison of Ti-407 Pancake Data Against Ti-834 Bar Stock Data

As a final comparison of product forms, some HCF testing was carried out on Ti-834 bar material. The microstructure and chemistry of Ti-834 are briefly summarised below. Figure 4.72 shows the microstructure, and Tables 4.13 and 4.14 shows the key microstructural parameters and chemical composition.

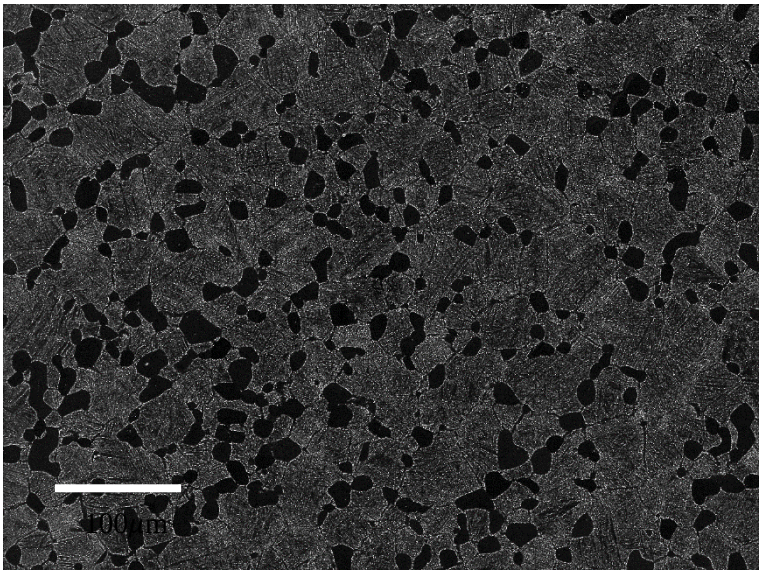

Figure 4.72: SEM secondary electron image of etched Ti-834 microstructure.

The primary alpha grains were, for the most part, of equiaxed morphology with the diameter varying from 10μm up to 30 μm. The volume fraction was roughly 25%. The secondary alpha lath structure was particularly fine with widths of 0.2–0.4 μm.

Table 4.13: Microstructural parameters of Ti-834

Primary alpha volume fraction (%)	25
Primary alpha grain diameter (μm)	10-30
Secondary alpha lath width (μm)	0.2-0.4

Table 4.14: Ti-834 chemical composition

Ti-834 bar stock	Bulk chemistry (wt %)	Primary alpha grain (wt %)	Beta grain (wt %)
Al	5.41	6.22	5.40
Sn	4.16	3.86	4.23
Zr	3.66	2.82	3.32
Nb	0.72	0.63	-
Mo	0.46	0.01	0.34
Si	0.33	0.30	0.36

4.8.1 Ti-834 Fatigue Data

The graph below in Figure 4.73 shows Ti-834 HCF (100Hz) data also plotted with 10Hz, 1Hz, 0.25Hz and 0.008Hz frequencies, data previously tested at the SMaRT laboratories [166]. As can be seen, the data across the whole range of frequencies used sit on a similar gradient with the exception of the two dwell tests at 975MPa and 1000MPa which are both considerably above the yield strength (roughly 930MPa). The intermediate frequencies, 1Hz and 10Hz, sit within the gap of the 100Hz HCF and 0.25Hz LCF of which there is roughly half an order of difference between.

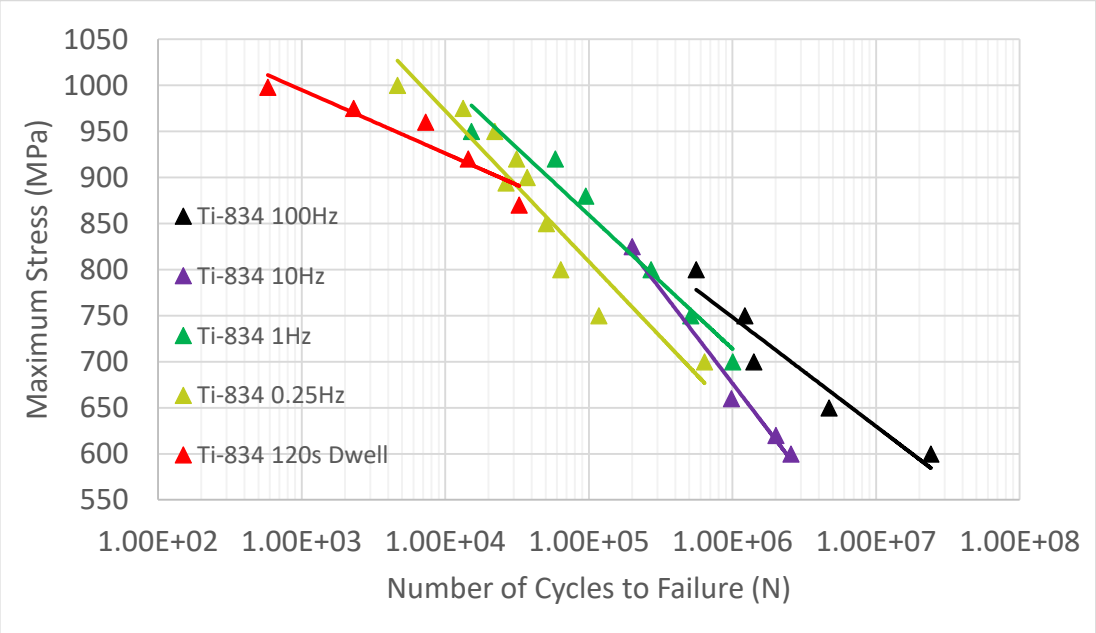

Figure 4.73: Combined fatigue data for Ti-834 bar stock.

Figure 4.74 below plots just the LCF and HCF data for Ti-412, Ti-407 and Ti-834. For Ti-407 and Ti-412 the characteristic change in gradient of the S/N curve is seen between the HCF and LCF loading regimes but for Ti-834 this gradient remains consistent.

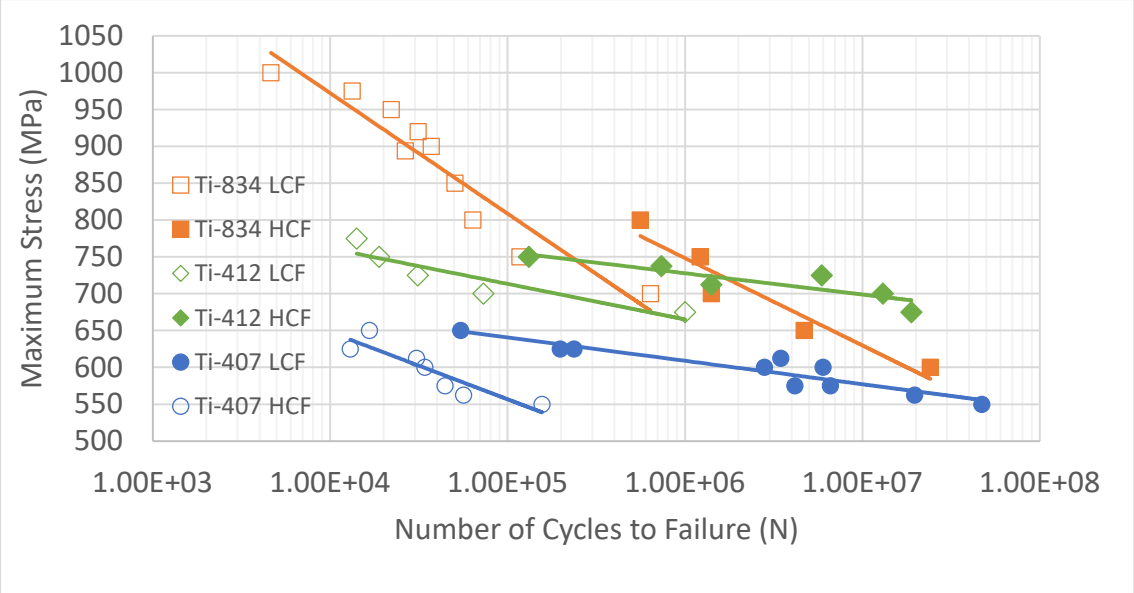

Figure 4.74: HCF and LCF comparison if Ti-407, Ti-412 and Ti-834.

The texture maps below (Figure 4.75 and 4.76) show the very low texture levels for Ti-834.

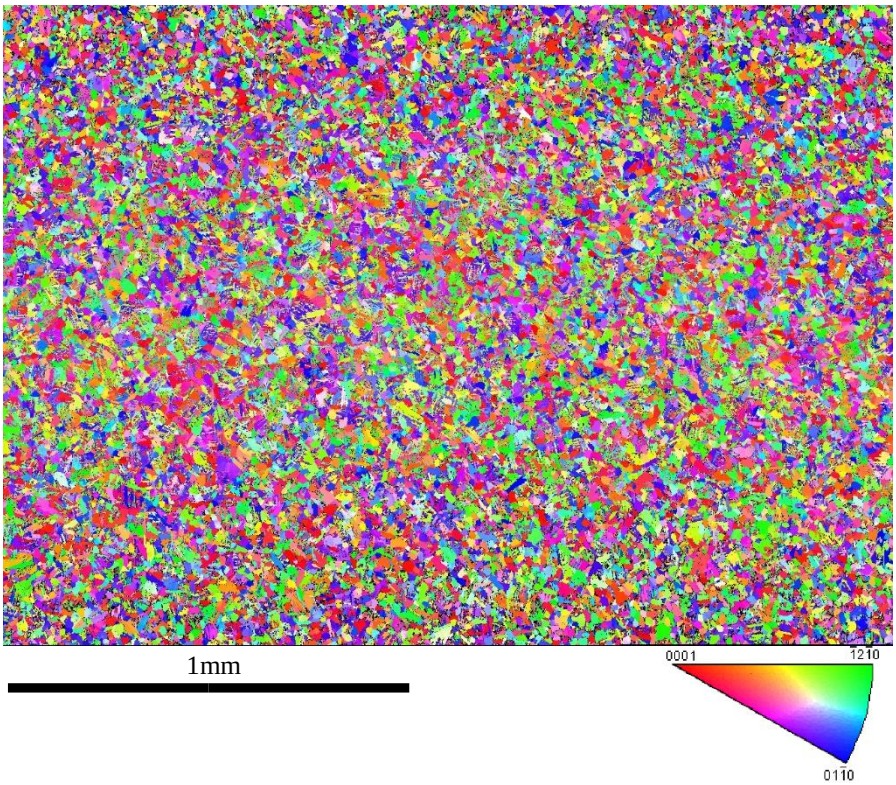

Figure 4.75: IPF map across the Ti-834 material.

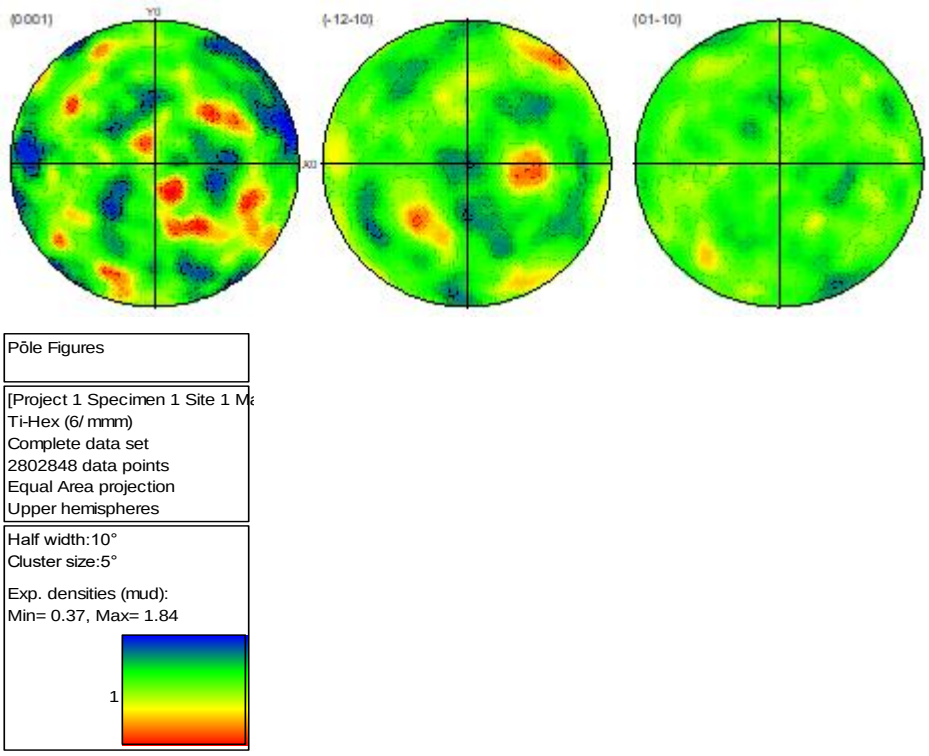

Figure 4.76: Poles figures associated with Figure 4.75.

4.9 Results of Facet Characterisation

Selected Ti-407 and Ti-412 specimens were analysed in more detail in order to better understand the initiating mechanism to help explain the impressive performance observed in the high cycle fatigue regime. Before presentation of the measurements described in section 3.6, some general discussion of relative frequency of surface and subsurface initiations amongst the high cycle fatigue test pieces, as well as facet size and morphology, is given. This section focuses on the Ti-407, Ti-412 and Ti-6-4 pancake forged material.

4.9.1 Ti-407 and Ti-412 HCF

Of the ten Ti-407 HCF tests, six revealed subsurface initiation sites, and four surface initiation sites. One of the six subsurface sites was near surface, but the faceted region was of similar size, morphology and spatial angle to the other subsurface initiations. For the Ti-412 material, of the six tests conducted, three revealed subsurface initiation sites and three surface initiation sites.

All of the subsurface initiation sites consisted of a cluster of facets. In previous research this has been found to be the result of crack initiating over a group of similarly orientated grains which provide a large continuous slip path. The group can effectively be seen to act as one grain. This was observed in the study by Jha et al on Ti-6246 [167] and by Sinah et al on Ti-6242 [168]. For the Ti-407 material, of the six subsurface initiations shown below in Figure 4.77, three consisted of long elongated grains and the other three of equiaxed grains.

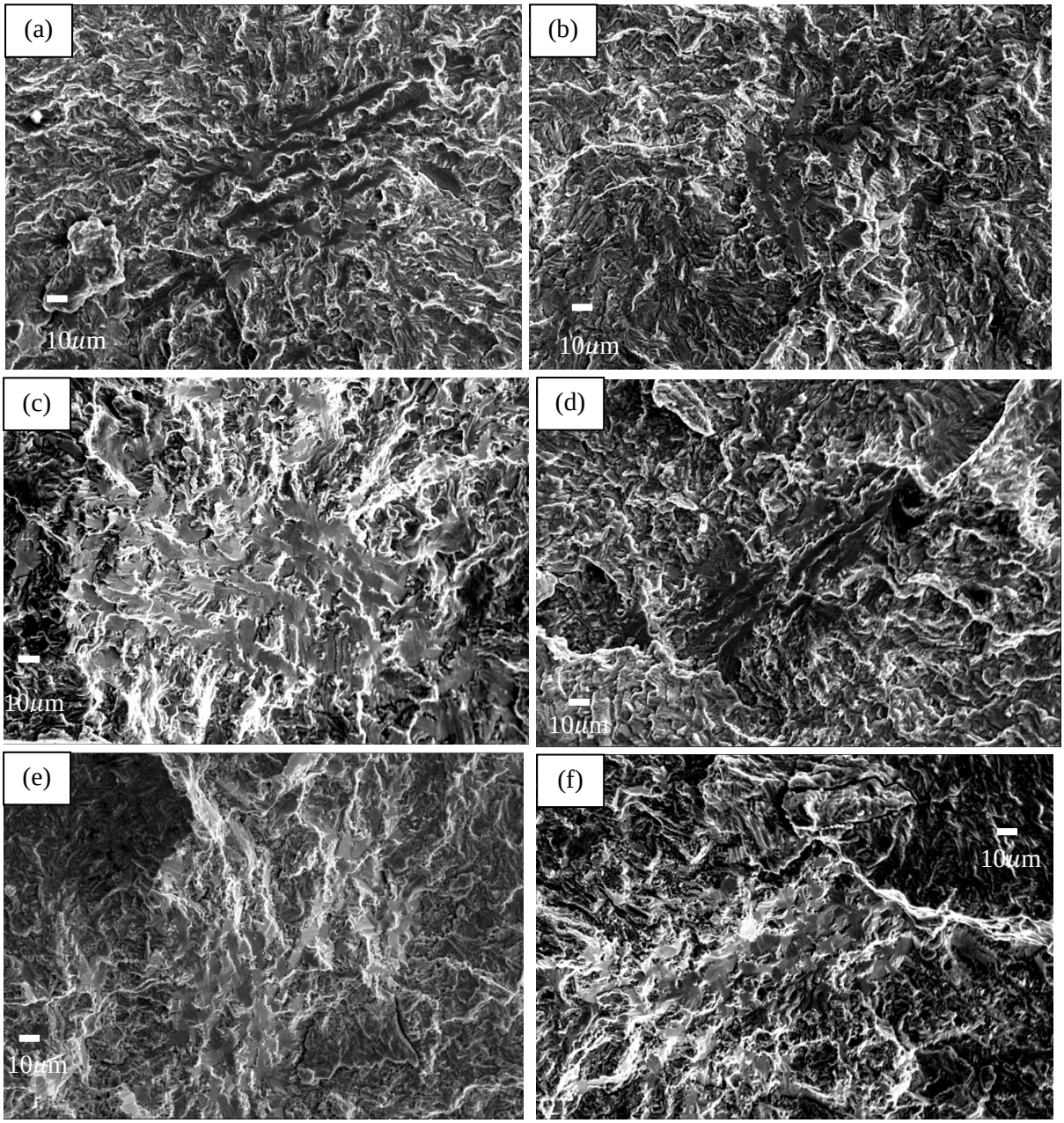

Figure 4.77: Subsurface facets of the Ti-407 pancake forged material tested at: (a) 612.5MPa (b) 600MPa (c) 575MPa (d) 575MPa (e) 562.5MPa and (f) 550MPa.

Based on these six examples, correlating facet morphology to stress level shows that the facets tend to be more elongated at higher stresses and more equiaxed at lower stresses. An interesting question is whether this is a result of a slightly different initiating mechanism as the stress is lowered and the number of cycles increases. Based on the small sample size, however, it is difficult to say.

The Ti-412 Subsurface initiation sites are presented below in Figure 4.78.

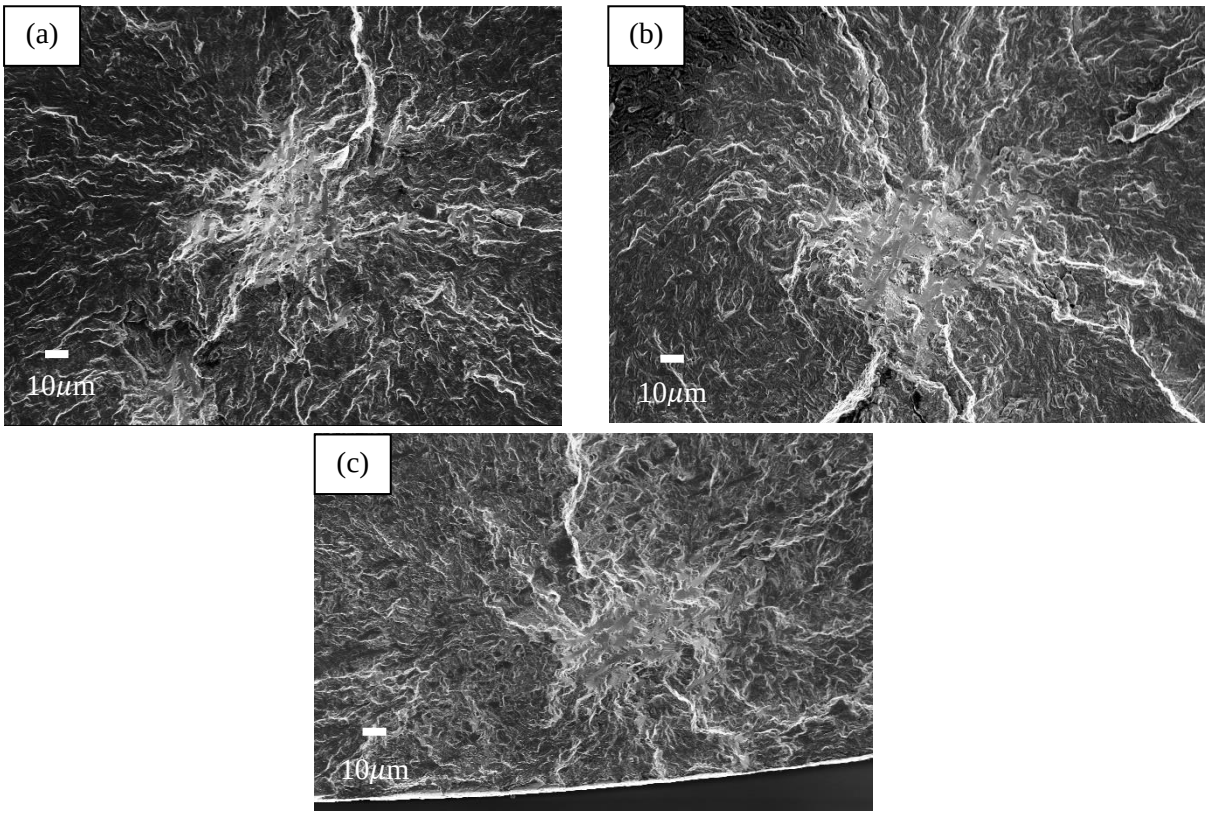

Figure 4.78: Ti-412 subsurface facets tested at (a) 725MPa (b) 700MPa and (c) 675MPa.

Referring to Figure 4.67, it can be seen the subsurface initiations correspond to the lower stresses of the range. In this case, each example shows elongated primary alpha grains. The size of the Ti-412 facets are clearly smaller, consistent with the finer microstructure.

An example of a Ti-407 surface initiation fracture and the possible initiating facet is shown below in Figure 4.79.

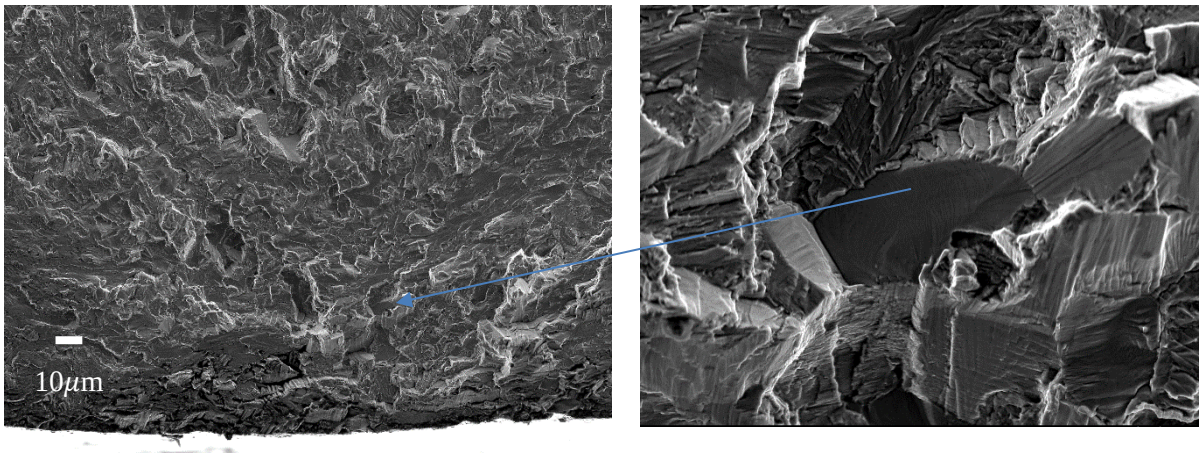

Figure 4.79: Ti-407 HCF surface initiation example.

For the case of the surface initiations, the facets tended to be grouped but not joined up as the subsurface facets were. In general, the surface facets were more equiaxed in morphology. Whilst QTF data is provided for surface facets, the more detailed discussion below focuses on the subsurface examples, as these exhibited the stronger fatigue performance. Further to this, EBSD measurements from the individual surface facets proved to be substantially more difficult than measurements from the subsurface clusters.

The two tables below (Table 4.15 and 4.16) define the spatial orientation of the Ti-407 and Ti-412 HCF facets, along with the crystallographic orientation where generation of data was possible. Images of the six x and y coordinate measurements required to determine the spatial angle of a given facet are displayed in Appendix B as an example of the process. The three examples are from sample Q1-4. Rough definition of the of the crystallographic angle from basal was estimated by overlaying an IPF legend to an IPF grid with angles defined, and correlating the colour from the IPF map, to its position within the overlaid legend (Figure 4.80). This, in itself, is a rather rudimentary method but as shown the results across the different specimens were very consistent.

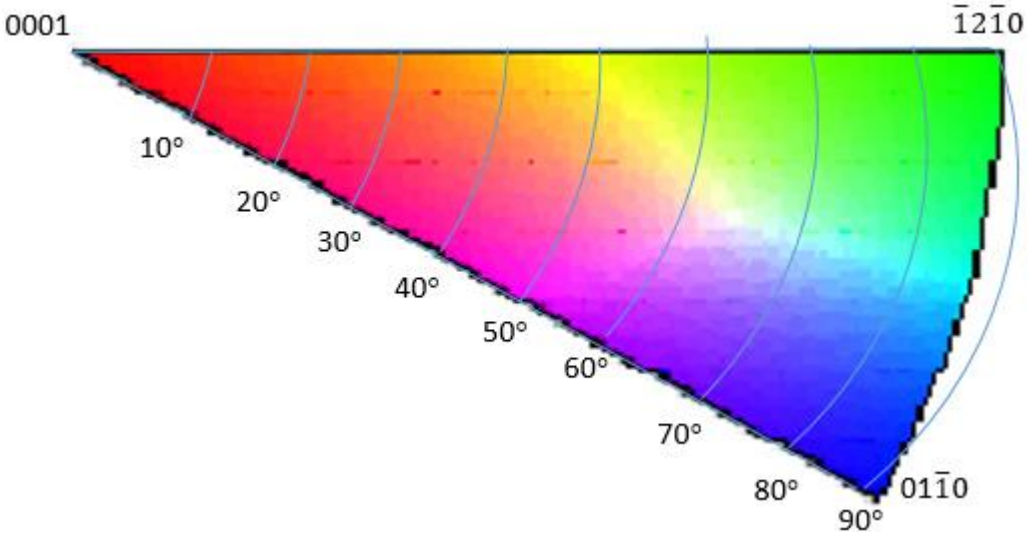

Figure 4.80: Overlaid IPF grid used to determine crystal orientation of the facets.

Table 4.15: Collection of data from Ti-407 forged pancake HCF initiation sites.

Ti-407 Forged Pancake HCF					
Specimen	**Stress (MPa)/ Cycles to failure**	**Initiation site**	**Spatial Orientation (°)**	**Crystal Orientation (degrees from basal) (°)**	**Facet Type**
Q1-2	575 4,175,000	Subsurface	44.6	~55	Cluster, multiple α_p **elongated grains**
Q1-3	550 47,224,300	Subsurface	43.0		Cluster, multiple α_p **equiaxed grains**
Q1-4	625 237,500	Surface	32.6		Group of equiaxed α_p grains
Q1-4		Surface	18.2		
Q1-4		Surface	27.8		
Q1-5	562.5 19,741,900	Subsurface	42	~55	Cluster, multiple α_p **equiaxed grains**
Q1-7	600 2,804,500	Surface	28.7		Separated individual α_p grains
Q1-7		Surface	28.5		
Q1-8	575 6,602,300	Subsurface	40.7	~50	Cluster, multiple α_p **elongated grains**

Table 4.16: Ti-412 facet data.

Ti-412 Forged Pancake HCF					
Specimen	**Stress (Mpa)/ Cycles to failure**	**Initiation site**	**Spatial Orientation (°)**	**Crystal Orientation (degrees from basal) (°)**	**Facet Type**
009	700 13,087,693	Subsurface	46.2	~60	Cluster, multiple α_p **elongated grains**
010	725 5,897,253	Subsurface	48.3	~55	Cluster, multiple α_p **elongated grains**
011	675 18,742,826	Near-subsurface	39.7	~55	Cluster, multiple α_p **elongated grains**

4.9.2 Subsurface Facets

Considering firstly the spatial angle of the subsurface sites for both Ti-407 and Ti-412, in each case, the facets are within $\pm 5°$ of 45°. From the EBSD data collected, the facets tended to cleave on the pyramidal plane. A typical example of an indexed facet is shown below in Figure 4.81. This particular example was Q1-8.

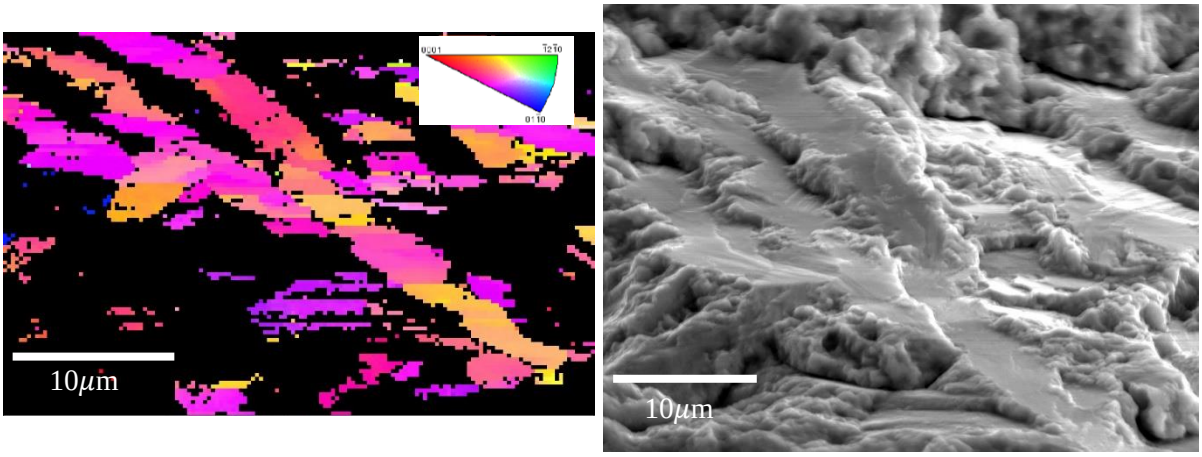

Figure 4.81: Typical example of an HCF indexed subsurface facet from Ti-407 forged pancake material.

Results from EBSD measurements across other test pieces are presented in Appendix C. A summary of subsurface crystallographic orientation across both the Ti-407 and Ti-412 samples is presented below in Figure 4.82.

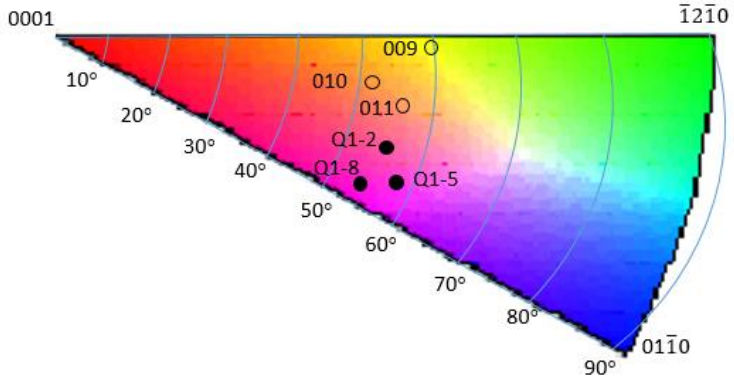

Figure 4.82: Summary of crystal orientation of measured facets from Ti-407 and Ti-412 subsurface initiation sites.

With the spatial facet angle of roughly 45° and the angle of the crystal at approximately 50° from basal there are two options for the c-axis orientation relative to the loading direction. Either the c-axis will be near parallel to the loading direction, or the c-axis will be near perpendicular. This is important information as it can signify the most likely slip plane, and the approximate value of the Schmid factor, and relate this to crack formation.

4.9.3 Transverse EBSD Characterisation

In order to fully define the crystal orientation, it was necessary to view the facet from the transverse direction. One Ti-407 and Ti-412 sample were observed in this manner. Specimens were sectioned in the longitudinal direction and the facet was reached by grinding in across the top of the fracture surface, as shown in Figure 4.83.

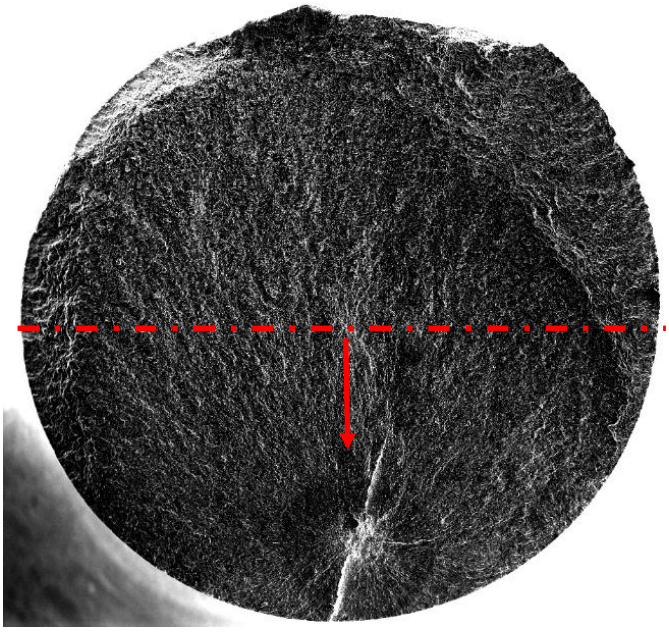

Figure 4.83: Schematic view of the sectioning and grinding process in order to view crystal orientation from the transverse view. This is a Ti-407 forged pancake fracture surface.

Following the sectioning of the test piece, measurements were taken to determine the distance to grind from the cut line to the facet (Figure 4.84). Further to this the position of the facet from the side of the specimen was measured when viewed front on (Figure 4.85), to establish the facet position when obtaining EBSD data. The specimen was then mounted and ground using the auto polisher, monitoring the distance using a micrometer.

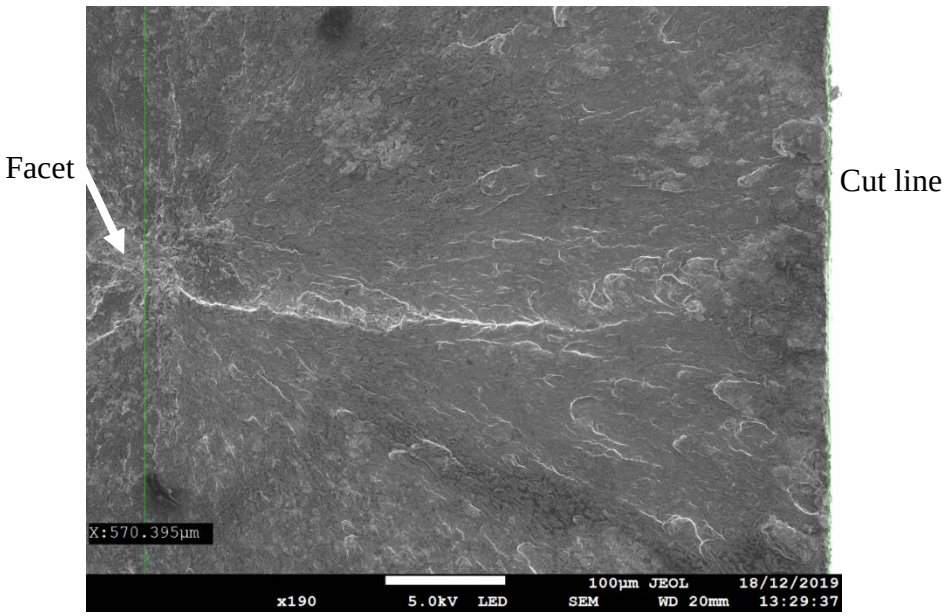

Figure 4.84: Measurement of the distance to grind.

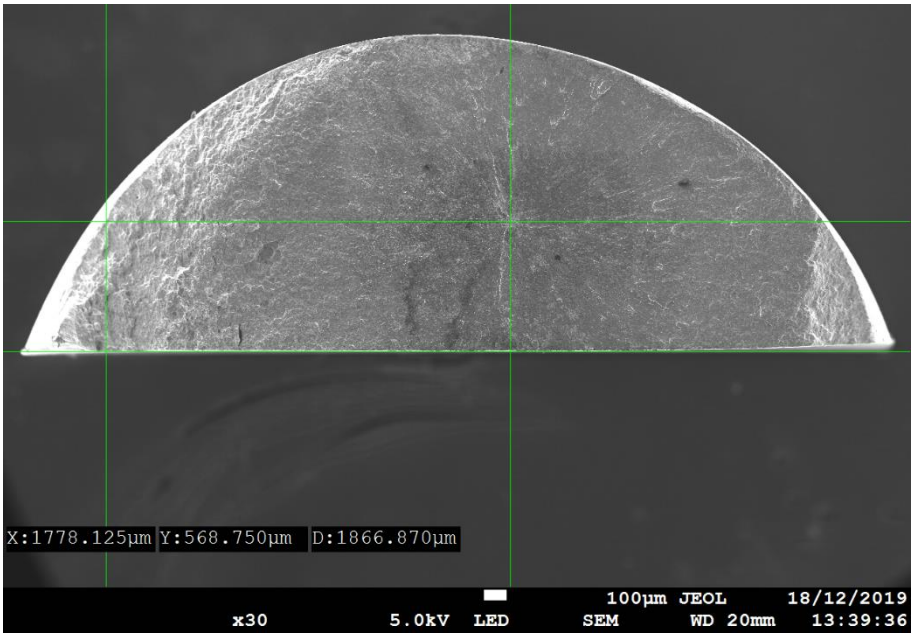

Figure 4.85: Distance to the facet from specimen edge.

It is difficult to quantify the level of accuracy from the results generated from this method. Whilst the process was carried out as systematically as possible, it was not possible to be certain that measurements taken were from the middle of the facets. Therefore, the results cannot be used as categorical confirmation of crystal orientation within the initiating region. However, used in combination with the measurements collected directly from the surface of the facets, the data can be used to hypothesise an explanation for the observed HCF performance. Based on the EBSD results generated directly from the facet surface, it is expected that the c-axis is either parallel to the

loading direction, or perpendicular to the loading direction. The main aim of this analysis therefore, was to get an indication one way or the other.

4.9.3.1 Sample 010 – Ti-412

The faceted region of the first sample analysed, 010 tested at 725MPa and completing roughly 5.9 million cycles, is displayed below in Figure 4.86.

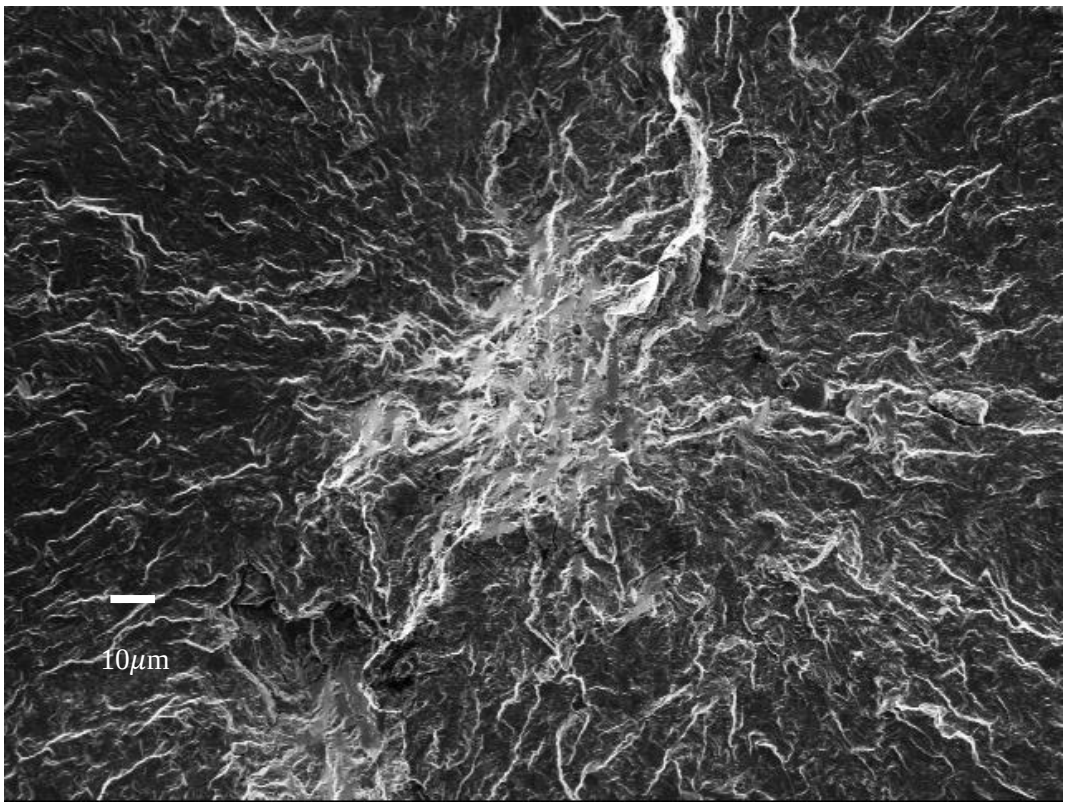

Figure 4.86: The Ti-412 analysed facet.

A map across the general region containing the faceted area, and an area focused on what is believed to be the initiating facet region is displayed below in Figure 4.87. Of note is the incline in the surface, consistent with the spatial angles of the subsurface facets measured using QTF.

(a)

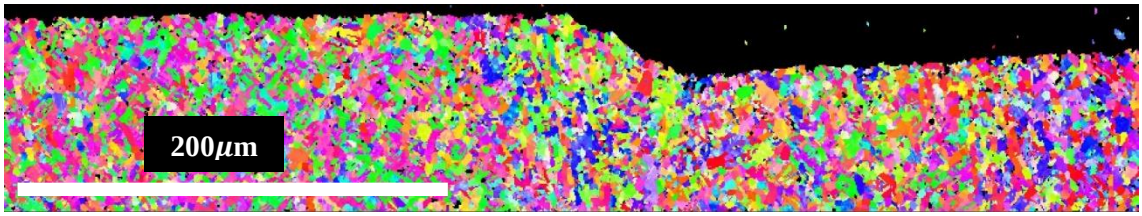

(b)

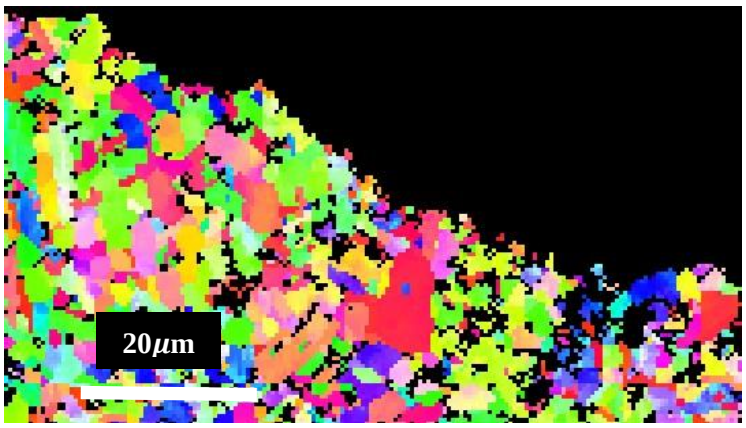

Figure 4.87: EBSD data looking side on at the specimen (a) Across the general region (b) Across the facet.

To visualise the crystal direction, point measurement images are shown below in Figure 4.88.

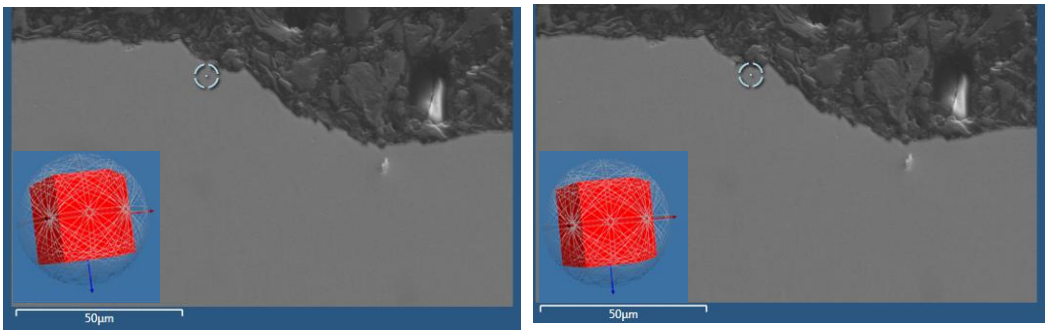

Figure 4.88: Point measurements from the side of the facet.

Comparing the point measurements in Figure 4.88, the map Figure 4.87(b), it can be seen the 'green' grains represents crystals with their c-axis parallel to the loading direction. The EBSD data generated is not completely clear cut. However, it can be said that around what is believed to be the facet, the density of green grains increases.

However, other point measurements around the faceted area, show measurements suggesting basal orientation of the facet as has been observed commonly among HCF facets for titanium alloys (Figure 4.89)

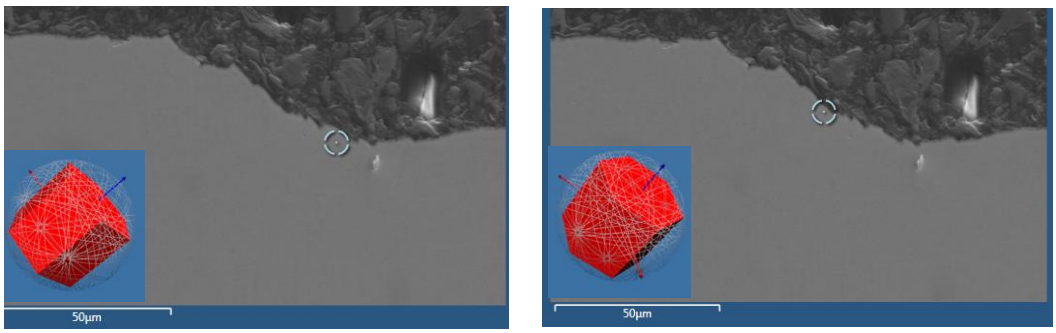

Figure 4.89: Point measuments showing basal plane incident to the facet plane.

Orientations of this sort would be defined by ‘pinkish’ shade, the density of which is significantly less than the green across the facet area. Moreover, this orientation is in contrast with the more comprehensive EBSD data collected directly from the facets suggesting that they are anomalies.

After completion of data collection, the final step in checking the accuracy of the process was measuring the position of the map and correlating it with the initial measurement of the distance from the edge of the specimen to the facet. This process is demonstrated in Figure 4.90 below. The EBSD mapped area is highlighted by the shaded area in Figure 4.90(b).

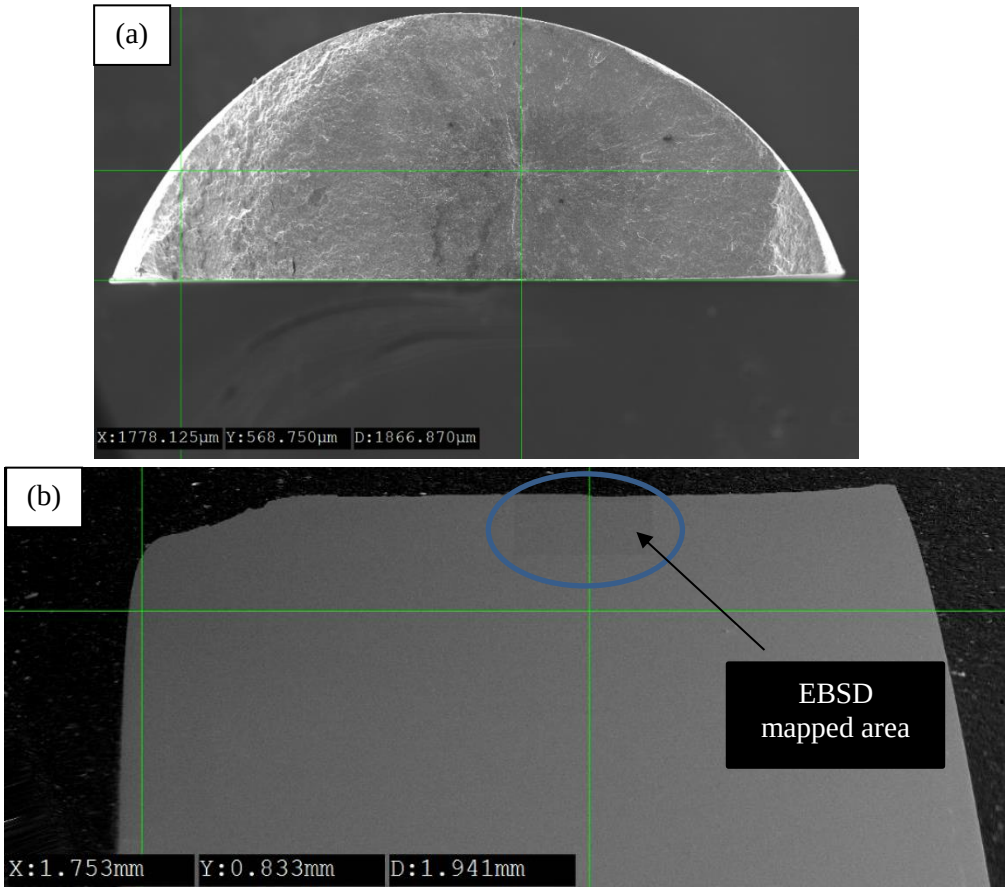

Figure 4.90: Final stage of checking correct position of EBSD map. (a) Distance from edge to facet centre (before) (b) Distance from edge to EBSD map (after).

4.9.3.2 Sample Q1-6 Ti-407

The second sample analysed was a Ti-407 specimen. Q1-6 was tested at 612.5MPa and completed roughly 3.5 million cycles. The fracture surface is shown in Figure 4.91 below.

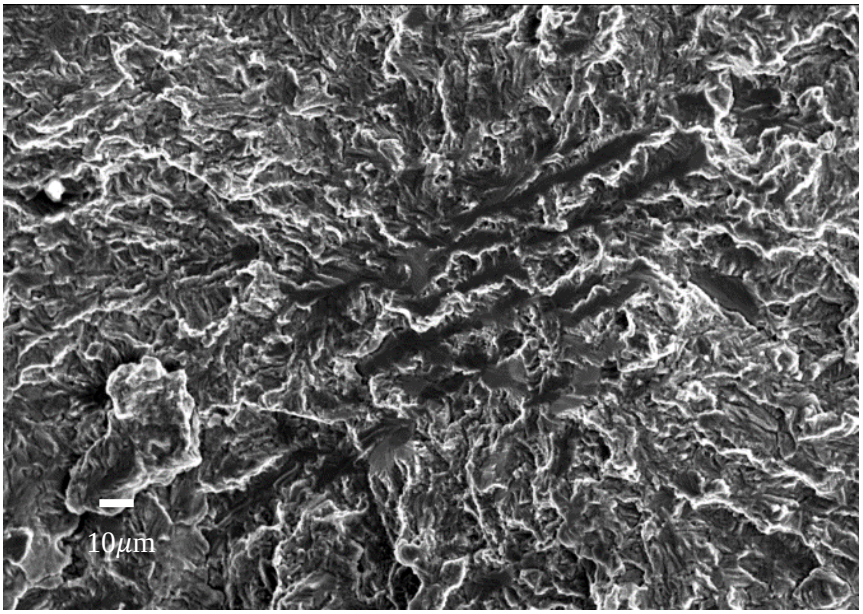

Figure 4.91: Fracture surface of specimen Q1-6.

As can be seen from the macroscopic EBSD map in Figure 4.92, unlike the Ti-412 sample, the inclined area denoting the facet is not visible. This is due to the orientation of the facet relative to the cutting plane. A relatively large number of $\bar{1}2\bar{1}0$ orientated grains can be seen implying an increased likelihood for the facet to also be of this orientation.

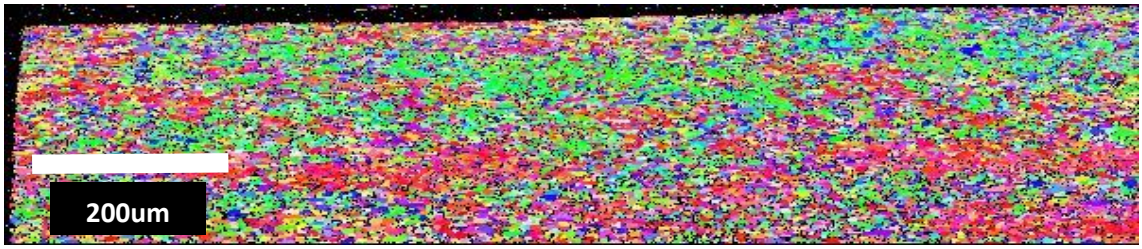

Figure 4.92: EBSD map across the facet region for sample Q1-6.

Some point orientations from across the facet area are shown below in Figure 4.93, again showing the c-axis parallel to the loading direction.

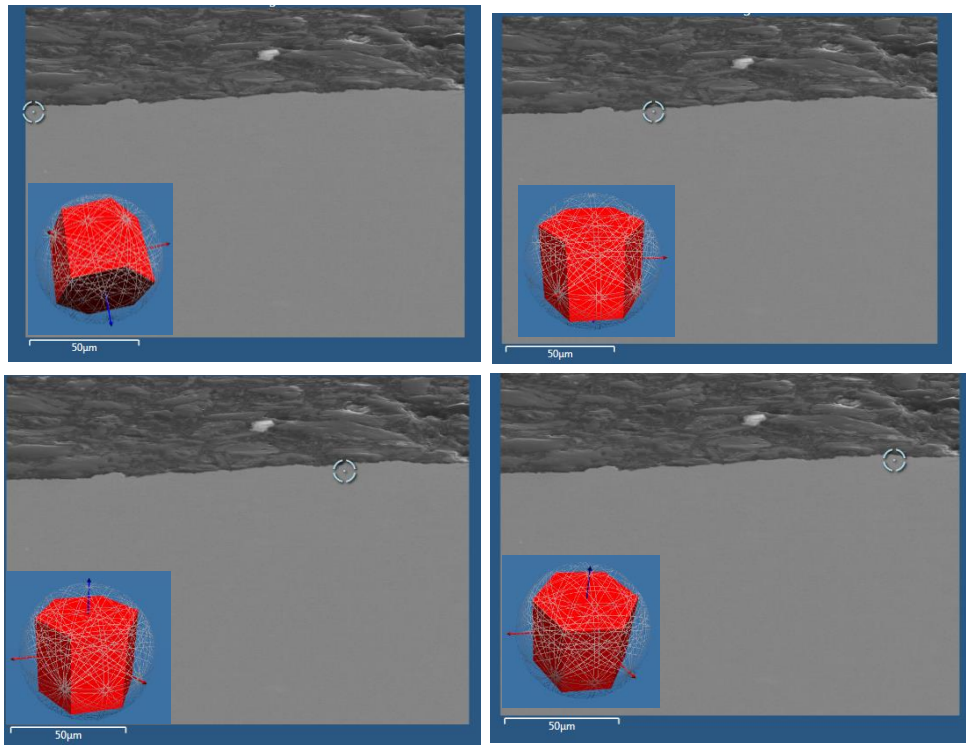

Figure 4.93: Point orientations for sample Q1-6.

There were again points of more random orientation (Figure 4.94) but looking at the fracture surface image there are regions between the facets that appear to be transformed beta.

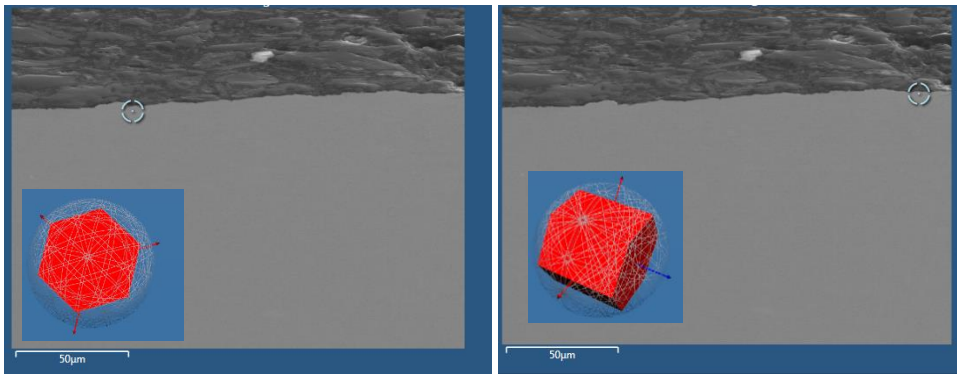

Figure 4.94: Random orientation of grains.

4.10 Ti-6-4 HCF facets

As mentioned above, all of the Ti-6-4 fracture surfaces manifested surface initiation sites, consisting of a number of both isolated and grouped facets. This result in itself is in contrast to the literature, where many studies have found a combination of surface and subsurface initiations for Ti-6-4 tested in the HCF regime [68] [169]. A similar process of quantitative tilt fractography, followed by EBSD analysis directly from the facets, was carried out to characterise the initiating areas in as much detail as possible. Figure 4.95 below gives an example of the fracture surface of an aged variant (a) and an annealed variant (b).

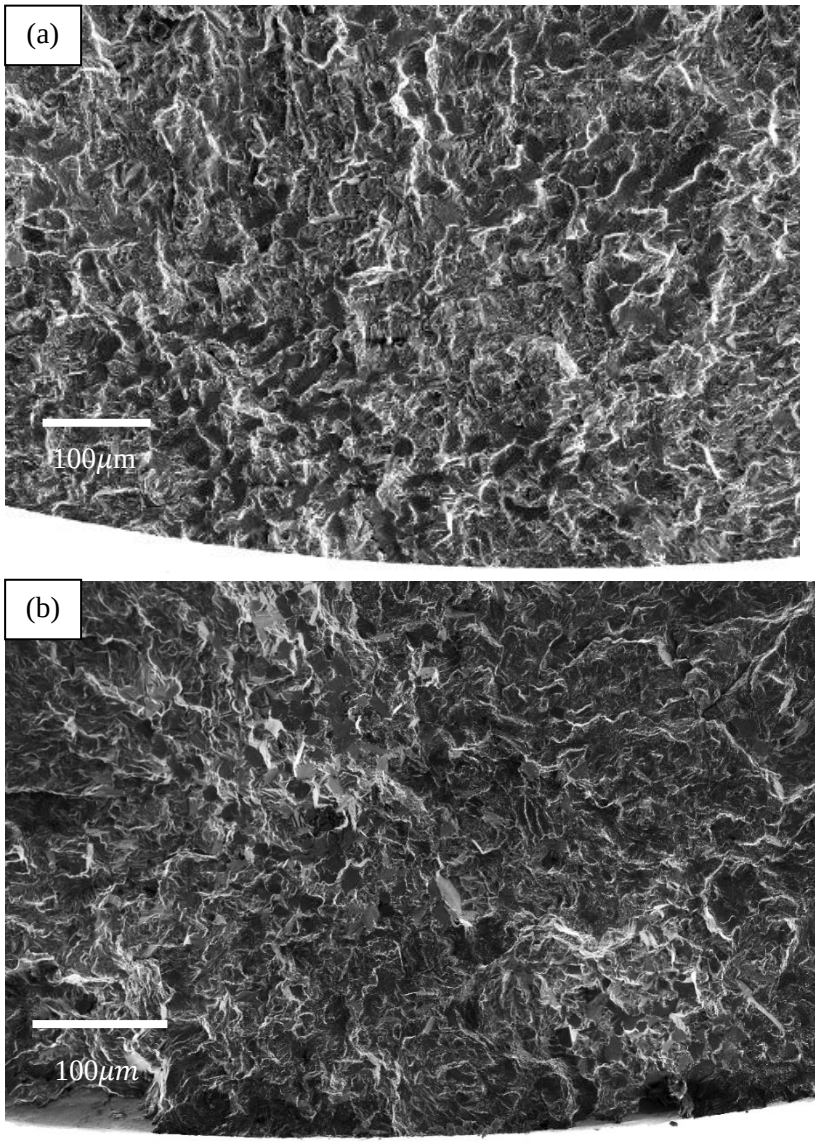

Figure 4.95: Ti-6-4 HCF fracture surface (a) Aged and (b) Annealed.

For the case of both the aged and annealed variant, a large number of faceted grains are evident. This was the case across all the specimens. QTF measurements showed

the spatial angle of the facets for the aged specimens to be between 20–30°, slightly flatter than the facets on the annealed specimens which were measured between 30–40°. In general, indexing across surface facets was significantly more difficult than the Ti-407 subsurface facets, and this was the case with the Ti-6-4 specimens. Of the limited measurements obtained, near basal orientation was seen, as shown in Figure 4.96.

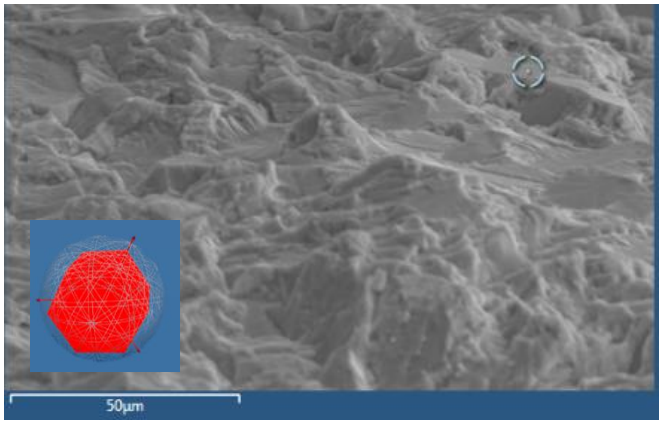

Figure 4.96: Near basal orientated facet from forged pancake Ti-6-4 material.

Whilst limited, the evidence suggests the Ti-6-4 HCF specimens tended to initiate via a more common mechanism with a high Shmid factor on basal orientated planes. With a measured facet spatial angle of between 20–40° across the Ti-6-4 specimens, this implies that basal slip was active in the formation of the facet. This provides an initating system with a moderately high Schmid factor, and a tensile stress component perpendicular to the basal plane. Contrary to the lack of subsurface initations found, the spatial angle and crystlopgraphic plane of the Ti-6-4 facets are similar to results that have been reported in the literature [100].

With so many faceted grains evident at the surface, it is impossible to locate precisely the grain that was first to crack. However, the large number of facets suggests that the sequence of events from initation to formation of a crack starts firstly with a number of facets cleaving independently. These facets then grow, with adjacents cracks coalescing to form a main crack which then grows until failure.

5 Discussion

The present study has developed strong initial indications of mechanical properties for the novel $\alpha + \beta$ titanium alloy, Ti-407, across two different product forms. Further, an initial testing database of a higher strength beta rich variant, Ti-412, has been developed. Mechanical testing was also carried out on Ti-6-4 and Ti-834 as a means of comparison to the data generated from the new alloys.

This study has generated an improved understanding of the fundamental mechanisms of fatigue damage and failure mechanisms associated with cyclic and dwell loading in this class of titanium alloy. The following section aims to interpret the results presented in a holistic manner, and to consider the results in an industrial context.

5.1 Tensile Performance

An attractive feature of Ti-407 is the high fracture toughness attained from a combination of moderate strength and high strain to failure, demonstrated in the stress/strain curve comparison of Ti-407 against Ti-6-4 (Figure 4.33). As can be seen in Table 4.9, the strain to failure is roughly 6% higher than Ti-6-4. Kloenne, based at Ohio State University recently completed high strain rate tensile tests on Ti-407 using a split-Hopkinson bar (SHB) apparatus [81]. The specimens had a bimodal microstructure with a 7.1μm grain size and a prismatic texture. Ti-407 was found to deform significantly by <c+a> slip and deformation twinning. This is surprising because further to the fact that generally in titanium alloys the resolved shear stress for c-axis slip is roughly 3 times higher than <a> slip at room temperature, previous research has shown the likelihood of <c+a> slip to decrease, with decreasing aluminium content [170]. In aluminium lean alloys, the deficiency of <c+a> systems is compensated to some extent by deformation twinning which is more prevalent because of the decrease in stacking fault energy. The deformation modes of Ti-407 were compared to Ti-6-4. When the Ti-6-4 samples were of a similar prismatic orientation, <c+a> slip was not seen. This difference in preferred slip mechanisms could contribute to the increased strain to failure observed in Ti-407.

In other alloys rich in aluminium, <c+a> dislocations have been found to occur but only in hard grains where the Schmid factor for <a> type slip is lower. Williams et al in fact have shown that <c+a> dislocations are completely absent in soft grains

orientated for <a> type slip [170]. This further highlights the uniqueness of the observations in Ti-407 for <c+a> slip to occur in soft grains.

An attractive response of Ti-407, most likely explained by the increased deformation along the c-axis, is the lack of catastrophic failures seen under high strain rate tests. Of course with fan and compressor casings, high strain rate performance is important as these are representative of FOD damage, or situations where blades from the fan or compressor disc are released and need to be contained by the casing. For alloys with a higher aluminium content, as the strain rate increases, strain localisation causes the formation of intense local shear in the form of shear bands, which act as failure sites and limit the extent of plastic deformation at the higher strain rates [171]. Strain localisation is associated with adiabatic heating. Here, there is a sudden re-orientation of the lattice, which can result from either twinning or dislocation interactions to form kink bands. Following lattice re-orientation, gross slip causes a rise in temperature due to adiabatic heating within the band. This is particularly important for titanium alloys because of the low thermal diffusivity [170]. Possibly due to the more active <c+a> slip systems, as well as increased levels of twinning, this mechanism is not activated in Ti-407, allowing for good high strain rate performance.

In the experimental methods it is mentioned that a strain rate of 0.002/min was applied up until yield and then a rate of 0.01/min to induce failure. Table 4.9 shows that where this higher strain rate was applied, a tensile strength 764MPa was obtained, whilst for the two tests where the strain rate remained at 0.002/min, a lower strength of 718 and 714MPa was measured. This is consistent with the findings of Zakaria and Wu, who showed for Ti-6-4 and Ti-555 that yield strength and energy absorbed will increase with increasing strain rate [171].

The tensile data in section 4.7.2 compares Ti-407 with Ti-412. The tensile strength of Ti-412 is approximately 115MPa higher than that of Ti-407. This comparison is consistent with the Hall-Petch relationship. The finer microstructure developed in the Ti-412 material is a consequence of the increased vanadium content.

5.2 Fatigue Behaviour

Across the entire fatigue test matrix generated for Ti-407 and Ti-412 a strong sensitivity between cycles to failure and waveform was observed. As discussed in section 3.4.3, HCF tests consisted of a 100 Hz sinusoidal wave form, LCF tests consisted of a 15 cycles per minute (0.25 Hz) trapezoidal waveform (1-1-1-1 timings) and dwell tests consisted of the same trapezoidal waveform with a 2 minute hold at peak stress (0.008 Hz). The influence of crack initiation mechanism and in particular the formation of quasi-cleavage facets will be considered.

Further, the impact of processing route on mechanical performance is examined through analysis of the ring rolled data, where a strong orientation effect on fatigue performance was seen from the material from manufacturer 2, whilst little to no orientation effect was seen from the material from manufacturer 1.

5.3 HCF Crack Initiation Mechanism

An obvious difference was noted from the HCF test pieces when compared to the LCF and dwell specimens, exemplified in Figures 4.67 and 4.69. The HCF regime produced a mixture of surface and sub-surface initiations, whilst the LCF and dwell tested pieces demonstrated solely surface initiation sites. This was a consistent finding for both the Ti-407 and Ti-412 variants. In all cases, facets were observed at the centre of the initiation area whether that be surface or subsurface. Indeed, a common observation across many studies has shown fatigue crack initiation to be accompanied by facet formation in the primary alpha grains for bimodal microstructures of both near alpha and $\alpha + \beta$ alloys [172] [100] [169]. Further to this, faceted crack initiation within alpha/beta colonies in lamellar structures has been reported [173]. However, the proposed mechanisms of facet formation vary quite significantly in the literature. This implies that the micro-mechanisms associated with facet formation are not fully understood. Whilst it is appreciated that some of these differences may be attributed to specific combinations of alloy composition, microstructure and fatigue loading regimes, in some cases different interpretation has been assigned to a common set of circumstances.

Clearly, essential to understanding the fatigue results reported in this work, is a comprehensive study of the initiating mechanisms, and how they differ across the high

cycle fatigue frequency of 100Hz, the low cycle fatigue frequency of 0.25Hz and the dwell frequency of 0.08Hz. The questions addressed in this section are:

1.) Why is the Ti-6-4 material weaker than Ti-407 under HCF loading, despite a 35% higher tensile strength?

2.) Why is the HCF performance demonstrated by Ti-407 and Ti-412 so much better than the LCF and dwell performance? More commonly observed amongst combined fatigue data is a continuous transition from the LCF to the HCF regime. This has been demonstrated for the corresponding Ti-6-4 pancake material as well as the Ti-834 bar stock material.

3.) Why in all cases under a similar applied peak stress, do subsurface initiation sites demonstrate a superior life to the surface initiation sites? Are there any differences in the facet characteristics?

In order to fully characterise the facets observed on the fractured test pieces, the inclination of the facet relative to the loading direction, and the crystallographic orientation of the facet planes were determined. The method was described in section 3.6 and the results presented in section 4.9. Notably, one of the earliest reported techniques describing the measurement of crystal orientation directly from fracture surface facets was developed at Swansea University by Davies et al [174].

The results in section 4.9 demonstrated that the spatial angle of the HCF subsurface facets for both Ti-407 and Ti-412 tended to be orientated at near 45° to the tensile loading axis, and the crystal orientation of the facets appeared to be near the pyramidal plane. These results were relatively consistent across the specimens measured. In order to confirm the crystal c-axis angle relative to the loading direction, crystallographic measurements were also obtained from a sectioned view of the test piece. These measurements suggests the c-axis to be near parallel to the loading direction.

Figure 5.1 below, taken from the paper studying high cycle fatigue initiation sites in Ti-6-4 by Bantounas et al [100], displays the relationship between c-axis orientation relative to loading direction, and slip system. This combined with the data referred to above, can help to link the active slip system to the facets.

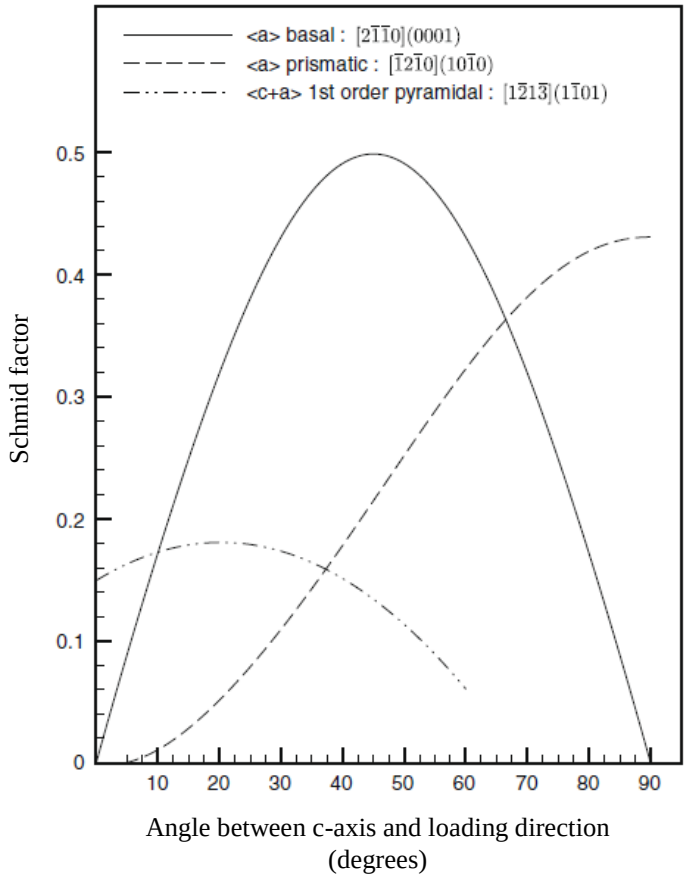

Figure 5.1: Plot of Schmid factor vs angle between the c-axis and the loading direction for basal, prismatic and first order pyramidal slip.

It is important to understand that the interactions shown in Figure 5.1 are chemistry dependent. As mentioned in section 5.1, Williams et al [170] demonstrated this in studying the effect of aluminum content on slip systems. They found an increased tendency of both basal slip and <c+a> slip with increasing aluminium concentration. Aluminium decreases the energy of the basal stacking fault, whilst it increases the energy of the prismatic fault (thus encouraging basal slip and discouraging prismatic slip). This would, of course, alter the positions of the basal, prismatic and 1st order pyramidal curves in Figure 5.1. Thus, for the case of Ti-407 and Ti-412, which both contain roughly 0.85 wt% aluminium, one would expect prismatic slip to be more prevalent. However, as noted in the discussion on the tensile results, an unexpected amount of <c+a> 1st order pyramidal slip was observed from high strain rate specimens.

The evidence presented is limited and was carried out on a very small sample size. The results, however, indicate that for the Ti-412 and Ti-407 samples analysed, the c-axis is near parallel to the loading direction within the faceted regions. This would suggest 1st order pyramidal slip being the active slip system, a system roughly three times more

difficult to activate relative to basal slip with the c-axis orientated 45 degrees to loading direction. Further to this, the combination of the reduced aluminium content of Ti-407 and Ti-412, and increased strain rate under HCF loading would suggest twinning to be a dominant deformation mechanism. Specifically, Kloenne et al found Ti-407 to deform via the $\{10\bar{1}2\}$ twinning mode under high strain rate tensile tests [81]. This may explain the reduced tendency for cracks to form via planar slip on the basal plane as is seen for the Ti-6-4 specimens. It appears that the combination of <c+a> slip and deformation by twinning results in a stronger HCF performance.

This answers the first question posed at the beginning of the section. It would seem there is a difference in deformation mechanisms which results in a reduced tendency for planar slip build up and faceting on the basal plane in Ti-407 and Ti-412. The resistance of crack initiation is highlighted when considering the fatigue performance normalised by yield stress. Ti-6-4 survived 10 million cycles at 55% of the yield, whilst both Ti-407 and Ti-412 achieve 10 million cycles at 90% of yield.

The second question posed, was why the HCF performance demonstrated by Ti-407 and Ti-412 is so much better than the LCF and dwell performance. This is perhaps also linked to the above answer. The HCF performance is significantly better than expected relative to its strength, and so sits further to the right than would be expected on the S/N curve. As a result, there is a large difference in life indicated from the HCF regime down to the LCF and dwell regimes. In section 4.4.5, it was highlighted that the normalised-by-yield LCF strength of Ti-407 and Ti-6-4 were much more comparable. The LCF and dwell fracture surfaces are analysed in more detail in the next section.

With respect to the longer life of the subsurface initiations, relative to the surface initiations, Table 4.15 does show a contrast between the spatial angles of the facets. The surface facets are less inclined relative to the loading axis with an average angle of 30° to the fracture plane, compared to the 45° angle measured from the subsurface sites. The aim of the study by Jha et al [169], was to distinguish between initiating mechanisms at the ‘short life’ and ‘long life’ end of the scatter across fatigue lives at the same stress. The most obvious difference was that the spatial angle of the facets for the ‘short life’ test was 30° whilst for the angles for the ‘long life’ specimen were in the range of 41-56°. This is consistent with the smaller spatial angles measured for the Ti-407 and Ti-412 surface facets. The lack of crystallographic data from the facets of the current study limits the explanation that can be given, but it can be suggested that the mechanism of the surface initiation is weaker than that of the subsurface

initiation. Further to this, early stage crack growth from a subsurface initiation site will effectively be under vacuum conditions, with the crack growth rate slower than the rate of growth when exposed to air.

5.4 LCF and Dwell Response

The following section analyses the LCF and dwell results of the pancake material. Firstly some discussion of Ti-6-4 LCF is given, and the results from the analysis is linked to the combined Ti-6-4 fatigue data across the LCF and HCF regime. Following this, some detailed discussion on the LCF and dwell behaviour of Ti-407 and Ti-412 is given and linked to previous studies in the literature.

5.4.1 Ti-6-4 LCF

As mentioned in section 4.4.5, only one Ti-6-4 LCF test from the pancake material stock was carried out. This result is displayed in Figure 4.39, and sits on the same trend line as the Ti-6-4 LCF dataset generated at the start of the project. The position of the LCF trendline appears to form a continuous curve as it transitions into the HCF regime.

The annealed Ti-6-4 LCF facets suggest a similar initiating mechanism to that reported in the literature, with cracking appearing to occur on the basal plane (shown in Figure 5.2 below) with a relatively flat inclination. The spatial angle for the facet highlighted in Figure 5.2, was measured as 13.0°.

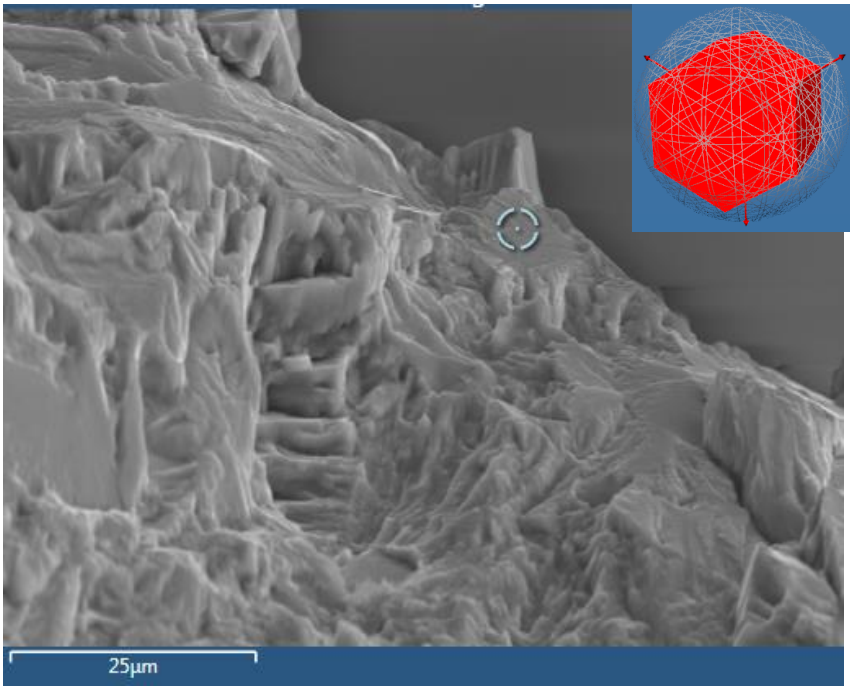

Figure 5.2: Example of a basal orientated facet on a Ti-6-4 LCF fracture surface.

5.4.2 Ti-407 and Ti-412 LCF and Dwell

The trend in fatigue strength relative to waveform frequency displayed by Ti-407 and Ti-412 across the LCF and HCF regimes demonstrates an effect of time-dependent deformation on crack initiation life. Analysis of the fracture surfaces was carried out in order to gain a more comprehensive understanding of the initiating mechanism for these LCF and dwell specimens. QTF fractography was again used to measure the inclination of the facets. Whilst EBSD readings directly from the fracture surface facets were attempted, unfortunately indexing was not possible. This could perhaps be attributed to increased dislocation densities within the faceted grains, preventing the generation of EBSD measurements. The QTF data are presented below in Table 5.1 and the fractography in Figure 5.3.

Table 5.1: Spatial orientation of LCF and Dwell facets

Ti-407 Forged Pancake LCF			
Specimen	**Stress (MPa)/ Lives**	**Initiation site**	**Spatial Orientation**
Q2-10	650 16 634	Surface	17.2
Q2-12	550 156,593	Surface	7.4
Q2-13	625 12,975	Surface	6.3
Q2-14	600 34,125	Surface	20.6
Ti-407 Forged Pancake Dwell			
A3	550 45,409	Surface	13.7

The measurements show that the facets are less inclined to the loading axis than those observed in the HCF specimen fractures.

Figure 5.3 below, exemplifies the faceted region at the initiation site of (a) a dwell test piece (A3) and (b) an LCF test piece (Q2-10).

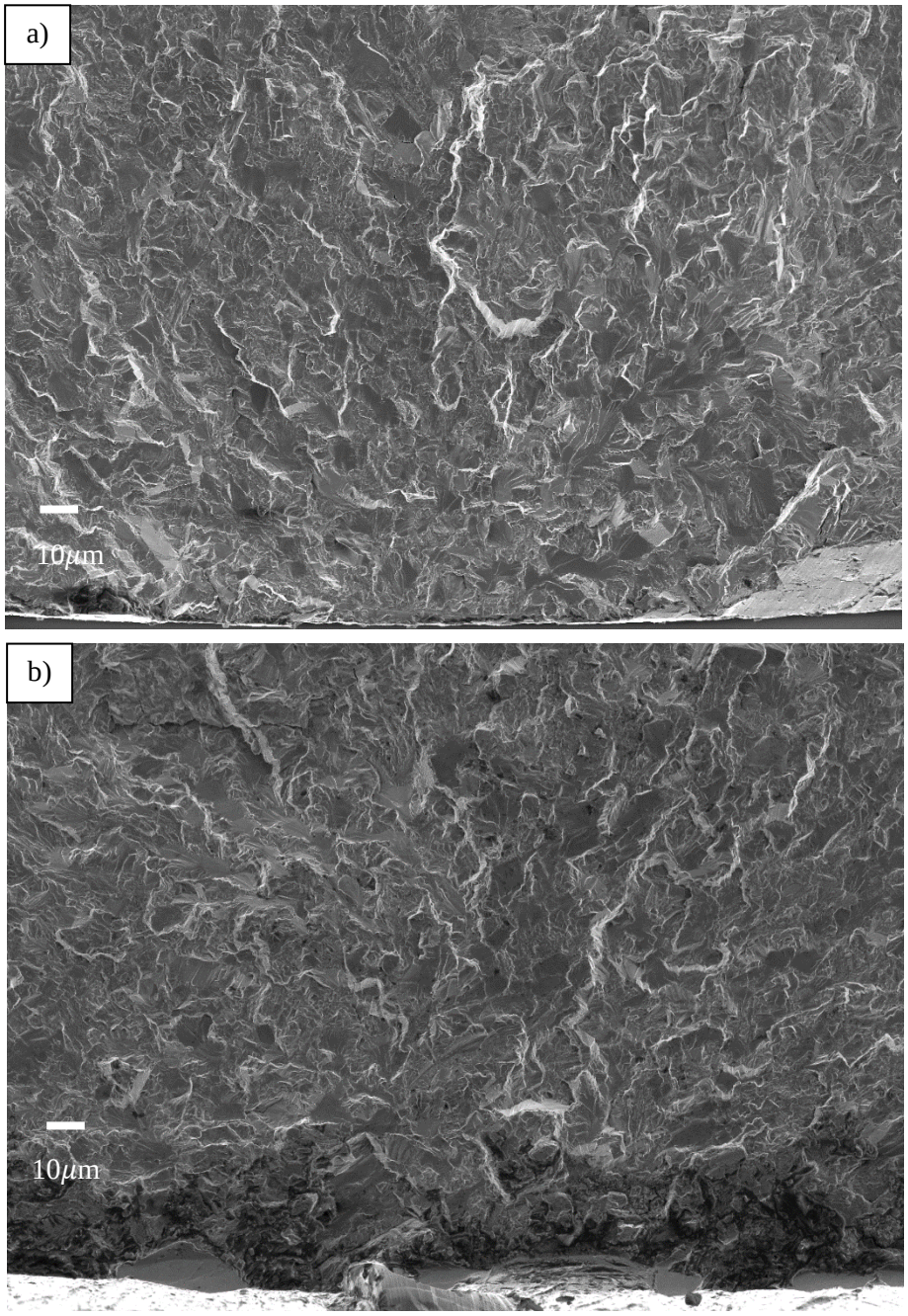

Figure 5.3: Examples of Ti-407 faceted initiation regions: (a) Dwell loading at a stress of 550MPa completing 45,409 cycles and (b) LCF loading tested at 550MPa completing 156,593 cycles.

Focusing on the LCF and dwell behaviour, from Figure 4.67 (also displayed below in Figure 5.5) it can be seen that there is a small knockdown in performance as the hold at maximum stress is increased from one second to two minutes for both Ti-407 and Ti-412. A frequency dependent trend on fatigue life was previously reported for the forged disc variant of the alloy Ti-834 and the alloy Ti-685 [146]. As shown in section 4.4.7 which displays an EBSD map across an entire test piece cross section, Ti-407 includes regions within the microstructure where individual α_p grains take a common basal plane orientation. These regions of common grain orientation or 'macrozones' can act as an effective structural unit within the material and control bulk mechanical response. Within the regions where the grains are orientated with the basal plane approximately perpendicular to the applied tensile stress, a relatively strong response will be generated. This is a consequence of the basal plane, the preferred slip system in the hexagonal α phase of titanium at room temperature being poorly orientated for shear and dislocation glide (i.e. offering low Schmid factors as demonstrated in Figure 5.1). Neighbouring regions, either with randomly orientated α_p grains or if textured with predominantly inclined α_p grains, would deform relatively easily. Here, grains could also promote prismatic or pyramidal slip in these weaker regions. Slip could be easily accommodated between the individual neighbouring grains with common crystal orientation, providing relatively long slip lengths. However, at the boundary between the adjacent regions, dislocation pile-ups would be generated. This proposed mechanism essentially mirrors the Stroh redistribution model [72] previously adopted by Evans and Bache [175] to explain quasi-cleavage facets formed in large grain near-α alloys but now considered on a regional, macro-zone scale. Empirical data confirming this mechanism has also supported the development of crystal plasticity models [108].

A revised schematic representation of the redistribution model is illustrated in Figure 5.4 and compared with a nominal α+β microstructure illustrating neighbouring regions of random (weak) and common (strong) grain orientation distributions. The Stroh model predicts that the degree of shear and tensile stress induced by dislocation pile ups at the boundary between weak and strong regions is directly proportional to the slip band length. Hence the larger the grain or macro-zone size, the greater the propensity for stress redistribution and dwell sensitivity.

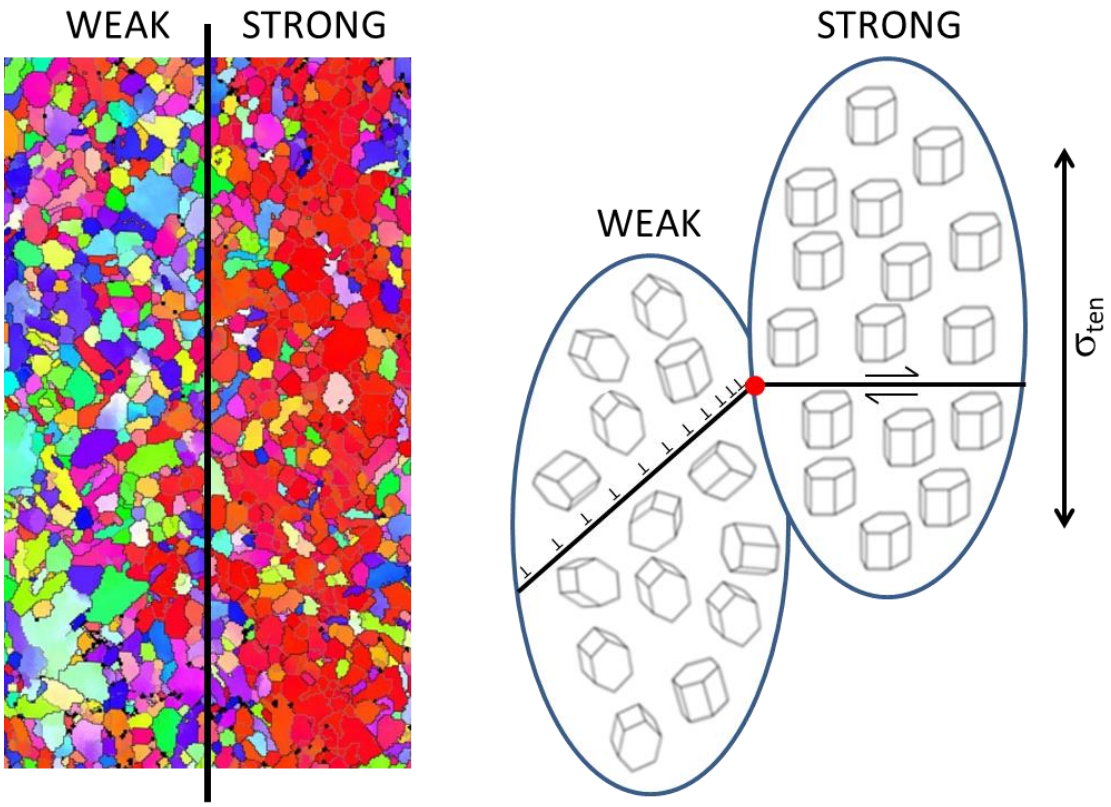

Figure 5.4: The Evans-Bache model [175] applied to weak and strong regions made up of multiple grains with random and common basal orientations, respectively.

Clearly, the dislocation glide mechanism behind stress redistribution and ultimately facet formation, often referred to as cold creep, would be encouraged by time at load. The faceted region, and the flat facets observed on the LCF and dwell specimens are evidence of the Stroh mechanism. However, further confirmation would require EBSD readings from the facets showing their orientation to be near basal.

If one assumes the Stroh model to be active in Ti-407 and Ti-412 under LCF and dwell conditions, it further explains the weaker response relative to the HCF performance. In the absence of dwell time on load, whether that be 1 second or 120 seconds, the stronger initiation mechanism described in section 5.3 above becomes active. The time-dependent control of facet orientation is consistent with the long-standing evidence generated by Evans, investigating dwell behaviour for the Royal Aircraft Establishment, Farnborough, who also reported that orthogonal orientated facets were generated under cyclic, dwell and creep experiments [176] but not under monotonic tensile tests to rupture.

The formation of quasi-cleavage facets is not exclusive to dwell behaviour. As demonstrated, they will still persist even under high frequency HCF loading. What is

unique under LCF and dwell failure, is the orientation of the facets being approximately orthogonal to the applied tensile stress. The time-dependent stress redistribution mechanism is essential to induce slip on the poorly orientated basal planes and later, in combination with the applied tensile loading, progressively open the facet to form an embryonic fatigue crack. This early stage discontinuity, now forming on a Mode I plane, may support crack extension assuming the critical combination of applied stress and crack size are exceeded, i.e. $\Delta K_{applied}$ exceeds the fatigue crack growth threshold value ΔK_{th}.

The presence of macrozones within the developmental Ti-407 pancake forgings (exemplified in Figures 4.47 and 4.48) could be pertinent to the frequency-sensitive fatigue response illustrated by the fatigue data, i.e. the relatively large separation between the HCF data to the LCF and dwell curves. However, an understanding of the dwell phenomenon and optimisation of thermo-mechanical process routes, to generate a random distribution of α_p grains without a strong micro-texture, could help to reduce dwell sensitivity in this class of alloy [58].

This is further illustrated here utilising fatigue data generated from a bar stock variant of Ti-834, displayed in Figure 4.73 of section 4.8.1. This was tested under waveforms of various frequency, from two minute dwell, through 15cpm trapezoid to 1Hz, 10Hz and 100Hz sine. Relatively consistent fatigue strength is measured independent of waveform frequency, with the scatter in fatigue life no greater than a single order of magnitude at any applied stress level.

In contrast, the Ti-834 disc material, which was highly dwell sensitive, was shown to have basal orientated grains extending into the transformed areas, resulting in large planar regions. EBSD analysis of the bar stock variant confirmed an even distribution in grain size and orientation, showing the prior beta grain structure to be in the bar stock material (Figures 4.75 and 4.76). Therefore, in the absence of macrozones or a large grain size, this class of alloy could potentially achieve the optimum fatigue performance, normally defined under HCF conditions, through the avoidance of redistribution between weak and strong regions.

The marked difference between monotonic and cyclic constitutive behaviour demonstrated in Figure 4.55 helps to explain the susceptibility to cyclic damage on the bulk scale. It can be assumed that all load controlled fatigue tests performed at a peak stress greater than the cyclic yield condition of 420MPa would experience considerable ‘ratchetting’ in strain, and previous studies have shown the propensity

for strain accumulation under dwell as opposed to regular fatigue cycles [73]. This effect would be enhanced by 'cold creep' and the relevant time spent at peak stress per fatigue cycle. The three cycle conditions employed during the current fatigue matrix are considered in Table 5.2 to demonstrate the total time spent at peak stress until failure under the HCF, LCF and dwell scenarios. For the HCF waveform the time spent above 90% of the applied sinusoidal stress has been assumed to impart the relevant damage. Clearly, the number of cycles required to accumulate the critical bulk strain is reduced under LCF and dwell loading.

Table 5.2: Time at maximum stress under different waveform conditions.

Peak stress (MPa)	HCF (Hrs)	LCF (Hrs)	Dwell (Hrs)
650	0.02	4.62	18.23
600	1.67	9.48	486.67
550	13.12	43.50	1513.66

In the overall context of titanium alloys, near alpha and alpha/beta alloy systems are more prone to suffer from dwell; indeed IMI685, Ti-829, Ti-834 and Ti-6242 have all shown the dwell effect [146][174]. The diagram in Figure 5.6 displays a range of alloys in order of percentage of aluminium stabiliser. The percentage is based on the total aluminium equivalent stabiliser and molybdenum equivalent stabiliser. As can be seen, the dwell sensitive alloys listed above are grouped towards the left hand side of the diagram.

A recent study was conducted examining the effect on dwell sensitivity by increasing the molybdenum content of Ti-6242 (Ti-6Al-2Sn-4Zr-2Mo) to eventually arrive at the composition of Ti-6246 (Ti-6Al-2Sn-4Zr-6Mo) [104]. Ti-6242 is widely used by General Electric as a high temperature engine compressor alloy with good mechanical properties up to 540℃. Ti-6246 is a stronger derivative but limited in temperature capability up to 450℃. In general, increased molybdenum content decreases the beta transus of titanium alloys and as a slower diffuser, reduces the rate of phase transformation from beta to alpha. Moreover, nucleation of multiple variants of alpha laths is encouraged through increased molybdenum and the transition from aligned colonies to a more basketweave structure is promoted. As a result, both the grain size and micro texture intensity of alpha grains is reduced. The smaller grain size results in a smaller slip band spacing and reduces the accumulated strain during dwell fatigue, thus delaying initiation.

Similarities to this study are found when comparing Ti-407 (Ti-0.85Al-3.9V-0.15O-0.25Si-0.25Fe) to Ti-412 (Ti-1Al-7V-0.2Si-0.7Fe). Highlighted on Figure 5.6 are the relative locations of the alloys based on their aluminium equivalence percentage.

Certainly the much finer grain size of Ti-412 results from the increased vanadium content. The tensile strength of Ti-6246 is approximately 200MPa greater than Ti-6242 and a tensile strength increase of approximately 115MPa is seen between Ti-407 and Ti-412. The EBSD data generated shows basal plane orientated macrozones to be more prevalent in Ti-407 than Ti-412.

In the case of Ti-6242, subsurface initiations were common among the tested samples and a transition to surface initiation sites was seen as the molybdenum content was increased. However, for both Ti-407 and Ti-412, only surface initiations were generated. In order to measure the dwell sensitivity and to compare this between the different alloys, the parameter dwell debit was defined. For a given stress, this is the number of lives completed under normal LCF conditions, divided by the number of lives completed under dwell conditions. A dwell debit of 7.9 was seen for Ti-6242 and a dwell debit of 3 was seen for Ti-6246. For ease of reference, the combined fatigue data for Ti-412 and Ti-407 are displayed below in Figure 5.5.

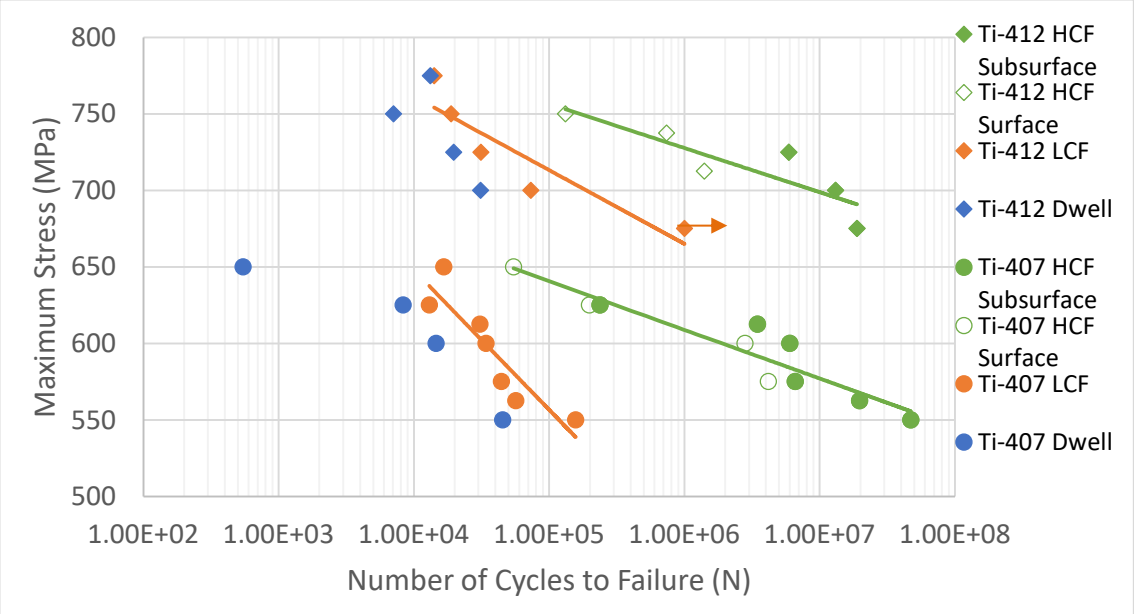

Figure 5.5: Combined fatigue data for Ti-407 and Ti-412.

For Ti-412, a reduced gap between the HCF and LCF fatigue regime was noted. Comparing HCF to LCF for Ti-407, a two and a half order of magnitude difference is seen at 550MPa, the lowest stress tested. For Ti-412, at the lowest tested stress (675MPa), less than an order and a half magnitude difference is seen between the HCF and LCF lives. It should also be noted that a fault with the fatigue test rig meant the

LCF test had to be terminated early - the test piece did not actually fail. At the midpoint of the stress range used (600MPa for Ti-407 and 725MPa for Ti-412) a two order of magnitude difference is seen for Ti-407 and a one and a half order of magnitude difference for Ti-412. It can be concluded that, consistent with the study of Qiu et al [104], a reduction in the effect of frequency on fatigue performance is seen as the beta content is increased. However, this correlation is not linearly proportional across the range of alloys presented in the Figure 5.6. Ti-6246 for example can be processed for employment in compressor discs to be totally dwell insensitive [177] whilst Ti-407 does show a degree of dwell sensitivity, implying that aluminium content is not the sole driving factor in dwell susceptibility.

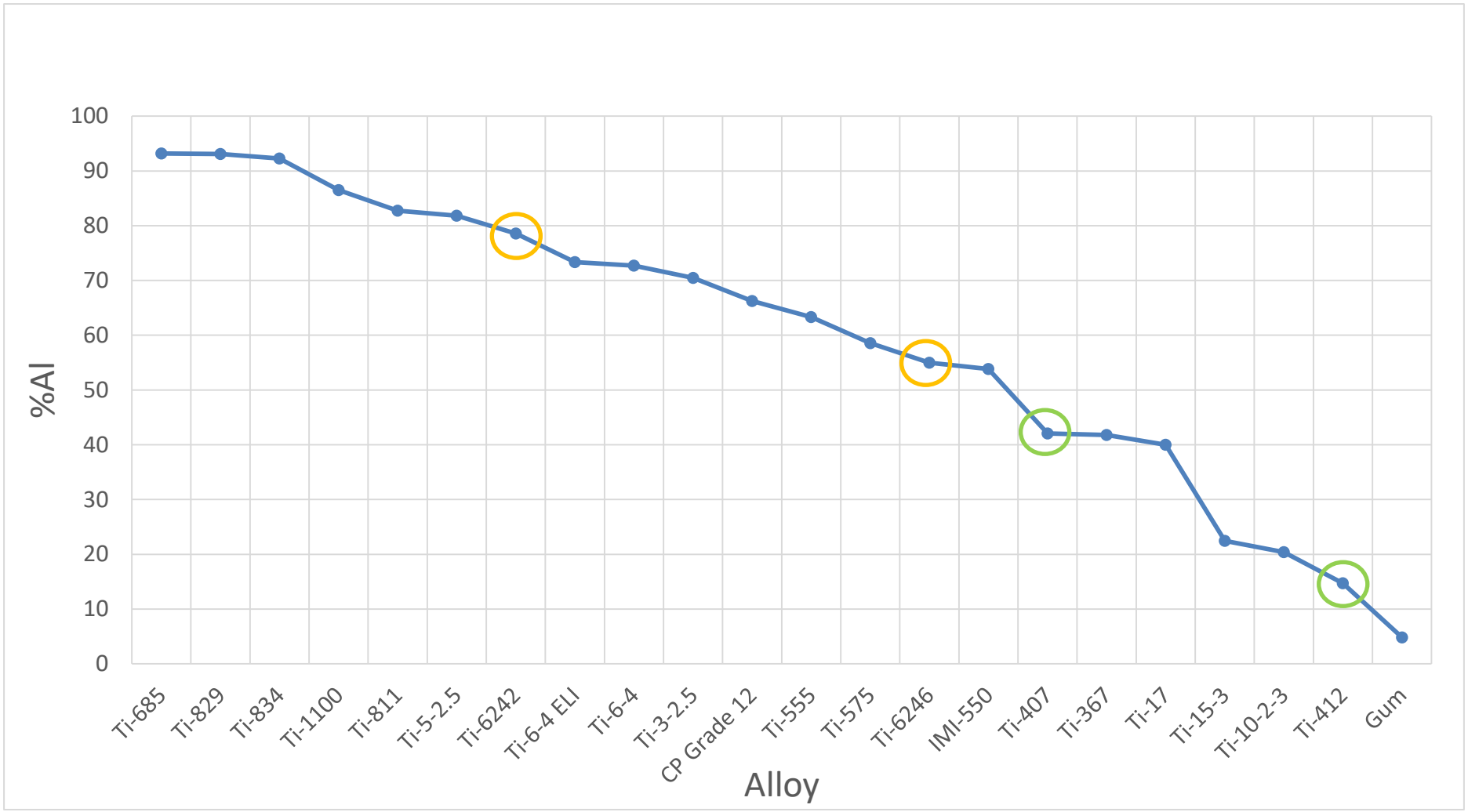

Figure 5.6: Titanium alloys as a function of percentage aluminium equivalence. Highlighted in the yellow circles are the alloys Ti-6242 and Ti-6246, and in the green circles, Ti-407 and Ti-412.

The location of Ti-412 material specimen extraction should be noted in the context of the fatigue results. Figure 5.8 labels each test piece. As mentioned in section 4.7.2, a higher yield strength was measured from the tensile test piece RLH1004_002 taken from the rim of the pancake (788MPa) compared to RLH1004_001 closer to the centre of the pancake (744MPa), Figure 5.7. Of particular note, the 775MPa dwell test piece (RLH8001_015) was taken from the stronger rim region of the pancake.

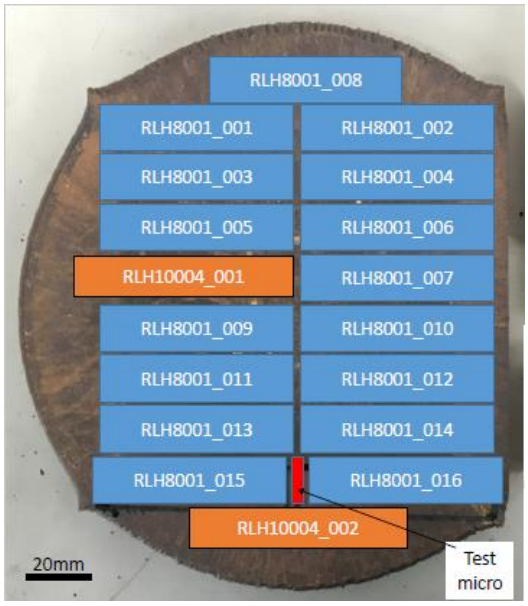

Figure 5.7: Location of Ti-412 test pieces on pancake.

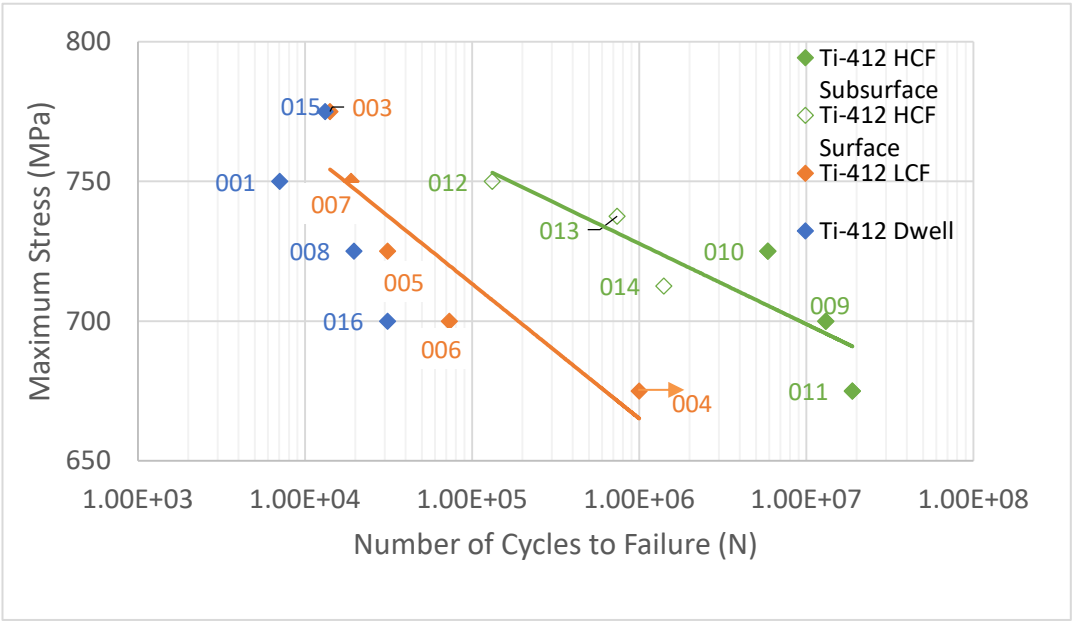

Figure 5.8: Fatigue data labelled by specimen number to identify pancake location.

Despite the influence of the variation of yield stress across the pancake on the fatigue results, which does add a level of uncertainty to the conclusion, it would still seem fair to say that there is a reduced frequency dependency compared to the Ti-407 data.

Looking at the lowest stress level, for example (675MPa), test pieces 004 and 011 come from similar positions relative to the centre of the pancake.

One final comparison between Ti-407 and Ti-412 to visualise the relative performance of the two alloys under the different loading regimes, are the plots of LCF and HCF normalised by their yield. For the Ti-412 data the yield was taken as the average of the two measurements. These are shown below in Figure 5.9.

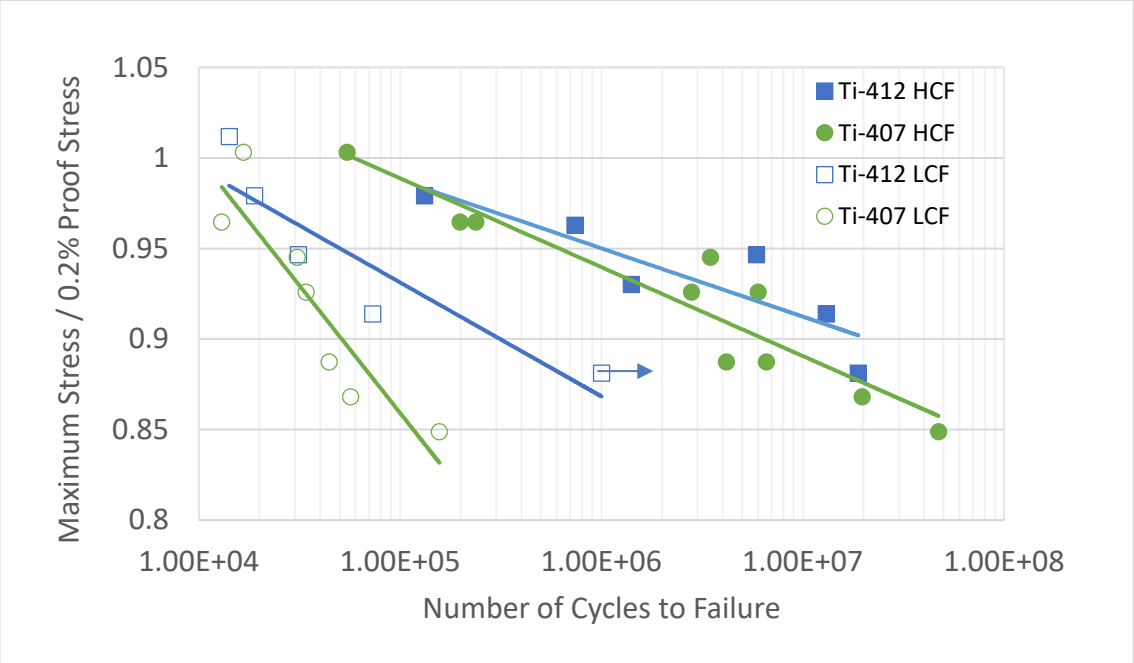

Figure 5.9: Plot of normalised HCF and LCF data for Ti-407 (circles) and Ti-412 (squares).

For the HCF normalised curves, the two sets of data are very similar, effectively superimposed on top of one another. In the high stress regime they are indistinguishable and at lower stress the Ti-412 data appear slightly stronger than Ti-407, although the difference between two lines of best fit is marginal. For the LCF normalised comparison, there is a larger difference between the two sets of data, and as with the HCF data, this gap widens as the stress level reduces, again with Ti-412 showing the stronger performance. This relative difference suggests increased resistance to the time-dependent initiating mechanisms under the LCF waveform for the Ti-412 material.

5.5 Ring Rolled Fatigue Data

Comparing the two sets of ring rolled data, an interesting observation is that no orientation effect was seen for the manufacturer 1 material, whilst a strong effect was seen for the manufacturer 2 material, with a 16% stronger yield for the axial direction relative to the tangential direction. It is well known that for titanium alloys, processing strongly influences the mechanical properties [100]. Metallographic inspection demonstrated that the material processed by manufacturer 2 contained elongated bands of commonly orientated basal grains throughout the structure. Whilst there was still a high degree of grain elongation within the manufacturer 1 material, these were more dispersed amongst equiaxed grains. The maximum texture intensity (x6.01 random) was lower from the manufacturer 1 pole figure than the manufacturer 2 pole figures (x6.68 and x7.45 random) and the obvious bands of basal macrozones seen in the manufacturer 2 texture were not present in the manufacturer 1 texture. These bands seem to be the cause of the difference in performance between the two manufacturers. A more comprehensive texture study of the axial versus tangential test pieces would enable more detailed conclusions. However, from the data that is available (presented in Figure 4.22 and 4.24) it could be argued that the tangential map shows more bands of basal orientation. This would be consistent with observations in the literature where the trend is a degradation in fatigue life when the loading direction is perpendicular to the predominant basal plane texture as described in section 1.8.12.

Looking at the combined ring rolled fatigue data (presented in section 4.3), the manufacturer 2 tangential versus manufacturer 1 comparison shows manufacturer 1 to be stronger in the HCF regime with the LCF data roughly equivalent. A single line of best fit could be plotted for the two LCF data sets apart from the results at 650MPa, where the manufacturer 1 test achieved a longer life of more than half an order of magnitude. However, this stress is significantly above the 574MPa yield stress of the tangential material.

For the HCF regime the performance difference is consistent across the whole stress range with the same gradient seen for the two best fit lines. At the higher stress levels, traditional theory would suggest that the propagation stage takes up a more significant proportion of the total life. This suggests the fatigue crack growth rate of the manufacturer 1 material to be slower to that of the manufacturer 2 material. Cracks could easily propagate through the large regions of elongated basal orientated grains present throughout the manufacturer 2 microstructure. Interestingly, from all of the Ti-

407 and Ti-412 fatigue data collected over the course of the project, the manufacturer 2 tangential fatigue data set was the only one not to show a significant gap between the two regimes. It was also the only HCF data set to reveal solely surface initiation sites, suggesting that further to the crack propagation rates, the initiating mechanism also had an influence on the weaker performance.

The manufacturer 2 axial comparison to the manufacturer 1 data shows the axial orientation to be stronger for both HCF and LCF. The difference is more pronounced under LCF loading. This is perhaps to be expected because it suggests the time-dependent effects the specimens would be subjected to under a trapezoidal wave-form would govern the initiation life more closely.

Clearly, the more broken up and even distribution of α_p in the manufacturer 1 material results in more isotropic mechanical properties, whilst the properties of the manufacturer 2 material are heavily reliant on loading direction.

For ease of reference, the combined manufacturer 2 fatigue data is presented in Figure 5.10. Fracture surfaces of the 4 points at 550MPa are examined in more detail below. There is almost a two order of magnitude difference between the axial and tangential HCF life at this stress and almost an order of magnitude difference between the LCF points.

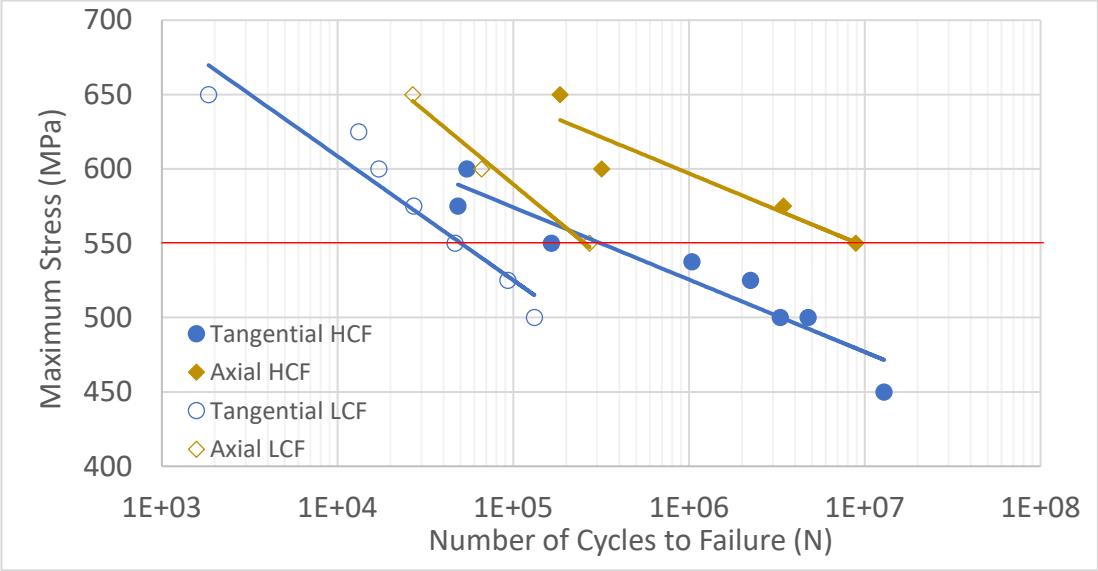

Figure 5.10: The combined fatigue data for the manufacturer 2 ring rolled Ti-407 material.

A summary of the fracture surfaces is detailed below in Table 5.3 and 5.4.

Table 5.3: Summary of manufacturer 2 ring rolled LCF test piece fracture surfaces tested at 550MPa. C01 represents the axial orientation and L01 the tangential orientation.

Ti-407 Manufacturer 2 Ring Rolled LCF			
Specimen	**Stress (MPa)/ Cycles to failure**	**Initiation site**	**Facet Spatial Orientation (°)**
C01	550 271,257	Surface	-
L01	550 46,614	Surface	12.15

Table 5.4: Summary of manufacturer 2 HCF fracture surfaces.

Ti-407 Manufacturer 2 Ring Rolled HCF			
Specimen	**Stress (MPa)/ Cycles to failure**	**Initiation site**	**Facet Spatial Orientation (°)**
C07	550 8,894,400	Subsurface	48.4
L15	550 164,400	Surface	63

Despite the order of magnitude difference in the LCF lives, the axial fracture surface (C01) displayed a faceted band of basal orientated grains at the initiation site, extending roughly 200μm (Figure 5.11). Figure 5.12 shows the corresponding tangential LCF fracture surface. This also shows flat faceted grains at the initiation site.

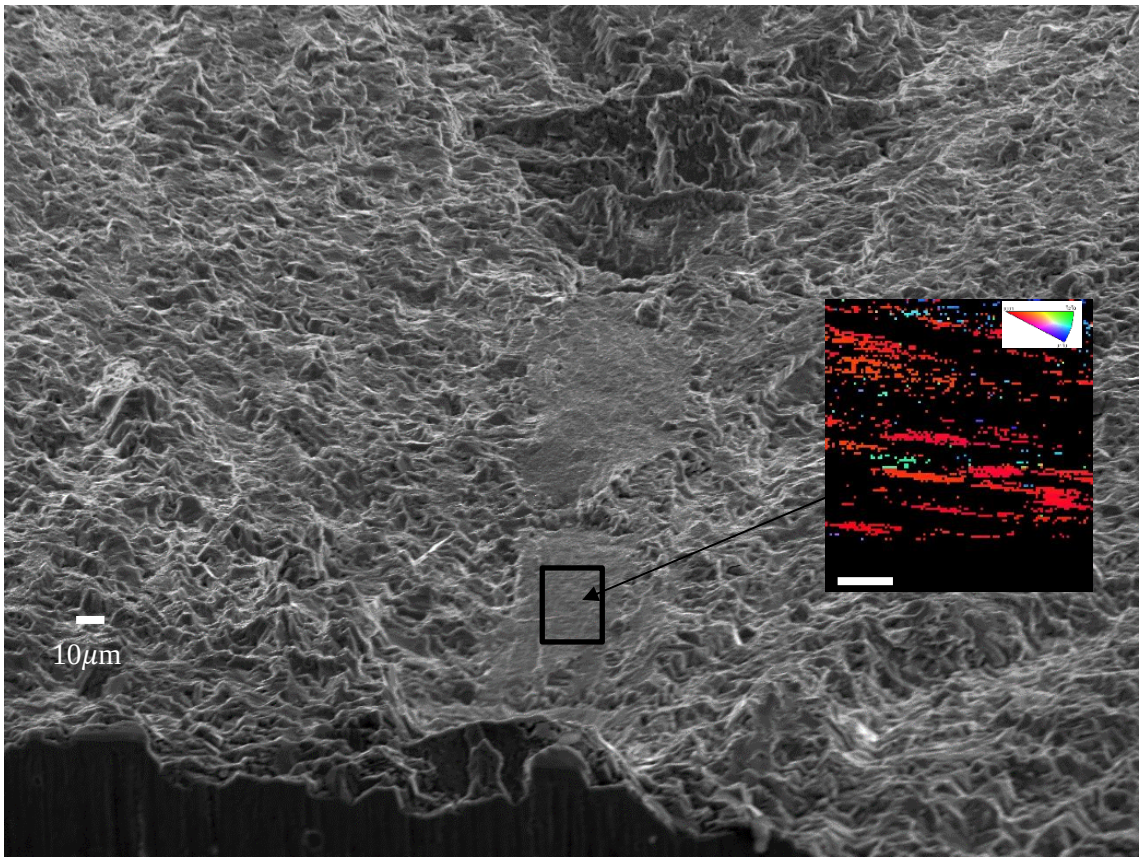

Figure 5.11: Axial LCF initiation site shows a long elongated band of basal orientated grains.

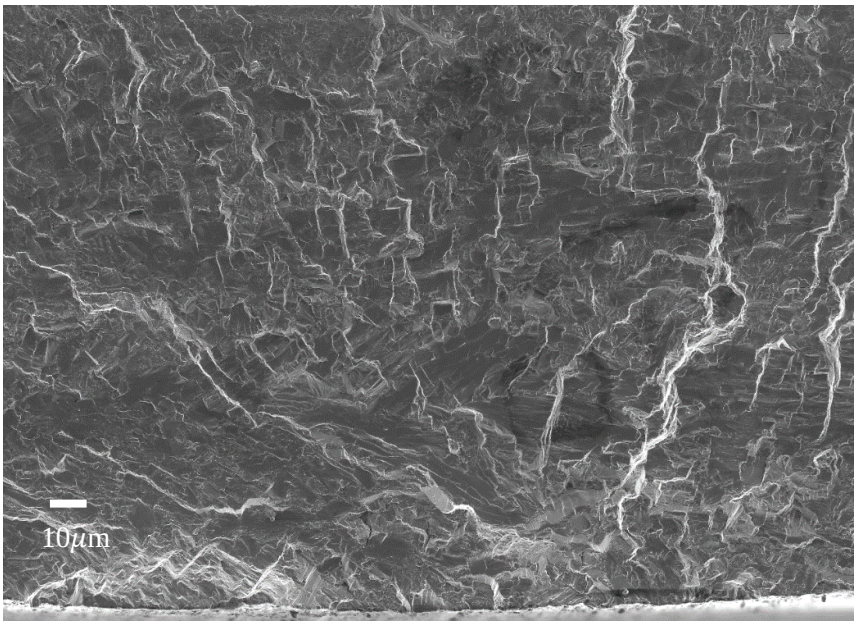

Figure 5.12: Tangential LCF initiation site.

It is not obvious why the axial specimen, with the appearance of the long faceted band at the initiation site, achieved an order of magnitude more cycles than the tangential counterpart. The explanation could lie within the delay to initiation.
The obvious contrast in the HCF surfaces is the subsurface initiation of the axial test piece (Figure 5.13), and the surface initiation of the tangential piece (Figure 5.14).

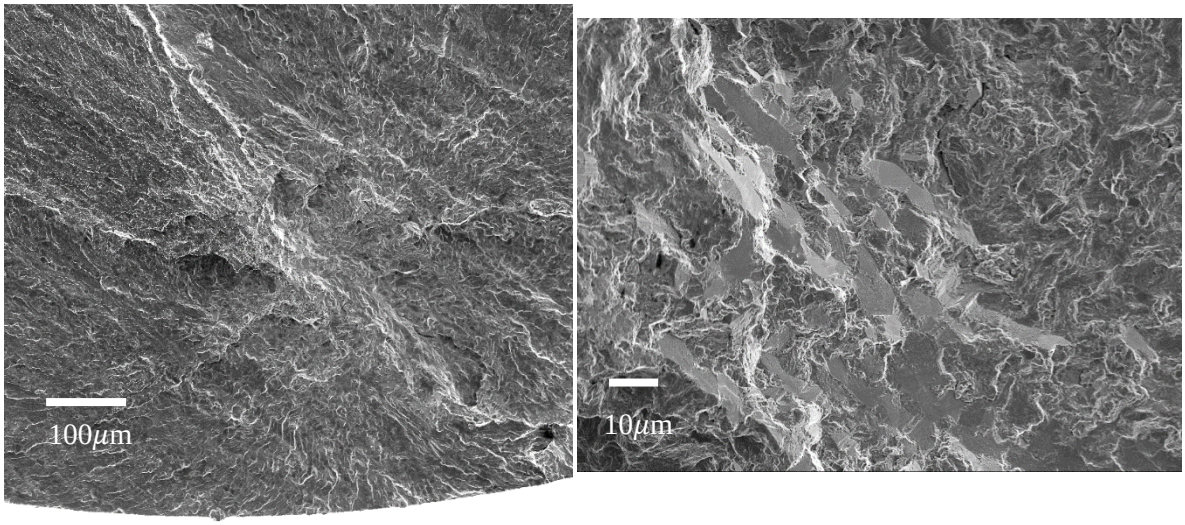

Figure 5.13: The Axial HCF initiation site (subsurface).

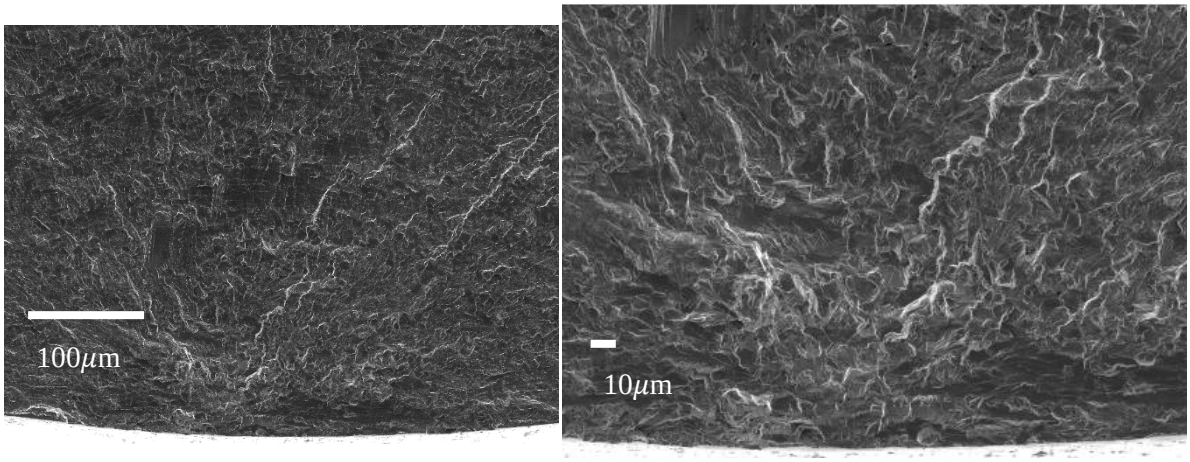

Figure 5.14: The tangential HCF initiation site (surface).

As highlighted in section 5.3, subsurface initiated fractures tend to be associated with relatively greater lives to failure. This suggests avoidance of the ‘weaker’ initiation mechanism associated with the surface failures and therefore a stronger response. On Figure 5.14, it looks as if there are several areas where soon after initiation, the crack has cleaved straight over basal orientated bands of grains.

5.6 Fatigue Crack Growth

For components designed on the damage tolerance and total life concept (lifing approaches discussed in sections 1.8.8 and 1.8.9), consideration of the fatigue crack growth behaviour of the material is important. With regards to microstructural influence on crack growth rate, the work of Skikai et al [57] showed that increasing the width of alpha lamellae helps to increase fatigue crack growth resistance, suggesting that better crack growth might be seen from the slower, vermiculite cooled test pieces. This is because the coarser structure causes crack branching and secondary crack creation which requires additional energy to form the new surface, thus slowing down the crack growth rate. It is also suggested that in a lamellar structure the crack grows perpendicular or parallel to the long axis of the alpha lamellar. Therefore, for optimal performance a balance must be found between coarseness of the structure to promote crack branching, with a large enough number of grains to increase the tortuous nature of the crack between differently orientated grains or colonies.

Focusing on the bimodal structure, it has been suggested that adding primary alpha helps to reduce the slip length and increase the obstacle strength of the beta phase [4][178][148]. However as demonstrated in section 4.4.4, it can be seen that for the material tested, the crack growth rate can be described as being near independent of both the microstructure and R ratio. The Paris coefficient of 2.9 fits the entire data set. This is consistent with the work carried out by K Nakajima et al [179] which found a microstructure effect on crack growth only for short cracks less than 200 microns, but an independence of growth rate above this. The different range of stress intensity factors is explained by the stress ratio effect, with the stress intensity reducing with the reducing stress amplitude.

The preparation and inspection of selected samples, prepared on an orthogonal plane to the crack growth, demonstrated the interaction of the crack with the local microstructure. A typical example shown below in Figure 5.15, demonstrates that the crack tip interacts with the α_p grains via both transgranular and intergranular mechanisms. Growth through the transformed regions was also varied, with both translamellar and interlamellar modes evident. A minor degree of crack bifurcation was evident, although the macroscopic plane of cracking was generally flat and perpendicular to the applied tensile stress axis.

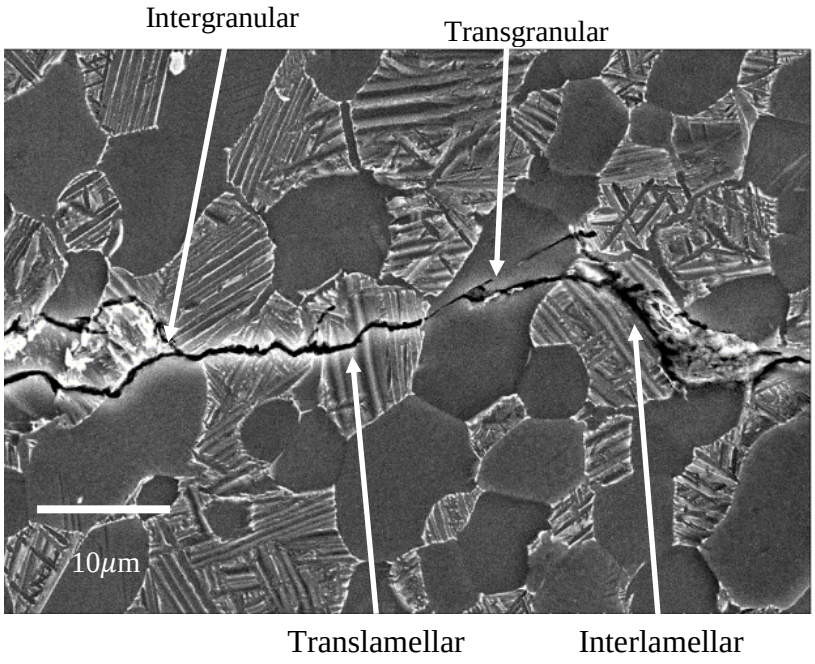

Figure 5.15: Local crack/ microstructure interactions in Ti-407 (crack growth from left to right).

Local electron back-scatter diffraction measurements conducted along the wake of the crack demonstrated that where the basal plane of α_p grains was close to co-planar with the plane of the crack growth, then the crack would seek a transgranular pathway, consistent with previous studies involving the alloy Ti-834 [146]. An example of this is shown below in Figure 5.16. In contrast, if the α_p grains presented either pyramidal of prismatic planes co-planar to crack growth, then the crack would tend to extend in the intergranular fashion.

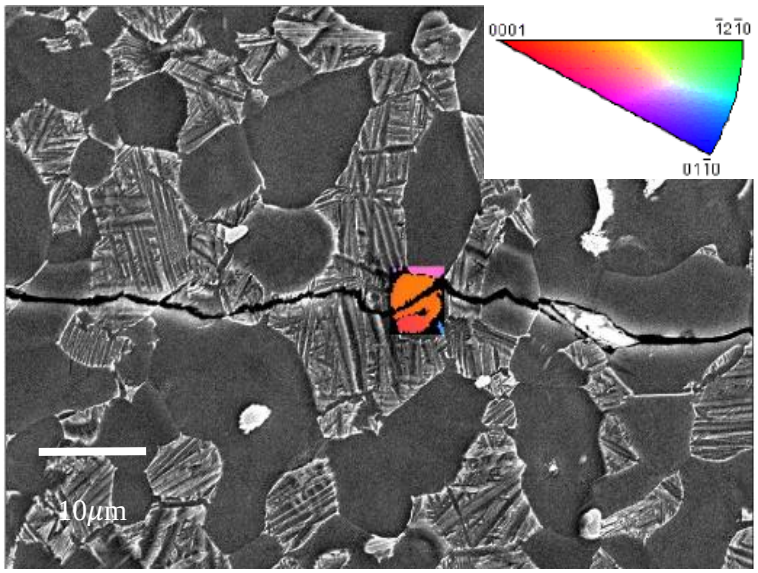

Figure 5.16: An example of transgranular crack growth through a near-basal orientated grain.

5.7 Commercial Impact

Focused development of bespoke titanium alloys, individually suited for specific applications is becoming ever more important to the titanium processing industries. This has been driven over the past decade by competition from technologies such as composite fan blades, as aero engine manufacturers search for new ways to increase efficiency and reduce cost.

The high energy absorption capability and good HCF strength relative to Ti-6-4 make Ti-407 and Ti-412 a considered choice for future containment materials. Coupled with the superior mechanical performance benefits, both alloys offer cost savings and improved sustainability during manufacturing through easier machining. A 6% material yield increase relative to the average across all alloys processed at the TIMET Waunarlwydd plant has already been proven. The development of Ti-407 and Ti-412 has shown that traditional alloy development routes through the optimisation of chemistry, followed by process optimisation, can still offer significant commercial benefits, and retain titanium as the alloy of choice for fan systems of the gas turbine.

The present study has generated a comprehensive mechanical database to support the potential application of Ti-407 and Ti-412 as a future structural alloy. The monotonic and fatigue properties have been evaluated from a range of products processed via traditional forging and ring rolling processes. A fundamental understanding has been developed to describe fatigue crack initiation and crack growth mechanisms.

However, during the course of the study, these alloys have also afforded a greater academic understanding of the cold dwell effect in near α and α/β titanium alloys. This was not envisaged as a core objective of the research since the alloys were never intended for use in dwell sensitive applications. However, fatigue assessments under various waveform frequencies soon indicated that these alloys demonstrate classic dwell performance. Indeed, few studies (if any) have previously employed the full range of cyclic frequencies from HCF, through LCF and dwell loading on a single alloy. This can be considered a unique factor of the present study.

The specific topic of dwell sensitivity arose from industrial application of near α titanium alloys and catastrophic in-service fan disc failures in particular. These events date back some 50 years to the early 1970s. Since this date, concerted efforts have been applied to understanding the dwell effect and help design safety critical rotating components that should avoid dwell failures. Academic and industrial expertise has

developed in the UK and USA in particular and numerous joint research initiatives have been convened, under the auspices of the Federal Aviation Administration (FAA) and Civil Aviation Authority (CAA) for example, over the intervening period. However, fan disc failures still persist as a result of the interaction between dwell loading and adverse microstructures.

Indeed, during the course of this EngD project, a significant engine failure event was reported for a Ti-6-4 fan disc in a Pratt & Whitney engine powering an Air France A380 flying over Greenland in 2017. After a prolonged investigation, the root cause was assigned to dwell fatigue loading in combination with macrozones within the forged fan disc [180]. One of the contributing factors was quoted as:

"engine designer's/manufacturer's lack of knowledge of the cold dwell fatigue phenomenon in the titanium alloy, Ti-6-4"

Their conclusion emphasises the commercial value and potential research impact of the present study.

6 Conclusions

Two novel titanium alloys evaluated in this thesis, Ti-407 and Ti-412, are commercially attractive because they are relatively inexpensive process compared to the most commonly employed titanium variants. Initial testing has shown Ti-407 to display double the tool life compared to Ti-6-4 based on V15 machining tests. Processing data at TIMET indicates Ti-407 to produce a 6% better than average yield, where the average is taken from the other alloys processed at TIMET's Waunarlwydd plant. This, combined with properties that make both Ti-407 and Ti-412 suitable for applications which require high energy absorption, good fracture toughness, and good high cycle fatigue strength, suggest that this pair of alloys has potential to be highly successful within the aerospace, automotive and other commercial sectors.

The main focus of this project was the fatigue performance across pancake forged and ring rolled material stock with particular emphasis placed on understanding the excellent HCF strength. High level conclusions are listed below.

6.1 Pancake Forged Material

- The grain size of the as received Ti-407 forged pancake material was determined to be between 5–10 microns in diameter.
- With the increased vanadium content, the as received Ti-412 microstructure was finer than the Ti-407 material, with primary alpha grain sizes of between 2.5–5 microns.
- Subject to the specific heat treatments applied to both alloys prior to mechanical testing, the effect of grain size was reflected in the tensile properties, with a tensile strength of approximately 765MPa measured for Ti-407, and a strength of 870MPa for Ti-412.
- Compared to the non-standard variants of Ti-6-4 tested, Ti-407 demonstrated a superior HCF fatigue strength. Ten million cycles was achieved at 575MPa for Ti-407, whilst for Ti-6-4, 10 million cycles was achieved at 475MPa.
- A further strength increase was noted for Ti-412 with 10 million cycles achieved at a stress of 700MPa.

- Fractography from the failed Ti-407 and Ti-412 HCF specimens displayed a mixture of surface and subsurface initiation sites. Test pieces where the cracks initiated subsurface tended to demonstrate a stronger fatigue response.
- Quantitative tilt fractography performed on facets exposed on the fatigue fracture surfaces revealed that HCF surface facets were inclined at approximately 30° to the tensile axis, whilst subsurface facets tended to be inclined near 45°.
- EBSD measurements taken directly from the facets of the subsurface initiated cracks on both the Ti-407 and Ti-412 showed faceting to occur near to the pyramidal plane. EBSD from a sectioned view of the test piece then showed the c-axis to be near parallel to the loading direction. This is contrary to the measurements generated from the Ti-6-4 facets which revealed basal plane faceting, on facets angled spatially between 20° and 40°.
- The HCF facet characteristics of the Ti-407 and Ti-412 specimens suggest an increase of <c+a> slip. Further to this, the combination of the low aluminium content and higher strain rate associated with the HCF frequency, suggest deformation twinning to also be a prevalent deformation mechanism. The alternative deformation mechanisms activated for the two new alloys seem to suppress the planar slip on basal planes observed for the Ti-6-4 specimens, and result in a stronger HCF response.
- Ti-407 and Ti-412 require much higher levels of applied stress relative to their static yield strength to initiate fatigue failures compared to Ti-6-4. Under HCF loading, Ti-6-4 achieved 10 million cycles at 55% of yield, whilst for Ti-407 and Ti-412, 10 million cycles were achieved at 90% of yield.
- A large difference in fatigue strength was observed between the high cycle and low cycle fatigue regimes for Ti-407. This was roughly two and a half orders of magnitude at the low end of the stress range. For Ti-412 this difference was smaller, at roughly one and a half orders of magnitude at the low end of the stress range. A further reduction in fatigue strength was noted for both alloys under 120 second dwell loading.
- The general frequency dependence on fatigue response was reduced for Ti-412, which notably contains an increased beta content.

- In contrast to the HCF fracture surfaces, for all LCF and dwell tests, cracks were invariably initiated at the surface and revealed isolated facets of equiaxed morphology.
- Near orthogonal facets were measured under 15cpm LCF and dwell loading waveforms, with spatial angles between 5° and 15°.
- Normalised stress levels were more comparable between Ti-407 and Ti-6-4 under LCF loading conditions.
- For the Ti-407 material, EBSD maps taken from test piece cross sections revealed concentrated areas of basal macrozones.
- Fatigue crack growth studies carried out on Ti-407 demonstrated an independence of crack growth rate across a range of different microstructures.

6.2 Ring Rolled Material

- Ring rolled materials supplied by two different manufacturers demonstrated different microstructures. The manufacturer 1 structure contained relatively elongated primary alpha grains, but these were evenly distributed within the transformed beta. The manufacturer 2 structure on the other hand, contained large bands of high aspect ratio primary alpha grains, which were orientated with a preferred basal plane orientation. It is assumed these differences arise from the precise proprietary thermo-mechanical process routes employed.
- Tensile behaviour was sensitive to orientation in the manufacturer 2 material, with an average proof stress in the axial direction of 664MPa, compared to 574MPa in the tangential direction.
- This orientation dependency was also reflected in the fatigue results. Under HCF loading, 10 million cycles were achieved at 550MPa in the axial direction, compared to 475MPa in the tangential direction.
- No orientation effect was noted in the manufacturer 1 material.
- Sensitivity to orientation was encouraged the by presence of regions of elongated primary alpha grains of common basal orientation.

6.3 Dwell Sensitive Fatigue

Ti-407 and Ti-412 were essentially developed for non-rotating aero-engine applications where low cycle fatigue performance is not a design limiting factor. However, the fundamental understanding of dwell sensitive fatigue has been extended as a result of the present study, not least because it is rare to find data in the open literature that describe the full range of fatigue assessment from a single alloy, i.e. data generated under HCF, LCF and dwell waveforms. A few key points:

- Both Ti-407 and Ti-412 were sensitive to waveform frequency in the general sense (i.e. cycles per unit of time) and the imposition of a dwell period at peak load. Dwell debits were greatest with increasing magnitudes of applied peak stress.
- Both alloys fall within the classification of α/β variants and contained a bi-modal microstructure. Therefore, recognition of the current dwell behaviour is highly relevant to industrial applications, since dwell sensitivity is less commonly reported in these forms of alloy (in particular Ti-6-4, although not entirely absent as recent service experience suggests).
- The sensitivity to dwell is encouraged, however, by the presence of macrozones. Under time dependent plasticity these features encourage stress redistribution over increased length scales.
- HCF loading waveforms restrict the accumulation of plastic deformation accrued per cycle and thereby generate a relatively strong response with crack initiation occurring under traditional local strain dominated mechanisms on inclined planes.
- Fatigue crack initiation in titanium alloys will inevitably be controlled by quasi-cleavage facets forming on specific crystallographic planes, although the present study has highlighted a distinction in preferred plane under HCF and LCF conditions.

7 Future Work

The fatigue performance of Ti-407 and Ti-412 has been comprehensively demonstrated during the present study. This has incorporated detailed characterisation of crack initiation sites and quasi-cleavage facet formation. However, there is potential for a deeper level of understanding to be obtained through the use of a transmission electron microscopy (TEM). Precise thin foils could be extracted from the fracture surfaces immediately through the facets or neighbouring regions to enable more accurate and precise measurement of crystal orientation as well as direct characterisation of activated slip systems and twinning modes.

Focused ion beam (FIB) extraction from the fracture surfaces could help to confirm the characterisation of the HCF subsurface facets described in this thesis. Further to this, the ability to conduct more precise analysis of the facets would allow the determination of the crystallography of the surface HCF facets which, could help to elucidate the superior fatigue performance for subsurface initiated cracks.

The analysis of the LCF and dwell Ti-407 and Ti-412 fracture surfaces revealed surface facets that were near orthogonal relative to the loading direction. The evidence suggests that the initiating mechanism can be described by the Evans/Bache model [74]. However, precise crystallography from the facets and the surrounding grains would help to confirm this.

Three Ti-407 specimens, all tested at a common peak stress condition, one dwell, one LCF and one HCF, have been supplied to Ohio State University, where this form of characterisation can be conducted. Figure 7.1 below, highlights the three specimens sent on the S/N curve. Building on the current work with a more detailed understanding of the deformation mechanisms under HCF loading could aid the development of a model to explain the observed performance. This model could then be utilised during the development of bespoke microstructures and even chemistries when the key consideration is HCF performance.

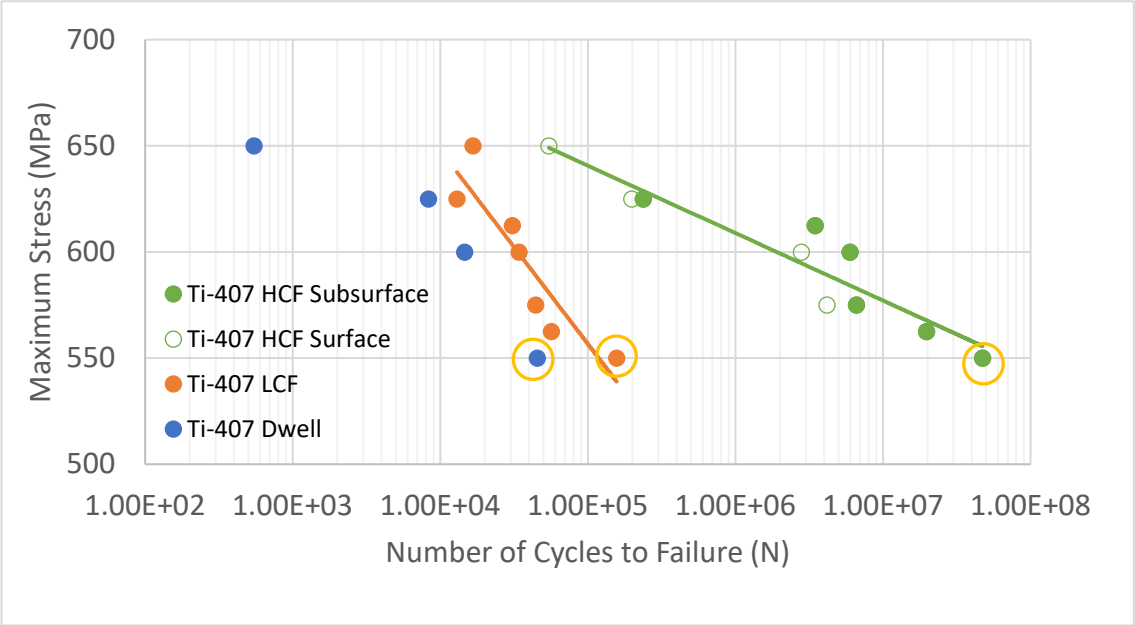

Figure 7.1: Three specimens supplied to Ohio State University.

As well as the work to be carried out at OSU, there are other areas where further work could be carried out to more precisely characterise and understand the performance of Ti-407 and Ti-412. A more detailed study of the dependence of strain rate on deformation mechanism could help to further the understanding of the overall fatigue performance. By determining the strain rate at which deformation by twinning is activated, it could be estimated which fatigue initiating mechanism is likely to be more dominant for a given frequency or waveform.

In the introduction it was mentioned that despite improved machinability as far as tool wear and cutting forces are concerned, the increased ductility and higher thermal conductivity of Ti-407 tends to promote a higher level of subsurface damage. Therefore, an assessment of the effect of these subsurface features on mechanical performance could guide the machining tolerances and help ascertain how much yield is likely to be lost as a result of the introduction of these features.

Further, a more comprehensive study of the effect of microstructural features on mechanical performance could develop a better understanding of processing parameters when developing Ti-407 and Ti-412 components. These features could include grain size, primary alpha volume fraction, levels of grain elongation, and texture levels.

8 References

[1] S. Birosca, “Aerospace Materials Engineering course notes - Titanium Alloys,” pp. 2–3, 2014.

[2] C. Leyens and M. Peters, *Titanium and Titanium Alloys*. Wiley online Library, 2003.

[3] “Greek Mythology.” [Online]. Available: https://www.greekmythology.com/Titans/. [Accessed: 15-Apr-2016].

[4] G. Lutjering and J. C. Williams, *Titanium*, 2nd ed. Berlin Heidelberg New York: Springer-Verlag, 2007.

[5] M. J. Donachie, “Titanium - A technical guide.” p. 6, 1988.

[6] K. M. Kelkar, S. V. Patankar, A. Mitchell, O. Kanou, N. Fukada, and K. Suzuki, “Computational Modeling of the Vacuum Arc Remelting (VAR) Process Used for the Production of Ingots of Titanium Alloys,” in *Proceedings of the Ti-2007 Conference.*, 2007, pp. 2–5.

[7] W. R. Chinnis, “Plasma cold hearth melting of titanium in a production furnace,” *Titan. 1990 Prod. Appl.*, vol. 2, pp. 830–835, 1990.

[8] Q. Liu, X. Li, and Y. Jiang, “Numerical simulation of EBCHM for the large scale TC4 alloy slab ingot during the solidification process,” *Vacuum*, vol. 141, pp. 1–9, 2017.

[9] G. Lutjering and J. C. Williams, *Titanium*, 2nd ed. Berlin: New York Springer, 2007.

[10] D. Eylon and S. S.R, “Titanium ’99, Science and Technology,” *Cris. “Prometery,”* p. 37, 2000.

[11] F. H. Froes, P. G. Allen, and M. Niionmi, “Non-Aerospace Applacations of Titanium,” *TMS*, p. 3, 1998.

[12] C. N. Elias, J. H. C. Lima, R. Valiev, and M. A. Meyers, “Biomedical applications of titanium and its alloys,” *JOM*, vol. 60, no. 3, pp. 46–49, 2008.

[13] D. Hu, A. Dolganov, M. Ma, B. Bhattachrya, M. T. Bishop, and G. Z. Chen, “Development of the Fray-Farthing-Chen Cambridge Process: Towards the Sustainable Production of Titanium and its Alloys,” *JOM*, vol. 70, no. 2, pp. 129–137, 2018.

[14] “Phase diagrams.” [Online]. Available: https://metalsandalloysblog.wordpress.com/tag/phase-diagrams/. [Accessed: 04-Aug-2020].

[15] D. Hull and D. J. Bacon, *Introduction to Dislocations*, 5th ed. Elsevier, 2011.

[16] “Physical Properties of Titanium and its Alloys.” [Online]. Available: http://www.keytometals.com/Article122.htm. [Accessed: 27-Mar-2017].

[17] “Nickel - Properties, Fabrication and Applications of Commercially Pure Nickel.” [Online]. Available: https://www.nickel-alloys.net/commercially_pure_nickel.html. [Accessed: 13-Mar-2017].

[18] C. E. Shamblen, “Embrittlement of titanium alloys by long time, high temperature exposure,” *Metall. Trans.*, vol. 2, no. 1, pp. 277–280, 1971.

[19] C. Pleydell-Pearce, “Gas Turbine Technology - Lecture Notes,” 2015.

[20] R. E. Smallman, *Plasticity of crystals with special reference to metals by E. Schmid and W. Boas*, vol. 25, no. 4. London: F. A. Hughes & Co. Limited, 1969.

[21] J. F. Nye, “Some geometrical relations in dislocated crystals,” *Acta Metall.*, vol. 1, no. 2, pp. 153–162, 1953.

[22] D. Dye, H. J. Stone, and R. C. Reed, “Intergranular and interphase microstresses,” *Curr. Opin. solid state Mater. Sci.*, vol. 5, no. 1, pp. 31–37, 2001.

[23] J. R. Cho, D. Dye, K. T. Conlon, M. R. Daymond, and R. C. Reed, “Intergranular strain

accumalation in a near-alpha titanium alloy during plastic deformation," *Acta Mater.*, vol. 50, no. 19, pp. 4847–4864, 2002.

[24] S. Balasubramanian, "Polycrystalline plasticity: application to deformation processing of lightweight metals," Massachusetts Institute of Technology, 1998.

[25] A. M. Stapleton, S. L. Raghunathan, I. Bantounas, H. J. Stone, T. C. Lindley, and D. Dye, "Evolution of lattice strain in Ti-6Al-4V during tensile loading at room temperature," *Acta Mater.*, vol. 56, no. 20, pp. 6186–6196, 2008.

[26] S. F. Pugh, "Relations between the elastic moduli and the plastic properties of polycrystalline pure metals," *London, Edinburgh, Dublin Philosphical Mag. J. Sci.*, vol. 45, no. 367, pp. 823–843, 1954.

[27] J. Gong and A. Wilkinson, "Anisotropy in the plastic flow properties of single-crystal alpha titanium determined from micro-cantilever beams," *Acta Mater.*, vol. 57, no. 19, pp. 5693–5705, 2009.

[28] A. Madsen and H. Ghonem, "Effects of Aging on the tensile and Fatiue Behaviour of the Near alpha Ti-1100 at Room Temperature and 593 C," *Mater. Sci. Eng. A*, vol. 177, no. 1–2, pp. 63–73, 1994.

[29] A. P. Woodfield and R. E. Smallman, "The effect of long-term high temperature exposure on the structure and properties of the titanium alloy Ti 5331S," *Acta Metall.*, vol. 36, no. 3, pp. 507–515, 1988.

[30] E.-S. M, "Creep deformation behaviour of three high-temperature near alpha-Ti alloys: IMI," *Metall. Mater. Trans. A*, vol. 32, no. 2, pp. 285–293, 2001.

[31] S. L. Semiatin, J. F. Thomas, and P. Dadras, "Processing microstrucutre relationships for Ti-6-Al-2Sn-4Zr-2Mo-0.1Si," *Metall. Trans. A*, vol. 14, no. 11, pp. 2363–2374, 1983.

[32] C. Leyens, P. Manfred, D. Weinem, and W. A. Kaysser, "Influence of long-term annealing on tensile properties and fracture of near-alpha titanium alloy Ti-6Al-2.75Sn-4Zr-0.4Mo-0.45Si," *Metall. Mater. Trans. A*, vol. 27, no. 6, pp. 1709–1717, 1996.

[33] M. G. Mendiratta, A. K. Chakrabarti, and J. A. Roberson, "Embrittlement of Ti-6Al-2Sn-4Zr-2Mo alloy by α2 - phase precipitation," *Metall. Trans.*, vol. 5, no. 8, pp. 1949–1951, 1974.

[34] A. H. Rosenberger, A. Madsen, and H. Ghomen, "Aging effects on the creep behaviour of the near-alpha titanium alloy Ti-1100," *J. Mater. Eng. Perform.*, vol. 4, no. 2, pp. 182–187, 1995.

[35] C. Ramachandra and V. Singh, "Precipitation of the ordered Ti3Al phase in alloy Ti-6.3Al-2Zr-3.3Mo-0.3Si," *Scr. Metall.*, vol. 20, no. 4, pp. 509–512, 1986.

[36] R. A. Wood and R. J. Favor, *Titanium Alloys Handbook*. Ohio, 1972.

[37] J. C. Williams, R. G. Baggerly, and N. E. Paton, "Deformation behaviour of HCP Ti-Al alloy single crytals," *Metall. Mater. Trans. A*, vol. 33, no. 3, pp. 837–850, 2002.

[38] S. Z. Zhang, H. Z. Xu, G. P. Li, Y. Y. Liu, and R. Yang, "Effect of carbon and aging treatment on precipitation of ordered ⌴ 2 in Ti – 5 . 6Al – 4 . 8Sn – 2Zr – 1Mo – 0 . 35Si – 0 . 7Nd alloy," *Mater. Sci. Eng. A*, vol. 408, pp. 290–296, 2005.

[39] S. Z. Zhang, G. P. Li, Q. J. Wang, Y. Y. Liu, and R. Yang, "Effect of carbon on upper (alpha+beta) phase field of Ti-5.6Al-4.8Sn-2.0Zr-1Mo-0.34Si-0.7Nd titanium alloy," *Mater. Sci. Technol.*, vol. 20, no. 2, pp. 167–172, 2004.

[40] D. F. Neal, "Development of Timetal 834," in *Materials Design Approaches and Experiences as held during the TMS Fall Meeting*, 2001, pp. 199–213.

[41] C. Leyens and P. Manfred, *Titanium and titanium alloys: fundamentals and applications*. John Wiley & sons, 2003.

[42] M. Chuddihy, Z. Zheng, J. Gong, T. Britton, A. Wilkinson, and F. Dunne, “Grain size effects in hcp polycrystals: from GND’s to blocky alpha,” 2016.

[43] F. Dunne, A. Walker, and D. Rugg, “A systematic study of HCP crystal orientation and morphology effects in polycrystal deformation and fatigue,” *Proc. R. Scociety London A Mathmatical, Phys. Eng. Sci.*, vol. 463, no. 2082, pp. 1467–1489, 2007.

[44] F. Dunne, D. Rugg, and A. Walker, “Lenghtscale-dependent, elastically anisotropic, physically based hcp crystal plasticity: application to cold-dwell fatigue in Ti-alloys,” *Int. J. Plast.*, vol. 23, no. 6, pp. 1061–1083, 2007.

[45] B. Soran, “Aerospace Materials Engineering - Titanium Alloys Lecutre notes.” p. Part 2-2 Slide 25, 2013.

[46] R. K. Nalla, B. L. Boyce, J. P. Campbell, J. O. Peters, and R. O. Ritchie, “Influence of microstructure on high-cycle fatigue of Ti-6Al-4V: Bimodal vs. lamellar structures,” *Metall. Mater. Trans. A*, vol. 33, no. 13, pp. 899–918, 2002.

[47] S. Kar, T. Searles, and E. Lee, “Modelling the tensile properties in beta-processed alpha/beta Ti alloys,” *Metall. Mater. Trans. A*, vol. 37, no. 3, pp. 559–566, 2006.

[48] E. O. Hall, “The deformation and ageing of mild steel: III discussion of results,” *Proc. Phys. Soc. Sect. B*, vol. 64, no. 9, p. 747, 1951.

[49] N. J. Petch, “The cleavage strenght of polycrystals,” *J. Iron Steel Inst.*, vol. 174, pp. 25–28, 1953.

[50] N. Hansen, “Hall-petch relation and boundary strengthening,” *Scr. Mater.*, vol. 51, no. 8 SPEC. ISS., pp. 801–806, 2004.

[51] G. Q. Wu, C. L. Shi, W. Sha, A. X. Sha, and H. R. Jiang, “Effect of microstructure on the fatigue properties of Ti-6Al-4V titanium alloys,” *Mater. Des.*, vol. 46, pp. 668–674, 2013.

[52] G. Lütjering, “Influence of processing on microstructure and mechanical properties of (α+β) titanium alloys,” *Mater. Sci. Eng. A*, vol. 243, no. 1–2, pp. 32–45, 1998.

[53] M. T. Whittaker, W. J. Evans, R. Lancaster, W. Harrison, and P. S. Webster, “The effect of microstructure and texture on mechanical properties of Ti6-4,” *Int. J. Fatigue*, vol. 31, no. 11–12, pp. 2022–2030, 2009.

[54] P. J. Ashton *et al.*, “The effect of the beta phase on the micromechanical response of dual-phase titanium alloys,” *Int. J. Fatigue*, vol. 100, 2017.

[55] S. Birosca, J. Y. Buffiere, F. A. Garcia-Pastor, M. Karadge, L. Babout, and M. Preuss, “Three-dimensional characteristation of fatigue cracks in Ti-6246 using X-ray tomography and electron backscatter diffraction,” *Acta Mater.*, vol. 57, no. 19, pp. 5834–5847, 2009.

[56] H. Knobbe, P. Köster, H. J. Christ, C. P. Fritzen, and M. Riedler, “Initiation and propagation of short fatigue cracks in forged Ti6Al4V,” *Procedia Eng.*, vol. 2, no. 1, pp. 931–940, 2010.

[57] S. Li, B. Xiong, S. Hui, W. Ye, and Y. Yu, “Effects of microstructure on fatigue crack growth behavior of Ti-6Al-2Zr-1Mo-1V ELI alloy,” *Mater. Charact.*, vol. 59, no. 4, pp. 397–401, 2008.

[58] M. R. Bache and M. Thomas, “Alloy development and optimisation informed by an understanding of cold dwell fatigue sensitivity,” in *14th World Conference on Titanium*, 2019.

[59] S. Birosca, “Aerospace Materials Engineering Lecture Notes - Mechanical Design,” pp. 5–13, 2015.

[60] P. C. Collins, B. Welk, T. Searles, J. Tiley, C. Russ, and H. L. Fraser, “Development of methods for the quantification of microstructural features in alpha + beta processed alpha/beta titanium alloys,” *Mater. Sci. Eng. A*, vol. 508, no. 1–2, pp. 174–182, 2009.

[61] Y. Fei, L. Zhou, H. Qu, Y. Zhao, and C. Huang, “The phase and microstructure of

TC21 alloy," *Mater. Sci. Eng. A*, vol. 494, no. 1–2, pp. 166–172, 2008.

[62] G. E. Dieter, *Mechanical Metallurgy*, SI Metric. Materials Science and Metallurgy, 1988.

[63] "ASTM International," 2016. [Online]. Available: https://www.astm.org/. [Accessed: 25-Mar-2016].

[64] G. P. Sendeckyj, "Constant life diagrams - a historical review," *Int. J. Fatigue*, vol. 23, no. 4, pp. 347–353, 2001.

[65] M. R. Bache, "The effects of texture in titanium alloys for engineering components under fatigue," *Int. J. Fatigue*, vol. 23, pp. 153–159, 2001.

[66] "S-N Fatigue Properties." [Online]. Available: https://www.nde-ed.org/EducationResources/CommunityCollege/Materials/Mechanical/S-NFatigue.htm. [Accessed: 10-Dec-2019].

[67] W. A. Wood, *Some Basic Studies of Fatigue in Metals, in "Fracture."* New York: John Wiley & sons, 1959.

[68] X. Liu, C. Sun, and Y. Hong, "Faceted crack initiation characteristics for high-cycle and very-high-cycle fatigue of a titanium alloy under different stress ratios," *Int. J. Fatigue*, vol. 92, pp. 434–441, 2016.

[69] K. S. Chain, "Roles of microstructure in fatigue crack initiation," *Int. J. Fatigue*, vol. 32, no. 9, pp. 1428–1447, 2010.

[70] W. A. Wood, "No Title," *Bull. Inst*, vol. 3, pp. 5–6, 1955.

[71] "Fatigue Properties." [Online]. Available: https://www.nde-ed.org/EducationResources/CommunityCollege/Materials/Mechanical/Fatigue.htm. [Accessed: 05-Jun-2016].

[72] A. H. Stroh, "The formation of cracks as a result of plastic flow," *Proc. R. Scociety London A Mathmatical, Phys. Eng. Sci.*, vol. 223, no. 1154, pp. 404–414, 1954.

[73] M. R. Bache, "A review of dwell sensitive fatigue in titanium alloys: the role of microstructure, texture and operating conditions," *Int. J. Fatigue*, vol. 25, no. 9–11, pp. 1079–1087, 2003.

[74] W. J. Evans and M. R. Bache, "The role of hydrogen in cyclic and dwell sensitive fatifue of a near alpha titanium alloy," *Froes FH*, pp. 1693–1700, 1993.

[75] C. Laird, "Fatigue Crack Propagation," *ASTM Spec. Tech*, no. Publ. 415, pp. 131–168, 1967.

[76] C. Pleydell-Pearce, "Structural Integrity of Aerospace Metals course notes," 2015.

[77] J. M. Larsen, B. D. Worth, C. G. Annis, and F. K. Haake, "An Assessment of the role of near-threshold crack growth in high-cycle-fatigue life prediction of aerospace titanium alloys under turbine engine spectra," *Int. J. Fract.*, vol. 80, no. 2–3, pp. 237–255, 1996.

[78] K. Tokaji, S. Takafuji, K. Ohya, Y. Kato, and K. Mori, "Fatigue behaviour of beta Ti-22V-4Al alloy subjected to surface-microstructural modification," *J. Mater. Sci.*, vol. 38, no. 6, pp. 1153–1159, 2003.

[79] T. Fett, D. Munz, and G. Thun, "Influence of frequency on cyclic fatigue of coarse grained Al2O3," *J. Mater. Sci. Lett.*, vol. 12, no. 4, pp. 220–222, 1993.

[80] H. Mayer and C. Laird, "Influence of cyclic frequency on strain localisation and cyclic deformation in fatigue," *Int. J. Fatigue*, vol. 18, no. 1, p. 62, 1996.

[81] Z. Kloenne, G. B. Viswanathan, M. Thomas, M. H. Lorreto, and H. L. Fraser, "A Comparative Study on the Substructure Evolution and Mechanical Properties of TIMETAL 407 and TI-6-4," in *Matec Web of Conferences*, 2019.

[82] L. D. Roth, L. E. Willertz, and T. R. Leax, "On the Fatigue of Copper up to Ultrasonic Frequencies," *Proc. First Int. Conf. Fatigue Corros. Fatigue up to Ultrason. Freq.*, pp.

265–282, 1981.

[83] M. Peters, A. Gysler, and G. LUtjering, “Influence of texture on fatigue properties of Ti-6Al-4V,” *Metall. Mater. Trans. A*, vol. 15, no. 8, pp. 1597–1605, 1984.

[84] X. Demulsant and J. Mendez, “Influence of environment on low cycle fatigue damage in Ti6Al4V and Ti 6246 titanium alloys,” *Mater. Sci. Eng. A*, vol. 219, no. 1–2, pp. 202–211, 1996.

[85] S. Adachi, L. Wagner, and G. Luetjering, “Influence of Mean Stress on the fatigue strength of Ti-6Al-4V,” *Proc. 7th Int. Conf. Strength Met. Alloy.*, pp. 2117–2122, 1986.

[86] S. Adachi, L. Wagner, and G. Luetjering, “Influence of Mean Stress on Fatigue Crack Nucleation in (alpha+beta) Ttanium Alloys,” *Int. Conf. Fatigue Egnineering Mater. Struct.*, pp. 67–74, 1986.

[87] J. O. Peters and R. O. Ritchie, “Foreign-object damage and high-cycle fatigue: role of microstructure in Ti–6Al–4V,” *Int. J. Fatigue*, vol. 23, pp. 413–421, 2001.

[88] M. A. Moshier, T. Nicholas, and B. M. Hillberry, “Load history effects on fatigue crack growth threshold for Ti–6Al–4V and Ti-17 titanium alloys,” *Int. J. Fatigue*, vol. 23, pp. 253–258, 2001.

[89] R. K. Nalla, J. P. Campbell, and R. O. Ritchie, “Mixed-mode, high-cycle fatigue-crack growth thresholds in Ti-6Al-4V: Role of small cracks,” *Int. J. Fatigue*, vol. 24, no. 10, pp. 1047–1062, 2002.

[90] “Fatigue Crack Growth Analysis Review.” [Online]. Available: https://www.engineersedge.com/material_science/fatigue_crack_growth_analysis_review_10071.htm. [Accessed: 30-May-2016].

[91] C. Pleydell-Pearce, “Fatigue Lifing Lifing Methods Methods Course Overview : Unit Overview : Fatigue Lifing Methods,” pp. 1–21, 2014.

[92] M. Ciavarella, “A ‘crack like’ notch analouge for a safe-life fretting fatigue design methodology,” *Fatigue Fract. Eng. Mater. Struct.*, vol. 26, no. 12, pp. 1159–1170, 2003.

[93] “Fail-Safe and Safe-Life Designs And Factor of Safety.” [Online]. Available: https://faculty.up.edu/lulay/MEStudentPage/failsafe.pdf. [Accessed: 06-Jul-2016].

[94] X. Zhang, M. Boscolo, D. Figueroa-Gordon, G. Allegri, and P. E. Irving, “Fail-safe design of integral metallic aircraft structures reinforced by bonded crack retarders,” *Eng. Fract. Mech.*, vol. 76, no. 1, pp. 114–133, 2009.

[95] W. J. Evans, “‘Advanced Lifing Correlations’ course notes.” Swansea, 2017.

[96] J. Goodman, *Mechanics applied to engineering*. Longmans, 1918.

[97] T. Nicholas, “Critical issues in high cycle fatigue,” *Int. J. Fatigue*, vol. 21, pp. 221–231, 1999.

[98] S. G. Ivanova, F. S. Cohen, R. R. Biederman, and R. D. Sisson Jr, “Role of microstructure in the mean stress dependence of fatigue strenght in Ti-6Al-4V alloy,” in *TMS Fall meeting ’98*, 1999.

[99] A. W. Bowen, “The effect of testing direction on the fatigue and tensile properties of a Ti-6Al-4V bar,” *Titan. Sci. Technol.*, pp. 1271–1281, 1973.

[100] I. Bantounas, D. Dye, and T. C. Lindley, “The effect of grain orientation on fracture morphology during high-cycle fatigue of Ti-6Al-4V,” *Acta Mater.*, vol. 57, no. 12, pp. 3584–3595, 2009.

[101] G. Lutjering, “Influence of processing on microstructure and mechanical properties of (alpha+beta) titanium alloys,” *Mater. Sci. Eng. A*, vol. 243, no. 1–2, pp. 32–45, 1998.

[102] M. R. Bache and W. J. Evans, “Impact of texture on mechanical properties in an advanced titanium alloy,” *Mater. Sci. Eng. A*, vol. 319, pp. 409–414, 2001.

[103] L. Germain and M. R. Bache, “Crystallographic texture and the definition of effective

structural unit size in titanium products," in *Ti-2007 Science and Technology*, 2007, pp. 953–956.

[104] J. Qiu, Y. Ma, J. Lei, A. Huang, D. Rugg, and R. Yang, "A comparative study on dwell fatigue of Ti-6Al-2Sn-4Zr-xMo (x= 2 to 6) alloys on a microstructure-normalised basis," *Metall. Mater. Trans. A*, vol. 45, no. 13, pp. 6075–6087, 2014.

[105] A. J.Ready, P. D. Haynes, B. Grabowski, D. Rugg, and A. P. Sutton, "The role of molybdenum in suppressing cold dwell fatigue in titanium alloys," *Proc. R. Scociety A Mathmatical, Phys. Eng. Sci.*, vol. 473, no. 2203, 2017.

[106] P. Ruffles, "Aerospace structural materials: present and future," *Materials World*, vol. 3, no. 10, pp. 469–470, 1995.

[107] P. Pugh, *The magic of a name, the Rolls-Royce story, part 2: the power behind the jets 1945-1987*. Icon Books/Totem Books, 2001.

[108] Z. Zheng, D. S. Balint, and F. P. E. Dunne, "Discrete dislocation and crystal plasticity analyses of load shedding in polycrystalline titanium alloys," *Int. J. Plast.*, vol. 87, pp. 15–31, 2016.

[109] W. J. Evans and M. R. Bache, "The role of hydrogen in cyclic and dwell sensitive fatigue of a near alpha titanium alloy," *Titan. '92 Sci. Technol.*, vol. 1, 1993.

[110] G. M, P. Lefranc, V. Doquet, and C. Sarrazin-Baudoux, "Deformation and damage mechanisms in alpha/beta 6242 Ti alloy in fatigue, dwell-fatigue and creep at room temperature. Influence of internal hydrogen," *Mater. Sci. Eng. A*, vol. 507, no. 1–2, pp. 132–143, 2008.

[111] S. Gosh, M. Mills, S. I. Rokhlin, V. Sinah, W. Soboyejo, and J. Williams, "No Title," 2007.

[112] V. Sinah, R. B. Schwarz, M. J. Mills, and J. C. Williams, "Influence of hydrogen on dwell-fatigue response of near-alpha titanium alloys," *Acta Mater.*, vol. 188, pp. 315–327, 2020.

[113] J. E. Hack and G. R. Leverant, "The influence of microstructure on the susceptibility of titanium alloys to internal hydrogen embrittlement," *Metall. Trans. A*, vol. 13, no. 10, pp. 1729–1738, 1982.

[114] W. J. Evans and M. R. Bache, "Hydrogen and fatigue behaviour in a near alpha titanium alloy," *Scr. Metall. Mater.*, vol. 32, no. 7, pp. 1019–1024, 1995.

[115] "Titanium Forgings - 3000 Tonne Hydralic Forging Press and 8 Ton Hydralic Forging Manipulator," *Sia Magazine*. [Online]. Available: https://siamagazin.com/titanium-forgings-3000-ton-hydraulic-forging-press-8-ton-hydraulic-forging-manipulator/. [Accessed: 03-Apr-2019].

[116] "Closed Die Forgings." [Online]. Available: https://www.aubertduval.com/products/forgings-aerospace-titanium-steel-aluminum-superalloy-closed-die-hammer-drop-forge/. [Accessed: 03-Apr-2019].

[117] A. G. Mamalis and W. Johnson, "Rolling of rings," *Int. Met. Rev.*, vol. 24, no. 1, 1979.

[118] J. M. Allwood, A. E. Tekkaya, and T. F. Stanistreet, "The Development of Ring Rolling Technology," *Steel Res. Int.*, vol. 76, no. 2–3, 2016.

[119] "The Ring Rolling Process," 2014. [Online]. Available: https://www.totalmateria.com/page.aspx?ID=CheckArticle&site=kts&NM=421. [Accessed: 30-Jan-2019].

[120] J. T. Yeom, H. J. Kim, N. K. Park, S. S. Choi, and C. S. Lee, "Ring-rolling design for a large-scale ring product of Ti-6Al-4V alloy," *J. Mater. Process. Technol.*, vol. 187–188, 2007.

[121] A. Kluge, Y.-H. Less, H. Wiegels, and R. Kopp, "Control of strain and temperature distribution in the ring rolling process," *J. Mater. Process. Technol.*, vol. 45, no. 1–4, pp. 137–141, 1994.

[122] L. YanXiang, Z. ShiAn, L. Ping, and Z. YaoZong, “A study of the precision rolling and thermomechanical treatment of bearing rings,” *J. Mater. Process. Technol.*, vol. 31, no. 1–2, pp. 179–187, 1992.

[123] A. Kharina and D. Rutherford, “Fuel Efficiency Trends for New Commercial Jet Aircraft: 1960 to 2014,” Berlin Brussels San Francisco Washington, 2015.

[124] D. S. Lee *et al.*, “Aviation and global climate change in the 21st century,” *Atmos. Environ.*, vol. 43, no. 22–23, pp. 3520–3537, 2009.

[125] “Global Market Forecast 2006-2026,” Airbus, France.

[126] A. Macintosh and L. Wallace, “International aviation emissions to 2025: Can emissions be stablised without restricting demand?,” *Energy Policy*, vol. 37, no. 1, pp. 264–273, 2009.

[127] M. Prather, R. Sausen, A. S. Grossman, J. M. Haywood, D. Rind, and B. H. Subbaraya, “Potential climate change from aviation,” *Aviat. Glob. Atmos.*, pp. 185–215, 1999.

[128] “Abradable Coatings Increase Gas Turbine Efficiency,” 2001. [Online]. Available: https://www.azom.com/article.aspx?ArticleID=739. [Accessed: 18-Jan-2019].

[129] “The Jet Engine: A Historical Introduction.” [Online]. Available: https://cs.stanford.edu/people/eroberts/courses/ww2/projects/jet-airplanes/how.html. [Accessed: 14-Feb-2019].

[130] *Rolls Royce - The Jet Engine*, 5th ed. Wiley, 1996.

[131] “Advanced Material Technology.” [Online]. Available: https://www.amt-advanced-materials-technology.com/materials/titanium-high-temperature/. [Accessed: 19-Feb-2019].

[132] R. R. Boyer, “An overview on the use of titanium in the aerospace industry,” *Mater. Sci. Eng. A*, vol. 213, no. 1–2, pp. 103–114, 1996.

[133] “Airbus says A380 superjumbo production will end,” 2019. [Online]. Available: https://www.bbc.com/news/business-47231504. [Accessed: 14-Feb-2019].

[134] D. Thomas, “Why did the Airbus A380 Fail?,” 2019. [Online]. Available: https://www.bbc.com/news/business-47225789. [Accessed: 14-Feb-2019].

[135] R. Wood and R. Favor, *Titanium Alloys Handbook*. Ohio: Metals and Ceramics Information Center, 1972.

[136] “No Title,” 2017. [Online]. Available: www.timet.com. [Accessed: 31-Oct-2017].

[137] H. J. Siekmann, “How to machine titanium,” *Tool Eng.*, vol. 34, no. 1, pp. 78–82, 1995.

[138] R. Komanduri and W. R. Reed, “Evalutation of carbide grades and a new cutting geometry for machining titanium alloys,” *Wear*, vol. 92, no. 1, pp. 113–123, 1983.

[139] E. O. Ezugwu and Z. M. Wang, “Titanium alloys and their machinability - a review,” *J. Mater. Process. Technol.*, vol. 63, no. 3, pp. 262–274, 1997.

[140] M. Rahman, Y. S. Wong, and A. R. Zareena, “Machinability of titanium alloys,” *JSME Int. J. Ser. C Mech. Syst. , Mach. Elem. Manuf.*, vol. 46, no. 1, pp. 107–115, 2003.

[141] H. Matsumoto, H. Yoneda, D. Fabregue, E. Maire, A. Chiba, and F. Gejima, “Mechanical behaviours of Ti-V-(Al, Sn) alloys with alpha prime martensite microstructure,” *J. Alloys Compd.*, vol. 509, no. 6, pp. 2684–2692, 2011.

[142] S. James, Y. Kosaka, R. Thomas, and P. Garratt, “Reduction, Timetal 407: A Titanium Alloy To Enable Cost Reduction,” in *Proceedings of the 13th World Conference on Titanium*, 2016.

[143] C. Dredge, R. M’Saoubi, B. Thomas, O. Hatt, M. Thomas, and M. Jackson, “A low-cost machinability approach to accelerate titanium alloy development,” *Proc. Inst. Mech. Eng. Part B J. Eng. Manuf.*, 2020.

[144] L. Kimsey, “What is radial, tangential and axial?,” 2017. [Online]. Available:

https://www.quora.com/What-is-radial-tangential-and-axial. [Accessed: 10-Sep-2019].

[145] "ETMM." [Online]. Available: https://www.etmm-online.com/what-is-electrical-discharge-machining-and-how-does-it-work-a-689686/. [Accessed: 13-Nov-2019].

[146] M. R. Bache, M. Cope, H. M. Davies, W. J. Evans, and G. Harrison, "Dwell sensitive fatigue in a near alpha titanium alloy at ambiant temperature," *Int. J. Fatigue*, vol. 19, no. 1, pp. 583–588, 1997.

[147] G. Q. Wu, C. L. Shi, W. Sha, A. X. Sha, and H. R. Jiang, "Effect of microstructure on the fatigue properties of Ti-6Al-4V titanium alloys," *Mater. Des.*, vol. 46, pp. 668–674, 2013.

[148] G. Wegmann, G. Lutjering, and J. Alberecht, "Improvement of the properties of (alpha + beta) titanium castings by modification of the lamellar structure.," *Titan. '95 Sci. Technol.*, pp. 895–901, 1996.

[149] Z. Shi, H. Guo, J. Han, and Z. Yao, "Microstructure and mechanical properties of TC21 titanium alloy after heat treatment," *Trans. Nonferrous Met. Soc. China*, vol. 23, no. 10, pp. 2882–2889, 2013.

[150] "Mipar," 2019. [Online]. Available: https://www.mipar.us/. [Accessed: 25-Sep-2019].

[151] J. Krautkrämer, H. Krautkrämer, T. Kundu, A. J. Croxford, P. D. Wilcox, and B. Drinkwater, "Standard Practice for Conducting Force Controlled Constant Amplitude Axial Fatigue Tests of Metallic Materials," *J. Appl. Phys.*, vol. 58, no. 3, pp. 6737–6741, 2006.

[152] "BS EN 2002-1:2005 Tensile testing at ambiant temperature."

[153] "No TMaterials, ASTM E92 - 82: Standard Test Method for Hardness of Metallicitle," 1997.

[154] "BS 3518-1:1993; 'Methods of fatigue testing. Guide to general principles.'"

[155] "BS EN 3987:2009. Aerospace Series. Test methods for metallic materials. Constant amplitude force-controlled high cycle fatigue testing," 2009.

[156] "BS 6072:2010 Aerospace series. Metallic materials. Test methods - Constant amplitude fatigue testing.," 2010.

[157] "BS ISO 12106:2017 'Metallic materials. Fatigue testing. Axial strain controlled method.'"

[158] "ASTM E647 - 15el: 'Standard Test Method for Measrument of Fatigue Crack Growth Rates.'"

[159] "Dirlik Controls," 2018. [Online]. Available: http://dirlik.co.uk/fatigue-crack-growth-and-threshold.html. [Accessed: 22-Apr-2021].

[160] L. M. Gammon, R. D. Briggs, J. M. Packard, K. W. Batson, R. Boyer, and C. W. Domby, "Metallography and Microstructures of Titaium and Its Alloys," *ASM Handb. 9*, pp. 899–917, 2004.

[161] T. Ben Britton, S. Birosca, M. Preuss, and A. Wilkinson, "Electron backscatter diffraction study of dislocation content of a macrozone in hot-rolled Ti-6Al-4V alloy," *Scr. Mater.*, vol. 62, no. 9, pp. 639–642, 2010.

[162] "OXFORD Instruments," 2021. [Online]. Available: https://nano.oxinst.com/products/aztec/. [Accessed: 22-Apr-2021].

[163] J. I. Goldstein, D. E. Newbury, J. R. Michael, N. W. Ritchie, J. H. J. Scott, and D. C. Joy, *Scanning electron microscopy and X-ray microanalysis*. Springer, 2017.

[164] G. Themelis, S. Chikwembani, and J. Weertman, "Determination of the orienation of Cu Bi grain boundary facets using a photogrammetric technique," *Mater. Charact.*, vol. 24, no. 1, pp. 27–40, 1990.

[165] G. Welsch, R. Boyer, and E. W. Collings, *Materials properties handbook: titanium*

alloys. ASM International, 1993.

[166] M. R. Bache, “Processing titanium alloys for optimum performance,” *Int. J. Fatigue*, vol. 21, pp. 105–111, 1999.

[167] S. Jha and J. Larsen, “No Title,” in *Proceedings of the fourth international conference on very high cycle fatigue*, 2007, pp. 385–396.

[168] V. Sinah, M. J. Mills, and J. C. Williams, “Determination of crystallographic orientation of dwell-fatigue fracture facets in Ti-6242 alloy,” *J. Mater. Sci.*, vol. 42, no. 19, pp. 8334–8341, 2007.

[169] S. K. Jha, C. J. Szczepanski, P. J. Golden, W. J. Porter III, and R. John, “Characterization of fatigue crack-initation facets in relation to lifetime variability in Ti-6Al-4V,” *Int. J. Fatigue*, vol. 42, pp. 248–257, 2012.

[170] J. C. Williams, R. G. Baggerly, and N. E. Paton, “Deformation behaviour of HCP Ti-Al alloy single crystals,” *Metall. Mater. Trans. A*, vol. 33, no. 3, pp. 837–850, 2002.

[171] M. Zakaria and W. Xu, “Response of titanium alloys to high strain rate deformation,” *Mater. Sci. Technol.*, vol. 21, no. 2, pp. 225–231, 2005.

[172] J. Everaets, B. Verlinden, and M. Wevers, “Investigation of fatigue crack initiation facets in Ti-6Al-4V using focused ion beam milling and electron backscatter diffraction,” *J. Microsc.*, vol. 267, pp. 57–69, 2017.

[173] A. L. Pilchak, R. E. A. Williams, and J. C. Williams, “Crystallography of fatigue crack initation and growth in fully lamellar Ti-6Al-4V,” *Metall. Mater. Trans. A*, vol. 41, no. 1, p. 106, 2010.

[174] M. R. Bache, W. J. Evans, and H. M. Davies, “Electron back scattered diffraction (EBSD) analysis of quasi-cleavage and hydrogen induced fractures under cyclic and dwell loading in titanium alloys,” *J. Mater. Sci.*, vol. 32, pp. 3435–3442, 1997.

[175] W. J. Evans and M. . Bache, “Dwell-sensitive fatigue under biaxial loads in the near-alpha titanium alloy IMI685,” *Int. J. Fatigue*, vol. 16, no. 7, pp. 443–452, 1994.

[176] W. J. Evans, “Optimising mechanical properties in alpha+beta titanium alloys,” *Mater. Sci. Eng. A*, vol. 243, pp. 89–96, 1998.

[177] S. H. Spence, W. J. Evans, and M. Cope, “Dwell fatigue on Ti 6246 at near ambiant temperatures.,” *Adv. Fract. Res.*, vol. 9, no. 3, pp. 1571–1578, 1997.

[178] G. Shroeder, J. Alberecht, and G. Lutjering, “Microstructure and mechanical properties of titaniun alloys with bi-lamellar microstructures.,” *Titan. ’95 Sci. Technol.*, pp. 545–552, 1996.

[179] K. Nakajima, K. Terao, and T. Miyata, “The effect of microstructure on fatigue crack propagation of α+β titanium alloys,” *Mater. Sci. Eng. A*, vol. 243, no. 1–2, pp. 176–181, 1998.

[180] “Technical Report - Accident to the Airbus A380 registered F-HPJE and operated by Air France on 30/09/2017 en route over Greenland,” 2019.

9 Appendices

Appendix A: Microstructures of Tested Product Forms

Appendix A display more detailed microstructures of the tested product forms in order to fully characterize the differences across alloys (Ti-407, Ti-6-4, Ti-412 and Ti-834) and product form (pancake forged and ring rolled for Ti-407). Four images for each product form are displayed (500x, 1000x, 5000x, and 10,000x) magnification.

A1: Ti-407 Manufacturer 1 Ring Rolled Microstructure

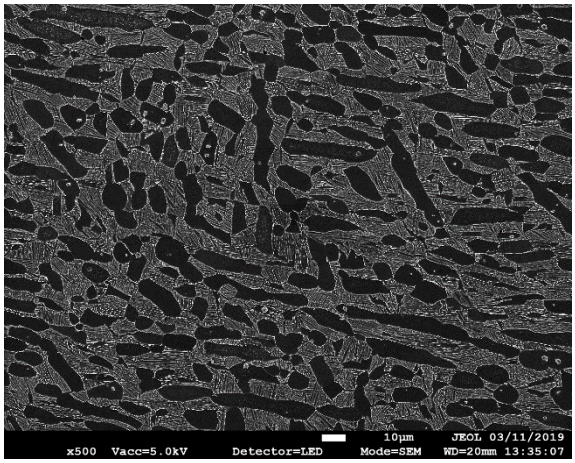

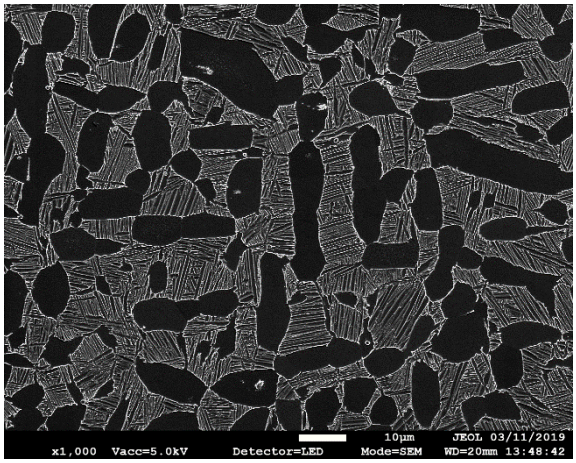

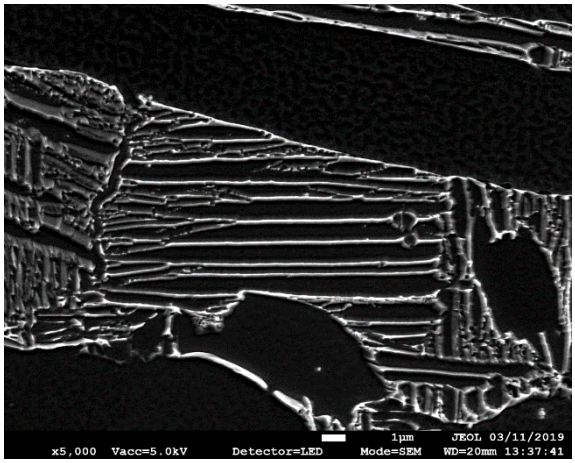

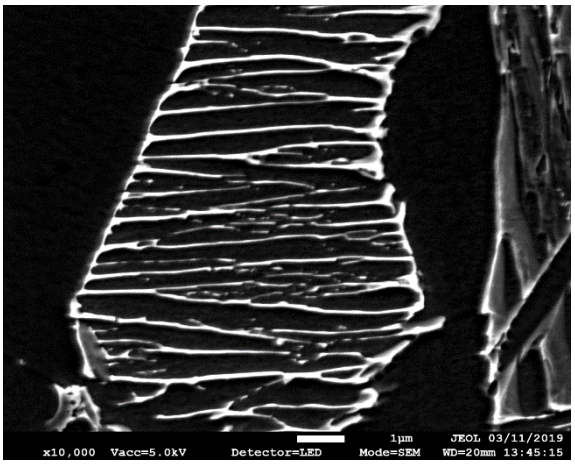

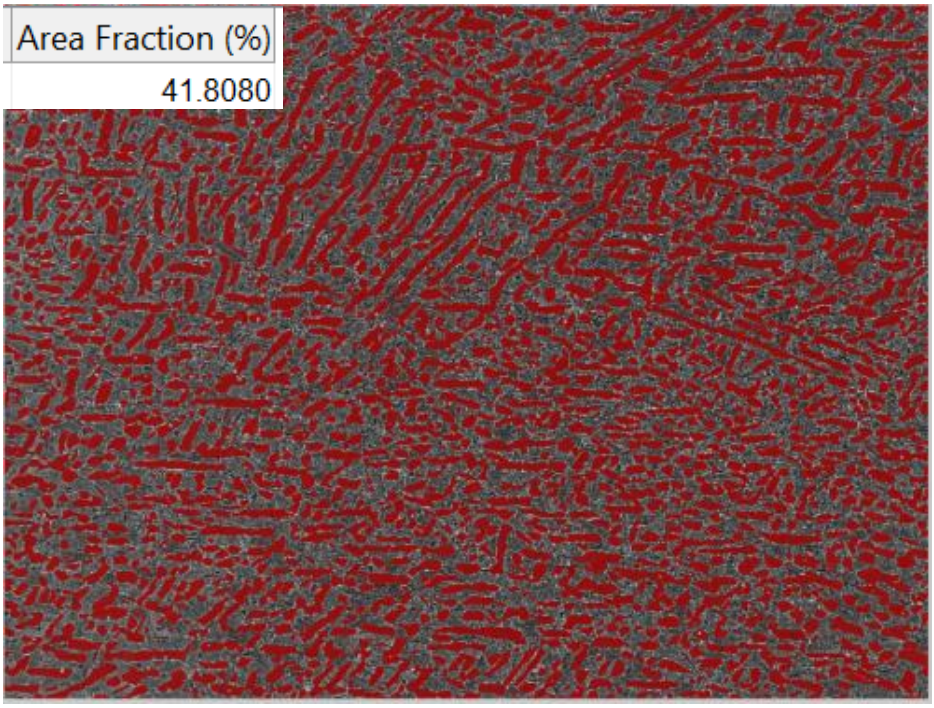
Area Fraction (%)
41.8080

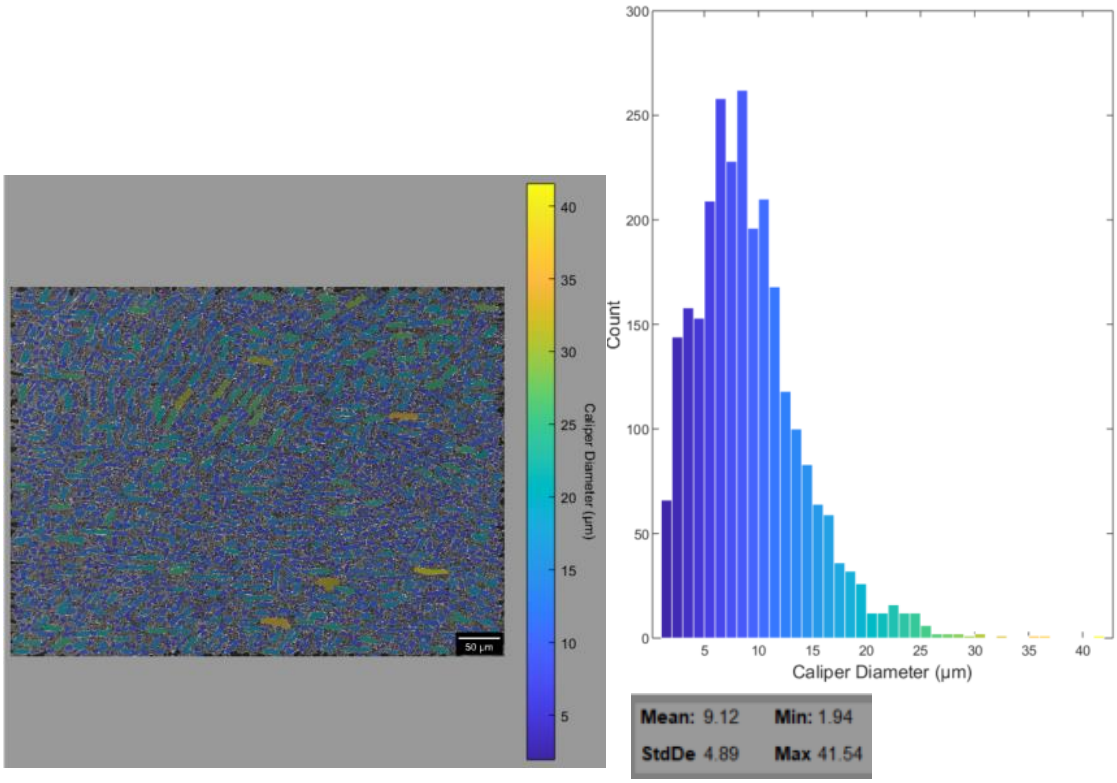
50 µm
Caliper Diameter (µm)
40
35
30
25
20
15
10
5
Count
300
250
200
150
100
50
0
5
10
15
20
25
30
35
40
Caliper Diameter (µm)
Mean: 9.12
Min: 1.94
StdDe 4.89
Max 41.54

A2: Ti-407 Manufacturer 2 Ring Rolled Microstructure

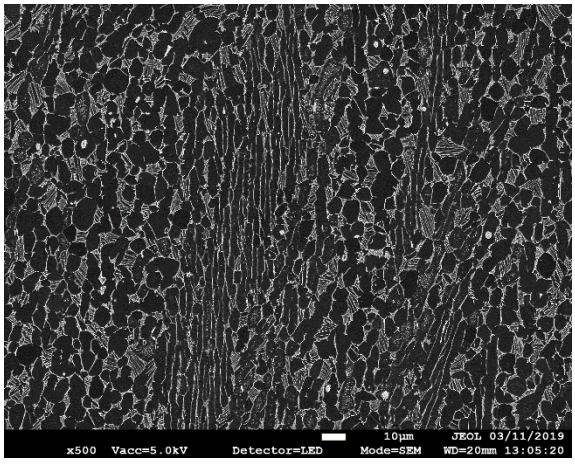

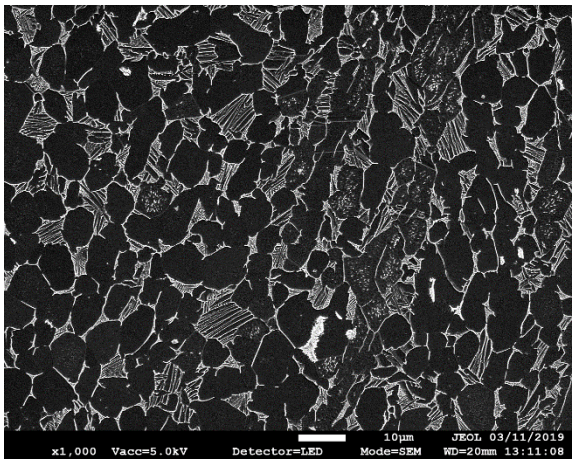

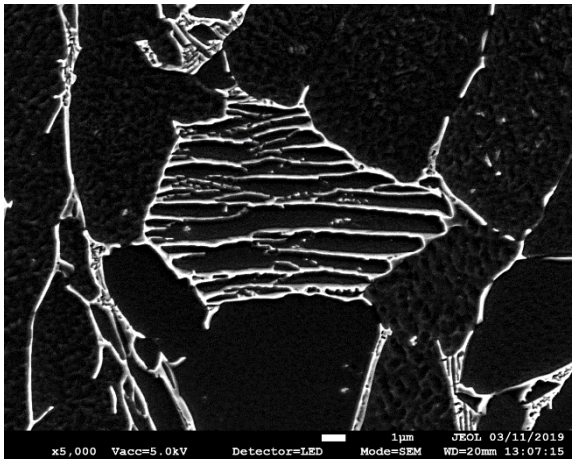

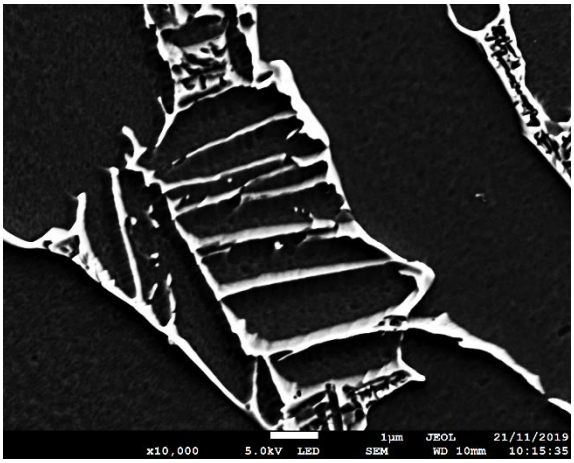

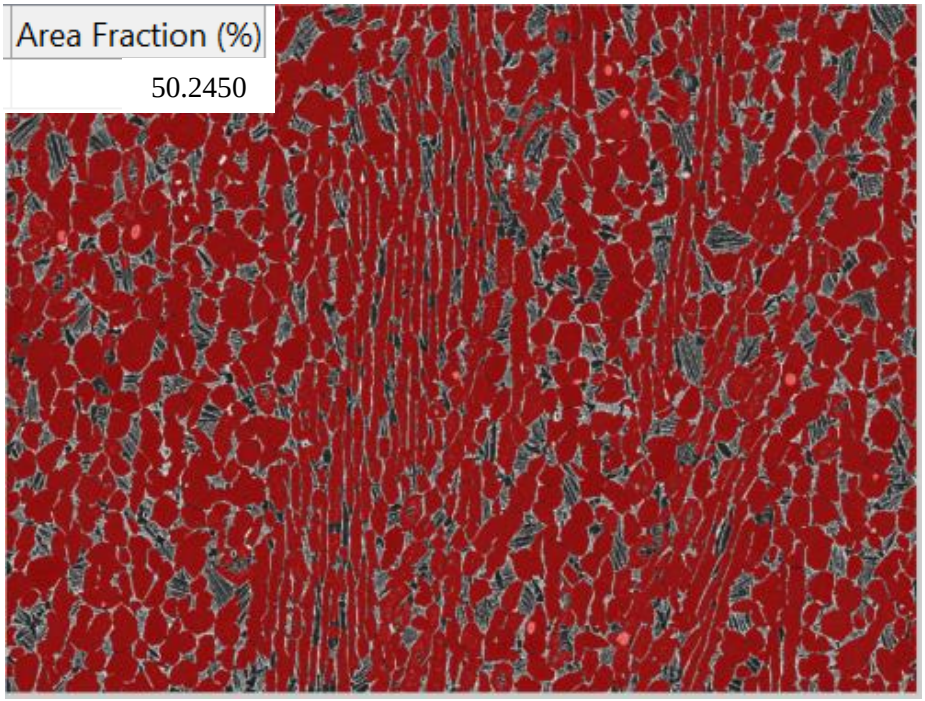
Area Fraction (%)
50.2450

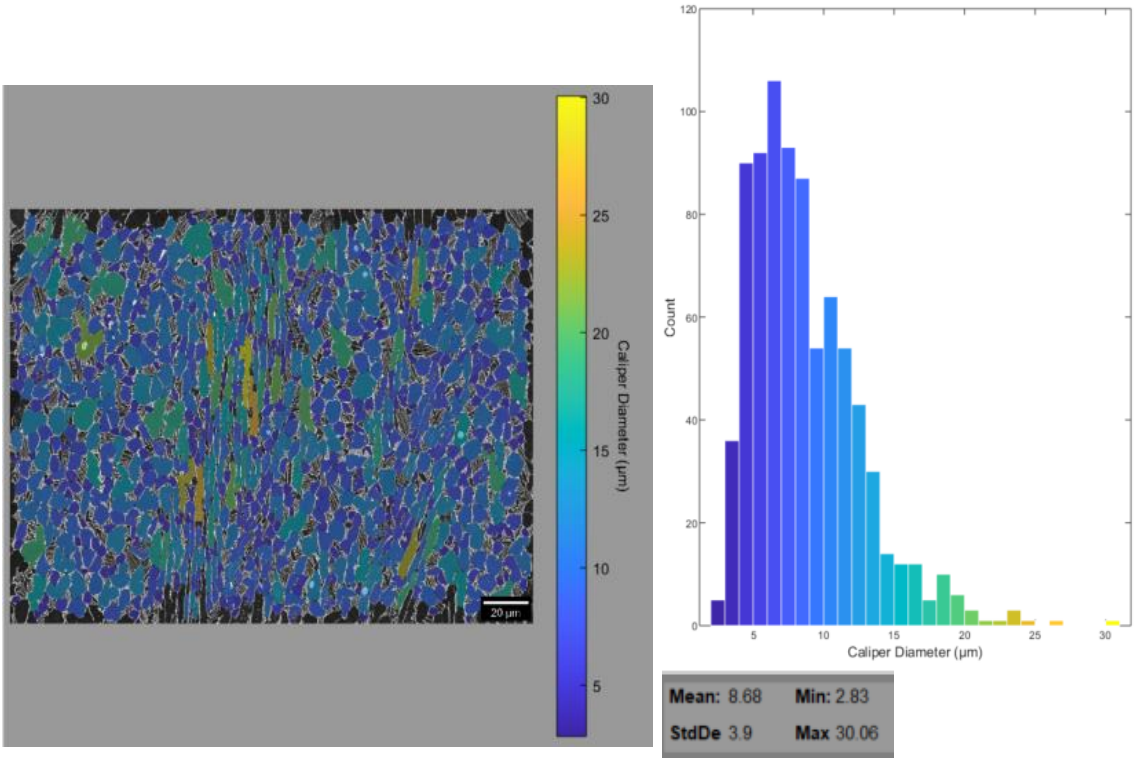
30
25
20
15
10
5
Caliper Diameter (µm)
20 µm
120
100
80
60
40
20
0
Count
5
10
15
20
25
30
Caliper Diameter (µm)
Mean: 8.68
Min: 2.83
StdDe 3.9
Max 30.06

A3: Ti-407 Pancake Forged Microstructure

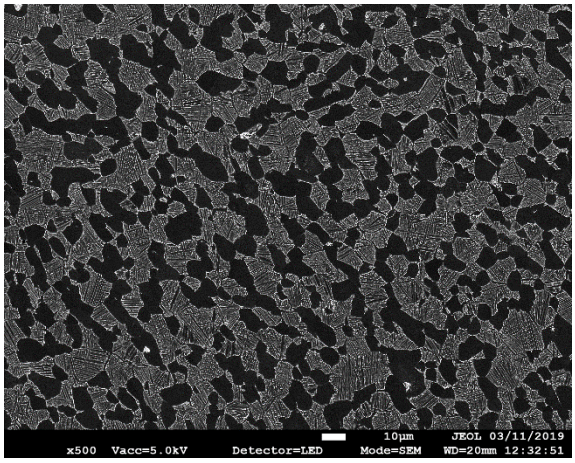

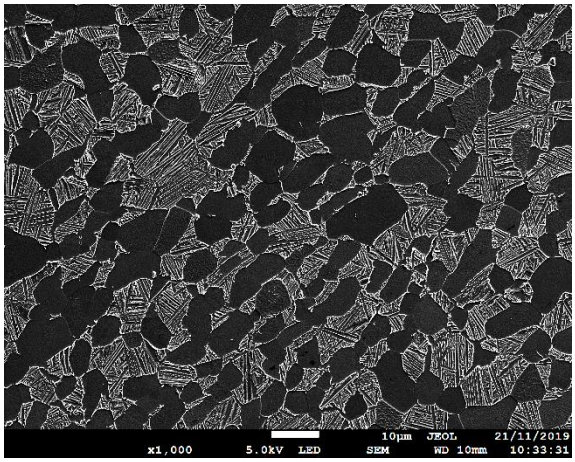

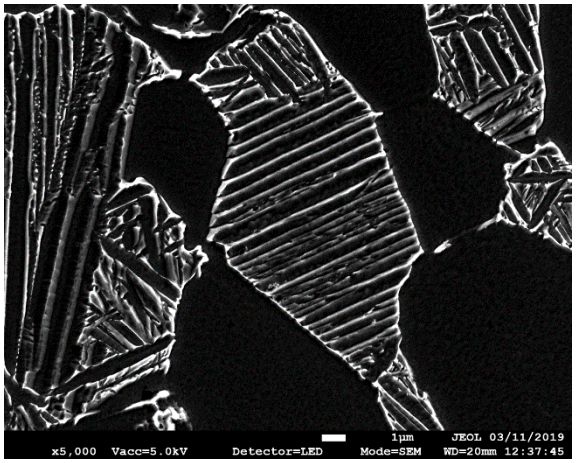

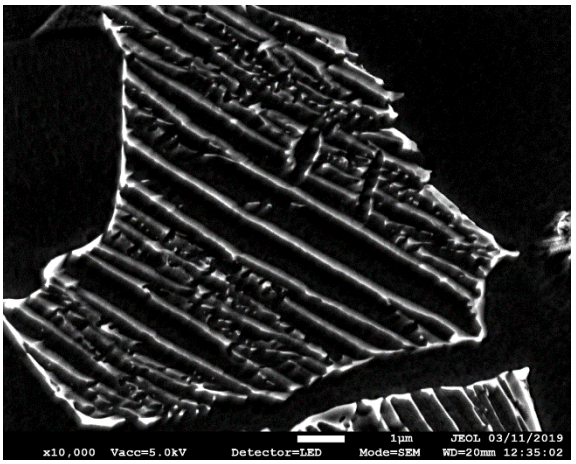

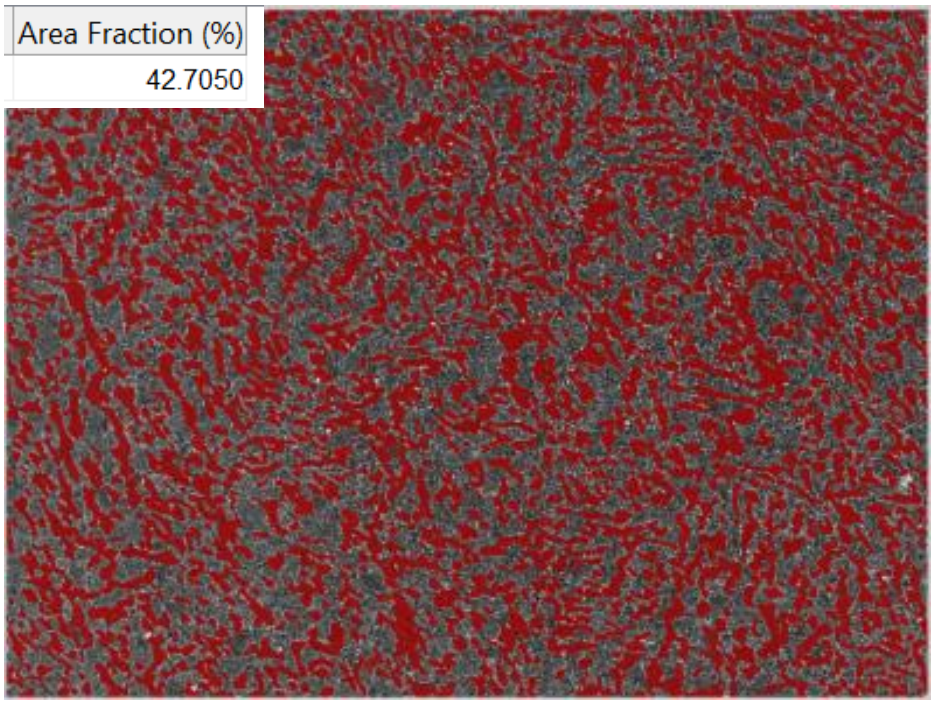
Area Fraction (%)
42.7050

`

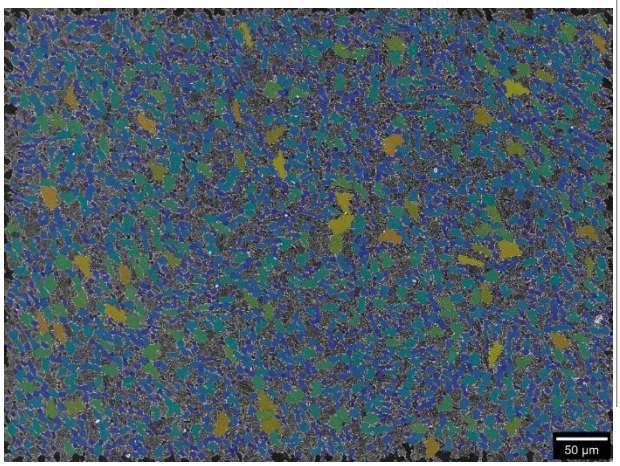
50 µm

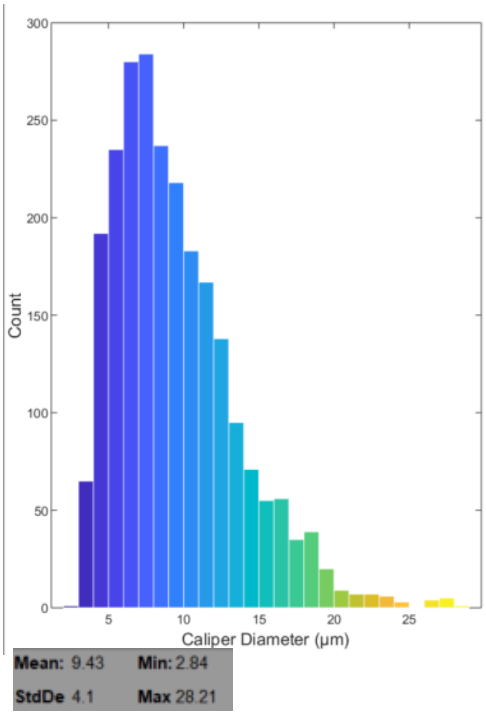
300
250
200
150
100
50
0
Count
5
10
15
20
25
Caliper Diameter (µm)
Mean: 9.43
Min: 2.84
StdDe 4.1
Max 28.21

A4 Ti-6-4 Pancake Forged Aged

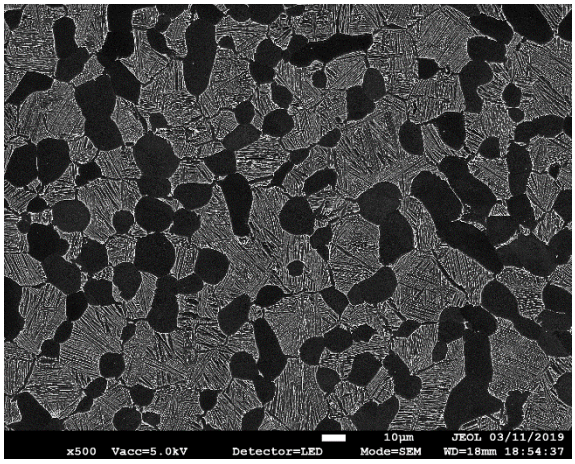

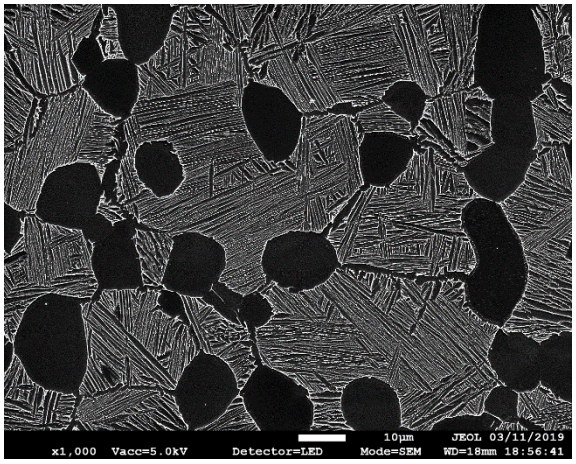

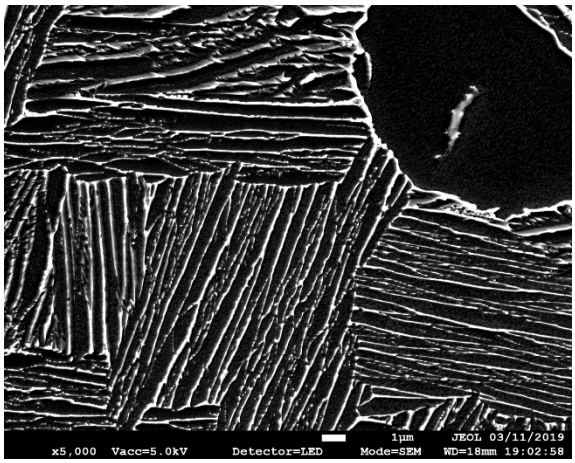

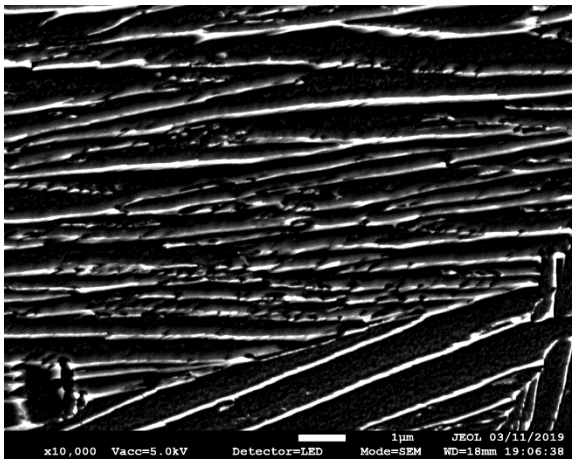

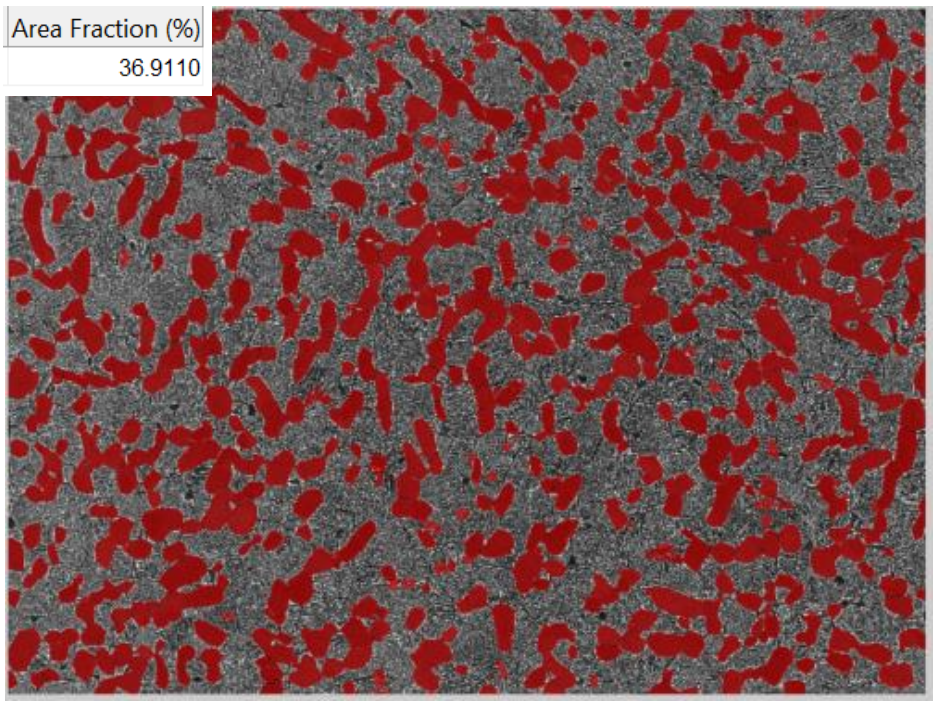

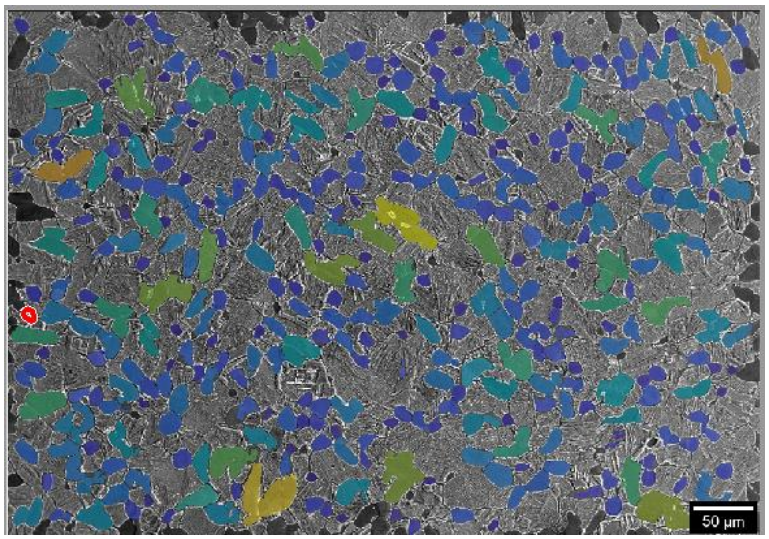

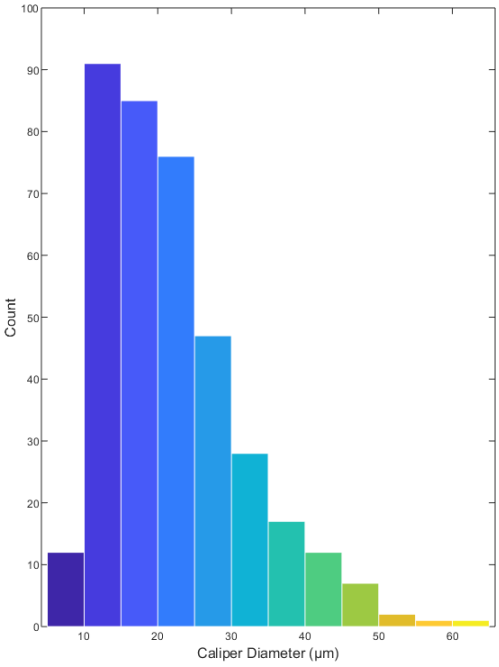

Mean: 21.88 **Min:** 8.1
StdDe 9.75 **Max** 64.62

A5: Ti-6-4 Pancake Forged Annealed

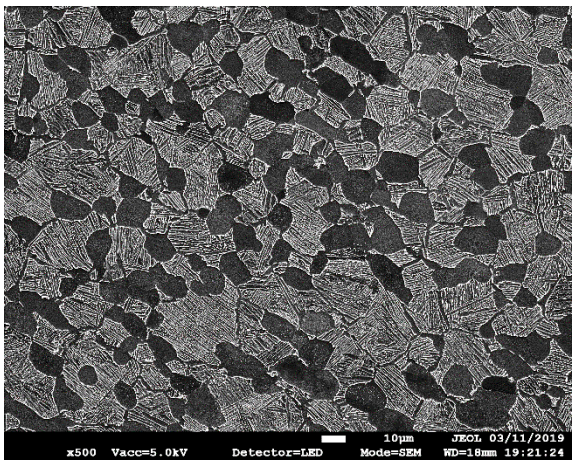

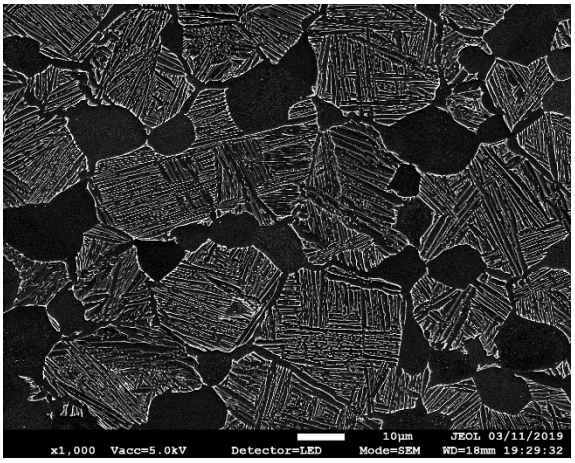

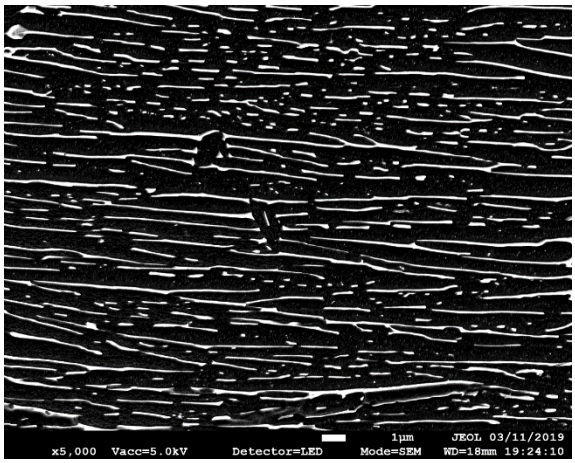

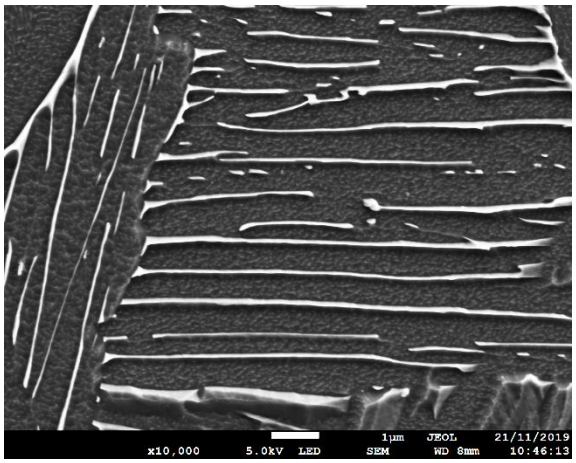

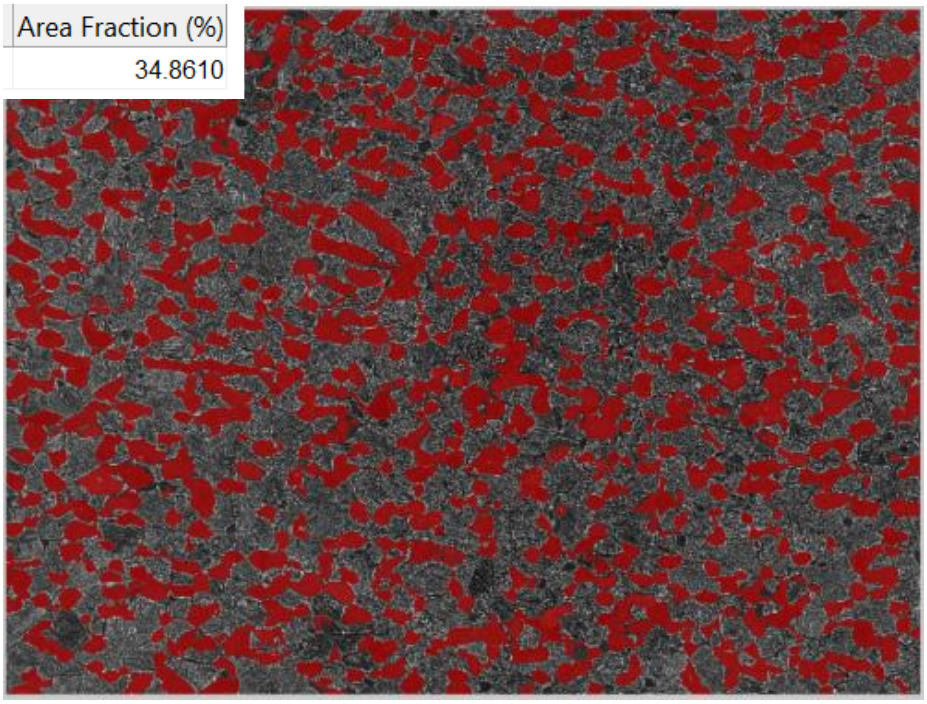

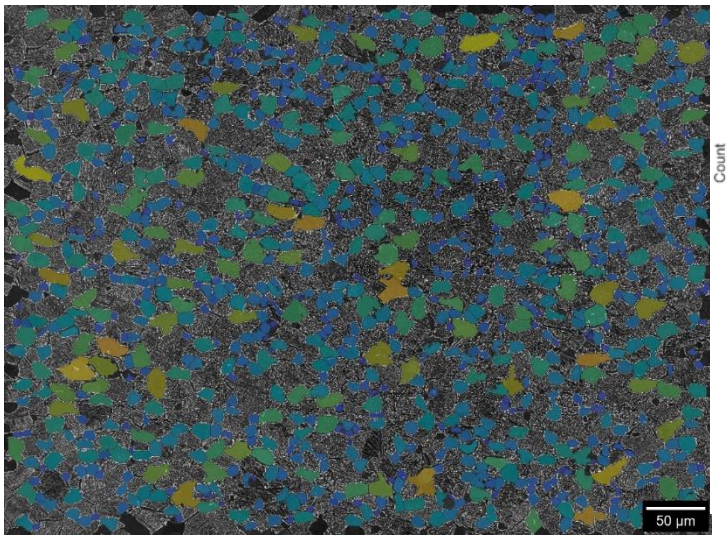

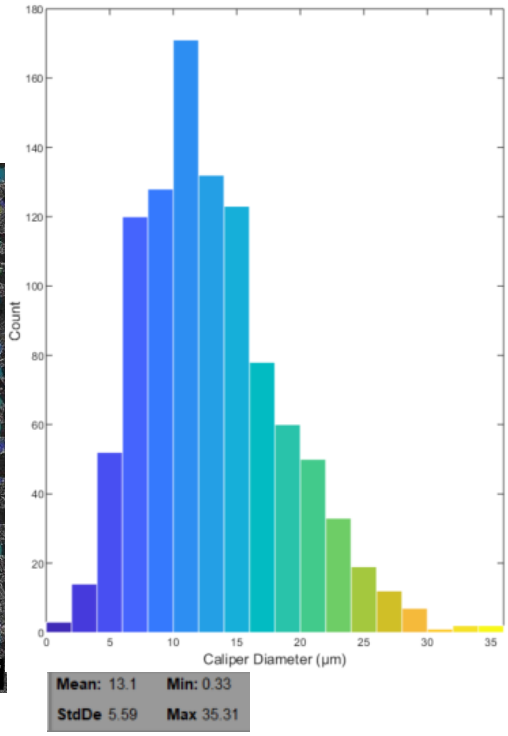

Mean: 13.1 **Min:** 0.33
StdDe 5.59 **Max** 35.31

A6: Ti-412 Pancake Forged

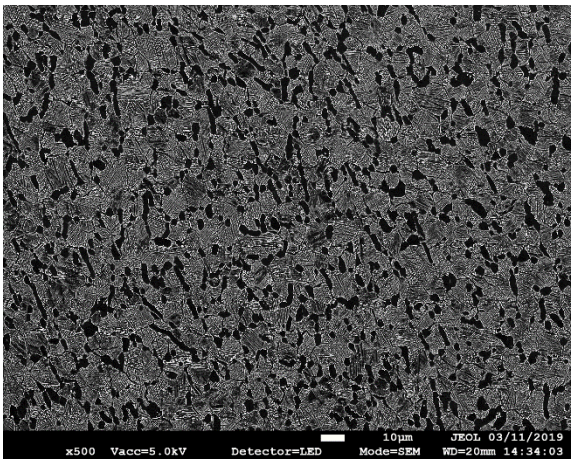

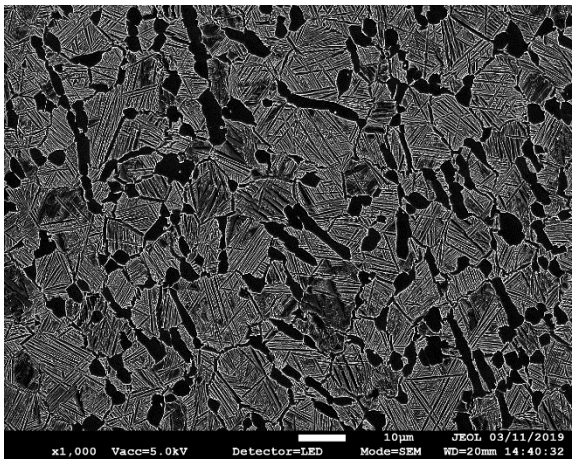

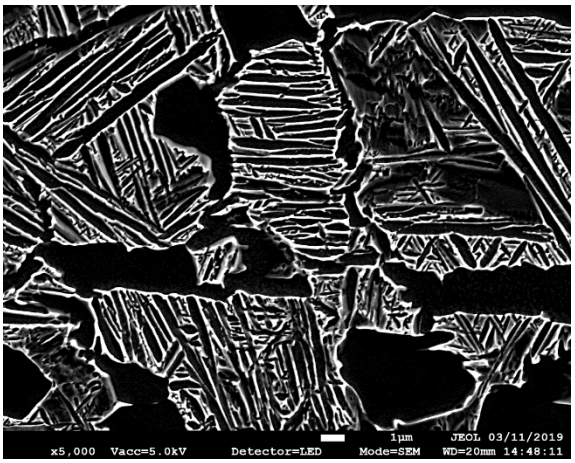

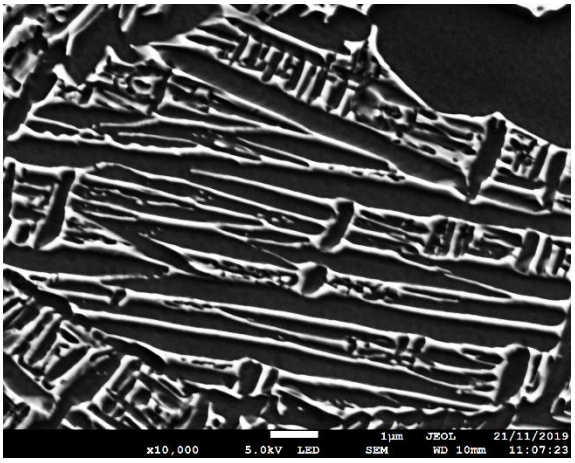

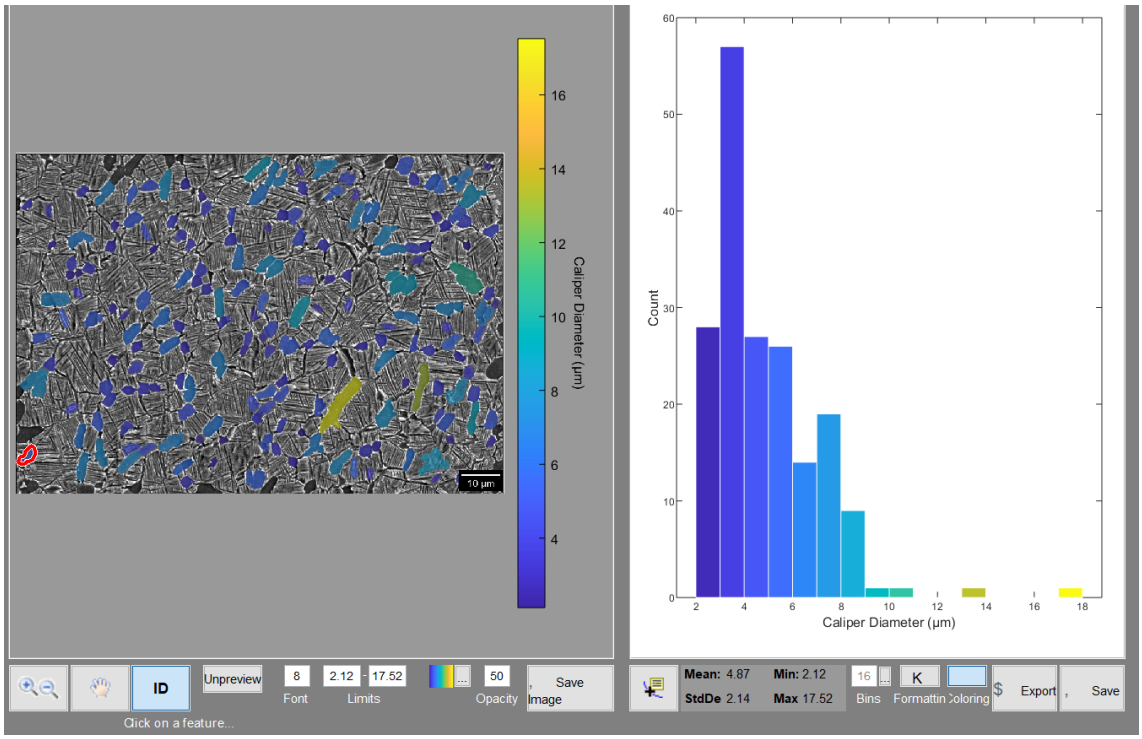

A7: Ti-834 Microstructure

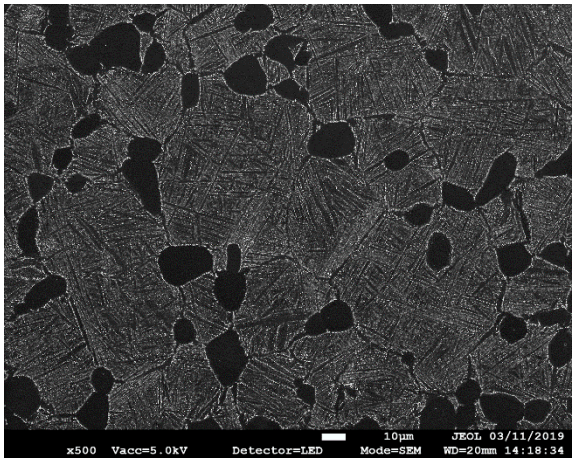

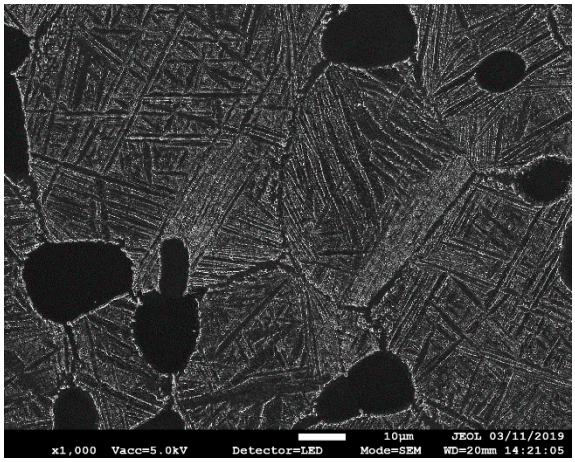

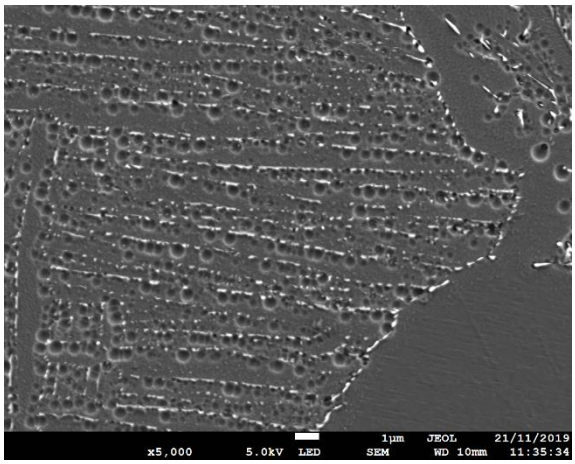

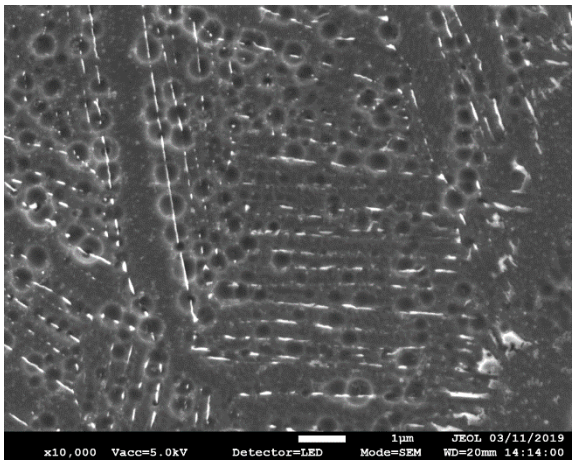

Appendix B: Images Used for Quantitative Tilt Fractography Angle Calculation

The images are displayed in 2 columns of 3. The column on the left displays the facets at 0 degrees tilt with the top image displaying the coordinates of point A, the middle image point B and the bottom image point C. An example of the excel spread sheet used is available on request.

B1: Flat Check

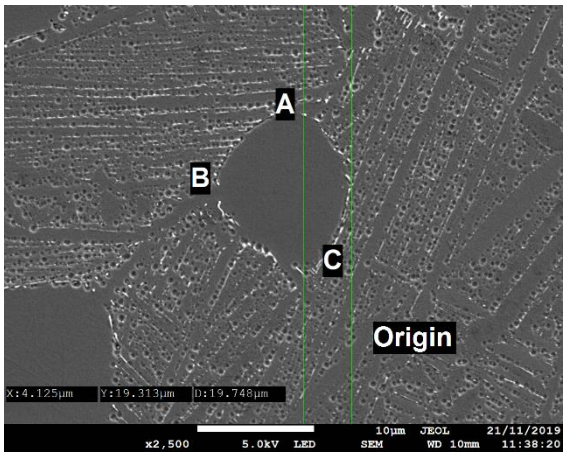

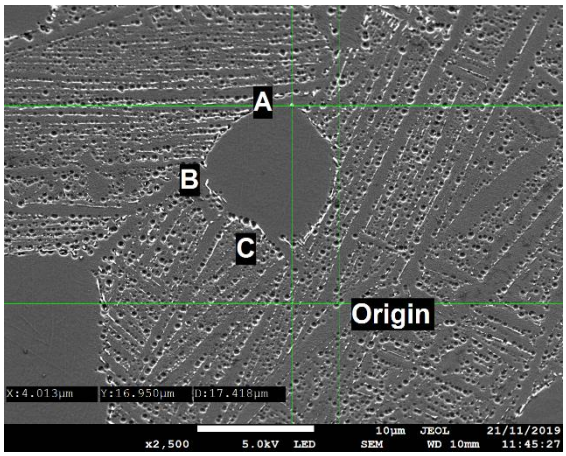

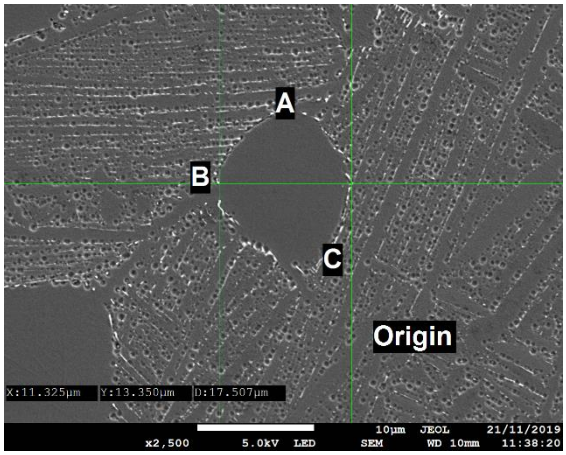

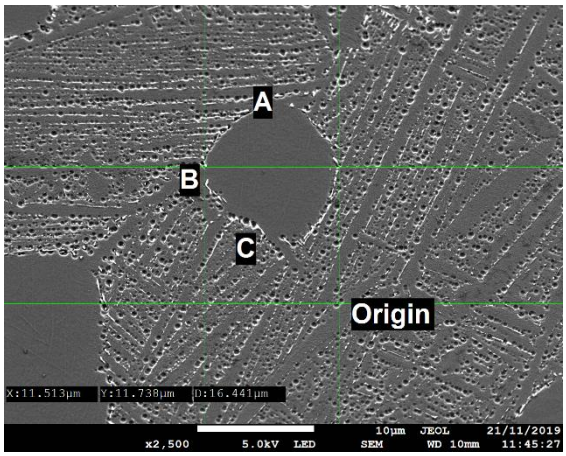

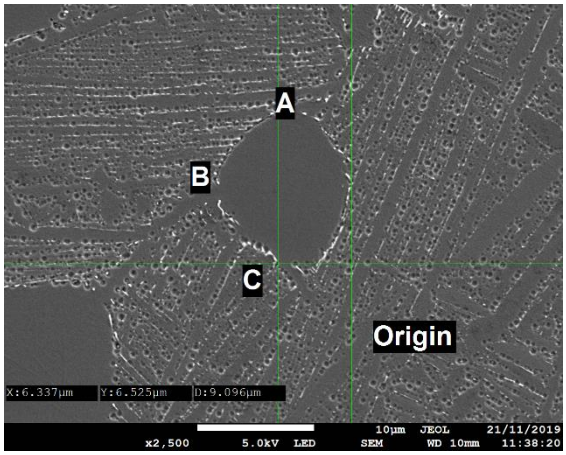

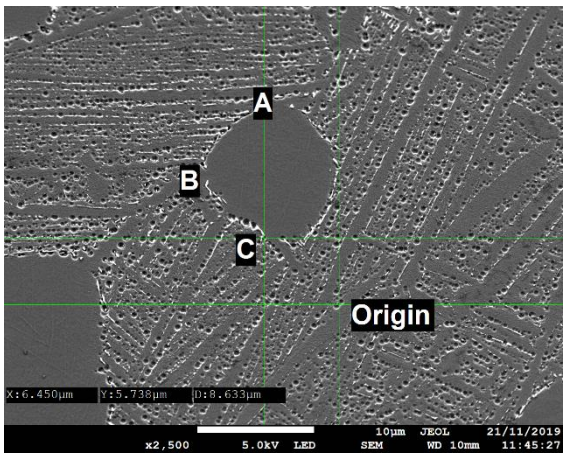

B2: Q1-4 Facet 1

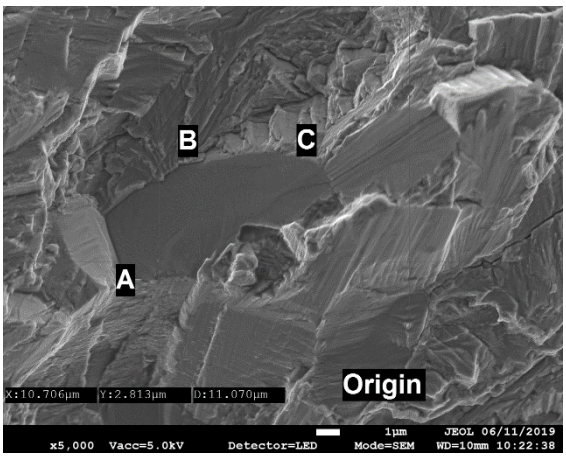

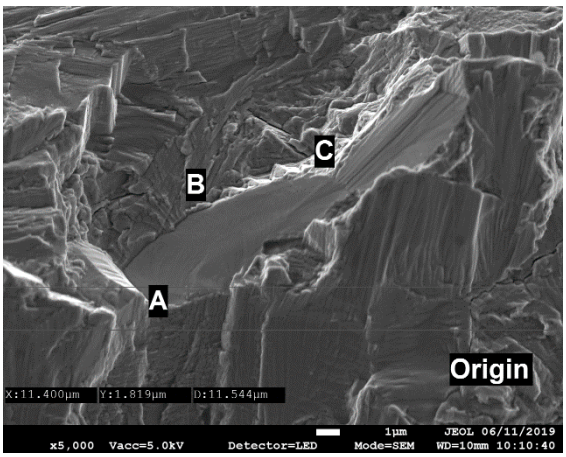

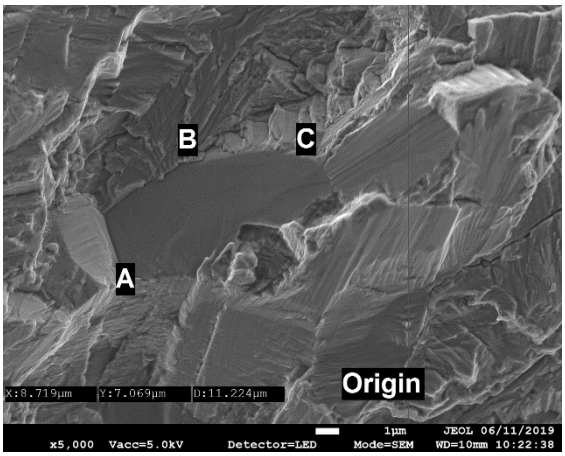

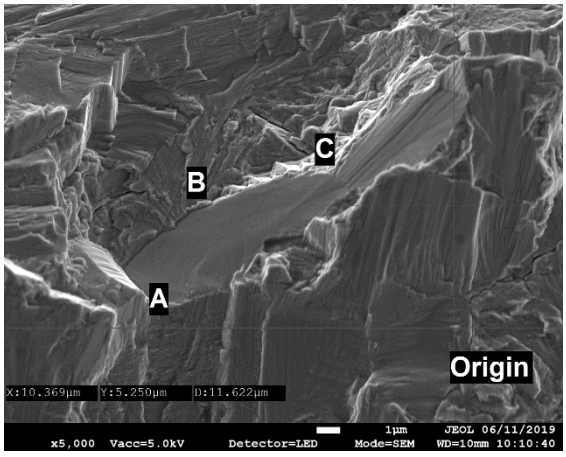

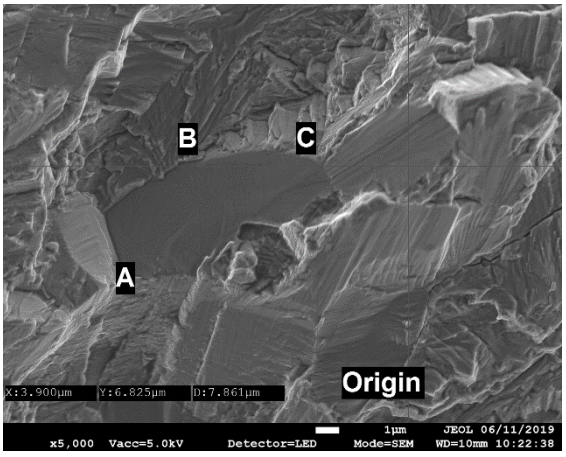

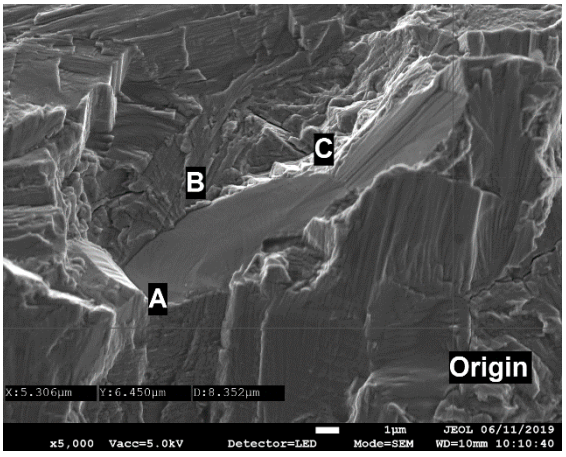

B3: Q1-4 Facet 2

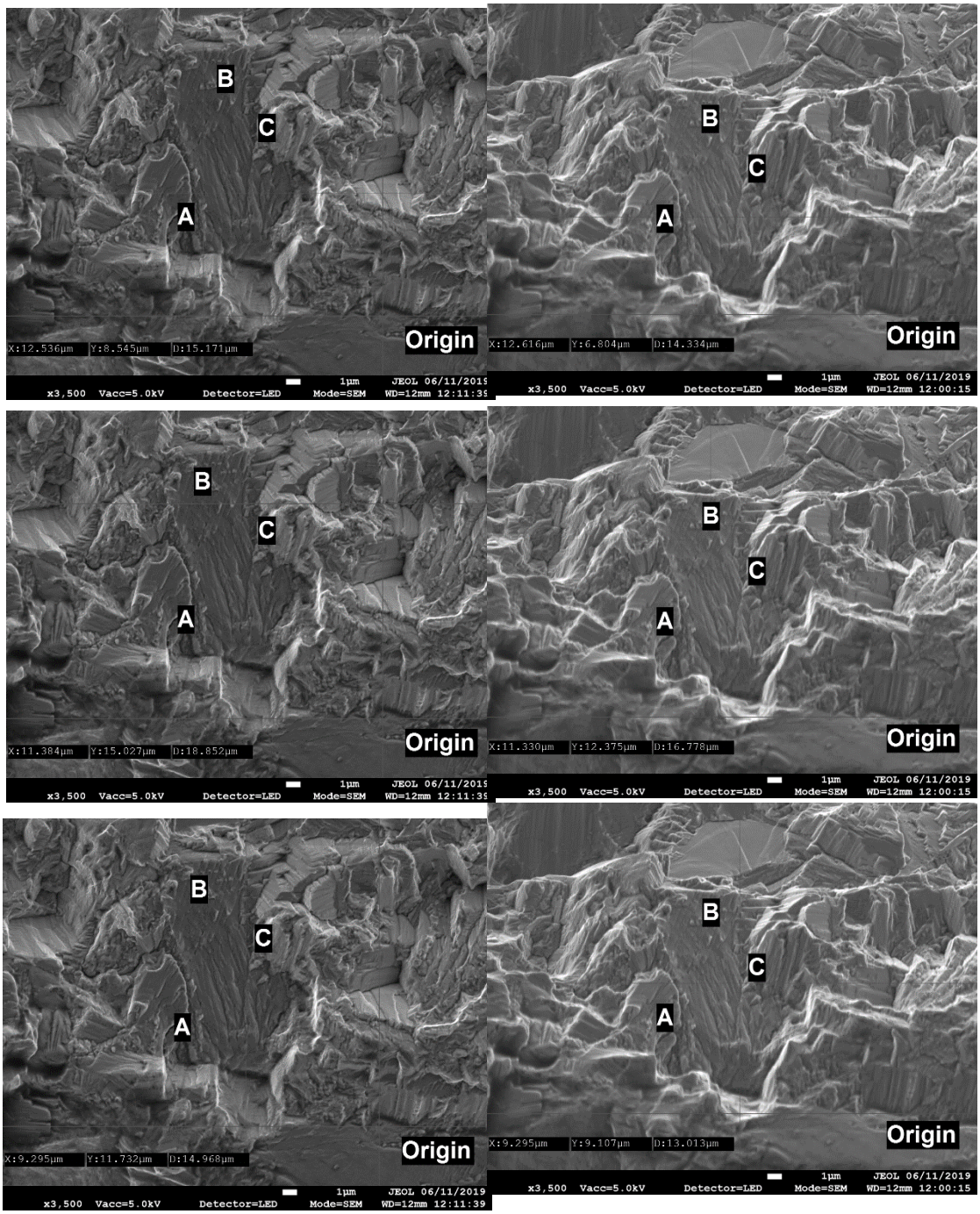

B4: Q1-4 Facet 3

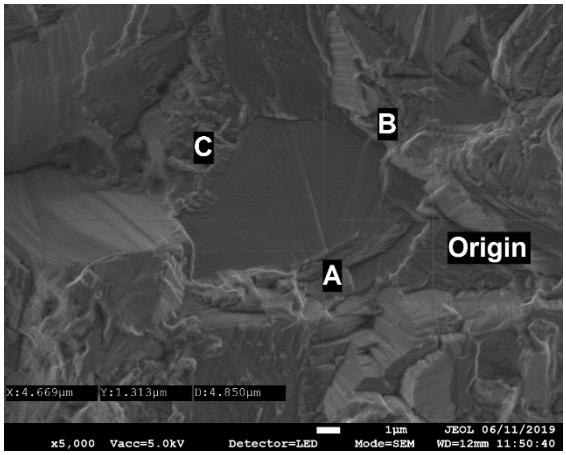

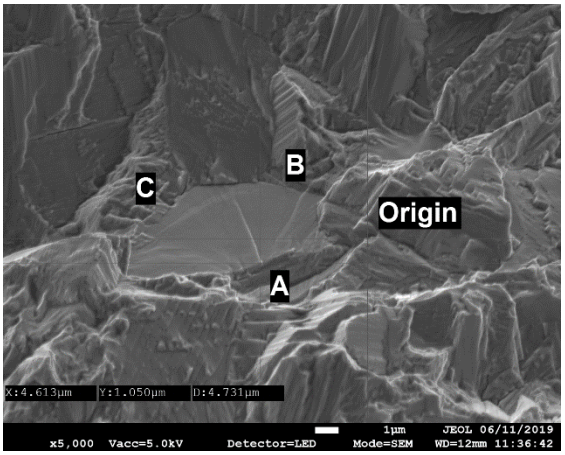

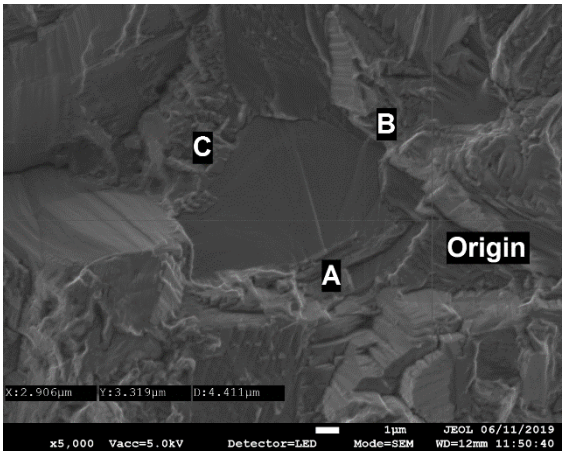

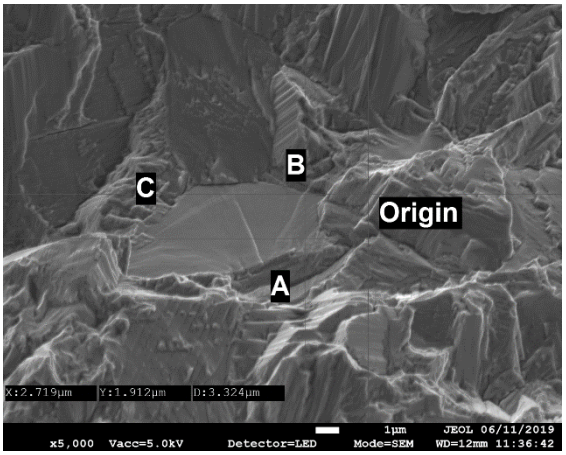

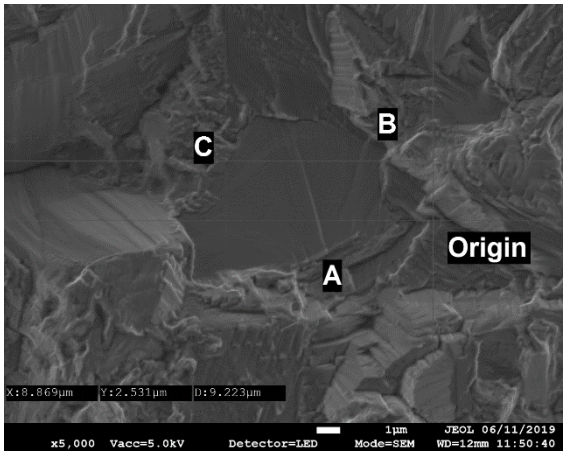

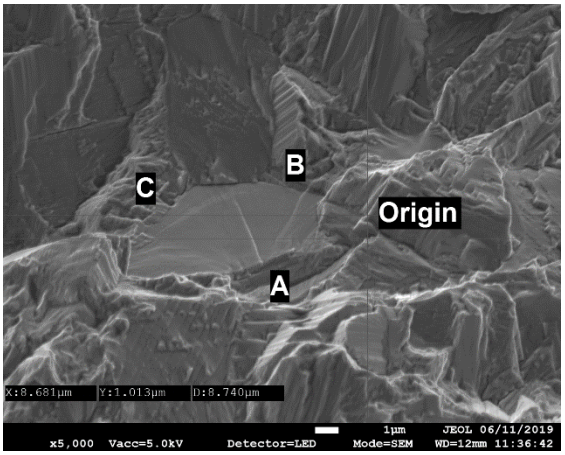

Appendix C: Facet Crystallographic Measurement Results

C1: Effect of Tilt Angle on Facet Indexing

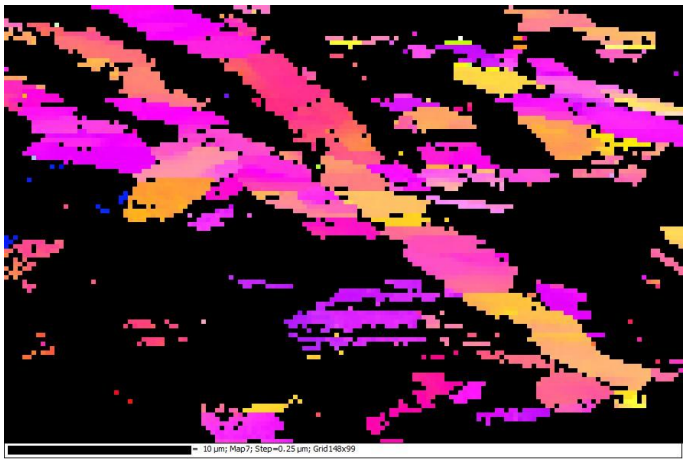

70 degrees total tilt (40 degree facet angle + 30 degrees stage tilt)

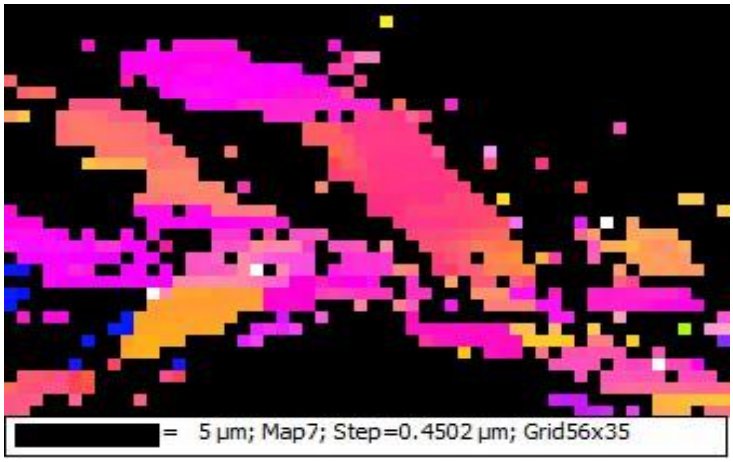

80 degrees total tilt (40 degree facet angle + 40 degree stage tilt)

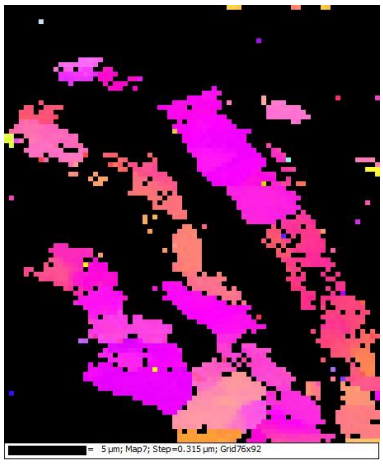

60 degree total tilt (40 degree facet angle + 20 degree stage tilt)

C2: Specimen Q1-2

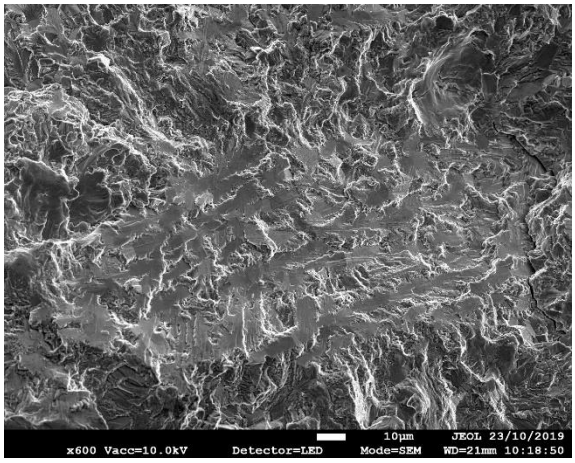

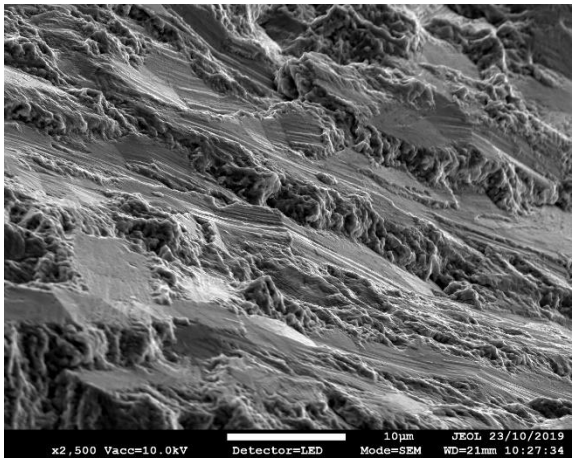

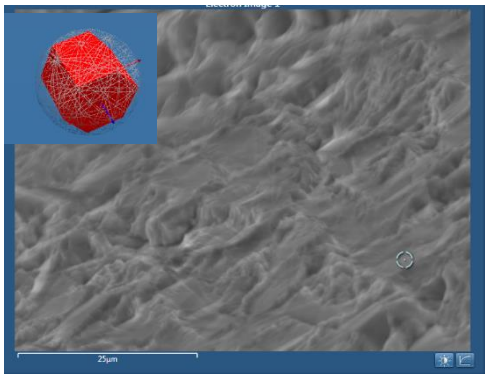

C3: Specimen Q1-5

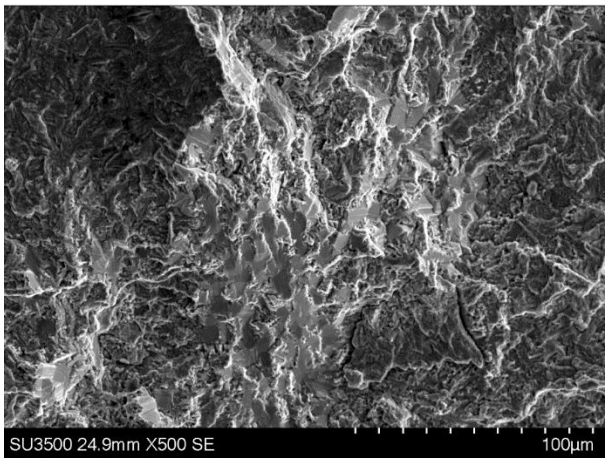

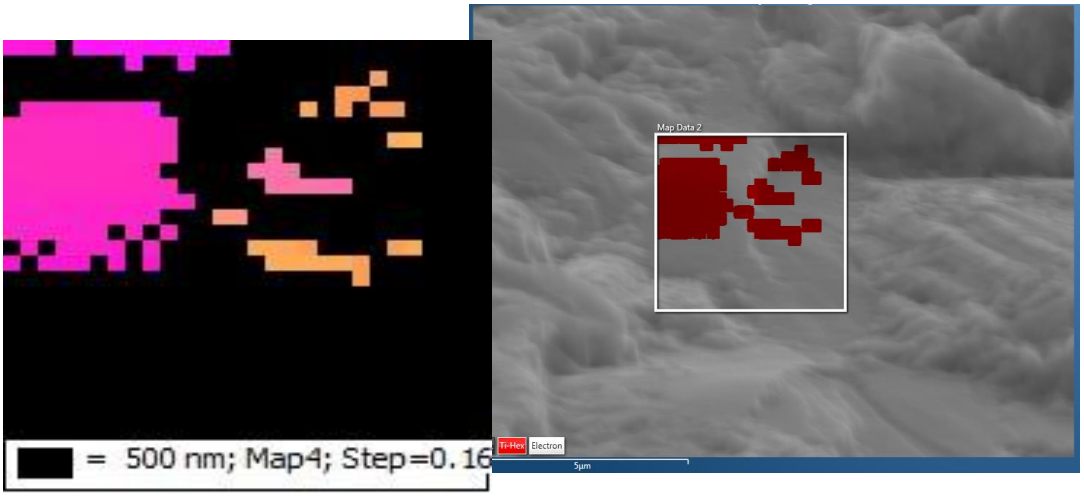

C4: Specimen 009

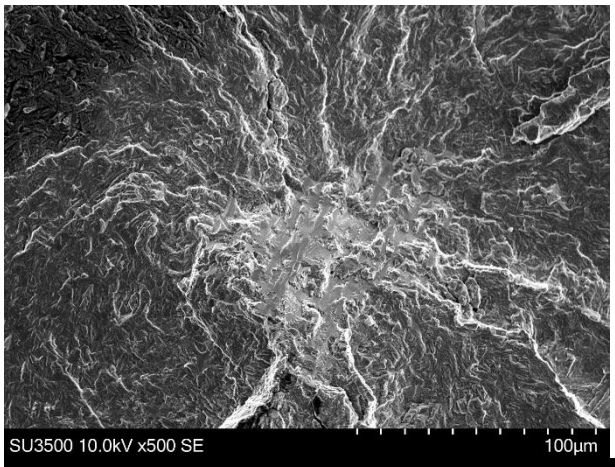

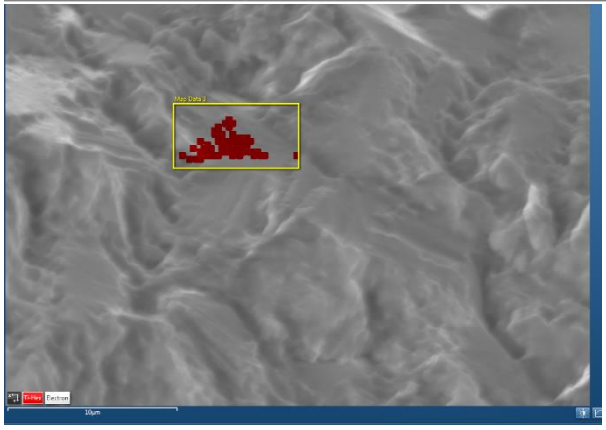

C5: Specimen 010

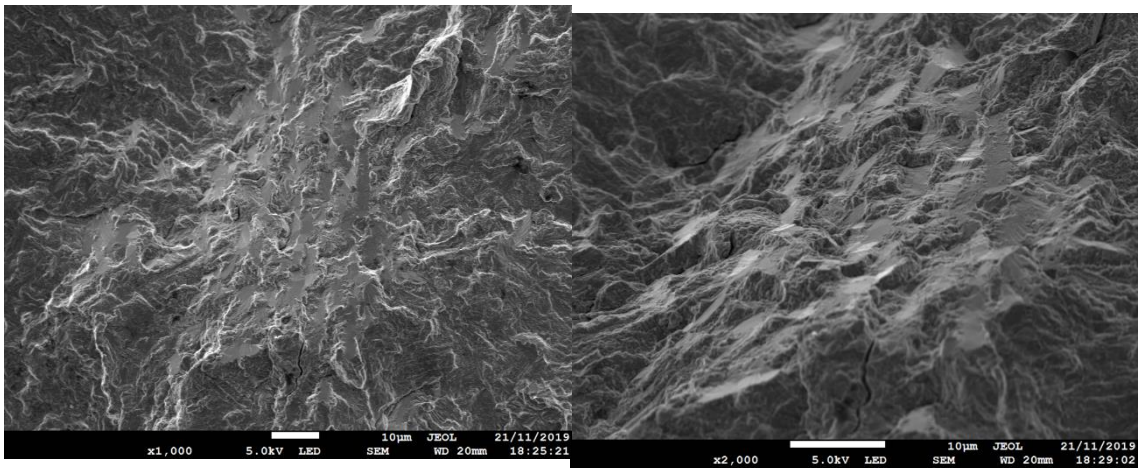

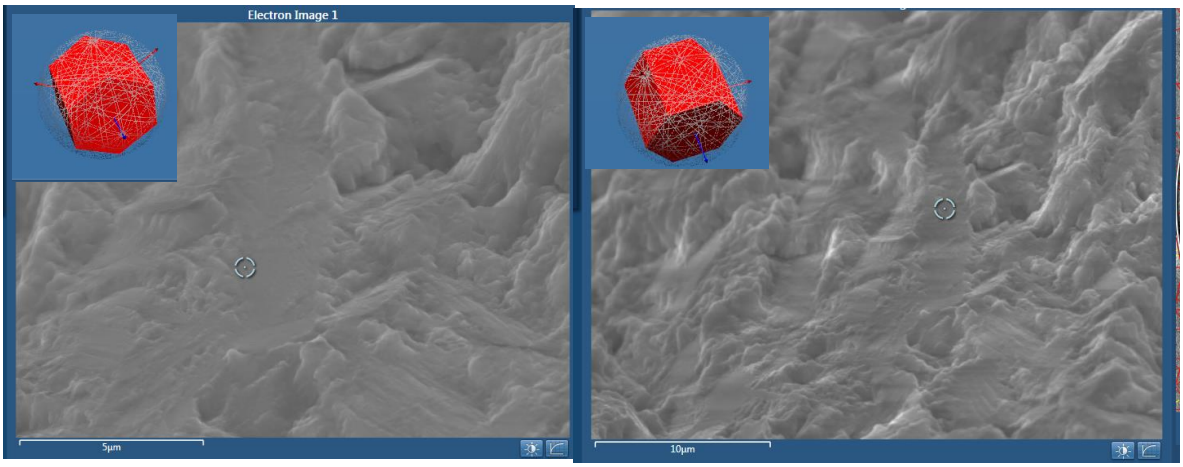

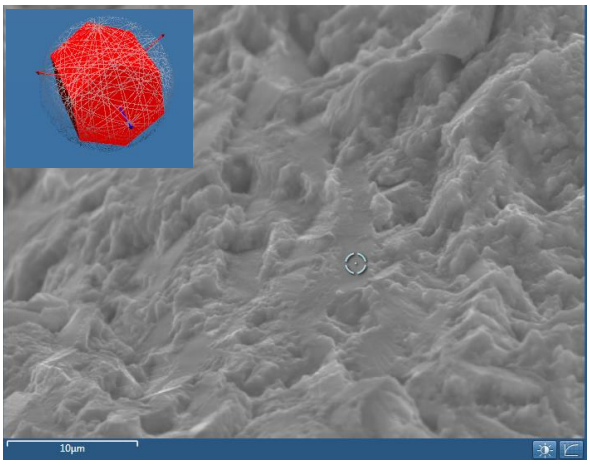

C6: Specimen 011